

ABSTRACT

THAXTON, CHRISTOPHER S., Investigations of grain size dependent sediment transport phenomena on multiple scales (under the direction of Dr. Lubos Mitas)

Sediment transport in coastal and fluvial environments resulting from short time-scale processes of disturbance such as urbanization, mining, agriculture and military operations have significant impact on channel network and shoreline morphology, downstream water quality and ecosystems, and the integrity of land use applications. The scale and spatial distribution of these effects are largely attributable to the size distribution of the sediment grains that become eligible for transport due to disturbance. An improved understanding of advective and diffusive grain size dependent sediment transport phenomena will lead to the development of more accurate predictive models and preventative measures. To this end, three studies were performed that investigate grain-size dependent sediment transport on three different scales. Discrete particle computer simulations of sheet flow bedload transport on the scale of 0.1-100 millimeters were performed on a heterogeneous population of grains of various grain sizes. The relative transport rates and diffusivities of grains under both oscillatory and uniform, steady flow conditions were quantified. These findings suggest that, due to preferential vertical sorting of the largest grains to the top of the bed, a representative grain size that is functionally dependent on the applied flow parameters should be employed when parameterizing bed roughness. On the scale of 1-10m, experiments were performed to quantify the hydrodynamics and sediment capture efficiency of various baffles installed in a sediment retention pond, a commonly used sedimentation control measure in

watershed applications. Analysis indicates that optimum sediment capture effectiveness may be achieved based on baffle permeability, pond geometry, and/or flow rate. Finally, on the scale of 10-1,000m, simulations were performed using a path sampling bivariate watershed erosion / deposition model in which grain size dependent terrain modification and pattern formation were integrated. Results correspond well to field observations and suggest that, with further refinements, the presented model may prove a valuable tool for further scientific advancement and engineering applications. Although a unique set of governing equations applies to each scale, an improved physics-based understanding of small and medium scale behavior may yield more accurate parameterization of key variables used in large scale predictive models.

INVESTIGATIONS OF GRAIN SIZE DEPENDENT SEDIMENT
TRANSPORT PHENOMENA ON MULTIPLE SCALES

by
CHRISTOPHER S. THAXTON

A dissertation submitted to the Graduate Faculty of
North Carolina State University
in partial fulfillment of the
requirements of the Degree of
Doctor of Philosophy

PHYSICS

Raleigh
2004

APPROVED BY:

Christopher Thaxton David M. Jang

Marta Eder

Co-Chair of Advisory Committee

Helena Nichols¹

Co-Chair of Advisory Committee

*In dedication to my loving parents
June and John Thaxton*

BIOGRAPHY

I was born in Lexington, Kentucky in September of 1965 and graduated from Tates Creek Senior High in Lexington in 1983. I attended the Georgia Institute of Technology in Atlanta, Georgia and earned a Bachelors Degree in Electrical Engineering with a minor in Computer Engineering in 1988. I worked at the International Business Machines Corporation in Research Triangle Park, North Carolina as a cooperative student while at Georgia Tech and became a full time employee there in 1989. After 5 years, I left IBM to pursue first a Masters Degree and then a Ph.D. in Physics at North Carolina State University in Raleigh.

The decision to leave industry marked a turning point in my life that was motivated by my passion for the study and teaching of science. Academia offered me the intellectual creativity, flexibility, and potential for growth aimed less towards the merits of enterprise and more towards a contributive understanding of nature and our roles within it. The problem solving methodologies and mathematical discipline of physics complimented my musical and engineering backgrounds and the wide range of physics applications made the subject a naturally attractive choice for my graduate studies. When coupled with my love and respect for the Earth, my scientific efforts became focused on environmental applications. This dissertation represents both the culmination of several years of study based on a life choice that originated in 1994 and a guidepost for the remainder of my career.

ACKNOWLEDGEMENTS

I wish to thank my advisory committee, Christopher Roland, Richard McLaughlin, Helena Mitasova, and Lubos Mitas. They provided the focus, motivation, and accessibility I needed to complete my work and continue to fuel my scientific creativity and professional growth.

I thank Thomas G. Drake for introducing me to the sediment transport community and for his patient encouragement during times of doubt. I thank Joseph Calantoni for sharing countless hours of insightful dialog and for the friendship and professional partnership that developed during our graduate studies together. I also thank him for his valuable contributions to Chapters 2 and 3. I thank David Pierson for his exemplary maintenance of the computer systems.

I thank Gayle and Barry Coffey for their gracious support and their unconditional acceptance of me into their family.

I thank my parents, June and John Thaxton, my Sister Sheree, and my Niece Candace for being an unwavering source of caring motivation.

Finally, I thank my dearest bride Tonya Shea Coffey whose loving understanding and tireless support made this dissertation possible.

TABLE OF CONTENTS

LIST OF FIGURES	VII
LIST OF TABLES	XIV
CHAPTER 1: INTRODUCTION	1
CHAPTER 2: DISCRETE PARTICLE SIMULATIONS OF GRAIN SIZE DEPENDENT BEDLOAD TRANSPORT	6
2.1 INTRODUCTION	6
2.2 DISCRETE PARTICLE MODEL	7
2.3 VERTICAL BEDLOAD SORTING	9
2.3.1 METHODS	11
2.3.2 RESULTS	13
2.4 REPRESENTATIVE GRAIN SIZE.....	18
2.4.1 METHODS	19
2.4.2 RESULTS	19
2.5 DIFFUSION	20
2.5.1 METHODS	21
2.5.2 RESULTS	22
2.6 DISCUSSION AND CONCLUSIONS	26
CHAPTER 3: HYDRODYNAMIC AND SEDIMENT CAPTURE ASSESSMENT OF VARIOUS BAFFLES IN A SEDIMENT RETENTION POND	28
3.1 INTRODUCTION	28
3.2 METHODS.....	31
3.3 RESULTS	36
3.3.1 HYDRODYNAMICS	36
3.3.1.1 <i>Mean Flow Field</i>	36
3.3.1.2 <i>Transverse Variance</i>	46
3.3.1.3 <i>Vertical velocities</i>	48
3.3.1.4 <i>Signal-to-Noise Ratio</i>	52
3.3.1.5 <i>Quickest Path Analysis (Clear water runs only)</i>	56
3.3.2 SEDIMENT CAPTURE	60
3.3.2.1 <i>Captured Volume</i>	60
3.3.2.2 <i>Turbidity and TSS</i>	62
3.3.2.3 <i>Grain Size Analysis</i>	63
3.4 RESULTS ANALYSIS	69
3.5 CONCLUSIONS	72
APPENDIX 3.A - HYDRODYNAMIC DATA	74
APPENDIX 3.B - VERTICAL VELOCITY MAPS.....	87
APPENDIX 3.C - VERTICAL VELOCITY STATISTICS	100

CHAPTER 4: INTEGRATION OF GRAIN-SIZE DEPENDENT TERRAIN EVOLUTION INTO DISTRIBUTED SOIL EROSION SIMULATIONS	101
4.1 INTRODUCTION	101
4.2 THEORETICAL REVIEW	102
4.2.1 WATER	102
4.2.2 SEDIMENT	106
4.3 LANDSCAPE-SCALE SEDIMENT TRANSPORT.....	111
4.3.1 THE UNIVERSAL SOIL LOSS EQUATION ((R/M)USLE)	111
4.3.2 WATER EROSION PREDICTION PROJECT (WEPP).....	113
4.3.3 SIMULATED WATER EROSION (SIMWE) MODEL	115
4.4 GRAIN-SIZE DEPENDENT SEDIMENT TRANSPORT.....	119
4.4.1 VERTICAL BEDLOAD SORTING	121
4.4.2 SOIL, LAND COVER, AND FLOW PROPERTY COEFFICIENTS	122
4.4.2.1 <i>Detachment and transport capacity coefficients</i>	123
4.4.2.2 <i>Critical Shear Stress</i>	124
4.4.3 WASH LOAD.....	124
4.4.4 SEDATE (SEDIMENT EROSION DEPOSITION AND TERRAIN EVOLUTION) MODEL: AN EXAMPLE APPLICATION	125
4.5 GRAIN SIZE DEPENDENT TERRAIN EVOLUTION IN SIMWE	132
4.5.1 GOVERNING EQUATIONS	132
4.5.2 IMPLEMENTATION VIA GRASS GIS MODULE R.TERRADYN.....	134
4.5.3 NUMERICAL STABILITY	136
4.5.4 BOUNDARY CONDITIONS	137
4.5.5 USE OF A COMPARATIVE BAND-PASS FILTER FOR TERRAIN CHANGE STABILITY	139
4.5.6 R.TERRADYN INPUT PARAMETERS.....	146
4.5.5.1 <i>Random Rainfall</i>	146
4.5.5.2 <i>Rainfall excess</i>	147
4.6 APPLICATION OF R.TERRADYN - LAKE WHEELER ROAD WATERSHED.....	149
4.6.1 BASELINE.....	151
4.6.2 RESULTS FROM DISTRIBUTED INFILTRATION	154
4.6.3 RESULTS FROM DISTRIBUTED LAND COVER.....	160
4.6.4 GRAIN SIZE DEPENDENT SIMULATIONS.....	163
4.6.4.1 <i>Investigations of soil erodibility</i>	163
4.6.4.2 <i>Terrain evolution for different soil types</i>	170
4.6.4.3 <i>Results from a disturbed watershed</i>	177
4.6.5 DISCUSSION AND CONCLUSIONS	179
APPENDIX 4.A - NEUMANN BOUNDARY ALGORITHM FOR USE WITH R.SLOPE.ASPECT	181
APPENDIX 4.B - RANDOM NUMBER GENERATOR (RNG.SH) FOR RANDOMIZING RAINFALL RATES.....	182
BIBLIOGRAPHY	183

LIST OF FIGURES

FIGURE 2.1: SNAPSHOT OF THE SIMULATION. THE LENGTH OF A FLUID SLAB (BLUE) IS PROPORTIONAL TO ITS VELOCITY. GRAINS LARGER THAN 1.5 MM DIAMETER ARE COLORED YELLOW TO AID IN VISUALIZATION OF PARTICLE SORTING PROCESSES.....	9
FIGURE 2.2: CONCENTRATION OF EACH OF THE 5 GRAIN SIZE BINS AS A FUNCTION OF DISTANCE FROM THE FIXED BOTTOM AFTER (A) 1 AND (B) 10, 6-SEC WAVE PERIODS. THE MAXIMUM FREE STREAM VELOCITY (U_{MAX}) WAS 1.0 M/S AND THE WAVEFORM PARAMETER (Φ) WAS $\pi/2$	13
FIGURE 2.3: THE MASS TRANSPORT RATE AS A FUNCTION OF TIME FOR THE OSCILLATORY SIMULATIONS. THE MAXIMUM FREE STREAM VELOCITY (U_{MAX}) WAS 1.0 M/S AND THE WAVEFORM PARAMETER (Φ) WAS $\pi/2$. AFTER 4 WAVE PERIODS, THE BED BECAME FULLY SORTED AND MAINTAINED APPROXIMATE EQUILIBRIUM UP TO AND BEYOND 10 WAVE PERIODS.....	14
FIGURE 2.4: CONCENTRATION OF EACH OF THE 5 GRAIN SIZE BINS AS A FUNCTION OF DISTANCE FROM THE FIXED BOTTOM AFTER (A) 1 SECOND AND (B) 20 SECONDS OF STEADY FLOW. THE MAXIMUM FREE STREAM VELOCITY (U_{MAX}) WAS 1.0 M/S.....	15
FIGURE 2.5: THE MASS TRANSPORT RATE AS A FUNCTION OF TIME FOR THE STEADY FLOW SIMULATIONS. THE MAXIMUM FREE STREAM VELOCITY (U_{MAX}) WAS 1.0 M/S. AFTER 4 SECONDS, THE BED BECAME FULLY SORTED AND MAINTAINED APPROXIMATE EQUILIBRIUM UP TO AND BEYOND 10 SECONDS.....	15
FIGURE 2.6: MOBILITY (FLUX/CONCENTRATION) FOR EACH SIZE BIN BY DEPTH FOR THE OSCILLATORY SIMULATIONS WITH MAXIMUM FREE STREAM VELOCITY (U_{MAX}) OF 1.0 M/S AND WAVEFORM PARAMETER (Φ) OF $\pi/2$	17
FIGURE 2.7: MOBILITY (FLUX/CONCENTRATION) FOR EACH SIZE BIN BY DEPTH FOR THE STEADY FLOW SIMULATIONS WITH MAXIMUM FREE STREAM VELOCITY (U_{MAX}) OF 1.0 M/S.....	18
FIGURE 2.8: THE REPRESENTATIVE GRAIN SIZES FOR THE THREE DIFFERENT WAVEFORMS (INSET) ARE IDENTIFIED WHERE THE PLOT OF THE % ERROR OF FIXED GRAIN-SIZE FLUX TO HETEROGENEOUS FLUX IS ZERO. THE CURVES REPRESENT A SECOND ORDER POLYNOMIAL FIT TO THE ACTUAL SIMULATION DATA.....	20
FIGURE 2.9: DIFFUSIVITIES FOR THE (A) SMALL ($D=0.9$ MM) AND (B) LARGE ($D=1.4$ MM) GRAINS FOR THE MAXIMUM FREE STREAM VELOCITY OF 1.0 M/S. NOTE THAT THE Y-AXES OF (A) AND (B) ARE ON DIFFERENT SCALES SUCH THAT THE DIFFUSIVITIES FOR THE SMALL GRAINS AT THE VARIOUS BED COMPOSITIONS CAN BE VISUALLY DISTINGUISHED.....	23
FIGURE 2.10: DIMENSIONLESS RATIO OF DIFFUSIVE TO ADVECTIVE FLUX FOR THE SMALL GRAINS (0.9 MM DIAMETER) AVERAGED OVER WAVE SHAPE (ϕ) FOR THE THREE MAXIMUM WAVE VELOCITIES AS A FUNCTION OF BED COMPOSITION. THE DEVIATIONS FROM FIT FOR THE $C=0.16$ SIMULATIONS CORRESPOND TO THE HIGH VARIANCE ASSOCIATED WITH NEAR-ZERO FLUX VALUES FOR THE SMALLEST GRAINS. THESE OUTLYING VALUES WERE NOT USED IN DETERMINING THE EMPIRICAL FIT (EQUATION 2.8).....	25
FIGURE 2.11: DIMENSIONLESS RATIO OF DIFFUSIVE TO ADVECTIVE FLUX FOR THE LARGE GRAINS (1.4 MM DIAMETER) AVERAGED OVER WAVE SHAPE (ϕ) FOR THE THREE MAXIMUM WAVE VELOCITIES AS A FUNCTION OF BED COMPOSITION.....	26
FIGURE 3.1. (A) PICTURE OF THE SEDIMENT RETENTION POND USED IN THE EXPERIMENTS. (B) GEOMETRY OF THE RETENTION POND AND THE LOCATION OF THE 5x5 DATA ACQUISITION GRID. THERE ARE ALSO 2 DEPTH LAYERS ALONG THE Z DIRECTION (NOT SHOWN) AT 0.13 M AND 0.26 M BELOW THE STILL POND SURFACE. FLOW IS LEFT-TO-RIGHT.....	33
FIGURE 3.2A. SURFACE-PARALLEL (PLAN VIEW) PROJECTION OF THE MEAN (TIME-AVERAGED) VELOCITIES (M/S) FOR FREE FLOW (NO BAFFLES) AT 28 L/S INFLOW RATE FOR THE CLEAR WATER RUNS. FLOW DIRECTION IS INDICATED BY THE ANGULAR DEVIATION FROM HORIZONTAL AND THE VELOCITY MAGNITUDE BY THE LENGTH OF THE RAY.....	38
FIGURE 3.2B. SURFACE-PARALLEL (PLAN VIEW) PROJECTION OF THE MEAN (TIME-AVERAGED) VELOCITIES (M/S) FOR FREE FLOW (NO BAFFLES) AT 42 L/S FLOW FOR THE CLEAR WATER RUNS. FLOW DIRECTION IS INDICATED BY THE ANGULAR DEVIATION FROM HORIZONTAL AND THE VELOCITY MAGNITUDE BY THE LENGTH OF THE RAY.....	39

FIGURE 3.3. SURFACE-PARALLEL (PLAN VIEW) PROJECTION OF THE MEAN (TIME-AVERAGED) VELOCITIES (M/S) FOR THE SILT FENCE BAFFLE CONFIGURATION AT 28 L/S FOR THE CLEAR WATER RUNS. FLOW DIRECTION IS INDICATED BY THE ANGULAR DEVIATION FROM HORIZONTAL AND THE VELOCITY MAGNITUDE BY THE LENGTH OF THE RAY.....	40
FIGURE 3.4. SURFACE-PARALLEL (PLAN VIEW) PROJECTION OF THE MEAN (TIME-AVERAGED) VELOCITIES (M/S) FOR THE TREE BAFFLE CONFIGURATION AT 28 L/S FLOW RATE FOR THE CLEAR WATER RUNS. FLOW DIRECTION IS INDICATED BY THE ANGULAR DEVIATION FROM HORIZONTAL AND THE VELOCITY MAGNITUDE BY THE LENGTH OF THE RAY.....	41
FIGURE 3.5. SURFACE-PARALLEL (PLAN VIEW) PROJECTION OF THE MEAN (TIME-AVERAGED) VELOCITIES (M/S) FOR THE JUTE/COIR BAFFLE CONFIGURATION AT 28 L/S FOR THE CLEAR WATER RUNS. FLOW DIRECTION IS INDICATED BY THE ANGULAR DEVIATION FROM HORIZONTAL AND THE VELOCITY MAGNITUDE BY THE LENGTH OF THE RAY.....	42
FIGURE 3.6: THE DEPTH-AVERAGED MEAN FLOW VELOCITY MAGNITUDE (SEE TEXT) FOR EACH FLOW RATE AVERAGED ALONG THE 5 TRANSVERSE GIRD POINTS PER X GRID POSITION FOR (A) 14 L/s, (B) 28 L/s, AND (C) 42 L/s. THIS IS FROM THE CLEAR WATER RUNS.....	45
FIGURE 3.7: THE DEPTH-AVERAGED MEAN FLOW VELOCITY MAGNITUDE (SEE TEXT) FOR EACH FLOW RATE AVERAGED ALONG THE 5 TRANSVERSE GIRD POINTS PER X GRID POSITION FOR (A) 14 L/s, (B) 28 L/s, AND (C) 42 L/s. THIS IS FROM THE SEDIMENT LADEN RUNS.....	45
FIGURE 3.8: THE DEPTH-AVERAGED MEAN FLOW VELOCITY MAGNITUDE (SEE TEXT) FOR EACH FLOW RATE AVERAGED ALONG THE 5 TRANSVERSE GIRD POINTS PER X GRID POSITION FOR (A) 14 L/s, (B) 28 L/s, AND (C) 42 L/s. THIS IS THE AVERAGE OF THE DATA FROM THE CLEAR WATER AND THE SEDIMENT LADEN RUNS.....	48
FIGURE 3.9. FOR EACH DEPTH, THE MEAN FLOW VELOCITY MAGNITUDE AND THE X- COMPONENT OF THE FLOW VELOCITY WERE AVERAGED OVER THE X AND Y DIRECTIONS FOR EACH CONFIGURATION AT THE 28 L/s FLOW RATE. THE JUTE/COIR BAFFLE MAINTAINS THE SMALLEST VERTICAL GRADIENT AVERAGED OVER THE FLOW FIELD INDICATIVE OF A HIGH TURBULENT ENERGY DIFFUSION RATE.....	48
FIGURE 3.10: A COMPOSITE OF DEPTH-AVERAGED VERTICAL VELOCITIES FOR THE CLEAR WATER RUNS AT 28 L/s.....	49
FIGURE 3.11: DEPTH AVERAGED VERTICAL VELOCITIES FOR THE SILT FENCE AT 28 L/s FOR (A) THE CLEAR WATER RUNS AND (B) THE SEDIMENT LADEN RUNS. APPROXIMATE BAFFLE LOCATIONS ARE INDICATED BY WHITE LINES. FLOW IS LEFT TO RIGHT.....	50
FIGURE 3.12: DEPTH AVERAGED VERTICAL VELOCITIES FOR THE SILT FENCE (SEDIMENT LADEN RUNS) AT (A) 14 L/s, (B) 28 L/s, AND (C) 42 L/s. APPROXIMATE BAFFLE LOCATIONS ARE INDICATED BY WHITE LINES. FLOW IS LEFT TO RIGHT.....	51
FIGURE 3.13: VERTICAL VELOCITY DATA PRESENTED FOR THE SILT BAFFLE SUGGESTS THAT, AT 28 L/s AND 42 L/s FLOW RATES, INDEPENDENT ZONES OF FLOW DIRECTION-ORTHOGONAL ROTATION ("SUB BASINS") DEVELOPED, INHIBITING NEW SEDIMENT FROM ENTERING THE SUB BASINS. THE SUB BASINS WERE ENERGIZED BY THE SHEAR STRESS APPLIED BY THE OVERTOPPING FLOW OBSERVED AT 28 L/s AND 42 L/s FLOW RATES (SILT BAFFLE ONLY).	52
FIGURE 3.14. SNR_x (THE DEPTH-AVERAGED SIGNAL TO NOISE RATIO, AVERAGED ACROSS THE TRANSVERSE (Y) DIRECTION PER X GRID POSITION) FOR FLOW RATES OF (A) 14 L/s, (B) 28 L/s, (C) 42 L/s.AVERAGED OVER ALL INFLOW RATES FOR THE CLEAR WATER RUNS.	54
FIGURE 3.15: THE DEPTH AVERAGED SIGNAL TO NOISE RATIO (SNR), AVERAGED TRANSVERSELY AND ACROSS ALL FLOW RATES, FOR THE (A) CLEAR WATER RUNS AND (B) THE SEDIMENT LADEN RUNS. (C) SHOWS THE REMAINDER WHEN (A) IS SUBTRACTED FROM (B), INDICATIVE OF THE SEDIMENT IN SUSPENSION.	55
FIGURE 3.16. AN EXAMPLE OF THE QUICKEST PATH DETERMINATION FOR THE JUTE/COIR BAFFLE CONFIGURATION AT 42 L/s FOR THE CLEAR WATER RUNS. THE VALUES AT EACH GRID POINT REPRESENT THE DEPTH-AVERAGED LONGITUDINAL (X) COMPONENT OF THE FLOW VELOCITIES AND ARE IN MM/s. THE RESULTING 5 VALUES, 1 PER X GRID POSITION (SHADED), WERE AVERAGED TO YIELD AN AVERAGE MAXIMUM MEAN FLOW VELOCITY, OR QUICKEST PATH VELOCITY, V_{QP} (SEE TEXT), THAT WAS USED IN PROJECTING A THEORETICAL POND TRAPPING EFFECTIVENESS.	57
FIGURE 3.17. ESTIMATE OF THE MINIMUM GRAIN CAPTURE SIZE ALONG THE QUICKEST PATH OF FLOW BASED ON STOKE'S SETTLING. ALL OTHER PATHS THROUGH THE POND RESULT IN HIGHER RESIDENCE TIMES, THEREFORE, THIS CHART ILLUSTRATES THE WORST CASE MINIMUM CAPTURE SIZE. THE JUTE/COIR BAFFLE MAY CAPTURE FINER PARTICLES (30-45MM) THAN THE FREE FLOW CASE (65-90MM).....	59

FIGURE 3.18: AN ESTIMATE OF THE VOLUME OF CAPTURED SEDIMENT AS A PERCENT OF SEDIMENT INJECTED.	60
FIGURE 3.19: THE DEPOSITION PATTERNS INTERPOLATED FROM THE 16 SOIL ACCUMULATION DEPTH SAMPLING POINTS. APPROXIMATE BAFFLES LOCATIONS ARE INDICATED WITH BLACK LINES.	61
FIGURE 3.20: TOTAL SUSPENDED SOLIDS AND TURBIDITY OBTAINED AT THE POND OUTLET.	62
FIGURE 3.21: MEASURED EXIT TURBIDITY OVER THE COURSE OF A SINGLE 40 MINUTE RUN (28 L/S SILT FENCE).	63
FIGURE 3.22: THE CORRECTED D_{50} (SEE TEXT) FOR EACH CONFIGURATION ACROSS THE POND LENGTH, WHICH INDICATES GRAIN SIZE DISTRIBUTIONS ONLY.	65
FIGURE 3.23: HYDROMETER RESULTS FOR EACH CONFIGURATION, AS A PERCENT OF THE 40G SAMPLES SUMMED OVER ALL 16 SAMPLE GRID LOCATION, CORRESPONDING TO FIGURE 3.20.	65
FIGURE 3.24: HERE, FIGURE 3.23 IS ADJUSTED BY MULTIPLYING BY THE VOLUME OF CAPTURED SEDIMENT AS A PERCENT OF THE INPUT SEDIMENT VOLUME PER CONFIGURATION (E.G. FIGURE 3.18).	66
FIGURE 3.25: THE TRANSVERSE-AVERAGED MEDIAN CAPTURE GRAIN SIZE AT THE X-GRID POSITION NEAREST THE EXIT ($X=5$) FOR EACH CONFIGURATION.	67
FIGURE 3.26: THE SAND SIEVE ANALYSIS RESULTS FOR EACH CONFIGURATION. THE TRANSVERSE-AVERAGED MEDIAN SAND GRAIN SIZE FOR EACH X-GRID POSITION IS PLOTTED SEPARATELY FOR THE (A) FREE FLOW, (B) SILT FENCE, (C) TREE PROTECTION FENCE, AND (D) JUTE/COIR.	68
FIGURE 3.27: (A) THE PROJECTED MEDIAN GRAIN CAPTURE DIAMETER ($D(V1)$) (BASED ON STOKE'S SETTLING AND THE MEASURED FLOW VELOCITIES) COMPARED TO THE D_{50} COMPUTED FROM THE SOIL SAMPLES AT THE X-GRID LOCATION NEAREST THE EXIT. (B) THE MEASURED TURBIDITY AND ESTIMATED VOLUME WITHIN THE MEASUREMENT GRID EXPRESSED AS A PERCENT OF THE VOLUME OF SEDIMENT INJECTED PER BAFFLE CONFIGURATION.	70
FIGURE 3.28: THE MEASURED MEDIAN GRAIN SIZE OF CAPTURED SEDIMENT VERSUS MEASURED BAFFLE OPEN PORE SPACE (OSP) - AN INDICATOR OF BAFFLE HYDRAULIC PERMEABILITY. FINDINGS SUGGEST THAT AN OPTIMAL PERMEABILITY EXISTS.	71
FIGURE 3.A.1: SEDIMENT RETENTION POND LAYOUT AND DIMENSIONS.	74
FIGURE 3.B.0: SEDIMENT RETENTION POND LAYOUT AND DIMENSIONS.	87
FIGURE 3.B.1: FREE FLOW AT 14 L/S FOR THE CLEAR WATER RUN. FLOW IS LEFT TO RIGHT.	88
FIGURE 3.B.2: FREE FLOW AT 14 L/S FOR THE SEDIMENT LADEN RUN. FLOW IS LEFT TO RIGHT.	88
FIGURE 3.B.3: FREE FLOW AT 28 L/S FOR THE CLEAR WATER RUN. FLOW IS LEFT TO RIGHT.	89
FIGURE 3.B.4: FREE FLOW AT 28 L/S FOR THE SEDIMENT LADEN RUN. FLOW IS LEFT TO RIGHT.	89
FIGURE 3.B.5: FREE FLOW AT 42 L/S FOR THE CLEAR WATER RUN. FLOW IS LEFT TO RIGHT.	90
FIGURE 3.B.6: FREE FLOW AT 42 L/S FOR THE SEDIMENT LADEN RUN. FLOW IS LEFT TO RIGHT.	90
FIGURE 3.B.7: SILT FENCE AT 14 L/S FOR THE CLEAR WATER RUN. APPROXIMATE BAFFLE LOCATIONS INDICATED BY WHITE LINES. FLOW IS LEFT TO RIGHT.	91
FIGURE 3.B.8: SILT FENCE AT 14 L/S FOR THE SEDIMENT LADEN RUN. APPROXIMATE BAFFLE LOCATIONS INDICATED BY WHITE LINES. FLOW IS LEFT TO RIGHT.	91
FIGURE 3.B.9: SILT FENCE AT 28 L/S FOR THE CLEAR WATER RUN. APPROXIMATE BAFFLE LOCATIONS INDICATED BY WHITE LINES. FLOW IS LEFT TO RIGHT.	92
FIGURE 3.B.10: SILT FENCE AT 28 L/S FOR THE SEDIMENT LADEN RUN. APPROXIMATE BAFFLE LOCATIONS INDICATED BY WHITE LINES. FLOW IS LEFT TO RIGHT.	92
FIGURE 3.B.11: SILT FENCE AT 42 L/S FOR THE CLEAR WATER RUN. APPROXIMATE BAFFLE LOCATIONS INDICATED BY WHITE LINES. FLOW IS LEFT TO RIGHT.	93
FIGURE 3.B.12: SILT FENCE AT 42 L/S FOR THE SEDIMENT LADEN RUN. APPROXIMATE BAFFLE LOCATIONS INDICATED BY WHITE LINES. FLOW IS LEFT TO RIGHT.	93
FIGURE 3.B.13: TREE PROTECTION FENCE AT 14 L/S FOR THE CLEAR WATER RUN. APPROXIMATE BAFFLE LOCATIONS INDICATED BY WHITE LINES. FLOW IS LEFT TO RIGHT.	94
FIGURE 3.B.14: TREE PROTECTION FENCE AT 14 L/S FOR THE SEDIMENT LADEN RUN. APPROXIMATE BAFFLE LOCATIONS INDICATED BY WHITE LINES. FLOW IS LEFT TO RIGHT.	94
FIGURE 3.B.15: TREE PROTECTION FENCE AT 28 L/S FOR THE CLEAR WATER RUN. APPROXIMATE BAFFLE LOCATIONS INDICATED BY WHITE LINES. FLOW IS LEFT TO RIGHT.	95
FIGURE 3.B.16: TREE PROTECTION FENCE AT 28 L/S FOR THE SEDIMENT LADEN RUN. APPROXIMATE BAFFLE LOCATIONS INDICATED BY WHITE LINES. FLOW IS LEFT TO RIGHT.	95
FIGURE 3.B.17: TREE PROTECTION FENCE AT 42 L/S FOR THE CLEAR WATER RUN. APPROXIMATE BAFFLE LOCATIONS INDICATED BY WHITE LINES. FLOW IS LEFT TO RIGHT.	96

FIGURE 3.B.18: TREE PROTECTION FENCE AT 42 L/S FOR THE SEDIMENT LADEN RUN. APPROXIMATE BAFFLE LOCATIONS INDICATED BY WHITE LINES. FLOW IS LEFT TO RIGHT.....	96
FIGURE 3.B.19: JUTE/COIR AT 14 L/S FOR THE CLEAR WATER RUN. APPROXIMATE BAFFLE LOCATIONS INDICATED BY WHITE LINES. FLOW IS LEFT TO RIGHT.	97
FIGURE 3.B.20: JUTE/COIR AT 14 L/S FOR THE SEDIMENT LADEN RUN. APPROXIMATE BAFFLE LOCATIONS INDICATED BY WHITE LINES. FLOW IS LEFT TO RIGHT.	97
FIGURE 3.B.21: JUTE/COIR AT 28 L/S FOR THE CLEAR WATER RUN. APPROXIMATE BAFFLE LOCATIONS INDICATED BY WHITE LINES. FLOW IS LEFT TO RIGHT.	98
FIGURE 3.B.22: JUTE/COIR AT 28 L/S FOR THE SEDIMENT LADEN RUN. APPROXIMATE BAFFLE LOCATIONS INDICATED BY WHITE LINES. FLOW IS LEFT TO RIGHT.	98
FIGURE 3.B.23: JUTE/COIR AT 42 L/S FOR THE CLEAR WATER RUN. APPROXIMATE BAFFLE LOCATIONS INDICATED BY WHITE LINES. FLOW IS LEFT TO RIGHT.	99
FIGURE 3.B.24: JUTE/COIR AT 42 L/S FOR THE SEDIMENT LADEN RUN. APPROXIMATE BAFFLE LOCATIONS INDICATED BY WHITE LINES. FLOW IS LEFT TO RIGHT.	99
 FIGURE 4.1: A MODIFICATION OF FOSTER & MEYER (1972) IN WHICH GRAIN-SIZE DEPENDENT PROCESSES HAVE BEEN INCLUDED. GRAIN SIZE SORTING OCCURS IN THE BED (BEDLOAD) WHEN STRESS IS APPLIED TO AN ERODIBLE (MOVABLE) BED. GRAINS ARE DETACHED AND DEPOSITED PREFERENTIALLY – FOR DETACHMENT, THE SIZE OF ENTRAINED GRAINS IS PROPORTIONAL TO THE APPLIED STRESS AND FOR DEPOSITION, LARGE GRAINS SETTLE FIRST.	120
FIGURE 4.2: A SIMPLE DOWNWARD SLOPE OF ANGLE 5.7^0 WITH $H=0.01$ M, USING THE INPUT PARAMETERS FOR CLAY: $\Sigma=0.009$ ($C_d=9E^{-5}$, $C_r=0.01$), $T_c=0.01$, $T_f=0$, $V_f=0.003$. TERRAIN CHANGE IS EXAGGERATED BY 2X. MODELS RAINFALL FOR 1 HOUR OF REAL TIME.	127
FIGURE 4.3: A SIMPLE DOWNWARD SLOPE OF ANGLE 5.7^0 WITH $H=0.01$ M, USING THE INPUT PARAMETERS FOR SILT: $\Sigma=0.074$ ($C_d=7.4E^{-4}$, $C_r=0.01$), $T_c=0.01$, $T_f=0$, $V_f=0.074$. MODELS RAINFALL FOR 1 HOUR OF REAL TIME.	128
FIGURE 4.4: A SIMPLE DOWNWARD SLOPE OF ANGLE 5.7^0 WITH $H=0.01$ M, USING THE INPUT PARAMETERS FOR SAND: $\Sigma=22$ ($C_d=0.22$, $C_r=0.01$), $T_c=0.01$, $T_f=0$, $V_f=0.381$. MODELS RAINFALL FOR 1 HOUR OF REAL TIME.	129
FIGURE 4.5: A TERRACED HILLSLOPE WITH $\Sigma=0.01$ (CLAY-SILT SIZED PARTICLES).	130
FIGURE 4.6: A TERRACED HILLSLOPE WITH $\Sigma=1.0$ (SMALL GRAVEL SIZED PARTICLES).	130
FIGURE 4.7: TERRACED HILLSLOPE - ON THE HILLSLOPES, $\Sigma=0.01$ (CLAY) AND ON THE TERRACES, $\Sigma=1.0$ (GRAVEL). THE SMOOTHING ALGORITHM (DIFFUSION) WAS EMPLOYED TO DETER UNRECOVERABLE INSTABILITIES ON THE DOWNSLOPE SIDE OF THE GRAVEL TERRACES.	131
FIGURE 4.8: FLOWCHART OF <i>R.TERRADYN</i> MODULE.	135
FIGURE 4.9: EXAMPLE OF A POORLY DEFINED REGION (BOX) FOR SIMWE AND <i>R.TERRADYN</i> SIMULATIONS. THE ARROWS INDICATE ZONES OF HIGH WATER AND SEDIMENT FLUX THAT WOULD BE EXCLUDED, UNLESS THEY ARE DEFINED AT THE BOUNDARIES MANUALLY.	138
FIGURE 4.10: THE HISTOGRAM OF REQUESTED ELEVATION CHANGES FOR ANY GIVEN RASTER CELL. THE X-AXIS REPRESENTS THE DISCRETE SERIES OF BINS OF REQUESTED HEIGHT CHANGE, THE Y-AXIS IS THE FREQUENCY (OR NUMBER OF CELLS) PER BIN	140
FIGURE 4.11: SAMPLE OF LAKE WHEELER ROAD WATERSHED (A) CHANGE IN TERRAIN VIA CONTINUITY WITHOUT FILTERING OR DIFFUSION OVER ONE TIME STEP; (B) SAME AS (A) BUT WITH BAND-PASS FILTER APPLIED WITH $\Sigma=0M$, $A=0$, AND <i>R.NEIGHBORS</i> AVERAGING SIZE=3. ELEVATION LEGEND IS IN METERS.....	142
FIGURE 4.12: SAMPLE OF LAKE WHEELER ROAD WATERSHED (A) CHANGE IN TERRAIN VIA CONTINUITY WITHOUT FILTERING OR DIFFUSION OVER ONE TIME STEP; (B) SAME AS (A) BUT WITH BAND-PASS FILTER APPLIED WITH $\Sigma=0M$, $A=0$, AND <i>R.NEIGHBORS</i> AVERAGING SIZE=5. ELEVATION LEGEND IS IN METERS.....	142
FIGURE 4.13: SAMPLE OF LAKE WHEELER ROAD WATERSHED (A) CHANGE IN TERRAIN VIA CONTINUITY WITHOUT FILTERING OR DIFFUSION OVER ONE TIME STEP; (B) SAME AS (A) BUT WITH BAND-PASS FILTER APPLIED WITH $\Sigma=0M$, $A=0$, AND <i>R.NEIGHBORS</i> AVERAGING SIZE=25. ELEVATION LEGEND IS IN METERS.....	142
FIGURE 4.14: A COMPARISON OF HISTOGRAMS FOR THE SAME LAKE WHEELER WATERSHED SECTION AS IN FIGURE 4.11. THE BAND-PASS FILTER IS APPLIED WITH <i>R.NEIGHBORS</i> AVERAGING SIZE=25 AND $A=0.5$. Σ VALES OF $0.01M$, $0.005M$, AND $0.001M$ ARE SHOWN WITH THE UNFILTERED HISTOGRAM.	144

FIGURE 4.15: APPLICATION OF THE BAND-PASS FILTER CORRESPONDING TO FIGURE 4.14 WITH <i>R.NEIGHBORS</i> AVERAGING SIZE=25 AND A=0.5. (A) ORIGINAL UNFILTERED TERRAIN CHANGE WITH NO DIFFUSION FOR ONE TIME ITERATION (B) WITH $\Sigma=0.01\text{m}$, (C) $\Sigma=0.005\text{m}$, (D) $\Sigma=0.001\text{m}$. ELEVATION LEGEND IS IN METERS.....	144
FIGURE 4.16: A COMPARISON OF HISTOGRAMS FOR THE SAME LAKE WHEELER WATERSHED SECTION AS IN FIGURE 4.11. THE BAND-PASS FILTER IS APPLIED WITH <i>R.NEIGHBORS</i> AVERAGING SIZE=25 AND A=0.1. Σ VALES OF 0.01M, 0.005M, AND 0.001M ARE SHOWN WITH THE UNFILTERED HISTOGRAM.	145
FIGURE 4.17: APPLICATION OF THE BAND-PASS FILTER CORRESPONDING TO FIGURE 4.16 WITH <i>R.NEIGHBORS</i> AVERAGING SIZE=25 AND A=0.1. (A) ORIGINAL UNFILTERED TERRAIN CHANGE WITH NO DIFFUSION FOR ONE TIME ITERATION (B) WITH $\Sigma=0.01\text{m}$, (C) $\Sigma=0.005\text{m}$, (D) $\Sigma=0.001\text{m}$. ELEVATION LEGEND IS IN METERS.....	145
FIGURE 4.18: THE LAKE WHEELER ROAD FARM WATERSHED AT NC STATE UNIVERSITY. LAND COVER IS INDICATED BY THE COLOR KEY. SIMULATIONS WERE PERFORMED ON THE SUB-REGION INDICATED BY THE BOX. ..	150
FIGURE 4.19: THE MASTER COLOR KEYS FOR ALL RESULTS PRESENTED (UNLESS OTHERWISE INDICATED): (A) ELEVATION CHANGE [M], (B) WATER DEPTH [M], (C) SEDIMENT FLUX [KG/M/S], (D) WATER DISCHARGE [M ³ /S], AND (E) EROSION/DEPOSITION RATE [KG/M ² /S] FROM SIMWE (ERDEP). ..	151
FIGURE 4.20: THE DEM OF THE SUB-WATERSHED OUTLINED IN FIGURE 4.19. THE CONTOUR LINES ARE AT 5FT INCREMENTS.	152
FIGURE 4.21: THE MODIFIED DEM OF THE LAKE WHEELER SUB-WATERSHED AFTER 30 R.TERRADYN ITERATIONS WITH UNIFORM LAND COVER AND INFILTRATION. ALSO INCLUDED ARE THE (A) WATER DEPTH [M], (B) SEDIMENT FLUX [KG/M/S], (C) FLOW DISCHARGE [M ³ /S], AND (D) EROSION / DEPOSITION PATTERN (SMOOTHED) [KG/M ² /S] FROM R.SIM.SEDIMENT (NOT USED BY R.TERRADYN) AT ITERATION #30 IN WHICH THE RAINFALL WAS 1.2E-5 M/S.	153
FIGURE 4.22: PHOTOGRAPHS OF THE STUDY REGION DURING A RAIN EVENT. PHOTOS WERE TAKEN AT THE LOCATION IN THE STUDY REGION INDICATED BY THE STAR IN THE TOPOGRAPHICAL REFERENCE MAPS. PERSPECTIVES ARE (A) DOWNHILL TOWARD THE REGION OF NET SEDIMENT DEPOSITION AND (B) UPHILL TOWARD THE CHANNEL INCISION.	154
FIGURE 4.23: THE INFILTRATION CONDITIONS SIMULATED FOR THE LAKE WHEELER SUB-WATERSHED. TABLE 4.3: SOIL TEXTURES (FROM HAAN, ET AL., 1994)	155
FIGURE 4.24: THE MODIFIED DEM OF THE LAKE WHEELER SUB-WATERSHED AFTER 30 R.TERRADYN ITERATIONS WITH CNI-A INFILTRATION CONDITIONS. ALSO INCLUDED ARE THE (A) WATER DEPTH [M], (B) SEDIMENT FLUX [KG/M/S], (C) FLOW DISCHARGE [M ³ /S], AND (D) EROSION / DEPOSITION PATTERN (SMOOTHED) [KG/M ² /S] FROM R.SIM.SEDIMENT (NOT USED BY R.TERRADYN) AT ITERATION #27 IN WHICH THE RAINFALL WAS 1.4E-5 M/S.	157
FIGURE 4.25: THE MODIFIED DEM OF THE LAKE WHEELER SUB-WATERSHED AFTER 30 R.TERRADYN ITERATIONS WITH CNII-D INFILTRATION CONDITIONS. ALSO INCLUDED ARE THE (A) WATER DEPTH [M], (B) SEDIMENT FLUX [KG/M/S], (C) FLOW DISCHARGE [M ³ /S], AND (D) EROSION / DEPOSITION PATTERN (SMOOTHED) [KG/M ² /S] FROM R.SIM.SEDIMENT (NOT USED BY R.TERRADYN) AT ITERATION #25, IN WHICH THE RAINFALL WAS 1.2E-5 M/S.	158
FIGURE 4.26: THE MODIFIED DEM OF THE LAKE WHEELER SUB-WATERSHED AFTER 30 R.TERRADYN ITERATIONS WITH CNIII-D INFILTRATION CONDITIONS. ALSO INCLUDED ARE THE (A) WATER DEPTH [M], (B) SEDIMENT FLUX [KG/M/S], (C) FLOW DISCHARGE [M ³ /S], AND (D) EROSION / DEPOSITION PATTERN (SMOOTHED) [KG/M ² /S] FROM R.SIM.SEDIMENT (NOT USED BY R.TERRADYN) AT ITERATION #30, IN WHICH THE RAINFALL WAS 1.3E-5 M/S.	159
FIGURE 4.27: THE DISTRIBUTED LAND COVER PARAMETERS (A) MANNING'S N, (B) CRITICAL SHEAR, (C) K _D , (D) K _T	160
FIGURE 4.28: THE MODIFIED DEM OF THE LAKE WHEELER SUB-WATERSHED AFTER 30 R.TERRADYN ITERATIONS WITH DISTRIBUTED LAND COVER PER TABLE 4.4 WITH CNII-D DISTRIBUTED INFILTRATION. ALSO INCLUDED ARE THE (A) WATER DEPTH [M], (B) SEDIMENT FLUX [KG/M/S], (C) FLOW DISCHARGE [M ³ /S], AND (D) EROSION / DEPOSITION PATTERN (SMOOTHED) [KG/M ² /S] FROM R.SIM.SEDIMENT (NOT USED BY R.TERRADYN) AT ITERATION #29, IN WHICH THE RAINFALL WAS 1.3E-5 M/S.	162
FIGURE 4.29: THE MODIFIED DEM OF THE LAKE WHEELER SUB-WATERSHED AFTER 30 R.TERRADYN ITERATIONS WITH DISTRIBUTED LAND COVER PER TABLE 4.4 AND DISTRIBUTED INFILTRATION VALUES FOR CNII-D. THE RAINFALL RATE WAS TWICE THE RAINFALL RATE OF FIGURE 4.30 WHICH PRODUCED A SUBSTANTIAL ELEVATION INCREASE IN THE WOODED AREA (BOTTOM RIGHT).	163

FIGURE 4.30: THE MODIFIED DEM OF THE LAKE WHEELER SUB-WATERSHED AFTER 30 R.TERRADYN ITERATIONS FOR THE BASELINE AND FOR THE 5 SOIL TYPES IN WHICH $K_t=0.1$ WAS CONSTANT AND $K_d=0.00089$ (CLAY), $=0.0074$ (SILT), $=0.031$ (SAND), $=2.2$ (SMALL AGGREGATES), $=3.2$ (LARGE AGGREGATES).	165
FIGURE 4.31: THE MODIFIED DEM OF THE LAKE WHEELER SUB-WATERSHED AFTER 30 R.TERRADYN ITERATIONS WITH $K_t=0.1$ AND $K_d=0.00089$ (CLAY). ALSO INCLUDED ARE THE (A) WATER DEPTH [M], (B) SEDIMENT FLUX [KG/M/S], (C) FLOW DISCHARGE [M^3/S], AND (D) EROSION / DEPOSITION PATTERN (SMOOTHED) [$KG/M^2/S$] FROM R.SIM.SEDIMENT (NOT USED BY R.TERRADYN) AT ITERATION #28, IN WHICH THE RAINFALL WAS $1.4E-5$ M/S.	166
FIGURE 4.32: THE MODIFIED DEM OF THE LAKE WHEELER SUB-WATERSHED AFTER 30 R.TERRADYN ITERATIONS WITH $K_t=0.1$ AND $K_d=0.0074$ (SILT). ALSO INCLUDED ARE THE (A) WATER DEPTH [M], (B) SEDIMENT FLUX [KG/M/S], (C) FLOW DISCHARGE [M^3/S], AND (D) EROSION / DEPOSITION PATTERN (SMOOTHED) [$KG/M^2/S$] FROM R.SIM.SEDIMENT (NOT USED BY R.TERRADYN) AT ITERATION #30, IN WHICH THE RAINFALL WAS $1.5E-5$ M/S.	167
FIGURE 4.33: THE MODIFIED DEM OF THE LAKE WHEELER SUB-WATERSHED AFTER 30 R.TERRADYN ITERATIONS WITH $K_t=0.1$ AND $K_d=0.031$ (SAND). ALSO INCLUDED ARE THE (A) WATER DEPTH [M], (B) SEDIMENT FLUX [KG/M/S], (C) FLOW DISCHARGE [M^3/S], AND (D) EROSION / DEPOSITION PATTERN (SMOOTHED) [$KG/M^2/S$] FROM R.SIM.SEDIMENT (NOT USED BY R.TERRADYN) AT ITERATION #27, IN WHICH THE RAINFALL WAS $1.5E-5$ M/S.	168
FIGURE 4.34: THE MODIFIED DEM OF THE LAKE WHEELER SUB-WATERSHED AFTER 30 R.TERRADYN ITERATIONS WITH $K_t=0.1$ AND $K_d=2.2$ (SMALL AGGREGATES). ALSO INCLUDED ARE THE (A) WATER DEPTH [M], (B) SEDIMENT FLUX [KG/M/S], (C) FLOW DISCHARGE [M^3/S], AND (D) EROSION / DEPOSITION PATTERN (SMOOTHED) [$KG/M^2/S$] FROM R.SIM.SEDIMENT (NOT USED BY R.TERRADYN) AT ITERATION #25, IN WHICH THE RAINFALL WAS $1.3E-5$ M/S.	169
FIGURE 4.35: THE MODIFIED DEM OF THE LAKE WHEELER SUB-WATERSHED AFTER 30 R.TERRADYN ITERATIONS FOR THE BASELINE AND FOR THE 5 SOIL TYPES IN WHICH $K_t=0.1$ AND $K_d=0.00089$ (CLAY), $K_t=0.02$ AND $K_d=0.00148$ (SILT), $K_t=0.005$ AND $K_d=0.00155$ (SAND), $K_t=0.0005$ AND $K_d=0.0110$ (SMALL AGGREGATES), AND $K_t=0.0004$ AND $K_d=0.0128$ (LARGE AGGREGATES).	171
FIGURE 4.36: THE MODIFIED DEM OF THE LAKE WHEELER SUB-WATERSHED AFTER 30 R.TERRADYN ITERATIONS FOR SAND WITH CRITICAL SHEAR STRESS F (A) 0.10 AND (B) 0.01 (ALL OTHER PARAMETERS WERE EQUIVALENT).	172
FIGURE 4.37: THE MODIFIED DEM OF THE LAKE WHEELER SUB-WATERSHED AFTER 30 R.TERRADYN ITERATIONS WITH $K_t=0.1$ AND $K_d=2.2$ (SMALL AGGREGATES). ALSO INCLUDED ARE THE (A) WATER DEPTH [M], (B) SEDIMENT FLUX [KG/M/S], (C) FLOW DISCHARGE [M^3/S], AND (D) EROSION / DEPOSITION PATTERN (SMOOTHED) [$KG/M^2/S$] FROM R.SIM.SEDIMENT (NOT USED BY R.TERRADYN) AT ITERATION #30, IN WHICH THE RAINFALL WAS $1.2E-5$ M/S.	173
FIGURE 4.38: THE MODIFIED DEM OF THE LAKE WHEELER SUB-WATERSHED AFTER 30 R.TERRADYN ITERATIONS WITH $K_t=0.1$ AND $K_d=2.2$ (SMALL AGGREGATES). ALSO INCLUDED ARE THE (A) WATER DEPTH [M], (B) SEDIMENT FLUX [KG/M/S], (C) FLOW DISCHARGE [M^3/S], AND (D) EROSION / DEPOSITION PATTERN (SMOOTHED) [$KG/M^2/S$] FROM R.SIM.SEDIMENT (NOT USED BY R.TERRADYN) AT ITERATION #30, IN WHICH THE RAINFALL WAS $1.2E-5$ M/S.	174
FIGURE 4.39: THE MODIFIED DEM OF THE LAKE WHEELER SUB-WATERSHED AFTER 30 R.TERRADYN ITERATIONS WITH $K_t=0.1$ AND $K_d=2.2$ (SMALL AGGREGATES). ALSO INCLUDED ARE THE (A) WATER DEPTH [M], (B) SEDIMENT FLUX [KG/M/S], (C) FLOW DISCHARGE [M^3/S], AND (D) EROSION / DEPOSITION PATTERN (SMOOTHED) [$KG/M^2/S$] FROM R.SIM.SEDIMENT (NOT USED BY R.TERRADYN) AT ITERATION #28, IN WHICH THE RAINFALL WAS $1.3E-5$ M/S.	175
FIGURE 4.40: THE MODIFIED DEM OF THE LAKE WHEELER SUB-WATERSHED AFTER 30 R.TERRADYN ITERATIONS WITH $K_t=0.1$ AND $K_d=2.2$ (SMALL AGGREGATES). ALSO INCLUDED ARE THE (A) WATER DEPTH [M], (B) SEDIMENT FLUX [KG/M/S], (C) FLOW DISCHARGE [M^3/S], AND (D) EROSION / DEPOSITION PATTERN (SMOOTHED) [$KG/M^2/S$] FROM R.SIM.SEDIMENT (NOT USED BY R.TERRADYN) AT ITERATION #30, IN WHICH THE RAINFALL WAS $1.0E-5$ M/S.	176
FIGURE 4.41: THE DISTURBED LAND COVER MAP OF THE LAKE WHEELER SUB-WATERSHED IN WHICH THE COVER PROPERTIES OF BARE CLAY WERE APPLIED IN THE AREAS PREVIOUSLY IDENTIFIED AS ROW CROPS.	177

FIGURE 4.42: THE MODIFIED DEM OF THE LAKE WHEELER SUB-WATERSHED AFTER 30 R.TERRADYN ITERATIONS WITH $K_t=0.1$ AND $K_d=2.2$ (SMALL AGGREGATES). ALSO INCLUDED ARE THE (A) (B) SEDIMENT FLUX [KG/M/S], (C) FLOW DISCHARGE [M^3/S], AND (D) EROSION / DEPOSITION PATTERN (SMOOTHED) [KG/ M^2/S] FROM R.SIM.SEDIMENT (NOT USED BY R.TERRADYN) AT ITERATION #12, IN WHICH THE RAINFALL WAS 1.3E-5 M/S.....	178
FIGURE 4.A.1: FOR SMOOTHLY VARYING BOUNDARIES, NEUMANN CONDITIONS ARE SATISFIED WELL. THE NORMAL GRADIENT IN THIS EXAMPLE IS EXACTLY ZERO.....	182
FIGURE 4.A.2: FOR STEEPLY VARYING BOUNDARIES, NEUMANN CONDITIONS ARE NOT WELL SATISFIED. HOWEVER, SINCE THE NORMAL GRADIENTS ARE LESS THAN THAT OF THE LATERAL VARIATIONS, BOUNDARY EVOLUTION REMAINS LOCALIZED AND STABLE OVER MANY ITERATIONS.....	182

LIST OF TABLES

TABLE 2.1: WAVEFORM PARAMETER, ϕ , AND THE CORRESPONDING VELOCITY SKEWNESS (ELGAR, 1987) AND WAVE SHAPE.....	12
TABLE 3.1. THE TRANSVERSE- AND DEPTH-AVERAGED MEAN FLOW VELOCITY MAGNITUDES (V'_x) IN [MM/S] FOR EACH BAFFLE CONFIGURATION AND FLOW RATE FOR THE X-GRID POSITIONS 1, 2 AND 5 FOR THE CLEAR WATER RUNS. ALSO SHOWN ARE THE PERCENT REDUCTIONS IN V'_x BETWEEN X-GRID POSITIONS 1 TO 2 AND BETWEEN X-GRID POSITIONS 1 TO 5 FOR EACH CONFIGURATION, AVERAGED OVER ALL FLOW RATES TESTED, AND V'_x AS A PERCENT OF V'_x FOR FREE FLOW AT X=5.....	44
TABLE 3.2: THE TRANSVERSE VARIANCE [M^2/S^2] FROM EQUATION 3.5, AVERAGED LONGITUDINALLY AND OVER ALL FLOW RATES, EXPRESSED AS A PERCENTAGE OF THE CORRESPONDING FREE FLOW VARIANCE.	47
TABLE 3.3. THE TRANSVERSE (Y-) AVERAGED SIGNAL TO NOISE RATIO (SNR_x) IN [DECIBELS] FOR EACH BAFFLE CONFIGURATION AND FLOW RATE FOR THE X-GRID POSITIONS 1, 2 AND 5 FOR THE CLEAR WATER RUNS. ALSO SHOWN ARE THE PERCENT REDUCTIONS IN SNR_x BETWEEN X-GRID POSITIONS 1 TO 2 AND BETWEEN X-GRID POSITIONS 1 TO 5, AVERAGED OVER ALL FLOW RATES TESTED.	54
TABLE 3.4. THE QUICKEST PATH VELOCITY, V_{qp} , DUE TO THE PRESENCE OF THE BAFFLES, AS A PERCENTAGE OF THE FREE FLOW V_{qp} AND THE SILT FENCE BAFFLE V_{qp} FOR EACH INFLOW RATE. THIS DATA IS FOR THE CLEAR WATER RUNS.....	57
TABLE 3.5. MINIMUM SETTLING (RESIDENCE) TIMES [SEC] AND CORRESPONDING MINIMUM CAPTURED GRAIN SIZE [MM] COMPUTED FROM THE QUICKEST PATH ANALYSIS AS DESCRIBED IN THE TEXT FOR THE CLEAR WATER RUNS.....	59
TABLE 3.A.1: FREE FLOW - CLEAR WATER RUNS - 14 L/s.....	75
TABLE 3.A.2: FREE FLOW - CLEAR WATER RUNS - 28 L/s.....	75
TABLE 3.A.3: FREE FLOW - CLEAR WATER RUNS - 42 L/s.....	76
TABLE 3.A.4: FREE FLOW - SEDIMENT LADEN RUNS - 14 L/s.....	76
TABLE 3.A.5: FREEFLOW - SEDIMENT LADEN RUNS - 28 L/s.....	77
TABLE 3.A.6: FREE FLOW - SEDIMENT LADEN RUNS - 42 L/s.....	77
TABLE 3.A.7: SILT FENCE - CLEAR WATER RUNS - 14 L/s.....	78
TABLE 3.A.8: SILT FENCE - CLEAR WATER RUNS - 28 L/s.....	78
TABLE 3.A.9: SILT FENCE - CLEAR WATER RUNS - 42 L/s.....	79
TABLE 3.A.10: SILT FENCE - SEDIMENT LADEN RUNS - 14 L/s.....	79
TABLE 3.A.11: SILT FENCE - SEDIMENT LADEN RUNS - 28 L/s.....	80
TABLE 3.A.12: SILT FENCE - SEDIMENT LADEN RUNS - 42 L/s.....	80
TABLE 3.A.13: TREE FENCE - CLEAR WATER RUNS - 14 L/s.....	81
TABLE 3.A.14: TREE FENCE - CLEAR WATER RUNS - 28 L/s.....	81
TABLE 3.A.15: TREE FENCE - CLEAR WATER RUNS - 42 L/s.....	82
TABLE 3.A.16: TREE FENCE - SEDIMENT LADEN RUNS - 14 L/s.....	82
TABLE 3.A.17: TREE FENCE - SEDIMENT LADEN RUNS - 28 L/s.....	83
TABLE 3.A.18: TREE FENCE - SEDIMENT LADEN RUNS - 42 L/s.....	83
TABLE 3.A.19: JUTE FENCE - CLEAR WATER RUNS - 14 L/s	84
TABLE 3.A.20: JUTE FENCE - CLEAR WATER RUNS - 28 L/s	84
TABLE 3.A.21: JUTE FENCE - CLEAR WATER RUNS - 42 L/s	85
TABLE 3.A.22: JUTE FENCE - SEDIMENT LADEN RUNS - 14 L/s	85
TABLE 3.A.23: JUTE FENCE - SEDIMENT LADEN RUNS - 28 L/s	86
TABLE 3.A.24: JUTE FENCE - SEDIMENT LADEN RUNS - 42 L/s	86
TABLE 3.C.1: V_z STATISTICS FOR EACH RUN.	100

TABLE 4.1: TYPICAL SEDIMENT CHARACTERISTICS FOR MIDWESTERN SOIL FROM YOUNG, ET. AL. (1978) AND FOSTER (1982). ALSO USED BY ANNAGNPS	122
TABLE 4.2: LAND COVER AND CURVE NUMBERS FOR THE LAKE WHEELER ROAD FARM.....	155
TABLE 4.3: SOIL TEXTURES (FROM HAAN, ET AL., 1994)	156
TABLE 4.4: COVER AND SOIL PARAMETERS USED IN THE DISTRIBUTED SIMULATIONS.	161
TABLE 4.5: TYPICAL SEDIMENT CHARACTERISTICS FOR MIDWESTERN SOIL FROM YOUNG, ET. AL. (1978) AND FOSTER (1982). ALSO USED BY ANNAGNPS	164
TABLE 4.6: GRAIN SIZE SPECIFIC PARAMETERS CHOSEN FOR THE SOIL TYPES SIMULATED.	170

Chapter 1

Introduction

The ongoing expansion of human land use continues to increase the strain placed on the natural environment and on existing sediment transport control practices.

Encroachment into previously undisturbed areas, including mountainous terrains, sensitive coastal areas, and zones that have been otherwise considered undesirable or inaccessible to development, amplifies the consequences if growth outpaces the advancement of scientific, engineering and construction sedimentation prediction and control technologies employed to minimize environmental impact and to insure the integrity of land use applications. As a result, fluvial and coastal sediment transport processes are of immediate concern to the public, private, and government sectors.

Human activity is both susceptible to and the primary cause of advanced erosion and the resulting downstream influences on water quality, macroinvertebrate populations and diversity, and channel, bank, and shoreline morphology. Federal (e.g. EPA, 1986) and state (e.g. NCDENR, 1995) government regulatory agencies have issued and continue to update guidelines to control these impacts; however, many challenges remain to motivate the scientific and engineering communities. Fortunately, new measurement technologies such as Light Detection And Ranging (LIDAR) and new sediment transport control measures such as long chain polymer flocculants and composite geo- and biotextiles continue to emerge.

The predictive sediment erosion, transport, and deposition model is a primary tool for scientists to test theoretical hypotheses and for engineers to develop and improve land

management practices. Due to limitations on numerical run-times, these models must employ simplifications of the governing equations and of the environment within which the models are run. Also, some systems of equations can not be solved analytically, requiring approximation to enable closure and simulation (e.g. mixing length model for closure of the Navier-Stokes equations). In either case, assumptions are usually made concerning smaller scale behavior based on the ever-increasing theoretical and empirical knowledge base available to the researcher. These assumptions often times arise in the higher scale models in the form of averaging techniques or representative parameters. For example, the vertical structure of overland and channel flow does not significantly influence outputs such as net water or sediment discharge rates in most watersheds. As a result, many modelers base their overland hydrology on equations that integrate the vertical flow structure within a given flow depth, such as the Saint-Venant equations of shallow water flow continuity and momentum (e.g. Dingman, 1984). Sensitivity of widely used models such as the Universal Soil Loss Equation [USLE] (Wischmeier and Smith, 1965, 1978; Williams, 1975, 1978; Foster et al., 2001) and the Water Erosion Prediction Project [WEPP] (Foster et al., 1989) to control parameters is often times performed in an effort to identify sources of model error or areas for future model refinement. One such refinement is the dependence of overland flow simulations that predict sediment erosion and deposition on the grain size distribution and availability. The need to address this issue on the watershed and coastal scale has been addressed by models such as WEPP and most recently the SIMulated Water Erosion [SIMWE] model (Mitas and Mitasova, 1998), but discussion continues concerning the benefits that this refinement may provide given the level of simulation acuity required for accurate

prediction of observables important to watershed and coastal management. This thesis presents research efforts chosen based on the premise that grain size dependent transport mechanisms play an important role in large scale predictive models and that the evolution of computational capabilities has reached a point in which the inclusion of such refinements is attainable.

The spectrum and population of grain sizes available for transport influence the rates and spatial distributions of entrainment and deposition. They also play a role in the morphology of bedforms and the formations of larger scale patterns that may influence subsequent flow and sedimentation processes. On the largest time and spatial scales, the widely observed effect of downstream fining - the exponential reduction in median grain size along the total length of an alluvial drainage network - has been attributed to particle abrasion (Kuenen, 1956; Knighton, 1999) and selective sorting (Ferguson et al., 1996; Paola et al., 1992; Seal et al., 1997) on the granular scale. Others have suggested that this effect can be ascribed to large-scale variables, such as the longitudinal decrease in river slope (Deigaard and Fredsoe, 1978) or the natural dynamic adjustment to variations in water, sediment, and energy inputs within the basin (Gasparini et al., 1999). River bank and coastline morphology and stability, of more immediate interest to land use developers and planners, are much more sensitive to the effects on flow due to intermediate scale phenomena such as ripples (Andersen, 2001), bedload sheets (Seminara et al., 1996; Whiting et al., 1988), grain size patchiness (Paola and Seal, 1995), sand bars (Gallagher et al., 1998), dunes (Werner, 1995; Kleinhaus, 2001) and other bedforms and their migration. All of these observables, to varying degrees, depend on grain size distributions, availability, and grain sorting processes. These intermediate

scale processes are themselves governed by the micro-scale physics of grain-grain and grain-flow interactions.

In Chapter 2, grain-size scale ($\sim 10^{-4}$ - 10^{-2} m) investigations were performed using a three-dimensional discrete particle computer model (Drake and Calantoni, 2001). We quantified relative transport rates and diffusivities via granular sorting mechanisms that occur during nearshore and fluvial sheet flow bedload transport for a heterogeneous mixture of grains. Within the constraints of our simulations, as much as 70% of the transport by mass was due to the largest grains, once the bed became vertically sorted. These results suggest that a significant refinement to the method of grain-size representation commonly used in boundary layer theoretical and numerical models is needed. In addition, the concept of equal mobility (Parker and Klingeman, 1982; Parker et al., 1982) was investigated. Finally, longitudinal diffusivities were quantified for a bimodal grain distribution as an empirical function of bed composition and applied shear stress.

A majority of sedimentation control measures, such as the sediment retention pond, operate on the scale $\sim 10^{-1}$ - 10 m. Studies on the hydrodynamics of the sediment retention pond are very limited in the literature yet a thorough understanding of the flow properties and their interaction with transported grains is critical for a physics-based approach to sedimentation control. Chapter 3 presents the results and analysis of experiments performed on a sediment retention pond in which we measured and analyzed the hydrodynamics and sediment capture effectiveness of various textiles for use as baffles for improvement to pond performance (Thaxton et al., 2004). Our results compliment existing data and conjecture about flow and sediment coupling behavior

within the pond (Haan et al., 1994) and shed light on the optimization of trapping efficiency as a function of flow velocity, pond geometry and baffle permeability. This may have significant influence on future retention pond design guidelines and may also help guide the sedimentation control community into more physics-based research styles.

Chapter 4 presents studies on the watershed scale ($\sim 10^2$ - 10^4 m) in which a new GRASS GIS (Geographical Information System) module *r.terrodyn* is introduced that evolves a given terrain based on the sediment flux provided by the distributed, bivariate, steady-state watershed scale sediment erosion, transport, and deposition GIS models *r.sim.water* and *r.sim.sediment* originally developed by Mitas and Mitasova (1998).

Development of module *r.terrodyn* enables terrain evolution based on grain-size dependent erosion, transport and deposition as governed by distributed soil and land cover parameters. We also introduced a new rainfall infiltration calculation methodology and a comparative band-pass filter for numerical stability during terrain evolution. Preliminary comparisons of results to field observations and previously published simulation results show that the model performs with skill in terrain evolution, prediction of modified water flow and sediment flux paths, and the identification of potentially sensitive areas in need of sedimentation control measures. Verification of the model is still ongoing as data becomes available.

Chapter 2

Discrete particle simulations of grain size dependent bedload transport

2.1 Introduction

Sediment transport under the action of waves and currents may be characterized by two primary modes, bedload and suspended load. Bedload transport involves the movement of sediment by slipping, rolling, or saltation confined to a layer of flow in close proximity to the bed. Sheet flow is a special case of bedload transport that occurs during energetic nearshore conditions in which bedforms are suppressed and the bed is nominally planar. The sheet flow layer is a highly concentrated two-phase flow of fluid and particles that may be up to several centimeters thick and has a distinct upper surface. Suspended load typically includes finer sediments that become entrained into the water column through lift forces or turbulence and may remain suspended for long time periods. In fluvial systems, the term "wash load" is also employed to describe particles finer than the channel bed material that originate either upstream or from the channel bank. In the nearshore, it is believed that sheet flow transport is a primary mechanism for bathymetric evolution (Drake and Calantoni, 2001).

Here a discrete particle model is employed to investigate the sorting of spherical grains, having a distribution of sizes ranging from 0.7mm - 1.7mm, under sheet flow conditions typical of the surf zone. A dependence of transport rate on wave maximum velocity and wave shape was observed. The results suggest that a single representative grain size (e.g. D_{50}) may not be adequate for parameterizing sediment transport rates in

the surf zone. Simulations were also performed on bimodal mixtures of grains to study the longitudinal diffusivities of grains in a bimodal distribution under similar sheet flow conditions.

2.2 Discrete particle model

All simulations were performed using the discrete particle model of Drake and Calantoni (2001). The two-phase model of the wave bottom boundary layer (WBBL) is comprised of a one-dimensional Eulerian fluid coupled to a three-dimensional Lagrangian particle model via Newton's Third Law through fluid-particle interaction forces of buoyancy, drag, and added-mass. Sand grains are simulated using spherical particles with the material properties of quartz. Normal and tangential forces generated at the contact points between grains are modeled with springs and friction, respectively (Drake and Calantoni, 2001). Fluid motion is realized as discrete slabs constrained to move parallel to the bed. Momentum is exchanged between slabs through an eddy viscosity determined from a mixing-length (e.g. Tennekes and Lumley, 1972). The governing equation for translational particle motion is given by (e.g. Madsen, 1991),

$$\begin{aligned} \rho_s V_s \frac{d\bar{u}_s}{dt} = & (\rho_s - \rho) V_s \bar{g} + \rho V_s \frac{D\bar{u}_f}{Dt} \Big|_{z=\infty} + \rho V_s c_m \left(\frac{D\bar{u}_f}{Dt} - \frac{d\bar{u}_s}{dt} \right) \\ & + \frac{1}{2} \rho C_D^* A |\bar{u}_f - \bar{u}_s| (\bar{u}_f - \bar{u}_s) + \vec{F}_\Phi, \end{aligned} \quad (2.1)$$

where ρ_s and ρ are the particle and fluid densities, respectively, V_s is the particle volume, \bar{g} is the acceleration due to gravity, \bar{u}_s and \bar{u}_f are the particle and fluid velocities, respectively, and A is the projected area of the spherical particle. All derivatives are evaluated at the center of the particle unless specifically noted. The first

term on the right-hand side represents the particle buoyancy, the second term is the horizontal pressure gradient acting on the particle, and the third term represents the added-mass effect with the coefficient of added mass $c_m = 0.5$ (Batchelor, 1967). The fourth term represents the particle drag force with the drag coefficient C_D^* , given by an approximate fit to the empirical drag law (e.g. Richardson and Zaki, 1954) for spheres, including a correction c^* , based on local particle concentration,

$$C_D^* = c^* (24 Re_s^{-1} + 4 Re_s^{-\frac{1}{2}} + 0.4), \quad (2.2)$$

where

$$c^* = \left(1 - c - \frac{1}{3} c^2\right)^{-\frac{5}{2}}, \quad (2.3)$$

Re_s is the relative particle Reynolds number, and c is the local particle concentration. The fifth term represents the forces due to intergranular collisions. All other fluid-particle interaction forces are omitted from the model. Equations governing the torques on the particles, analogous to equation (2.1), are integrated at every model time step.

Motion of fluid and particles in simulations is driven by a time-varying horizontal pressure gradient acting on the WBBL approximating the passage of surface gravity waves determined from the linear wave theory of Guza and Thornton (1980). The horizontal pressure acts on both the fluid and the embedded particles. The typical simulation domain is a ($\delta z \times \delta x \times \delta y$) $4\text{cm} \times 2\text{cm} \times 1\text{cm}$ box with periodic boundaries in the horizontal directions and a hard bottom in the vertical. The horizontal pressure gradient is assumed to have the same value everywhere inside the small computational domain. Several grains are fixed to the smooth basal plane to prevent wholesale sliding of the granular assemblage. A typical simulation uses 1600 grains with a distribution of

sizes around a median of 1.1 mm (King, 1991). The simulations use 40 fluid slabs, each 1 mm thick, to implement the mixing length fluid model (see Figure 2.1 for snapshot of the simulation).

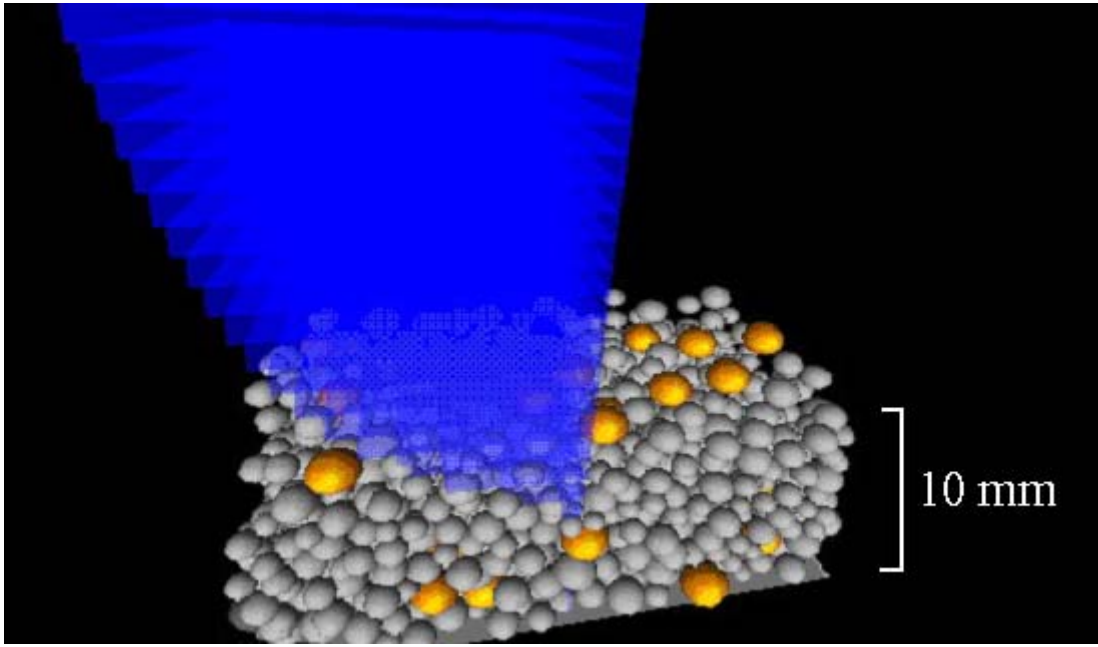


Figure 2.1: Snapshot of the simulation. The length of a fluid slab (blue) is proportional to its velocity. Grains larger than 1.5 mm diameter are colored yellow to aid in visualization of particle sorting processes.

2.3 Vertical bedload sorting

Granular sorting by size has been extensively investigated for dry granular flows as well as for oscillatory and fluvial transport systems. Savage and Lun (1988) argued that for relatively slow fluid-free flows and flows in which the velocity fluctuations of the individual grains are small, large grains drift to the top of the bed due primarily to gravity-induced void-filling, in which small grains infiltrate downward through gaps in the mobile bed structure. The downward migration of the smallest grains increases the rate of "squeeze expulsion" (Savage and Lun, 1988) for the largest grains in a direction preferentially upward. Breu et al. (2003), in vertical shaker experiments performed on

spheres of various sizes and densities, found that the regime in which the "brazil nut effect" (large grains migrating to the top of the bed) was observed depended upon relative grain diameter and density, as well as the applied vibrational acceleration.

Drake et al. (1988) performed extensive analysis of film of mixed grain size sediment transport and found that the individual grains move at the same velocity, regardless of size. The relative abundance of grains of different sizes undergoing bedload transport would therefore dictate the relative transport rates of grains by size. Parker and Klingeman (1982) and Parker et al. (1982) introduced the concept of "equal mobility" which was an extension of earlier work (e.g. Einstein, 1950). The equal mobility hypothesis states that grains of all sizes in a mixture are entrained at the same stress and exhibit the same transport rate when normalized by their respective concentrations. This concept is grounded on the assumption that the coarsest grains are inherently more difficult to entrain and therefore a larger number of the coarse grains must be available as mobile armor to equalize the mobility.

The presumption is made that, given an initially heterogeneous mixture of grains, over time, the largest grains should exhibit the highest transport rates due to their tendency to sort vertically to the top of the bed. To investigate this hypothesis, a discrete particle model was used to investigate the sorting of sand-sized spherical grains under sheet flow conditions typical of the surf zone. After 4 monochromatic wave cycles of 6 s each, independent of applied wave shape, the bed became fully sorted down to the maximum depth of motion such that the largest grains comprised approximately 70% of the mass transport. Equal mobility was observed to occur. Steady flow simulations were also performed for comparison to the oscillatory simulations.

2.3.1 Methods

Simulations used a distribution of grains having sizes that correspond to laboratory experiments of sheet flow by King (1991). The grains ranged in size from 0.7 mm to 1.7 mm and had a median size of 1.1 mm. For analysis, the distribution was divided into 5 grain-size bins identified as D_{0-20} , D_{20-40} , D_{40-60} , D_{60-80} , and D_{80-100} (where D_{xx} is the diameter for which xx percent of the grains by weight are finer than D .) The instantaneous transport rate, q , was defined as the sum over all grains of the grain momentum (mass times velocity) divided by the area of the simulation bed,

$$q(t) = \frac{1}{\delta x \delta y} \sum_{i=1}^N m_i u_{sx_i}, \quad (2.4)$$

where N is the total number of particles and u_{sx} is the component of \bar{u}_s along \hat{x} . In general, q is a vector quantity, but here only the transport along the flow direction is of concern, which for these simulations was \hat{x} .

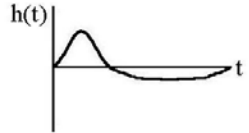
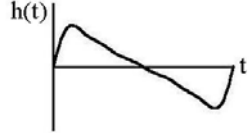
The horizontal pressure gradient acting on the WBBL was determined by fixing the free stream fluid velocity,

$$u_f(t) = u_{fo} \sum_{k=1}^5 2^{1-k} \cos(k\omega t + (k-1)\phi). \quad (2.5)$$

Here u_f is the free stream fluid velocity along \hat{x} , u_{fo} is the velocity amplitude, $\omega = 2\pi/T$ is the angular frequency, where T is the wave period. The waveform parameter, ϕ , describes the wave shape; in these simulations ϕ varied between zero and $\pi/2$ (see table 2.1). Three waveforms were generated that roughly correspond to shoaling, near-breaking and broken waves. For each waveform the value of u_{fo} was varied to produce maximum

free stream fluid velocities, u_{\max} , of 0.75 m s^{-1} , 1.0 m s^{-1} , and 1.25 m s^{-1} . Each set of hydrodynamic conditions was run out for 10 consecutive, 6-second wave periods.

Table 2.1: Waveform parameter, ϕ , and the corresponding velocity skewness (Elgar, 1987) and wave shape.

Waveform parameter (ϕ)	Velocity skewness	Nearshore waveform	Wave height vs. time
0	1.2	Shoaling	
$\pi/4$	0.8	Near-breaking	
$\pi/2$	0.0	Bore (broken wave)	

Simulations were also performed with the same grain size distributions under steady-flow conditions with a fixed u_{\max} of 1.0 m s^{-1} for 20 seconds of continuous flow. The instantaneous transport rate and the concentration for each grain size were recorded as a function of depth and time for both the oscillatory and steady flow simulations.

2.3.2 Results

For all waves, an initially random bed became well sorted after 4 wave periods down to the depth of motion. The largest grains tended to migrate to the region of greatest shear, which occurred near the top of the granular fluid layer. In all cases the transport rates were dominated by the largest grains, which moved near the top of the mobile bed at the highest velocities.

Figures 2.2a and 2.2b illustrate the vertical concentration of grains for each of the 5 grain size bins for the waveform with $u_{\max} = 1.0 \text{ m s}^{-1}$ and $\phi = \pi/2$ after 1 period and 10 periods, respectively. Figure 2.3 shows the percent of total flux for each of the 5 grain size bins over time for the waveform with $u_{\max} = 1.0 \text{ m s}^{-1}$ and $\phi = \pi/2$. In this case, the largest grains comprised $\sim 70\%$ of the total mass transport. All other cases simulated did not significantly deviate from this behavior.

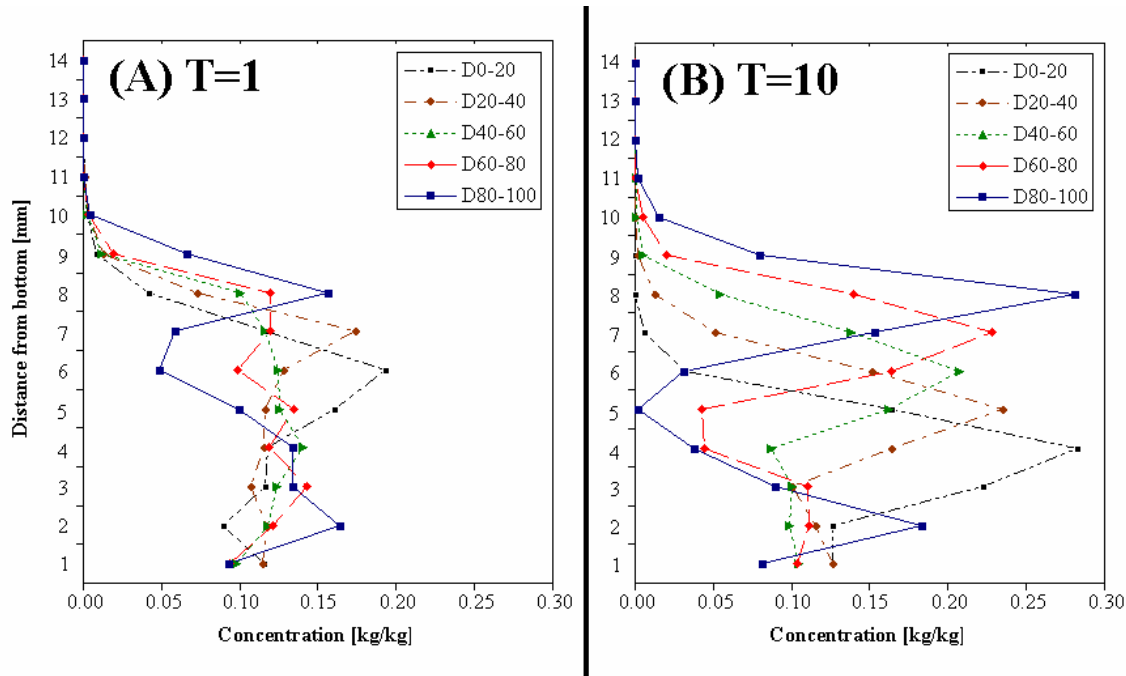


Figure 2.2: Concentration of each of the 5 grain size bins as a function of distance from the fixed bottom after (A) 1 and (B) 10, 6-sec wave periods. The maximum free stream velocity (u_{\max}) was 1.0 m/s and the waveform parameter (ϕ) was $\pi/2$.

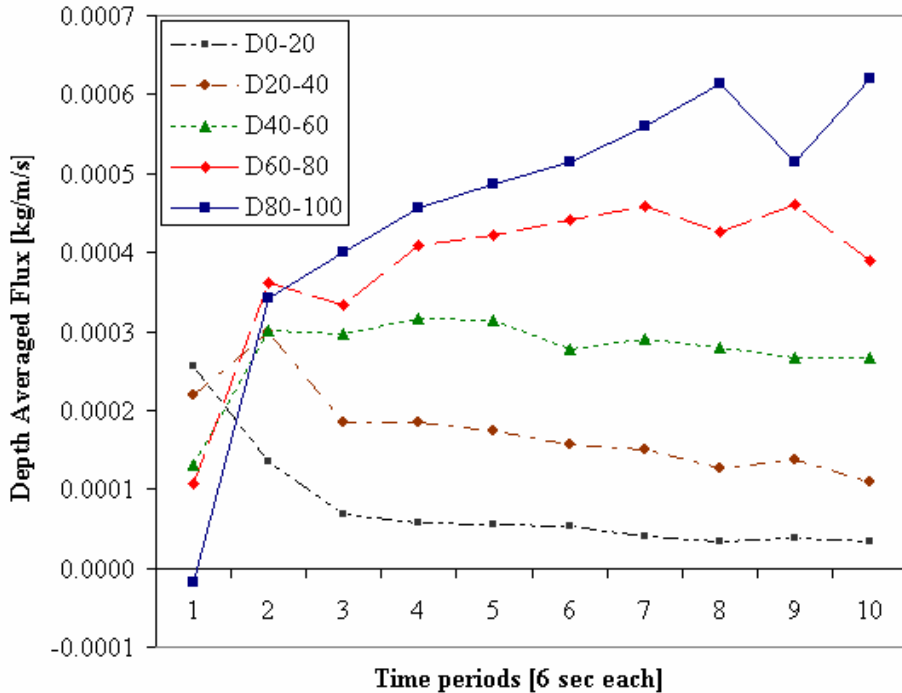


Figure 2.3: The mass transport rate as a function of time for the oscillatory simulations. The maximum free stream velocity (u_{max}) was 1.0 m/s and the waveform parameter (ϕ) was $\pi/2$. After 4 wave periods, the bed became fully sorted and maintained approximate equilibrium up to and beyond 10 wave periods.

The same behavior was observed for the steady flow simulations. Figures 2.4a and 2.4b illustrate the vertical concentration of grains for each of the 5 grain size bins for steady flow with $u_{max} = 1.0 \text{ m s}^{-1}$ after 1 second and 20 seconds, respectively. Figure 2.5 shows the percent of depth averaged flux for each of the 5 grain size bins over time. The initially random bed became fully sorted after 4 seconds and the largest grains again comprised $\sim 70\%$ of the total flux. Note that within the first second of the steady flow simulations, the fluid is accelerated to reach steady state much faster than if the model was left to do so otherwise.

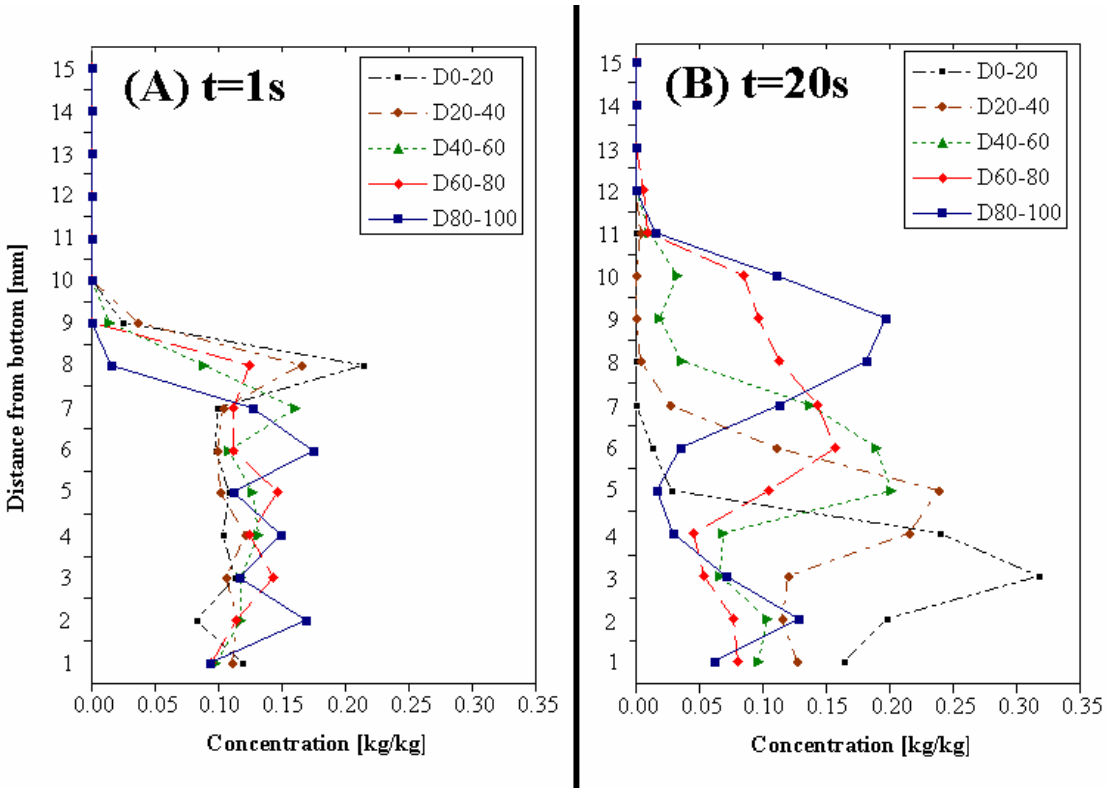


Figure 2.4: Concentration of each of the 5 grain size bins as a function of distance from the fixed bottom after (A) 1 second and (B) 20 seconds of steady flow. The maximum free stream velocity (u_{max}) was 1.0 m/s.

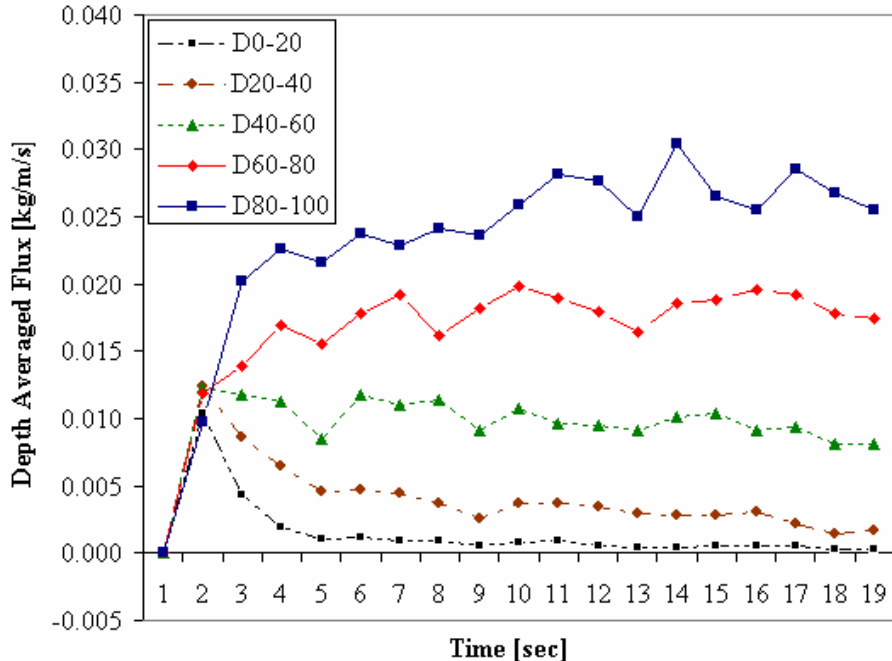


Figure 2.5: The mass transport rate as a function of time for the steady flow simulations. The maximum free stream velocity (u_{max}) was 1.0 m/s. After 4 seconds, the bed became fully sorted and maintained approximate equilibrium up to and beyond 10 seconds.

The "equal mobility" hypothesis can be stated simply that the sediment transport rates for each grain size, when scaled by their respective concentrations, are equal. To investigate equal mobility, the transport rates and concentrations for each grain size bin were time averaged over the last 6 of 10 wave periods, corresponding to conditions in which the bed had reached a state of sorted equilibrium. Mobility was then computed as the time-averaged transport rate divided by the time-averaged concentration per grain size bin, i :

$$M_i = \frac{\langle q_i \rangle}{\langle c_i \rangle}.$$

Figure 2.6 shows the mobilities for each grain size by depth for the oscillatory flow at $u_{\max} = 1.0 \text{ m s}^{-1}$ and $\phi = \pi/2$. Equal mobility is approximately satisfied with a slightly higher mobility for the smaller grain sizes. Figure 2.7 shows the mobilities for each grain size by depth for the steady flow case with $u_{\max} = 1.0 \text{ m s}^{-1}$. Here, equal mobility is well satisfied down through the depth of motion. In the steady flow simulations, the observed variability from equal mobility for the D_{0-20} bin near the bed surface may have been due to the fact that very few grains of that size traveled near the surface, resulting in a higher variance.

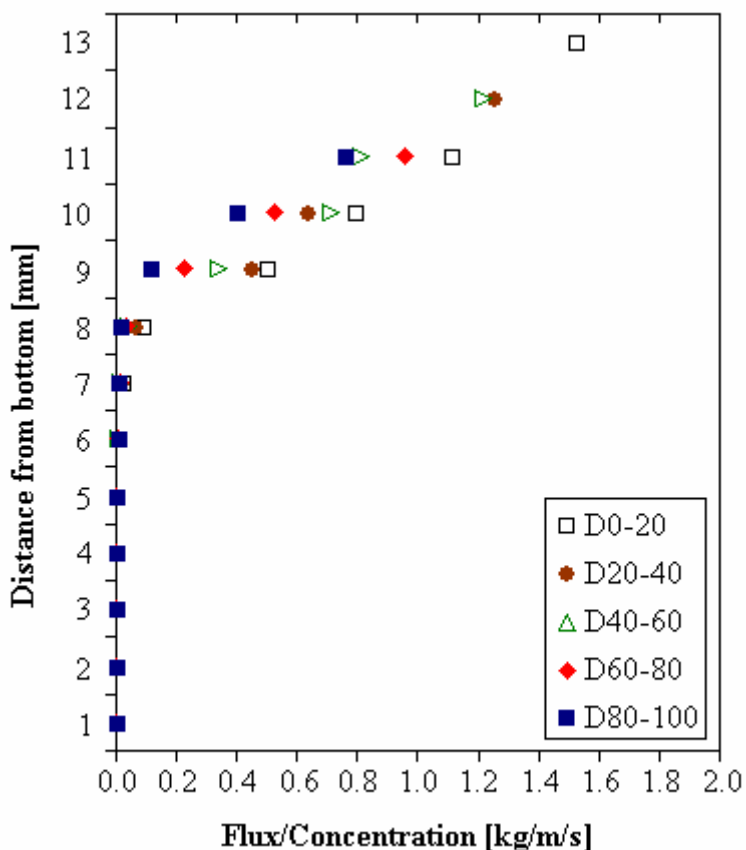


Figure 2.6: Mobility (flux/concentration) for each size bin by depth for the oscillatory simulations with maximum free stream velocity (u_{max}) of 1.0 m/s and waveform parameter (ϕ) of $\pi/2$.

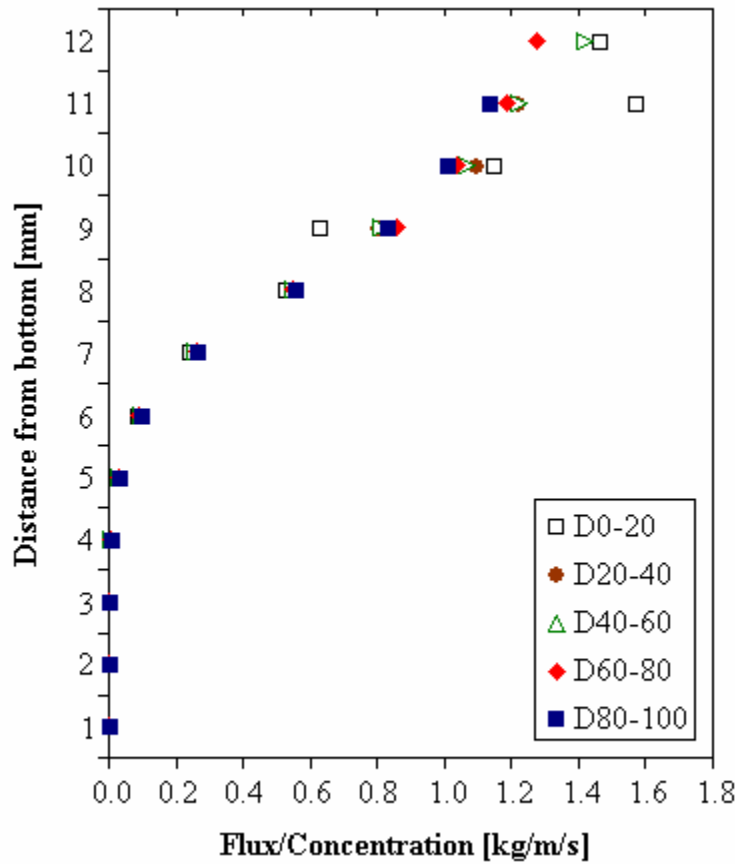


Figure 2.7: Mobility (flux/concentration) for each size bin by depth for the steady flow simulations with maximum free stream velocity (u_{max}) of 1.0 m/s.

2.4 Representative grain size

Bed load transport models for nearshore environments typically represent the distribution of grain sizes with a single grain size, often D_{50} . Results from discrete particle computer simulations of bed load transport in the surf zone challenge the assumption that a single representative grain size can appropriately describe the behavior of a collection of mixed size sediments.

2.4.1 Methods

The previous numerical experiments used a heterogeneous distribution of coarse grains ranging from 0.7 mm to 1.7 mm in diameter having $D_{50} = 1.1$ mm. This series of experiments uses six sharply peaked ($\pm 5\%$) unimodal size distributions having nominal diameters of 0.7 mm, 0.9 mm, 1.0 mm, 1.2 mm, 1.3 mm, and 1.7 mm, which correspond to D_{00} , D_{20} , D_{40} , D_{60} , D_{80} , and D_{100} , respectively, from the heterogeneous distribution. All simulations performed used waveforms found in table 2.1 with a maximum free stream velocity of $u_{\max} = 1.0 \text{ m s}^{-1}$ and were run for 10 consecutive, 6-second wave periods.

2.4.2 Results

The transport rate of each of the three heterogeneous simulations corresponding to the three waveforms in table 2.1 was computed as a percent error deviation from the transport rates of each of the six homogeneous runs for waves with $u_{\max} = 1.0 \text{ m s}^{-1}$. The percent error was then plotted as a function of grain diameter and fit to a 2nd degree polynomial (figure 2.8) which, of the simple regression functions attempted, had the highest overall coefficient of determination. For each of the three heterogeneous runs, the root of the resulting curve (0% error) corresponds to an equivalent transport rate for a homogeneous mixture. Since the grain size distributions simulated here were mono-disperse there was no vertical sorting by size to consider. Under these wave conditions, the single representative grain size whose bed load transport rate is equivalent to the mixed size distribution increases from roughly D_{75} under Stokes-like (shoaling) waves, to D_{85} under near-breaking waves, to D_{95} under a bore (figure 2.8).

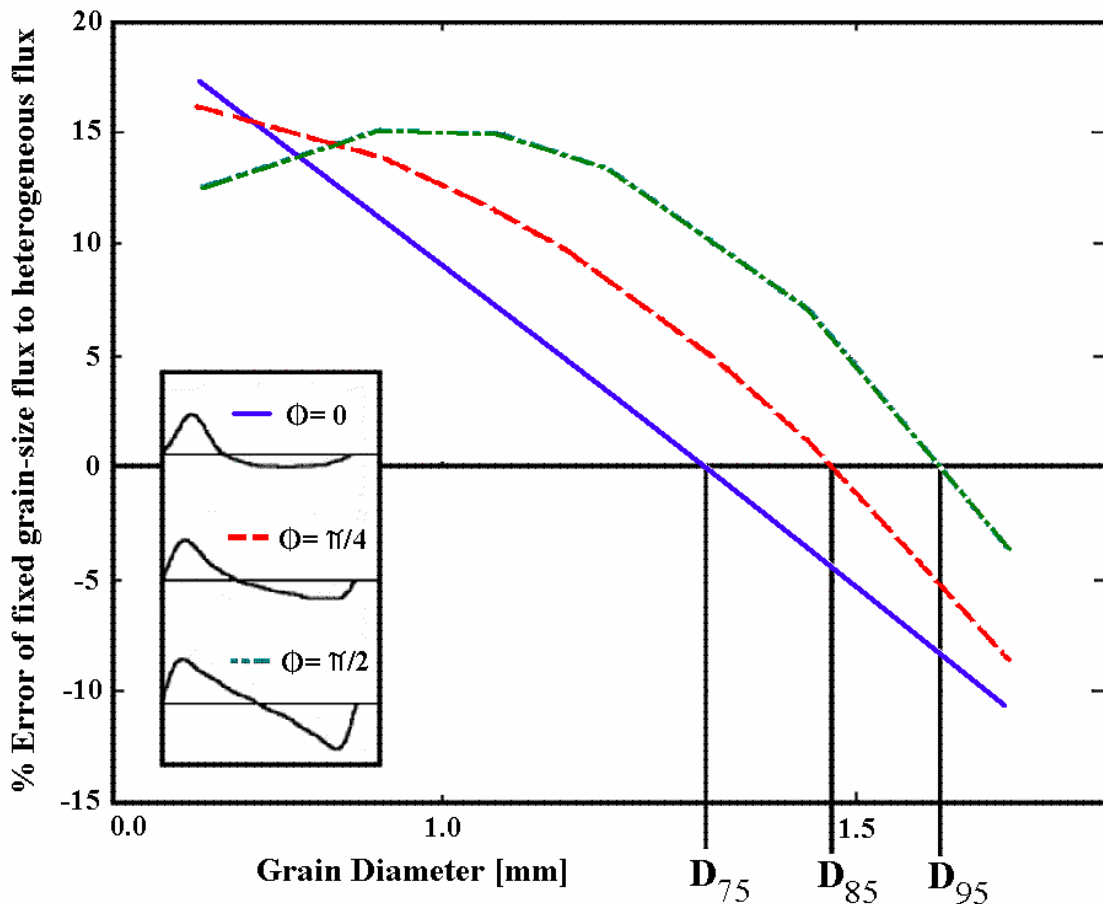


Figure 2.8: The representative grains sizes for the three different waveforms (inset) are identified where the plot of the % error of fixed grain-size flux to heterogeneous flux is zero. The curves represent a second order polynomial fit to the actual simulation data.

2.5 Diffusion

Exploration of the diffusive processes of grains in the nearshore is necessary for both the development and validation of nearshore bedload transport formulae. Accurate modeling of the diffusivity of nearshore sediments by size may also lead to more robust models of beach contaminant transport.

2.5.1 Methods

A suite of simulations was performed for bimodal distributions of grains in which the diameter of the grains for the smaller mode was 0.900 ± 0.045 mm while the diameter of the grains in the larger mode was 1.400 ± 0.070 mm. The composition of the bed is defined as

$$C = \frac{M_s}{M}, \quad (2.6)$$

where M_s is the mass of smaller grains and M is the total mass of grains inside the computational domain. Simulations were performed with bed compositions of 0.16, 0.25, 0.40, 0.50, 0.60, 0.75, and 0.84. For each of the bed compositions, monochromatic waveforms were simulated with ϕ values of 0, $\pi/8$, $\pi/4$, $3\pi/8$, and $\pi/2$ and maximum free stream velocities, u_{\max} , of 0.75 m s^{-1} , 1.0 m s^{-1} , and 1.25 m s^{-1} . The matrix of simulation results spanned 105 unique sets of simulations all run for 10 consecutive, 6-second wave period cycles.

The simulation data included the necessary information to compute the horizontal mean-square deviation from centroid along the flow direction (x) as

$$d_{i,j} = \frac{1}{M_{i,j}^2} \sum_{k=1}^{n_i} (m_{i,j}(k) \cdot (\langle x \rangle_{i,j} - x_{i,j}(k))^2, \quad i=1,2 \quad (2.7a)$$

where

$$\langle x \rangle_{i,j} = \frac{1}{M_{i,j}} \sum_{k=1}^{n_i} (m_{i,j}(k) x_{i,j}(k)). \quad (2.7b)$$

The index, i , refers to the grain size mode (smaller or larger); the index, j , tracks each 6-second period, and n_i is the number of grains within grain size mode i that moves more

than one small grain diameter (0.9 mm). Here, $x_{i,j}(k)$ is the distance traveled by the center of mass of grain, k , $m_{i,j}(k)$ is mass of grain k , and $M_{i,j}$ is the total mass of grains in size bin i that move more than one small grain diameter (0.9 mm). The diffusivity, D_i [m^2/s], for each grain size (small and large) per waveform parameter, maximum free stream velocity, and bed composition, is calculated as a least squares fit to the series of $d_{i,j}$ versus time.

2.5.2 Results

Figures 2.9a and 2.9b show the diffusivities in the flow direction for the small diameter (0.9 mm) grains and large diameter grains (1.4 mm), respectively, for each bed composition as a function of ϕ and u_{\max} of 1.0 m s^{-1} . The results from the simulations for the u_{\max} of 0.75 m s^{-1} and 1.25 m s^{-1} were similar (not shown). The diffusivities for both the small and large grains generally increased with waveform parameter ϕ , except for the $\phi = \pi/2$ case. The diffusivities dropped for $\phi = \pi/2$ since, for this waveform, flux occurs in both the positive-x and negative-x directions within one wave cycle (Drake and Calantoni, 2001), reducing the absolute distance traveled by the grains. In addition, the diffusivities for both the small and large grains increased with the bed composition and u_{\max} (not shown). The large grain diffusivities were generally 2-3 times that of the small grain diffusivities across the full span of maximum free stream velocity, waveform parameter, and bed composition.

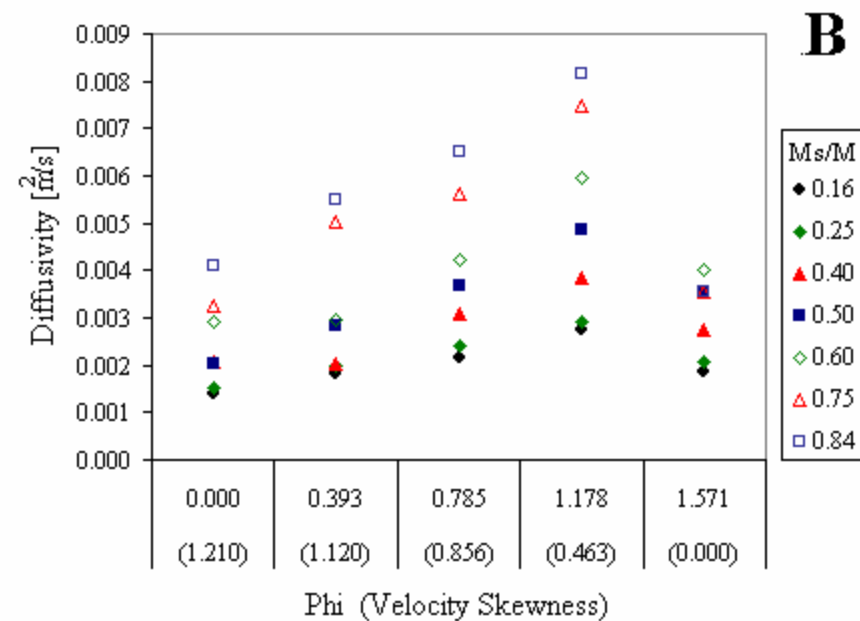
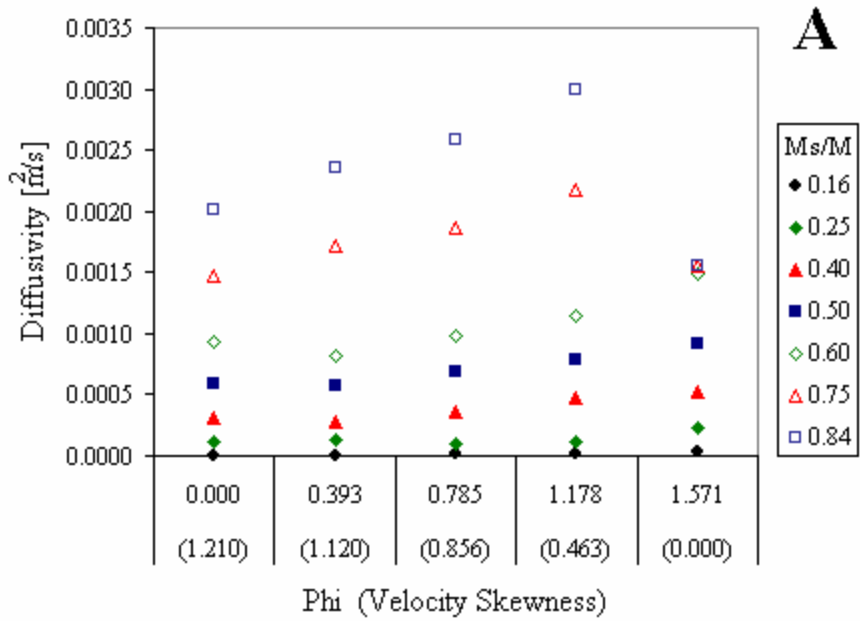


Figure 2.9: Diffusivities for the (A) small ($D=0.9$ mm) and (B) large ($D=1.4$ mm) grains for the maximum free stream velocity of 1.0 m/s. Note that the y-axes of (A) and (B) are on different scales such that the diffusivities for the small grains at the various bed compositions can be visually distinguished.

Results from the suite of simulations described were analyzed with the intent of developing a functional parameterization for coarse sand diffusion that can be utilized in

larger scale models. For each maximum free stream velocity, waveform parameter, and bed composition, the diffusivities were divided by the flux averaged over wave periods 4-10 (after the bed became fully sorted) - this was done for the small and large grains independently. The dimensionless ratio (when multiplied by the density of the grains) of diffusive to advective flux was independent of waveform parameter, with the exception of the $\phi = \pi/2$ runs (since flux occurred in both the positive-x and negative-x directions within one wave cycle).

Figure 2.10 shows the dimensionless ratio of diffusive to advective flux, averaged over waveform parameter, plotted against bed composition for the small grains. The data was best fit by the empirical formula:

$$\rho_s \frac{D_x}{Q_x} = \alpha \rho_s u_{\max}^{3/2}. \quad (2.8)$$

where ρ_s is the grain density (2650 kg m^{-3}), u_{\max} is the maximum free stream velocity, and α is an empirical coefficient set to 0.06. Because the dimensionless ratio of diffusive to advective transport remained constant for all bed composition values above 0.16, it is dependent on the maximum free stream velocity only. The deviations from fit for the $C=0.16$ simulations are consistent with the high variance associated with near-zero flux for the smallest grains. These outlying values were not included in the determination of the empirical fit (equation 2.8).

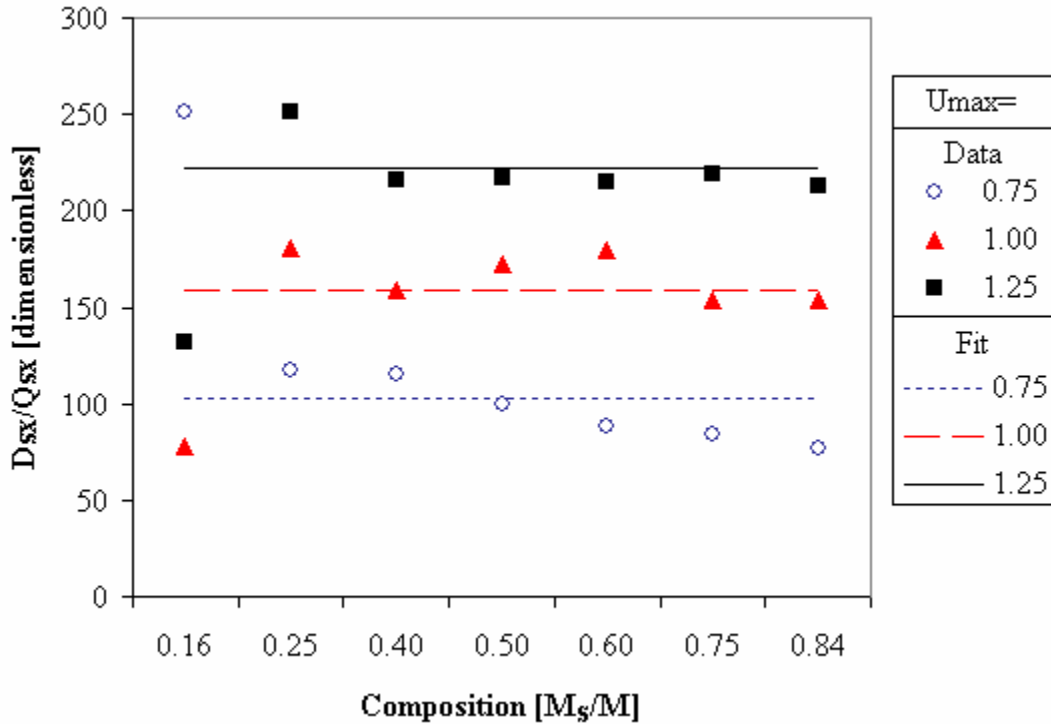


Figure 2.10: Dimensionless ratio of diffusive to advective flux for the small grains (0.9 mm diameter) averaged over wave shape (ϕ) for the three maximum wave velocities as a function of bed composition. The deviations from fit for the $C=0.16$ simulations correspond to the high variance associated with near-zero flux values for the smallest grains. These outlying values were not used in determining the empirical fit (equation 2.8).

Figure 2.11 shows the dimensionless ratio of diffusive to advective flux, averaged over waveform parameter, plotted against bed composition for the large grains. The data was best fit by the empirical formula:

$$\rho_s \frac{D_x}{Q_x} = \beta \tan\left(C \frac{\pi}{2}\right), \quad (2.9)$$

where C is the bed composition (see equation 2.6) and β is an empirical coefficient set to 220. Equation 2.9 assumes that the dimensionless ratio of diffusive to advective flux for large grains is independent of the maximum free stream velocity - the fit is less skillful for higher bed compositions, where small grains dominate the bed population.

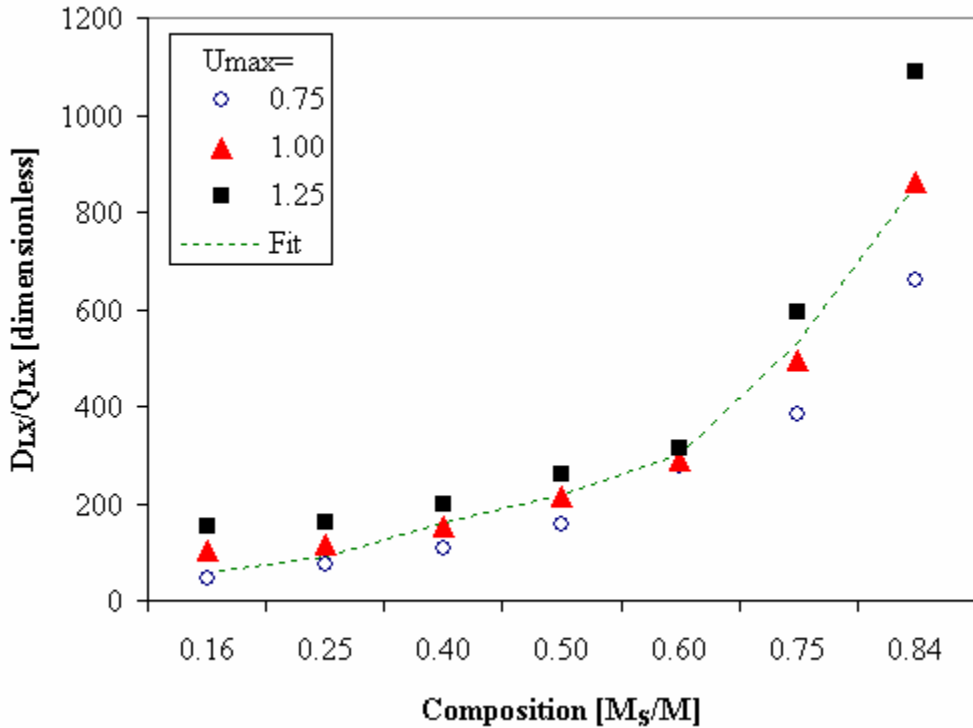


Figure 2.11: Dimensionless ratio of diffusive to advective flux for the large grains (1.4 mm diameter) averaged over wave shape (ϕ) for the three maximum wave velocities as a function of bed composition.

2.6 Discussion and Conclusions

For sheet flow conditions simulated here, momentum transfer is dominated by intergranular collisions (Bagnold, 1956). In the inertial regime, granular sorting occurs approximately independently of grain-fluid coupling and is governed by the internal granular dynamics within the bedload layer. The mechanics at work in this model are similar to the "Brazil-nut effect" (Rosato et al., 1987); large grains end up on top of the bed due to either convective motion of the smaller particles or the filling of voids by small particles (thereby lifting the larger ones). The vertical sorting occurs very rapidly when compared to the time scales for bathymetric evolution of the surf zone. Once the

grains are vertically sorted, the relative transport rates of the larger grains will be larger than the smaller grains, thereby influencing the representative grain size of the mobile sediment bed. Modelers who always adopt D_{50} as a representative grain size for sediment mixtures are cautioned. The simulations show that even for a narrow distribution of coarse sediments the choice of representative grain size can lead to prediction errors of as much as +/- 15%. These errors could be compensated for by adjusting other parameters in transport formulae at the expense of possibly misrepresenting the relevant physics.

The representative grain size shifts from D_{75} to D_{95} as the simulated monochromatic waves move from Stokes-like to bore-like. For beaches with cross-shore uniform sediments, the results indicate that the representative grain size may be expressed as a function of cross shore distance. Similarly, the representative grain size increases as the waveforms simulated become more energetic. The mechanics of vertical size-sorting processes during transport may explain these observations. For the mixed size sediment distribution the portion of the total transport rate attributed to the coarsest fraction of grains is large, since the largest grains migrate to the top of the bed load layer, which is also the location of the largest shear stress in the WBBL.

Finally, simulation results suggest that diffusion of the bed should not only be a function of the driving fluid parameters, but also a function of grain size distribution. Under certain wave conditions, it has been demonstrated that diffusivities for small diameter particulates, such as contaminants or chemical aggregates, can be parameterized as a function of maximum wave velocity. The large grain diffusivities are weakly dependent upon maximum wave velocity but increase with a decrease in large grain population.

Chapter 3

Hydrodynamic and Sediment Capture Assessment of Various Baffles in a Sediment Retention Pond

Portions of this chapter are to be published in the Transactions of the American Society of Agricultural Engineers in 2004, in collaboration with Dr. Joseph Calantoni and Dr. Richard A. McLaughlin.

3.1 Introduction

The sediment retention pond is a widely used device for trapping total suspended solids from a disturbed watershed. Effluent sediments and pollutants from construction sites, surfaces mines, and existing urban areas alter downstream ecosystems by reducing both benthic populations (Gray and Ward, 1982; Cairns and Dickson, 1971) and species richness and diversity (Erhardt et al., 2002; Mayack and Waterhouse, 1983; Cline et al., 1982). Small catchments, such as retention ponds, provide sufficient time of residence for solids within an available volume to be removed from the effluent flow. Nominally, colloids, clays, silts, and very fine sands escape capture in retention structures due to their very small settling velocities (Haan et al., 1994), regardless of shape (Graf, 1971; Simons and Senturk, 1992), unless they aggregate either through natural or artificially induced flocculation (Chen, 1975; Camp, 1973). Federal (e.g. EPA, 1986) and state (e.g. NC DENR, 1995) government agencies have issued retention pond design guidelines based on widely implemented design methodologies such as that developed by Brune (1953) which relates pond trapping efficiency to the ratio of pond capacity and the average annual runoff for the source watershed.

Although inflow hydrographs and sedigraphs as well as source soil composition directly correlate to the effluent grain size distribution from a pond (e.g. Line and White, 2001; Greb and Bannerman, 1997), for a given watershed, retention pond size and shape are the primary characteristics that most influence trapping efficiency by affecting flow patterns and residence times. Pioneering work by Hazen (1904) showed that retention pond trapping efficiency is proportional to pond surface area yet independent of depth. Chen (1975) further concluded that to optimize pond performance, retention ponds should be long and narrow. Barfield et al. (1983) and Mills and Clar (1976) recommended a length to width ratio of at least 2:1 to maximize the effectiveness and minimize dead storage of a rectangular pond. (Haan, et. al. [1994] define dead storage as the volume within a given pond that is bypassed by the flow which reduces the amount of pond volume participating in TSS capture.) This is in agreement with the results of Griffin et al. (1985) whose plug flow and “continuous stirred tank reactor” models showed that, independent of inflow momentum, a minimization of dead storage occurs at a length-to-width ratio of 2:1. However, at high flow rates in which significant recirculation velocities are established at the pond walls or if the width or depth of the pond is on the scale of the inflow channel, sediment scour from the pond walls and floor may contribute to the effluent sediment load (Fennessey and Jarrett, 1997; Goldman et al., 1986; Chen, 1975; Einstein, 1950; Camp, 1946), reducing the pond’s efficiency during high runoff events (e.g. Wilson and Barfield (1985) BASIN model). For example, Fennessey & Jarrett (1997) demonstrated that under controlled conditions, 39% of the total soil lost from their permanent pool detention pond was due to the degradation of their pond walls and floor.

Different sediment pond dewatering methods have been studied in an effort to maximize pond performance. Principal spillways such as rectangular weirs and perforated risers work by removing the clearest water near the surface of the pond and are the most common dewatering method. Fennessey and Jarrett (1997) found that perforated risers work roughly as well as single orifice risers, although they state that “seemingly small changes in perforation diameters or spacings can dramatically alter discharge hydraulics and water retention times.” Millen et. al. (1997) found that a skimmer (floating outlet) has higher retention efficiency for grains ranging in size from 0.1 to 100 microns over that of their perforated riser. A retention pond may retain a permanent pool of standing water which increases sediment retention as the depth is increased (Fennessey and Jarrett, 1997; Goldman et al., 1986; Chen, 1975). If a detention pond has a small sediment-storage volume or it is not cleaned out per its recommended schedule, permanent pool depths will be limited rendering the pond less efficient.

Turbulent diffusion within the water column contributes to prolonged suspension (Graf, 1971), effectively increasing the amount of transmitted sediment from a retention pond over that of quiescent flow (Goldman et al., 1986). In most treatments, however, turbulent effects have been either parameterized or neglected (e.g. Ward et al., 1979, DEPOSITS model). Brown (1950) developed a set of trap efficiency curves based on Camp (1946) and Dobbins (1944) depth-dependent “mixing coefficient” for use in practical applications, of which a subset is commonly used today (e.g. Goldman et al., 1986, surface area sizing formula).

Baffles installed in a pond increase sediment retention rates by reducing the flow energy and turbulence within the pond and increasing the “hydraulically effective width,”

defined by Chen (1975) as “the width over which flow is uniformly distributed.” Goldman et al. (1986) stated that a baffle should be installed at the inlet of any basin whose length to width ratio is less than 10:1. Jarrett (1996) and Millen et al. (1997) confirmed that the installation of baffles reduces short-circuiting and thus increases trapping effectiveness, although in an undersized pond, baffles may not significantly improve total sediment capture (Rauhoffer et al., 2001). In an evaluation of geotextiles for sediment control, Barrett et al. (1998) concluded that sediment removal from highway construction sites was due to the formation of sediment ponds that formed behind the installed silt fabric fences. Observations during tests that we performed on the interaction between porous baffles made of jute germination biotextile backed by coir fiber with polyacrylamide suggested that the baffles substantially improved flow characteristics within the basin in favor of sediment retention. To evaluate the potential of different materials commonly used on construction sites for use as baffles, we measured the hydrodynamics within a small sediment retention pond under steady flow conditions with and without three types of baffles installed: silt fence, tree protection fence, and jute/coir.

3.2 Methods

A 2:1 rectangular, 23-m³ retention pond with a 1-m permanent pool was constructed at the Sediment and Erosion Control Research and Education Facility (SECREF) (McLaughlin et al., 2001) at North Carolina State University. Water from an upstream source pond was piped through a variable control valve to an H-flume that fed the water into the retention pond. The H-flume was 0.96 m tall, 1.92 m wide and 4.8 m long. It was constructed of a rigid fiberglass frame and leveled such that the flow volume was proportional only to the head height, allowing for accurate inflow rates to be

measured using an Isco™ (Isco, Inc. 4700 Superior St., P.O. Box 82531, Lincoln, NE, 68504) 6712 portable sampler with an Isco™ 730 bubble flow module set in the H-flume configuration. Two wire baffles, 0.20-m high, were installed in the base of the H-flume to reduce flow turbulence prior to flow rate measurement. The outflow side of the H-flume fed water into the pond at an average spill height of approximately 0.30 m. The retention pond was roughly rectangular in shape, measuring 8.0 m in length (from intake to spillway), 5.2 m in width on average, and 0.92 m deep at its deepest point at the center. The water exited the pond over a 1.10-m wide plywood weir at the top of the dam which had a 50% slope. The side slopes averaged 80% and the front slope did not exceed 40%. The floor and walls of the pond were lined with geotextile fabric secured with landscape staples to prevent soil detachment within the pond. In addition, rubber sheeting was stapled onto the intake wall to prevent erosion as the water entered the pond.

Experiments were performed with baffles made from three different types of materials: silt fence, tree protection fence, and jute/coir. The jute/coir material was comprised of standard 4 x 100 jute mesh backed by a woven coir erosion control blanket (North American Green C-125), joined with zip ties along the top and bottom edges and at several locations throughout the baffle. The medium weight, orange polyethylene tree protection fence had rectangular openings of 0.10 m x 0.050 m. It was folded into three layers and secured with zip ties along the top and bottom edges and at various locations throughout the baffle to reduce its effective permittivity to be closer to that of the jute/coir material. The silt fence material was a standard woven polypropylene fiber with 670 threads/m. A fourth set of experiments was performed for the free flow case with no baffles installed.

For the experiments that included baffles, three parallel baffles were installed at 0.92 m intervals centered roughly on the pond's midpoint and perpendicular to the axis of the pond as defined by the inlet and outlet midpoints (see fig. 3.1b). The baffles were supported by three metal stakes spaced evenly across the pond width and were secured with landscape staples along the pond floor and walls to prevent water from "leaking" around the edges. Each silt fence baffle had one 0.30-m x 0.30-m weir centered 0.75 m from the center axis of the pond. The weir on the first silt fence baffle was set to the left of the pond's axis relative to the flow direction, the second to the right, and the third to the left. Once installed, the height of the jute/coir and the tree protection baffles exceeded the ponded water surface height by at least 0.10 m. The pond surface height and the height of the installed silt fence baffles were roughly equivalent during the 14 L/s experiments; however, in the 28 L/s experiments, the water occasionally overtopped the baffles at various locations. During the 42 L/s experiments, the water consistently overtopped the baffles by approximately 50 mm.

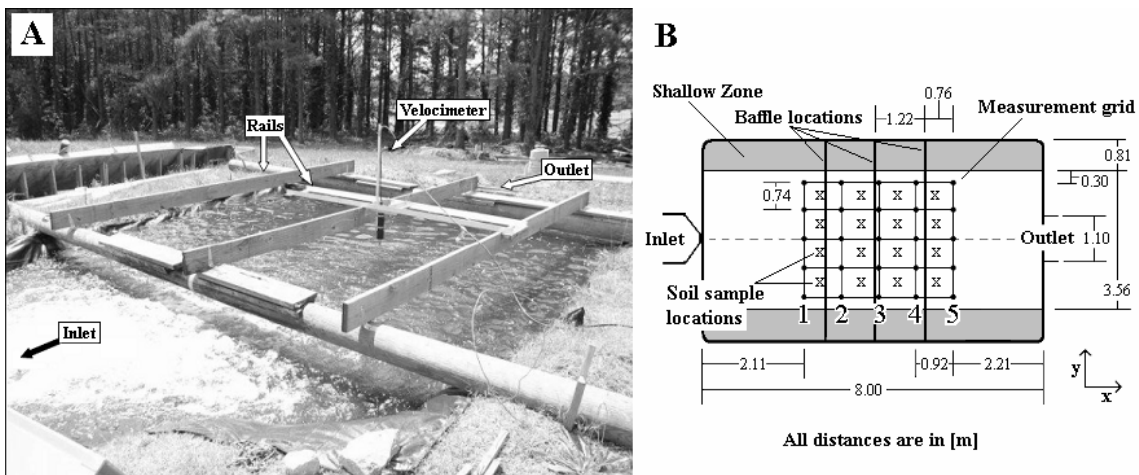


Figure 3.1. (A) Picture of the sediment retention pond used in the experiments. (B) Geometry of the retention pond and the location of the 5x5 data acquisition grid. There are also 2 depth layers along the z direction (not shown) at 0.13 m and 0.26 m below the still pond surface. Flow is left-to-right.

In order to take velocity measurements in the pond, a wooden frame was constructed above the pond. Two telephone poles were laid perpendicular to the flow direction across the width of the pond. Grid rails made of 2" x 6" treated lumber were mounted onto the telephone poles and leveled. A Sontek™ (Sontek/YSI, Inc. 6837 Nancy Ridge Rd., Ste. A, San Diego, CA, 92121) 10 MHz ADV-1 acoustic-Doppler velocimeter was secured to a vertical mount that was free to slide along an aluminum frame which itself could slide along the grid rails (fig. 3.1a). The three fluid velocity spatial components and the corresponding signal-to-noise ratios were taken using the velocimeter at depths of 0.13 m and 0.26 m below the still ponded water surface for 25 points per depth corresponding to a 5 x 5 data sampling grid (fig. 3.1b). The data sampling grid was defined with a right-handed coordinate system where the positive x-axis (longitudinal) is oriented in the downstream mean flow direction and the y-axis (transverse) is positive starting from the far right grid point as seen from the pond inlet facing downstream. For analysis, the x-grid positions were labeled 1 through 5, with x-grid position 1 being nearest the inlet. The grid was centered at the pond's center point to minimize boundary effects. As a result of the installed baffle locations, the pond was divided into four "cells" such that at least one transverse column of grid points lay between each baffle (fig. 3.1b). At least 1,024 timed data points were taken per position at a sampling rate of 25 Hz with an acoustic frequency of 1MHz. The unfiltered data was then processed using the WinADV program version 1.849 (Wahl, 2001).

For each of the baffle configurations tested, pond flow data were taken at three fixed intake flow rates: 14 L/s, 28 L/s, and 42 L/s. The intake flow rates were monitored during each test, and the intake control valve was adjusted as needed to maintain the flow

rate to within 10% of the target rate for each test. Measurements were taken only when the monitored flow at the outlet equilibrated at the intended flow rate. Source pond water level and time of day were recorded at the beginning and the end of each run. Source pond water temperature remained between 26⁰C and 28⁰C for all experiments performed. All of these experiments were run with essentially clear water and will be identified hereafter as the "clear water" runs.

All clear water runs were repeated with a previously characterized soil being injected upstream at a rate of ~5.6 kg/minute (hereafter identified as the "sediment laden" runs). Water samples were taken at the outlet at timed intervals with an Isco™ 712 sampler and later analyzed for turbidity levels. Hydrodynamic data as described above was collected and compared to the non-sediment runs. After the experiments were performed for each baffle configuration, the pond was drained and sediment accumulation depths were measured at 16 points along the pond bottom within the data acquisition grid (see figure 3.1b). Sediment accumulation depths were also measured at the point of peak accumulation which, in every case, was located on the intake side of the 1st x-grid position. These depths were used to derive estimates of the volume of captured sediment per baffle configuration. 40g- soil samples were also taken at these locations and analyzed for sand, silt, and clay composition via the standard hydrometer method (Loch, 2001). For each of the samples, the silt and clay were removed and the remaining sand was sieved into 6 bins corresponding to the standard sieve sizes of 1000, 500, 250, 106, 63, and 53 μm . As a result, a representative grain size, D_{50} , was obtained at each sample location and compared to the captured grain size projected from the hydrodynamic data.

3.3 Results

The hydrodynamic results from the "clear water runs" and the "sediment laden runs" are presented together, followed by the sediment analysis. The relationship between the hydrodynamics within the pond and the sediment capture effectiveness, for each baffle configuration and free flow, is discussed within the sediment capture section (3.4.2) and within the discussion section (3.5).

3.3.1 Hydrodynamics

Using the method of Reynolds decomposition (e.g. Tennekes and Lumley, 1972), the measured flow velocity at grid position i (with coordinates (x, y, z)), each having three spatial components, j , is decomposed into a mean flow velocity, V , and flow velocity fluctuations, v .

$$\tilde{V}_{i,j} = V_{i,j} + v_{i,j} ; \quad i = (x, y, z); j = \{e_1, e_2, e_3\} \quad (3.1)$$

Analysis of the mean field properties is discussed first, followed by the analysis of the signal-to-noise ratio, which for our runs, represents the turbulent energy density (the density of velocity fluctuations) within the flow.

3.3.1.1 Mean Flow Field

The mean flow velocity at each location was computed by time-averaging the $n=1,024$ timed data points acquired by the velocimeter.

$$V_{i,j} = \frac{1}{n} \sum_{\tau=1}^n \tilde{V}_{i,j}(\tau) ; \quad n = 1024 \quad (3.2)$$

$$\bar{V}_i = \sqrt{\sum_{j=1}^3 V_{i,j}^2} \quad (3.3)$$

Equation 3.3 defines the mean flow velocity magnitude at grid location i .

Work by Griffin et al. (1985) has shown that much of the inflow volume of a rectangular sediment pond bypasses the outlet, forming a recirculation pattern and dead zones that do not contribute to the sedimentation process. For the free flow experiments, a large recirculation current was observed as well as dead storage zones in each of the four corners and at the center of the largest recirculation flow. We also observed the typical pond flow behavior in which the outflow was comprised of a combination of recirculated flow and flow that short-circuited the pond, passing directly along the surface to the spillway (Haan et al., 1994). The ratio of short-circuited flow to recirculated flow at the spillway was visually observed to increase as the input flow rate increased. For all treatments in which the baffles were evaluated, large-scale recirculation flow and direct short-circuiting were greatly reduced or eliminated. Downstream flow appeared much more quiescent, although not fully laminar, and spanned nearly the entire width and depth of the pond. Mapping the mean flow velocity field allowed for the quantification and analysis of the large scale currents and recirculation patterns used in estimating a theoretical pond sediment trapping effectiveness based on residence times and pond volume dead storage percentage.

Figures 3.2 through 3.5 illustrate, for a subset of the clear water experiments performed, the x - y (plan-view) projection of the mean flow velocity magnitude at each of the 25 grid points and at the 0.13-m and 0.26-m depths below the still ponded water surface. For the free flow field at the 14 L/s (not shown) and 28 L/s (fig. 3.2a) inflow rates, the flow at 0.13 -m depth displayed a large scale clockwise motion, while the flow at 0.26-m depth was counterclockwise. However, the free flow field displayed a strong

counterclockwise motion independent of depth for the 42 L/s inflow rate (fig. 3.2b).

Unlike the free flow experiments that showed recirculation patterns, the experiments with the baffles installed (figs. 3.3 through 3.5) showed a marked decrease in flow velocity and organization beyond the first baffle.

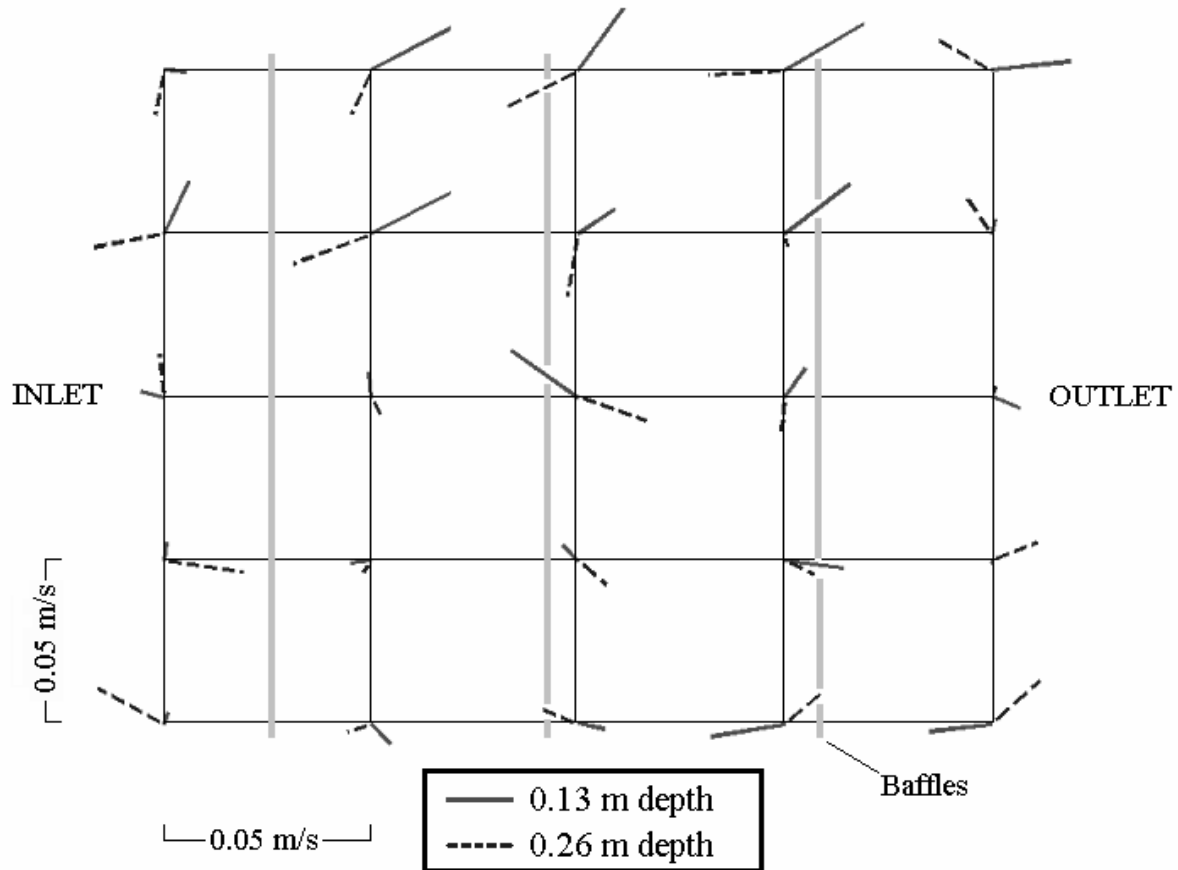


Figure 3.2a. Surface-parallel (plan view) projection of the mean (time-averaged) velocities (m/s) for free flow (no baffles) at 28 L/s inflow rate for the clear water runs. Flow direction is indicated by the angular deviation from horizontal and the velocity magnitude by the length of the ray.

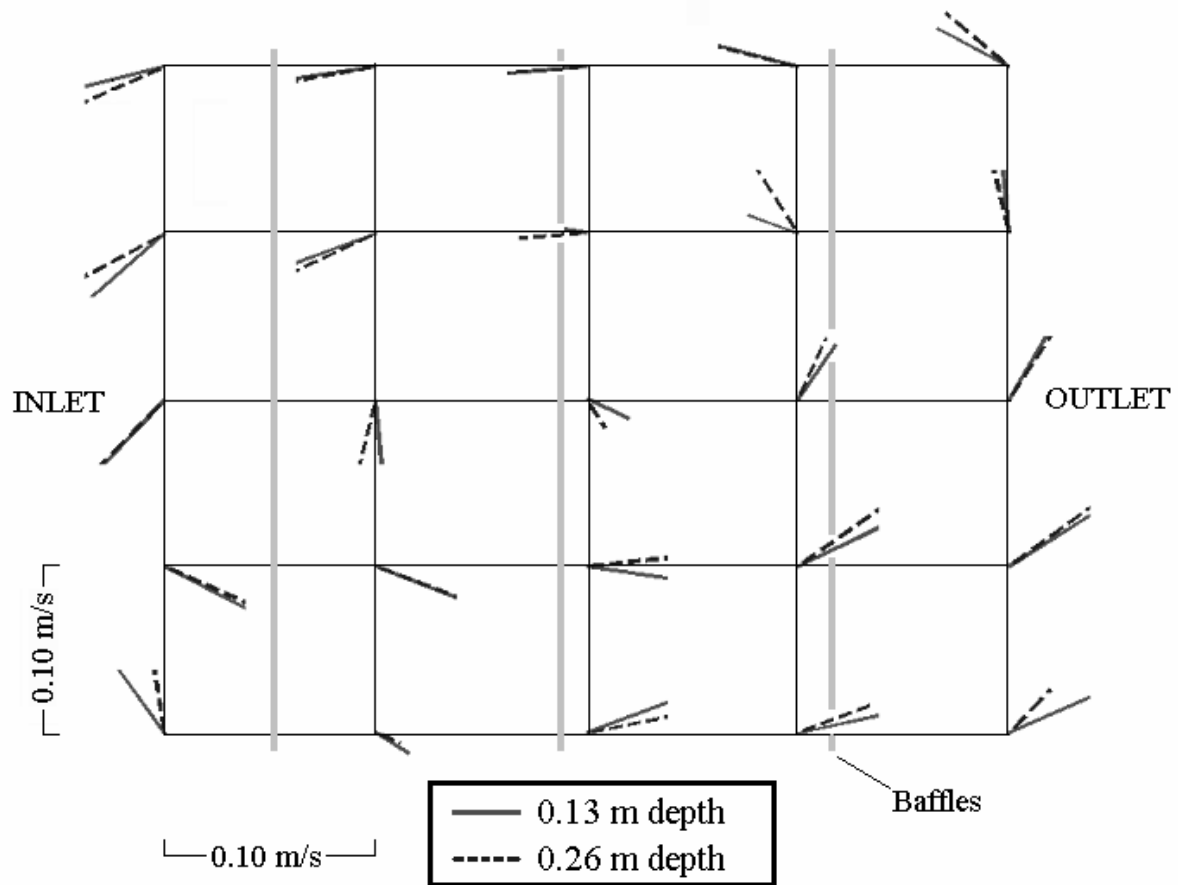


Figure 3.2b. Surface-parallel (plan view) projection of the mean (time-averaged) velocities (m/s) for free flow (no baffles) at 42 L/s flow for the clear water runs. Flow direction is indicated by the angular deviation from horizontal and the velocity magnitude by the length of the ray.

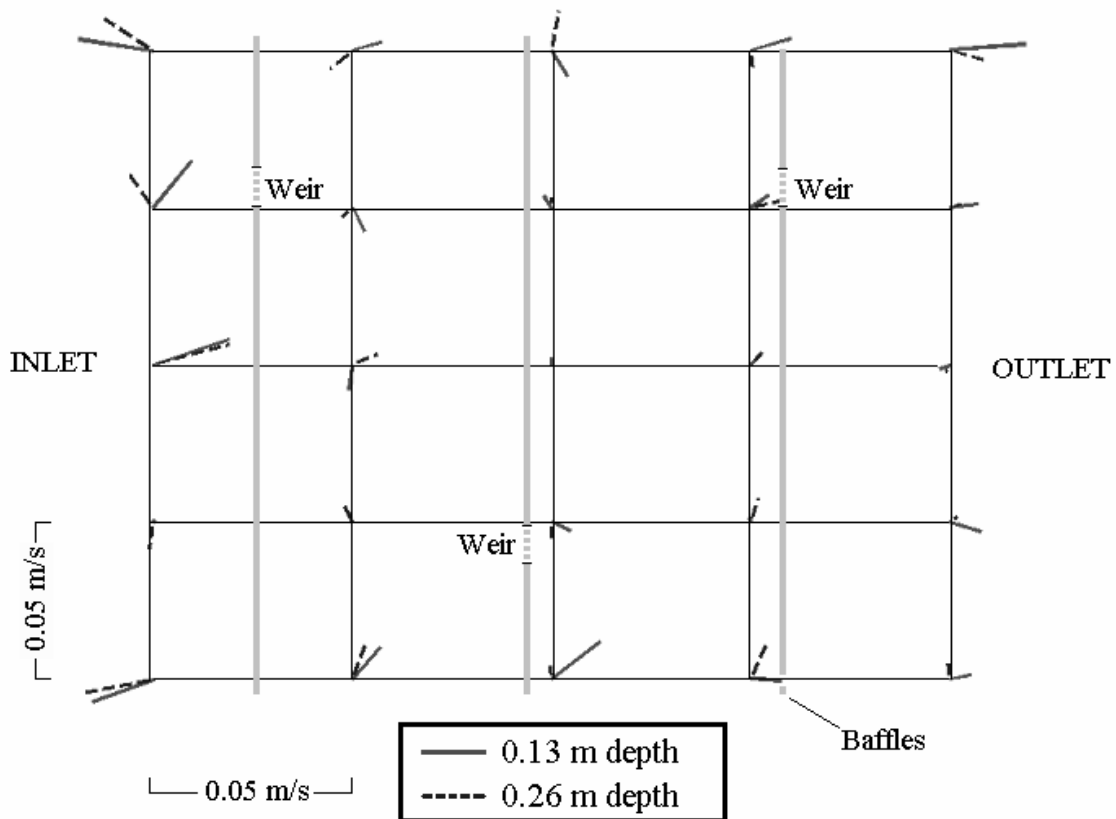


Figure 3.3. Surface-parallel (plan view) projection of the mean (time-averaged) velocities (m/s) for the silt fence baffle configuration at 28 L/s for the clear water runs. Flow direction is indicated by the angular deviation from horizontal and the velocity magnitude by the length of the ray.

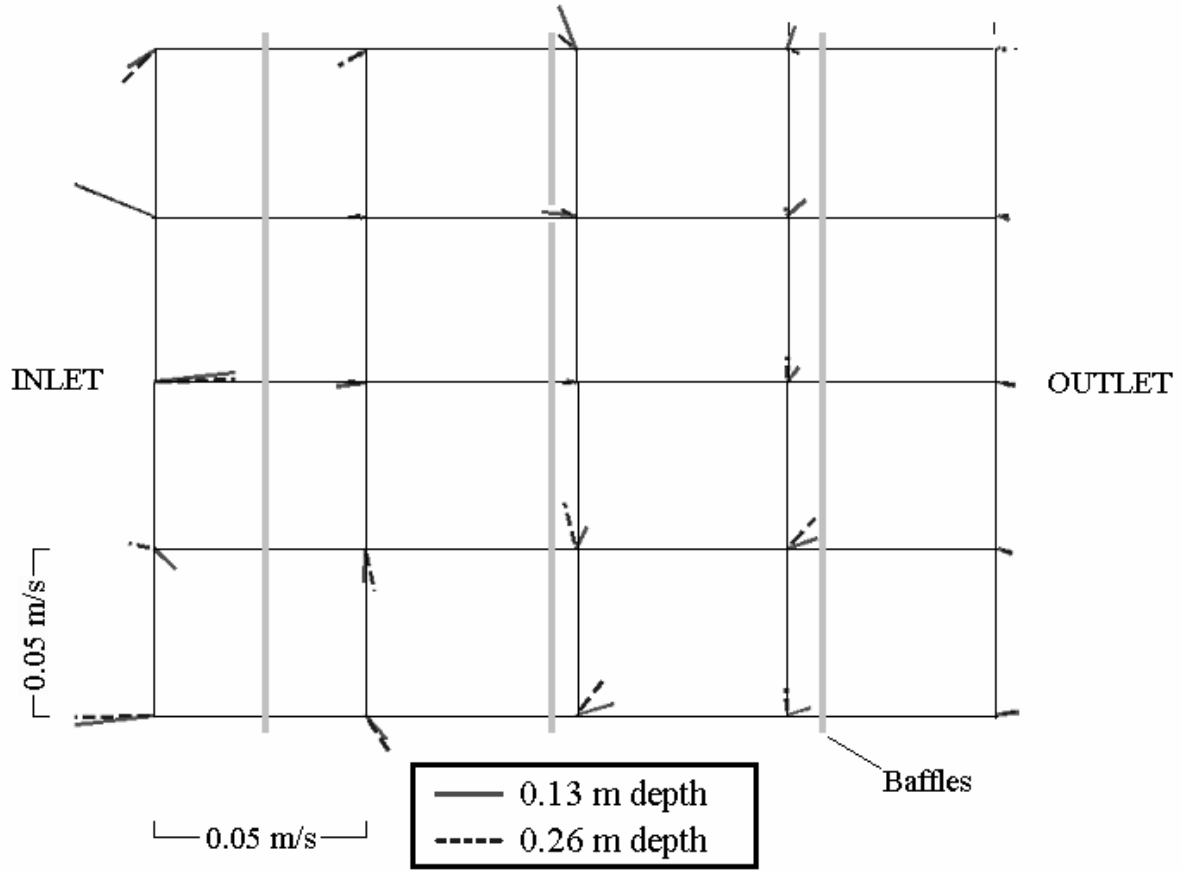


Figure 3.4. Surface-parallel (plan view) projection of the mean (time-averaged) velocities (m/s) for the tree baffle configuration at 28 L/s flow rate for the clear water runs. Flow direction is indicated by the angular deviation from horizontal and the velocity magnitude by the length of the ray.

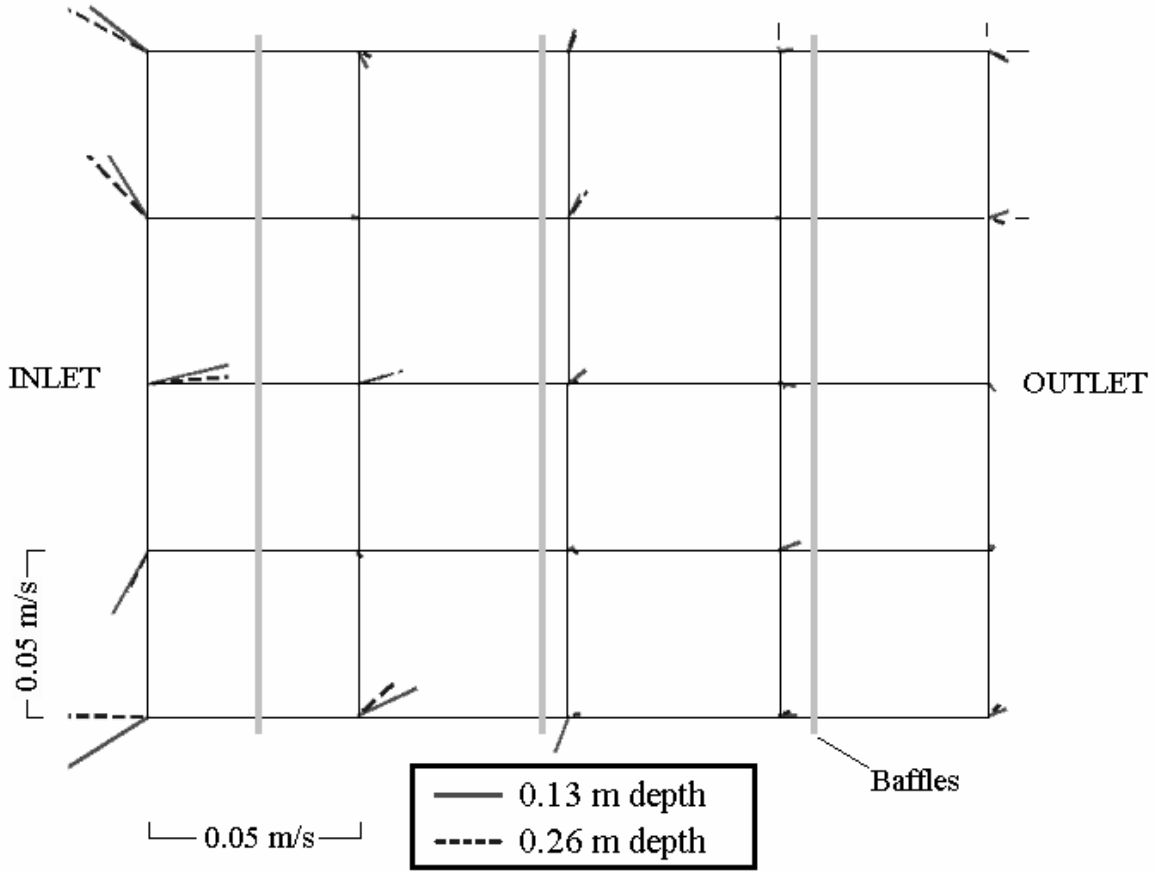


Figure 3.5. Surface-parallel (plan view) projection of the mean (time-averaged) velocities (m/s) for the jute/coir baffle configuration at 28 L/s for the clear water runs. Flow direction is indicated by the angular deviation from horizontal and the velocity magnitude by the length of the ray.

To quantify the generalized downstream reduction in flow field intensity, the mean flow velocity magnitudes (eq. 3.3) were depth-averaged at each grid location and the resulting depth-averaged values at the five transverse grid points per x-grid position were averaged together to yield V'_x , defined as:

$$V'_x \equiv \bar{V}_{i=(x,\bar{y},\bar{z})} = \frac{1}{n} \sum_{y=1}^n \left[\frac{1}{m} \sum_{z=1}^m \bar{V}_{i=(x,y,z)} \right]; \quad n = 5; m = 2 \quad (3.4)$$

The process was repeated for each of the inflow rates and for both the clear water and the sediment laden runs. The result of this analysis shows that, with baffles installed, the

transverse- and depth-averaged mean flow velocity magnitude per x grid position, V'_x , diminished significantly beyond the first baffle and incrementally at each successive downstream location (table 3.1; figures 3.6 and 3.7; see Appendix 3.A for the complete set of data for the clear water and sediment laden runs). The values of V'_x for the clear water and sediment laden runs were averaged together as shown in figure 3.8. Although measured flows were generally higher, the sediment laden runs showed the same behavior and trends as the clear water runs with the following exceptions: (1) the jute/coir baffles dampened the flow velocity more quickly than the other configurations as seen by the 90% drop in V'_x at $x=2$ for the sediment laden runs, (2) the silt fence generally performed more poorly as evidenced by the higher V'_x for all x-grid positions relative to the other baffle configurations, (3) the flow rates were notably higher in the intake cell for the baffle configurations. These results suggest that the silt fence permeability is further reduced due to clogging by the sediment. The higher V'_x for the sediment laden runs may have been a result of the higher signal to noise ratios relative to the clear water runs - as will be discussed, we argue that the clear water backscatter signals were due to the turbulent density fronts which may have lower velocities relative to the suspended sediment which dominated backscatter in the sediment laden runs.

For each baffle at various flow rates and depths (depths not shown), an increase in V'_x was often measured from the 2nd to the 3rd x-grid position, followed by a subsequent decrease from the 3rd to the 4th x-grid position (see fig. 3.6). A larger oscillatory flow velocity component (variance in the time averaging that yields the mean flow rates) was measured for all baffle configurations at the 3rd x-grid position (not shown). We suspect this was due to the close proximity of the velocimeter to the 2nd baffle at the 3rd x-grid

position: a higher density of sampling points at $x=3$ may suppress this effect when averaging transversely to obtain V'_x . For the free flow configuration at 28 L/s and 42 L/s flow rates, a decrease in V'_x was measured from the 2nd to the 3rd x-grid position, followed by a subsequent increase from the 3rd to the 4th x-grid position. This was most likely due to the higher flow rates associated with streamline divergence and compression at the inlet and outlet, respectively.

Table 3.1. The transverse- and depth-averaged mean flow velocity magnitudes (V'_x) in [mm/s] for each baffle configuration and flow rate for the x-grid positions 1, 2 and 5 for the clear water runs. Also shown are the percent reductions in V'_x between x-grid positions 1 to 2 and between x-grid positions 1 to 5 for each configuration, averaged over all flow rates tested, and V'_x as a percent of V'_x for free flow at $x=5$.

Baffle	Flow rate	x grid position					drop in V'_x (%)	drop in V'_x (%)	as a % of free
		[L/s]	x=1	x=2	x=3	x=4			
Free flow	Clear water runs	14	63.36	55.43	53.43	53.20	47.37	20.2	-
		28	83.97	65.66	58.01	62.25	57.96		
		42	105.19	77.46	60.18	70.91	72.17		
	Sediment laden runs	14	42.96	42.24	32.54	30.65	21.40	5.8	-
		28	60.02	60.89	51.57	50.02	41.31		
		42	99.42	85.14	77.77	70.81	66.83		
Silt fence	Clear water runs	14	40.61	10.61	18.01	9.97	12.37	69.4	31.5
		28	65.60	24.27	27.42	18.91	19.09		
		42	102.18	29.18	33.60	23.94	25.68		
	Sediment laden runs	14	87.23	40.95	45.16	20.63	19.96	62.6	67.7
		28	122.11	36.98	53.10	25.10	21.24		
		42	116.38	40.77	86.52	36.15	31.44		
Tree fence	Clear water runs	14	33.83	9.01	8.98	7.60	8.53	68.7	20.5
		28	66.89	20.36	24.30	18.29	9.47		
		42	64.22	23.70	40.71	28.33	19.52		
	Sediment laden runs	14	53.34	24.53	24.92	6.19	5.18	65.3	28.5
		28	116.64	29.18	32.37	13.06	9.93		
		42	109.24	36.10	32.59	11.95	13.16		
Jute/ coir	Clear water runs	14	37.07	5.47	7.04	4.07	5.29	75.4	13.7
		28	79.81	16.70	15.63	7.17	8.13		
		42	55.11	21.03	18.12	17.63	11.44		
	Sediment laden runs	14	57.61	8.03	7.81	6.63	7.08	90.3	36.3
		28	105.89	10.05	13.44	11.28	12.32		
		42	152.70	8.51	12.72	12.96	17.12		

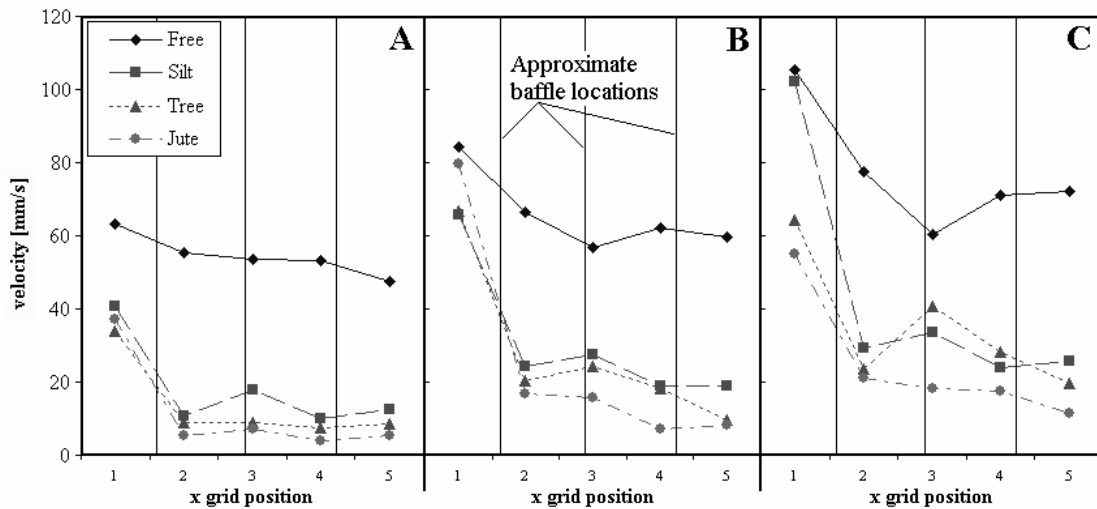


Figure 3.6: The depth-averaged mean flow velocity magnitude (see text) for each flow rate averaged along the 5 transverse gird points per x grid position for (A) 14 L/s, (B) 28 L/s, and (C) 42 L/s. This is from the clear water runs.

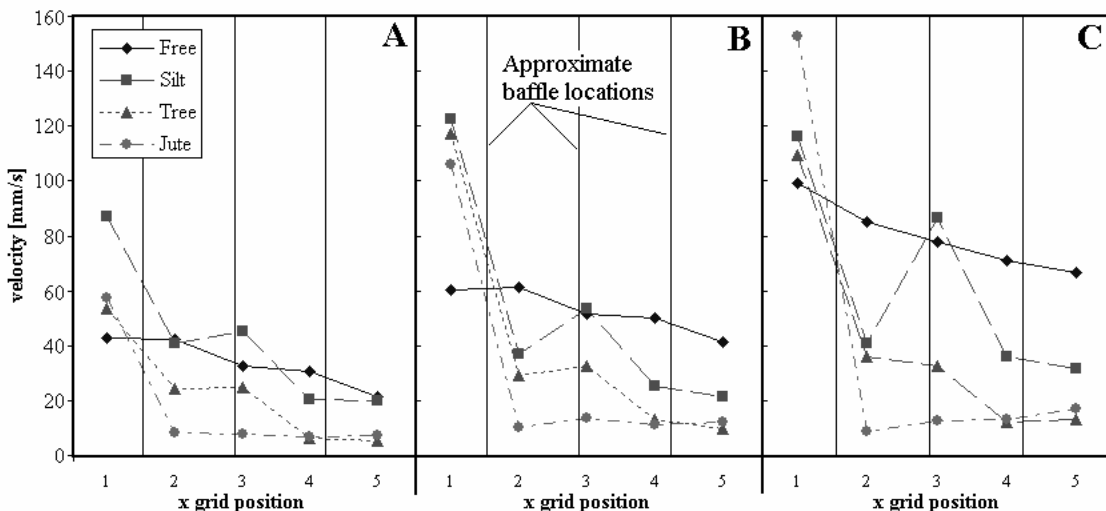


Figure 3.7: The depth-averaged mean flow velocity magnitude (see text) for each flow rate averaged along the 5 transverse gird points per x grid position for (A) 14 L/s, (B) 28 L/s, and (C) 42 L/s. This is from the sediment laden runs.

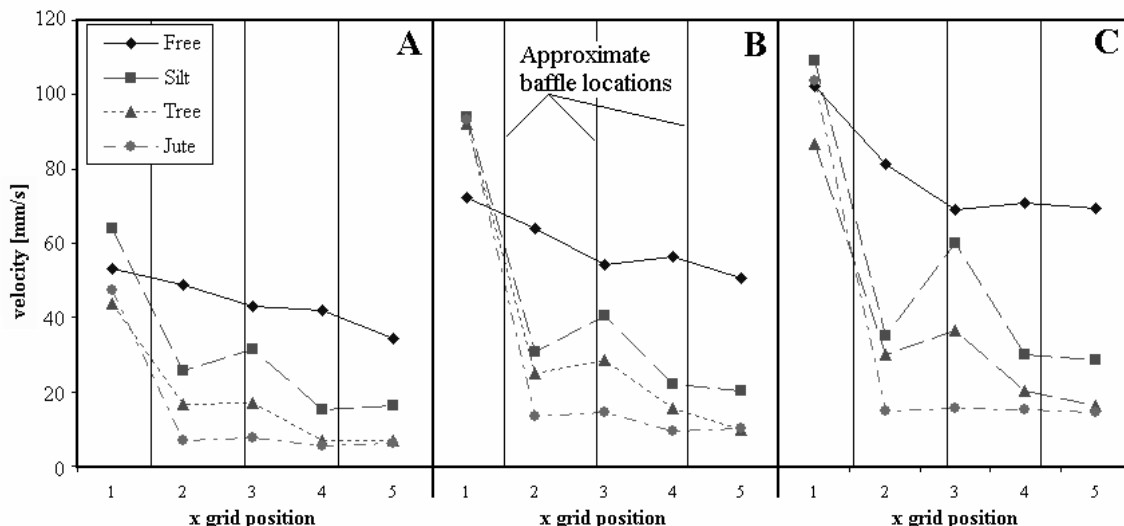


Figure 3.8: The depth-averaged mean flow velocity magnitude (see text) for each flow rate averaged along the 5 transverse grid points per x grid position for (A) 14 L/s, (B) 28 L/s, and (C) 42 L/s. This is the average of the data from the clear water and the sediment laden runs.

3.3.1.2 Transverse Variance

Although the longitudinal reduction in the transverse- and depth-averaged mean flow velocity magnitude, V'_x (eq. 3.4, figs. 3.6-3.8) was similar for each of the baffle configurations, the method for calculating $V'(x)$ suppressed any transverse flow behavior that may shed light on the relative effectiveness of the different baffles. The transverse variance of the depth-averaged mean flow velocity magnitudes at each x grid position was calculated as:

$$\sigma_x^2 = \frac{n \sum_{y=1}^n \bar{V}_{i=(x,y,\bar{z})}^2 - \left(\sum_{y=1}^n \bar{V}_{i=(x,y,\bar{z})} \right)^2}{n(n-1)}; \quad n = 5 \quad (3.5)$$

Transverse variance illustrates the degree to which the mean flow varied across the width of the pond. For the free flow case, the transverse variance of 7.47 (m/s)^2 was high due to large scale recirculation currents. Table 3.2 shows the transverse variance of each

baffle configuration, averaged longitudinally and expressed as a percentage of the free flow variance, for both the clear water and the sediment laden runs. Because the variances at $x=1$ were exceedingly high for the sediment laden runs, only x grid locations 2 through 5 were included in the calculation.

Table 3.2: The transverse variance [m^2/s^2] from equation 3.5, averaged longitudinally and over all flow rates, expressed as a percentage of the corresponding free flow variance.

	Silt fence	Tree protection fence	Jute/coir
Clear water runs	95%	34%	27%
Sediment laden runs [†]	76%	21%	3%

[†]Averaged over $x=2 \rightarrow x=5$ only.

The low transverse variance of the jute/coir and tree fence baffles indicate a rapidly diffused and stable mean flow across the full width of the pond, in support of observations. Although the transverse variance of the silt fence baffle configuration was roughly equivalent to the free flow case, no large scale recirculations were observed. The high transverse variance in the silt fence baffle most likely occurred due to (1) the weirs introducing localized jets of mean and turbulent flow as the water passed through them and (2) the low permittivity of the silt fence geotextile caused moderately intense flows to occur at unpredictable locations as overtopping or through weak points in the baffle structure. Although the silt fence baffle reduced the mean flow velocity magnitude, $V'(x)$, similarly to the tree and jute/coir baffles, the high variation in transverse flow intensity indicated conditions for solids resuspension and an overall poor trapping effectiveness, especially at higher flow rates in which overtopping or localized baffle failure occurred.

3.3.1.3 Vertical velocities

Comparison of data from the 0.13-m and 0.26-m depths suggests that the baffles reduced the vertical rotation over that of the free flow field. The free flow field encountered large vertical gradients in the 14 L/s and 28 L/s runs with a general clockwise motion at 0.13-m depth (e.g. fig. 3.2a). The baffled configurations, however, showed a reduction in vertical flow structure. For each depth, the mean flow velocity magnitude and the longitudinal component of the flow velocity were averaged over the x and y directions for each baffle configuration and at each inflow rate. The results for the 28 L/s inflow rate for the clear water runs showed that the jute/coir baffle maintained the smallest vertical gradient averaged over the flow field which was indicative of a high turbulent energy diffusion rate (fig. 3.9).

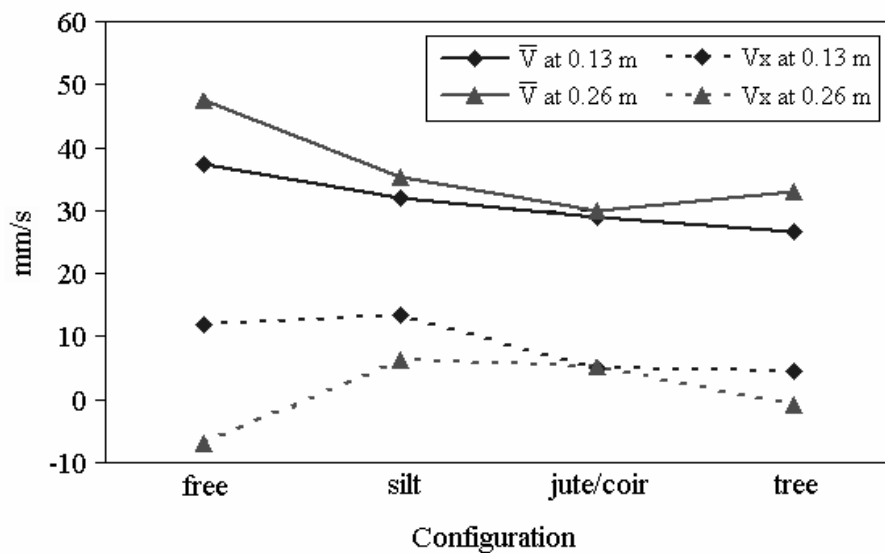


Figure 3.9. For each depth, the mean flow velocity magnitude and the x- component of the flow velocity were averaged over the x and y directions for each configuration at the 28 L/s flow rate. The jute/coir baffle maintains the smallest vertical gradient averaged over the flow field indicative of a high turbulent energy diffusion rate.

Figure 3.10 shows the depth-averaged vertical velocities for each baffle configuration at 28 L/s for the clear water runs. Similar patterns existed for each baffle configuration for 14 L/s and 48 L/s (see Appendix 3.B for a complete archive of vertical velocity maps for each of the clear water and sediment laden runs) except for the silt fence, to be discussed below. To obtain figure 3.10, interpolation was applied to the 25 grid data points via GRASS GIS module *r.surf.rst* with tension strength of 50 and a smoothness value of 0.1. The free flow field exhibited a basin wide rotation about the axis of flow direction in which water rose (brown color in figure 3.10) in the center and fell (blue-green color in figure 3.10) along the pond walls. For each of the baffles, at least two flow direction-parallel rotations were established in the intake cell (prior to the 1st baffle) due to the confinement of turbulent energy by the 1st baffle. For the tree and jute/coir baffles, vertical rotations were significantly reduced beyond the 1st baffle.

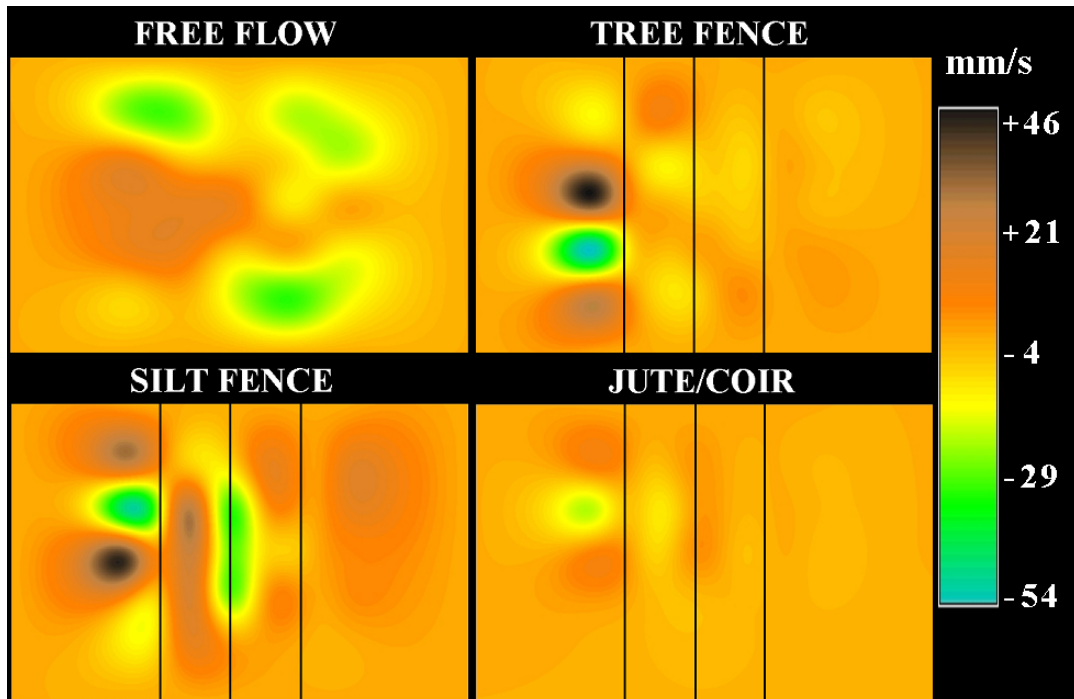


Figure 3.10: A composite of depth-averaged vertical velocities for the clear water runs at 28 L/s.

Similar to the clear water runs, the sediment laden runs depth averaged vertical velocities were mapped via GRASS GIS module *r.surf.rst* with a tension strength of 50 and a smoothness value of 0.1. Figure 3.11 shows the primary difference between the clear water and sediment laden runs: the sediment laden runs had higher vertical velocities and velocity variations. This trend was seen in all baffle configurations, although not for the jute/coir fence (Appendix 3.B, figures 3.B.19-3.B.24). Note that the scale is smaller than that of figure 3.10.

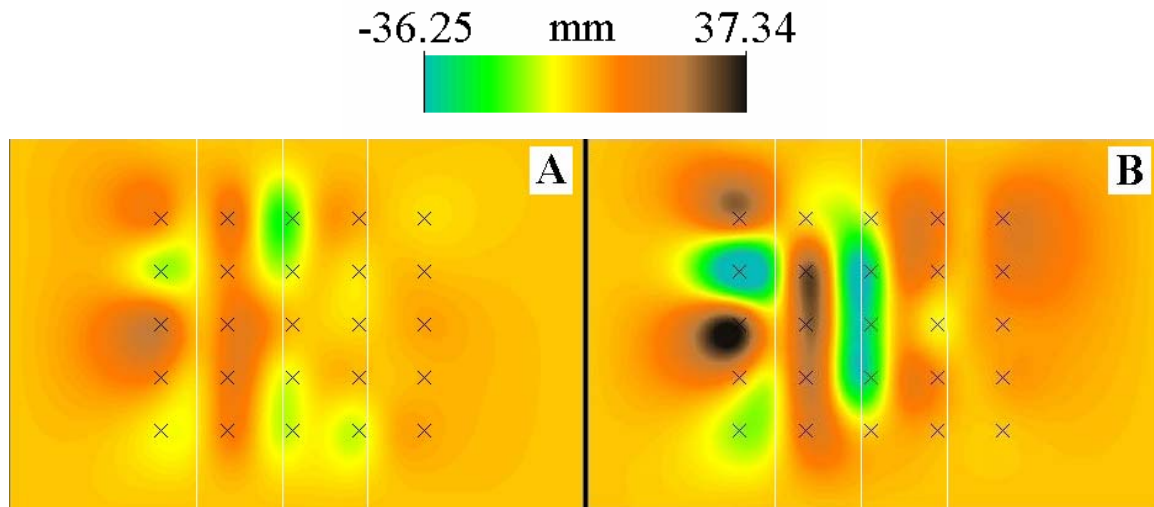


Figure 3.11: Depth averaged vertical velocities for the silt fence at 28 L/s for (A) the clear water runs and (B) the sediment laden runs. Approximate baffle locations are indicated by white lines. Flow is left to right.

For the silt fence at 28 L/s and 42 L/s flow rates, large flow direction-orthogonal rotations developed between the baffles, which did not develop for the 14 L/s flow rate (figure 3.12). This indicated that independent zones of rotational flow between the baffles, energized by the shear stress from overtopping flow, may inhibit new sediment from entering, reducing the pond volume accessible for sediment capture (figure 3.13). Because independent zones of flow direction-orthogonal rotation between baffles did not develop at the lowest flow rate (fig. 3.12-A), it is feasible to postulate that, for higher

expected flow rates, a larger baffle separation distance would be necessary to shrink and diffuse the vortices of rotation in these zones, thus maximizing sediment capture. For higher baffle permeabilities, such as that for the jute/coir, these zones did not develop nor were they encouraged by overtopping which did not occur, independent of flow rate or baffle separation distance.

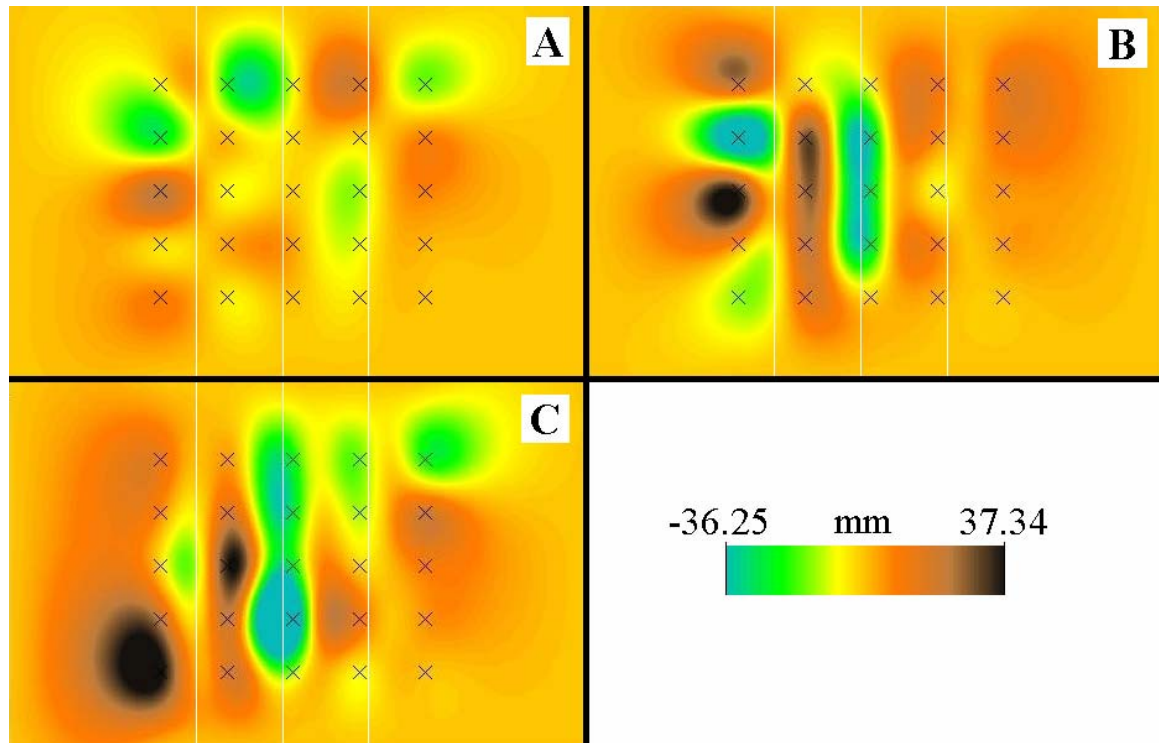


Figure 3.12: Depth averaged vertical velocities for the silt fence (sediment laden runs) at (A) 14 L/s, (B) 28 L/s, and (C) 42 L/s. Approximate baffle locations are indicated by white lines. Flow is left to right.

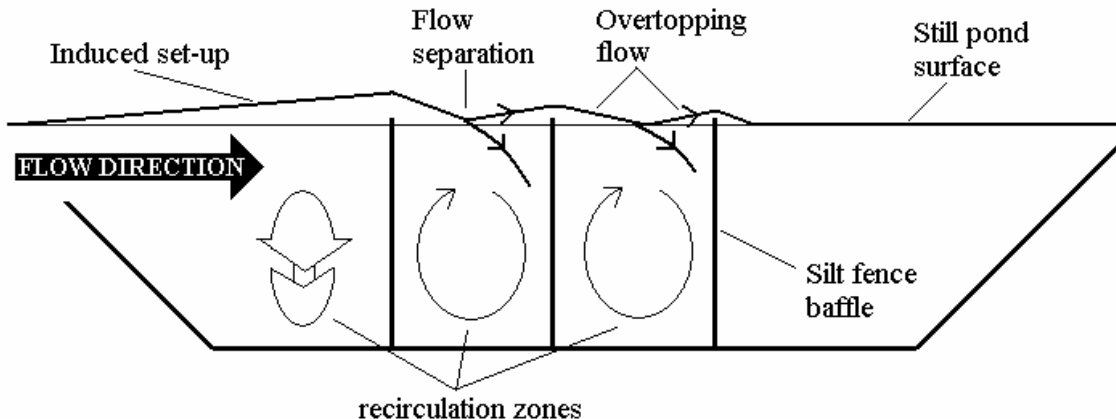


Figure 3.13: Vertical velocity data presented for the silt baffle suggests that, at 28 L/s and 42 L/s flow rates, independent zones of flow direction-orthogonal rotation ("sub basins") developed, inhibiting new sediment from entering the sub basins. The sub basins were energized by the shear stress applied by the overtopping flow observed at 28 L/s and 42 L/s flow rates (silt baffle only).

3.3.1.4 Signal-to-Noise Ratio

Lemmin and Lhermitte (1999) suggested that the larger the signal-to-noise ratio (SNR), the more suspended particulates are available in the water column for Doppler backscatter. However, Song, et al. (1994) stated that "density fronts resulting from turbulent dissipation" also contribute to the backscattered signal. Although all data used in our analysis met the minimum 20-dB signal to noise ratio for reliable velocity measurement as recommended by Kraus et al. (1994), the clear water runs were not seeded with additional sediment and the source pond water was sufficiently clear to assume no source pond suspended solids were available for acoustic interaction. In addition, the geotextile installed at the floor and intake of the pond prevented any erosion within the pond or the pond intake. As a result, we concluded that the fluid density fronts within the water column were the primary contributing factors to backscatter signal in our clear water experiments. For the sediment laden experiment, the backscatter signal was due to both turbulent density fronts and suspended sediment.

At each grid location, the three directional components of the signal to noise ratio, provided by the velocimeter, were averaged together to yield SNR_i . The SNR_i values were averaged over depth and over the y- direction to yield a representative signal to noise ratio at each x grid position, SNR_x . For the clear water runs, the downstream reduction in SNR_x for the baffled configurations (table 3.3, fig. 3.14) correlates directly to the reduction in turbulent energy density as flow propagates the length of the pond. An increase in SNR_x was measured from the 2nd to the 3rd x-grid position, followed by a subsequent decrease from the 3rd to the 4th x-grid position, for the silt fence baffle at all flow rates (see fig. 3.14). The same effect was measured sporadically for the other baffles at various flow rates and depths (depths not shown). As in the case of the transverse- and depth-averaged mean flow velocity magnitude (see fig. 3.6), this was due to the close proximity of the velocimeter to the 2nd baffle at the 3rd x-grid position. However, for SNR_x we do not believe that this effect would be suppressed by more sampling points at x=3; on the contrary, this behavior in SNR_x was the result of a measured increase in localized turbulence just downstream from the second baffle. For the case of the silt fence, the amplified SNR_x at x=3 corresponds to the increased turbulence due to overtopping and flow through the weirs. The jute/coir and tree baffles had the lowest turbulence as compared to the silt fence baffle and the free flow field, with the jute/coir generally performing the best.

Table 3.3. The transverse (y-) averaged signal to noise ratio (SNR_x) in [decibels] for each baffle configuration and flow rate for the x-grid positions 1, 2 and 5 for the clear water runs. Also shown are the percent reductions in SNR_x between x-grid positions 1 to 2 and between x-grid positions 1 to 5, averaged over all flow rates tested.

Baffle		Flow rate [L/s]	x grid position					drop in SNR_x (%)	drop in SNR_x (%)	SNR_x as a % of free
			x=1	x=2	x=3	x=4	x=5			
Free flow	Clear water runs	14	46.89	43.47	43.39	43.70	44.28	3.6	5.4	-
		28	45.99	45.01	43.67	43.11	42.13			
		42	48.37	49.04	47.78	49.96	49.43			
	Sediment laden runs	14	78.44	77.63	76.27	74.70	74.10	1.1	3.7	-
		28	75.11	74.06	74.23	73.99	72.18			
		42	73.55	74.19	73.48	72.25	72.41			
Silt fence	Clear water runs	14	49.16	38.90	42.77	39.06	38.01	23.0	28.6	89.9
		28	59.92	43.98	50.38	41.88	39.04			
		42	62.86	49.30	56.69	48.58	45.06			
	Sediment laden runs	14	76.58	78.17	77.89	73.31	72.34	2.0	6.5	98.6
		28	76.72	77.90	75.25	76.55	73.40			
		42	77.27	75.35	75.45	74.81	69.77			
Tree fence	Clear water runs	14	46.50	35.10	30.71	31.97	31.71	20.7	26.3	79.3
		28	52.02	42.03	41.03	39.54	36.27			
		42	47.73	39.02	44.76	42.84	39.71			
	Sediment laden runs	14	82.01	76.85	77.01	72.30	70.39	3.7	12.5	98.8
		28	81.84	78.97	78.31	73.92	71.40			
		42	82.86	81.89	79.14	75.42	74.20			
Jute/ coir	Clear water runs	14	49.03	33.94	39.26	32.60	30.80	27.4	40.6	71.9
		28	58.30	42.27	39.29	34.77	31.35			
		42	57.66	43.93	44.49	41.58	35.48			
	Sediment laden runs	14	79.28	73.27	63.90	69.29	68.27	7.4	15.6	92.3
		28	79.64	74.17	65.68	67.63	67.75			
		42	80.13	73.97	55.65	67.74	65.73			

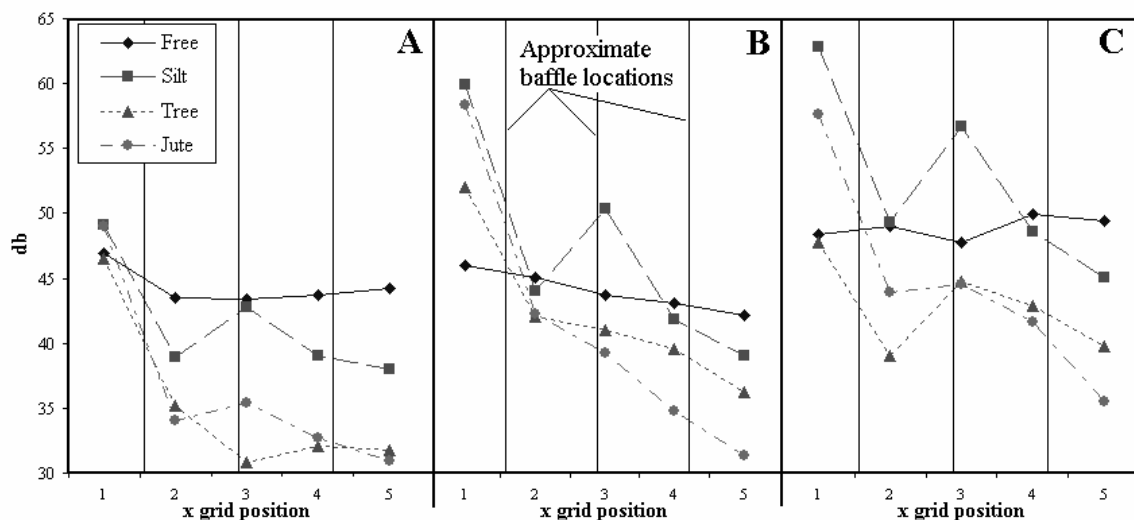


Figure 3.14. SNR_x (the depth-averaged signal to noise ratio, averaged across the transverse (y) direction per x grid position) for flow rates of (A) 14 L/s, (B) 28 L/s, (C) 42 L/s. averaged over all inflow rates for the clear water runs.

For the sediment laden runs, the higher overall *SNR* values were due to the additional suspended sediment in the water available for Doppler backscatter. Aside from the 1st x- grid position, the free flow, silt baffle and tree baffle had roughly the same *SNR* values with the jute/coir baffle exhibiting a marked reduction in *SNR* (fig. 3.15b). When the clear water data is subtracted from the sediment laden data, the remainder should correlate to the *SNR* due strictly to the amount of sediment in suspension (fig. 3.15c). Notice that the *SNR* values remained roughly constant across the domain - when averaged longitudinally, the free flow, jute/coir, and silt *SNR* values are within 1% of each other, indicating that the amount of small sediment (<0.053mm) remained constant across the domain regardless of the existence of the baffles.

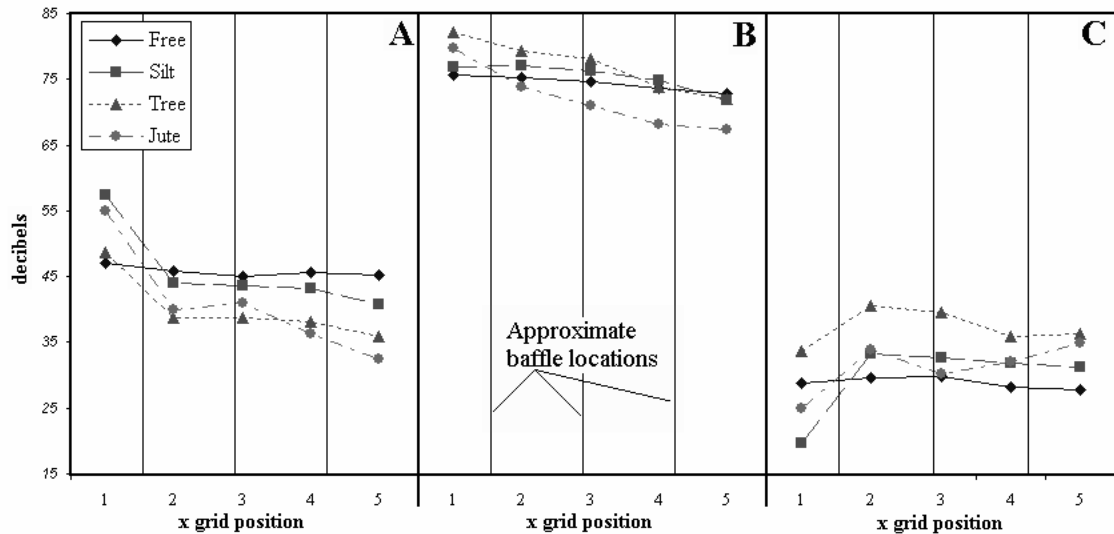


Figure 3.15: The depth averaged signal to noise ratio (*SNR*), averaged transversely and across all flow rates, for the (A) clear water runs and (B) the sediment laden runs. (C) shows the remainder when (A) is subtracted from (B), indicative of the sediment in suspension.

3.3.1.5 Quickest Path Analysis (Clear water runs only)

To determine the effect of the observed flow patterns on sediment capture in the clear water runs, we chose to quantify a minimum trapping effectiveness based on a “quickest path” analysis that would lead to a worst-case (shortest) residence time for each of the basin configurations. The x- component of the mean flow velocities, $V_{i,l} \equiv V_{i,j=e1}$, was depth-averaged at each grid location, i . The maximum transverse value of $V_{i,l}$ at each x grid position was identified (denoted $V_{x,l}^{\max}$) as:

$$V_{x,l}^{\max} \equiv V_{i=(x,y(\max),z);j=e1} = \max \text{ along } y \left(\frac{1}{m} \sum_{z=1}^m V_{i=(xyz),j=e1} \right); \quad m = 2 \quad (3.6)$$

By concatenating the $V_{x,l}^{\max}$ values per x-grid position, the quickest contiguous flow path through the grid was constructed (fig. 3.16). The resulting series of $V_{x,l}^{\max}$ values representing the quickest path was averaged to yield an average maximum mean flow velocity for each run, denoted as the “quickest path velocity,”

$$V_{qp} = \frac{1}{n} \sum_{x=1}^n V_{x,l}^{\max}; \quad n = 5. \quad (3.7)$$

This process was performed for each baffle configuration and for each flow rate. Table 3.4 summarizes the results of this analysis by showing the quickest path velocity, V_{qp} , due to the presence of the baffles, as a percentage of the free flow V_{qp} . The jute/coir baffle consistently had the lowest V_{qp} . These results were expected since the free flow field was observed to have a concentrated surface channel of high current along the central contour of recirculation while the baffles, notably the tree fence and jute/coir baffles, distributed the flow evenly across the width of the pond.

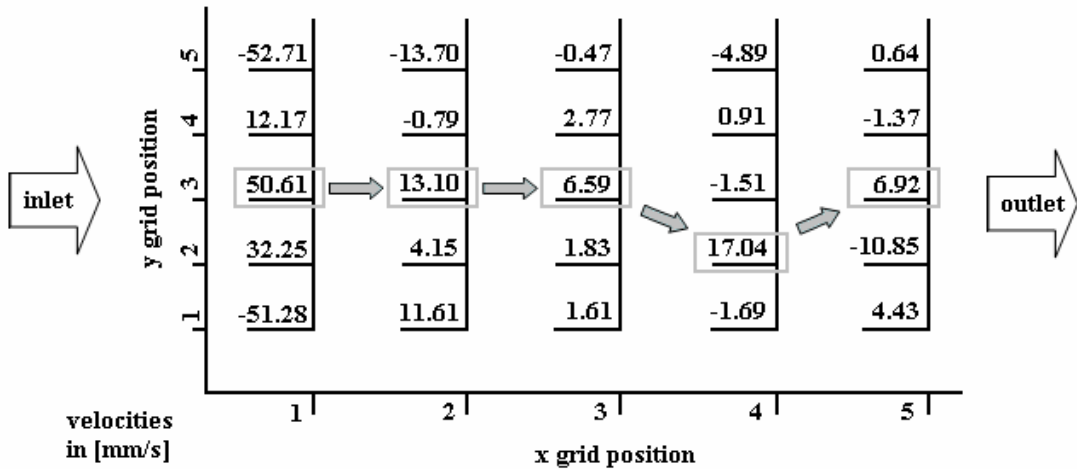


Figure 3.16. An example of the quickest path determination for the jute/coir baffle configuration at 42 L/s for the clear water runs. The values at each grid point represent the depth-averaged longitudinal (x) component of the flow velocities and are in mm/s. The resulting 5 values, 1 per x grid position (shaded), were averaged to yield an average maximum mean flow velocity, or quickest path velocity, V_{qp} (see text), that was used in projecting a theoretical pond trapping effectiveness.

Table 3.4. The quickest path velocity, V_{qp} , due to the presence of the baffles, as a percentage of the free flow V_{qp} and the silt fence baffle V_{qp} for each inflow rate. This data is for the clear water runs.

Baffle Setup	% of free flow				% of silt fence baffle			
	14 [L/s]	28 [L/s]	42 [L/s]	Ave. over flow rate	14 [L/s]	28 [L/s]	42 [L/s]	Ave. over flow rate
Jute/coir	20	22	24	22	51	49	49	50
Tree fence	26	34	38	33	67	75	78	73
Silt fence	39	46	50	45	-	-	-	-

The effect on the pond's sediment trapping effectiveness due to the reduction in and diffusion of mean flow velocities with the use of baffles can be calculated for typical sediment particle sizes. Here, we assume Stokes settling conditions for discrete spherical grains since the source water in our experiments was essentially clear and the particle Reynolds numbers, computed from measured flow velocities, were consistently less than unity. This assumption allowed us to divide the total length of the pond by the quickest path velocities to yield an estimate of the worst-case (shortest) residence times per run. The shortest residence time corresponds to a minimum available settling time for

sediment grains. The Stokes settling equation is given as (e.g. Daily and Harleman, 1966):

$$V_s = \frac{1}{18} \left[\frac{d^2 g}{\nu} (SG - 1) \right], \quad (3.8)$$

where $SG=2.65$ is the specific gravity of quartz grains, d is the grain diameter in m, $g=9.81$ m/s is the acceleration of gravity and $\nu=85.13 \times 10^{-6}$ m²/s is the kinematic viscosity of water at 27°C. By equating the Stokes settling velocity with the ratio of pond depth, h (=0.92 m), to minimum residence time, T_r , extracted from the “quickest path” flow line,

$$\frac{h}{T_r} = V_s , \quad (3.9)$$

the minimum grain diameter captured was projected for each scenario as:

$$d_{\min}(T_r) = \sqrt{\frac{18\nu}{g(SG - 1)} \frac{h}{T_r}} . \quad (3.10)$$

The results of this analysis are summarized in table 3.5. Note that these results were based on depth-averaged velocities: the near-surface volume, which was a small percentage of the overall pond volume participating in particulate capture, was observed to flow with a higher velocity than the depth-averaged values for the silt fence baffle and free flow configurations. In the case of the silt fence baffle, this was due to sporadic overtopping which occurred at the 28 L/s flow rate and near-continuous overtopping which occurred at the 42 L/s flow rate. In the free flow case, the higher observed near-surface flow rates were due to the pond's boundary layer structure which included large-scale rotations and a central short-circuiting current. For all flow rates tested, it was estimated that the jute/coir baffle will at worst capture very fine sand and the largest silt particles, whereas the silt fence baffle may only capture very fine sand at the lowest flow

rates (fig. 3.17). A vast majority of fine silt- and clay-size particles would be expected to escape the pond, regardless of the use of baffles. However, silt and clay particles may be trapped if they are part of aggregates (Haan et al., 1994).

Table 3.5. Minimum settling (residence) times [sec] and corresponding minimum captured grain size [μm] computed from the quickest path analysis as described in the text for the clear water runs.

Baffle Setup	Minimum Residence Times [sec] per flow rate			Minimum Captured Grain Size [μm] per flow rate		
	14 [L/s]	28 [L/s]	42 [L/s]	14 [L/s]	28 [L/s]	42 [L/s]
Jute/coir	965	649	489	30	37	42
Tree protection	725	427	302	35	45	54
Silt fence	489	319	237	42	52	61
Free flow	191	145	118	68	77	86

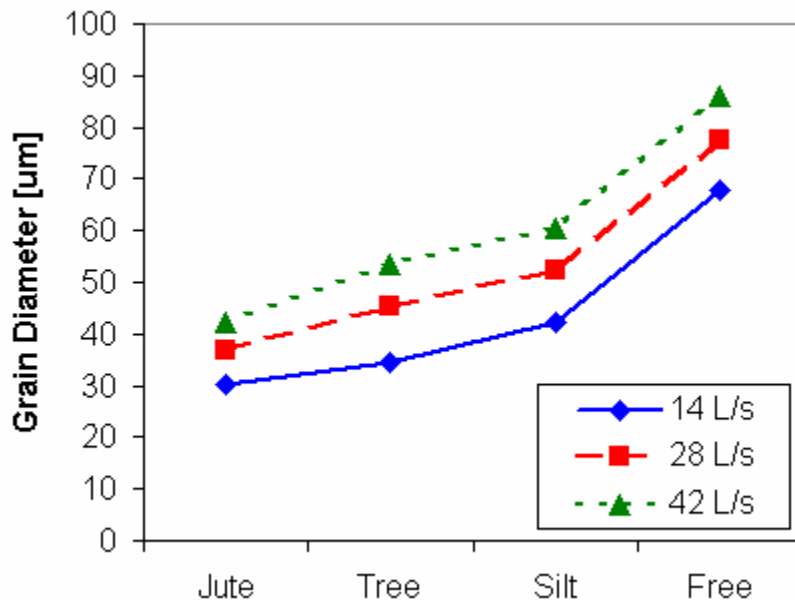


Figure 3.17. Estimate of the minimum grain capture size along the quickest path of flow based on Stoke's settling. All other paths through the pond result in higher residence times, therefore, this chart illustrates the worst case minimum capture size. The jute/coir baffle may capture finer particles ($30-45\mu\text{m}$) than the free flow case ($65-90\mu\text{m}$).

3.3.2 Sediment Capture

3.3.2.1 Captured Volume

The volume of captured sediment was estimated as a percent of the total sediment injected. Accumulated sediment height measurements were taken at 16 locations along the pond bottom and interpolated to yield a captured volume. The captured volume was then normalized by the amount of sediment injected as determined from the number of 19- liter buckets emptied over the course of all measurements per baffle configuration (Figure 3.18). The jute fence also captured a volume of sediment within its fabric, which was determined from a rough estimate of the weight of the fencing at time of removal. The actual percentage of captured sediment is higher than illustrated since a considerable amount of sediment accumulated outside of the control grid, especially near the intake, which is not accounted for in these calculations. The jute/coir and tree baffles captured the most sediment, as was expected from the velocity profiles (Figure 3.6) which correlates to longer residence times.

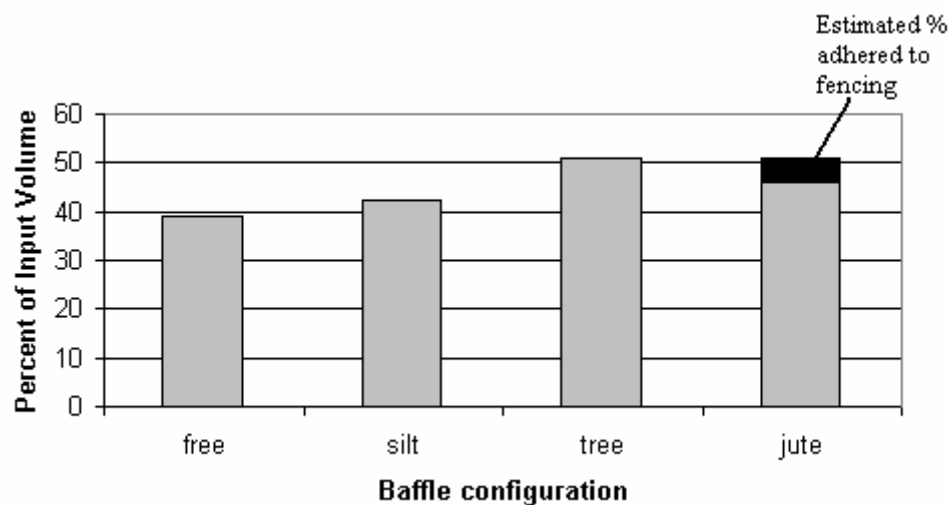


Figure 3.18: An estimate of the volume of captured sediment as a percent of sediment injected.

Figure 3.19 illustrates the deposition patterns for each of the configurations, determined from interpolation of the 16 sampling points within the pond via GRASS GIS module *r.surf.rst* with tension = 50 and smoothness = 0.1. Note that the plotted values in figure 3.19 have not been normalized by the input volume such that a relative comparison is not valid. All runs showed that a majority of the sediment was captured near the intake. The free flow pattern was more dispersed than the baffled runs. The tree fence, due to high hydraulic permeability, had a majority of measured sediment accumulate beyond the first baffle.

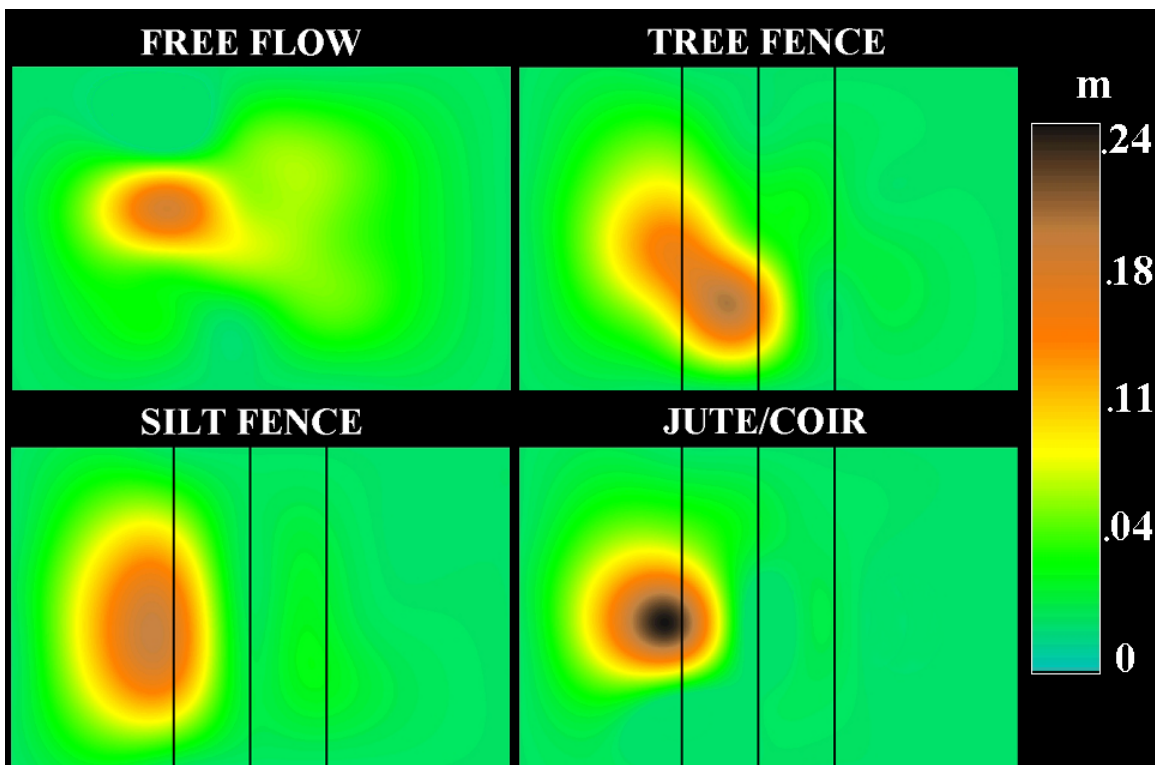


Figure 3.19: The deposition patterns interpolated from the 16 soil accumulation depth sampling points. Approximate baffles locations are indicated with black lines.

3.3.2.2 Turbidity and TSS

Measured total suspended solids (TSS) [mg/L] (Clesceri et al., 1998) and corrected turbidity [NTU] (Hayes, 2003) were obtained at the pond outlet by the Isco™ 712 sampler and averaged across all flow rates for each baffle configuration (see Figure 3.20). The turbidity showed an expected trend that correlates to the reduction in inflow momentum (Figure 3.6) and the estimated volume of sediment captured (Figure 3.18) per configuration. Figure 3.21 shows the exit turbidity for the 40 minute silt fence baffle, 28 L/s flow rate run (0.13 m depth). Once the pond reached equilibrium and flow rate was stabilized, sediment was injected and turbidity measurements began. Initially, source pond water was registered at very low turbidity, but an equilibrium turbidity level was reached after about 20 minutes.

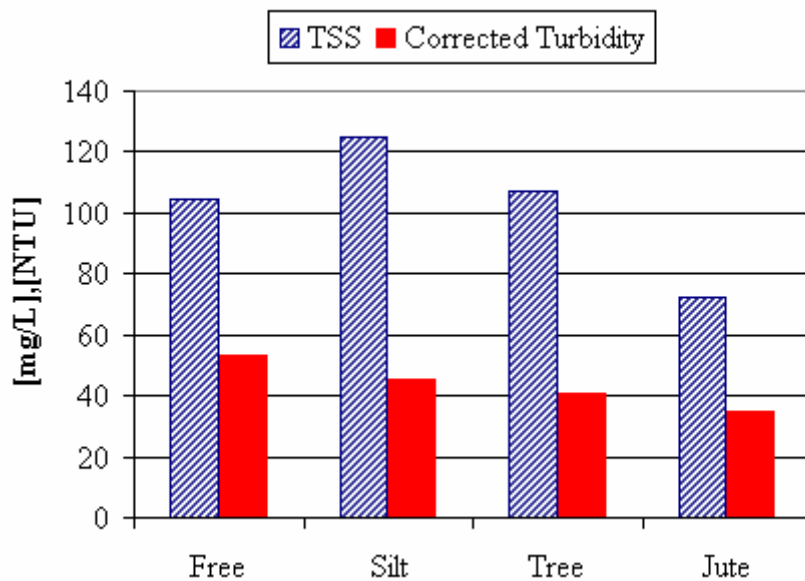


Figure 3.20: Total suspended solids and turbidity obtained at the pond outlet.

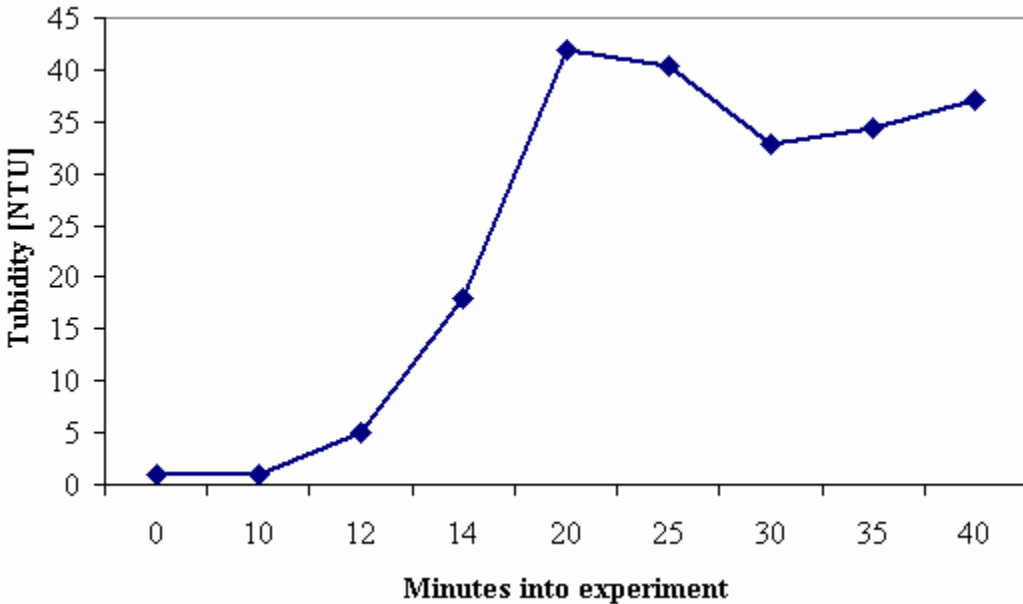


Figure 3.21: Measured exit turbidity over the course of a single 40 minute run (28 L/s silt fence).

3.3.2.3 Grain Size Analysis

After each set of flow rate runs per configuration, the pond was drained and soil was sampled at the 16 sampling locations identified in figure 3.1b. 40 grams of each sample soil was then analyzed using the standard hydrometer method (Loch, 2001). The $D_{50,i}$, a representation of median grain size per sample, was found for each gird location, i , via:

$$D_{50,i} = f_i^{sand} d_{50,i}^{sand} + f_i^{silt} d_{50,i}^{silt} + f_i^{clay} d_{50,i}^{clay}. \quad (3.11)$$

Here, f is the fraction of sand, silt, and clay of the 40g sample as determined from the hydrometer analysis, and:

$$\begin{aligned} d_{50,i}^{clay} [\mu m] &= 26.0 \\ d_{50,i}^{silt} [\mu m] &= 1.00 \\ d_{50,i}^{sand} [\mu m] &= \frac{1}{w_i^{sand}} \sum_{j=1}^6 w_{i,j}^{sand} \bar{d}_j \end{aligned} \quad (3.12a)$$

where

$$\begin{aligned} w_i^{\text{sand}} &= \text{weight of sand sample} \\ w_{i,j} &= \text{weight of sand in bin } j \\ \bar{d}_j &= \text{median diameter of sand bin } j \end{aligned} \quad . \quad (3.12b)$$

The median diameters of each of the 6 sand size bins are defined as:

$$\bar{d}_{j=1..6} = \{1500, 750, 375, 178, 85, 58 \mu\text{m}\} . \quad (3.12c)$$

The measured weight of the sand sample as a percent of the 40g sample per location should equate to the percent of sand as determined from the hydrometer readings. At most locations, the percent difference between these values did not exceed 5%; however, any excess or missing mass as measured by the scale (assumed to be more precise than the hydrometer method) was added/subtracted back to/from the silt and clay percentages determined by the hydrometer method to yield corrected silt and clay fractions used in equation (3.11). This correction was divided evenly between the silt and clay fractions as an approximation. Since the corrections were normally small, the approximation is assumed valid for our purposes. The corrected $D_{50,i}$ was averaged transversely at each x-grid position to yield a representative grain size distribution as a function of pond length only, $D_{50,x}$ (see Figure 3.22). The transversely-averaged hydrometer results for each configuration, as a percent of the 40g samples summed over all 16 sampling locations, are shown in figure 3.23.

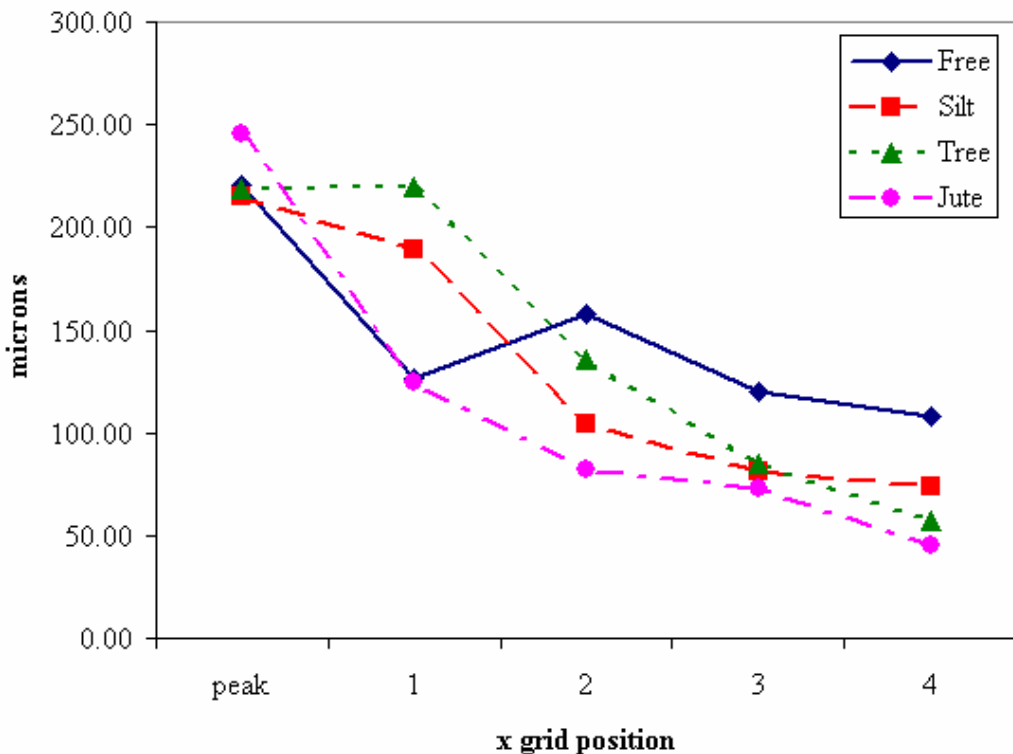


Figure 3.22: The corrected D_{50} (see text) for each configuration across the pond length, which indicates grain size distributions only.

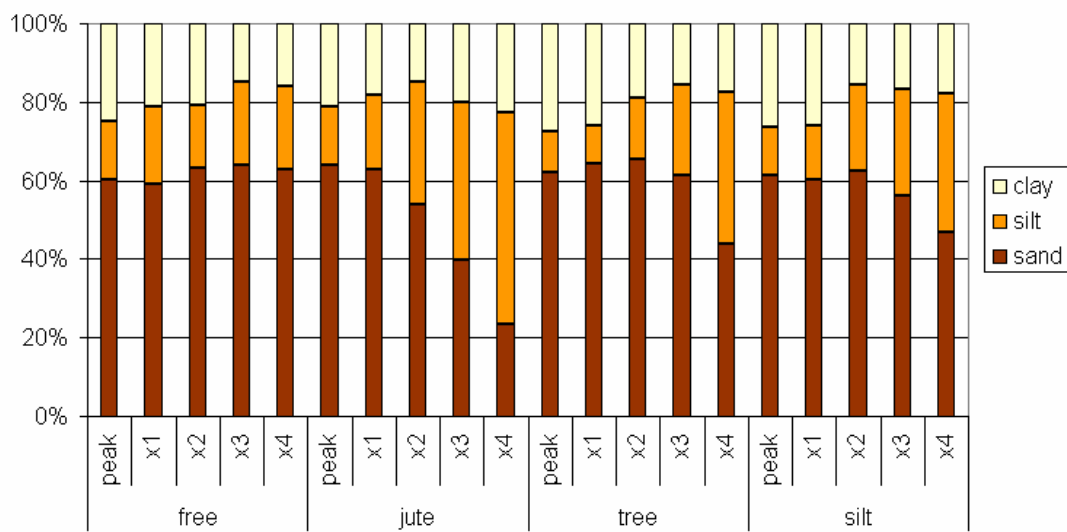


Figure 3.23: Hydrometer results for each configuration, as a percent of the 40g samples summed over all 16 sample grid location, corresponding to figure 3.20.

The baffled configurations capture smaller sediment than the free flow case.

Contrary to expectations based on the reduction of inflow momentum (Figure 3.6) and the estimate of captured sediment (Figure 3.18), the silt and tree baffle perform almost identically. This result is consistent with the composite SNR values (Figure 3.15b) for the silt and tree baffles. However, when the grain size distribution is multiplied by the volume of captured sediment (as a percent of input volume), the tree fence outperforms the silt fence (Figure 3.24). Although the distribution (D_{50}) of grains is the same for the silt and tree fences, the greater quantity of captured sediment by the tree fence configuration makes it a more effective baffle. The jute/coir baffle outperforms all baffle configurations.

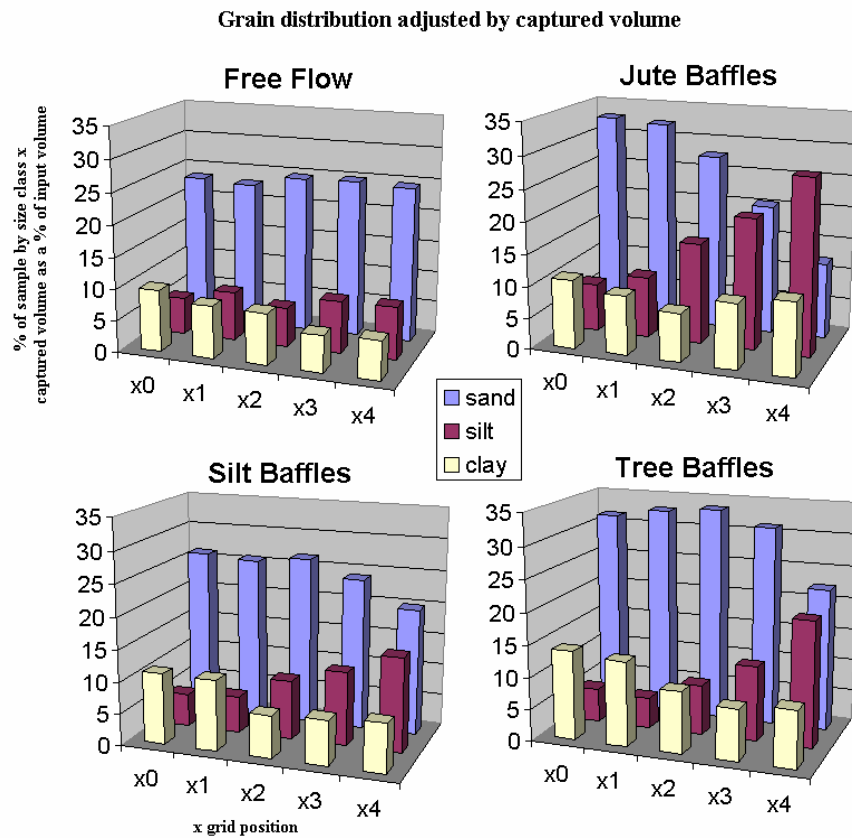


Figure 3.24: Here, Figure 3.23 is adjusted by multiplying by the volume of captured sediment as a percent of the input sediment volume per configuration (e.g. Figure 3.18).

The median captured grain size (D_{50} at the x grid position nearest the outlet (x=5), averaged over the transverse grid positions, is shown in figure 3.25. This value may be most indicative of the relative capture effectiveness since it is at this point that flow is most quiescent. These results are consistent with the relative hydrodynamic results for each configuration.

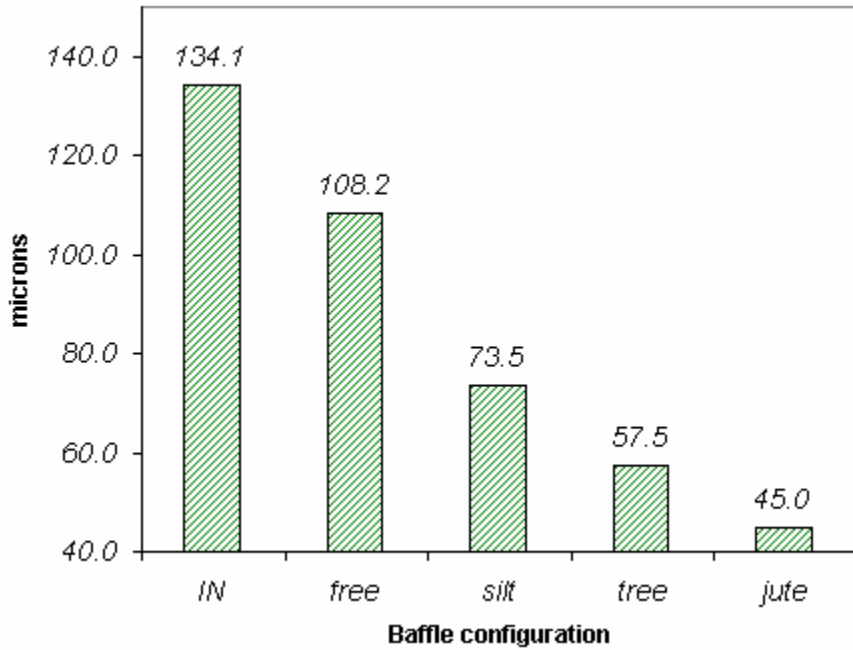


Figure 3.25: The transverse-averaged median capture grain size at the x-grid position nearest the exit (x=5) for each configuration.

The transverse-averaged sand sieve results for the different configurations are shown in figure 3.26. Note that the sand sieving was done after the silt and clay particles had been filtered off, although some residual small grains remained. For the free flow case (fig. 3.26a), the median grain size remained constant along the full length of the pond, although the larger grains were confined to the peak and the 1st x grid position near the intake. The median sand size for the baffles migrates downward as the distance traveled within the pond increases, with the jute/coir (fig. 3.26d) performing best.

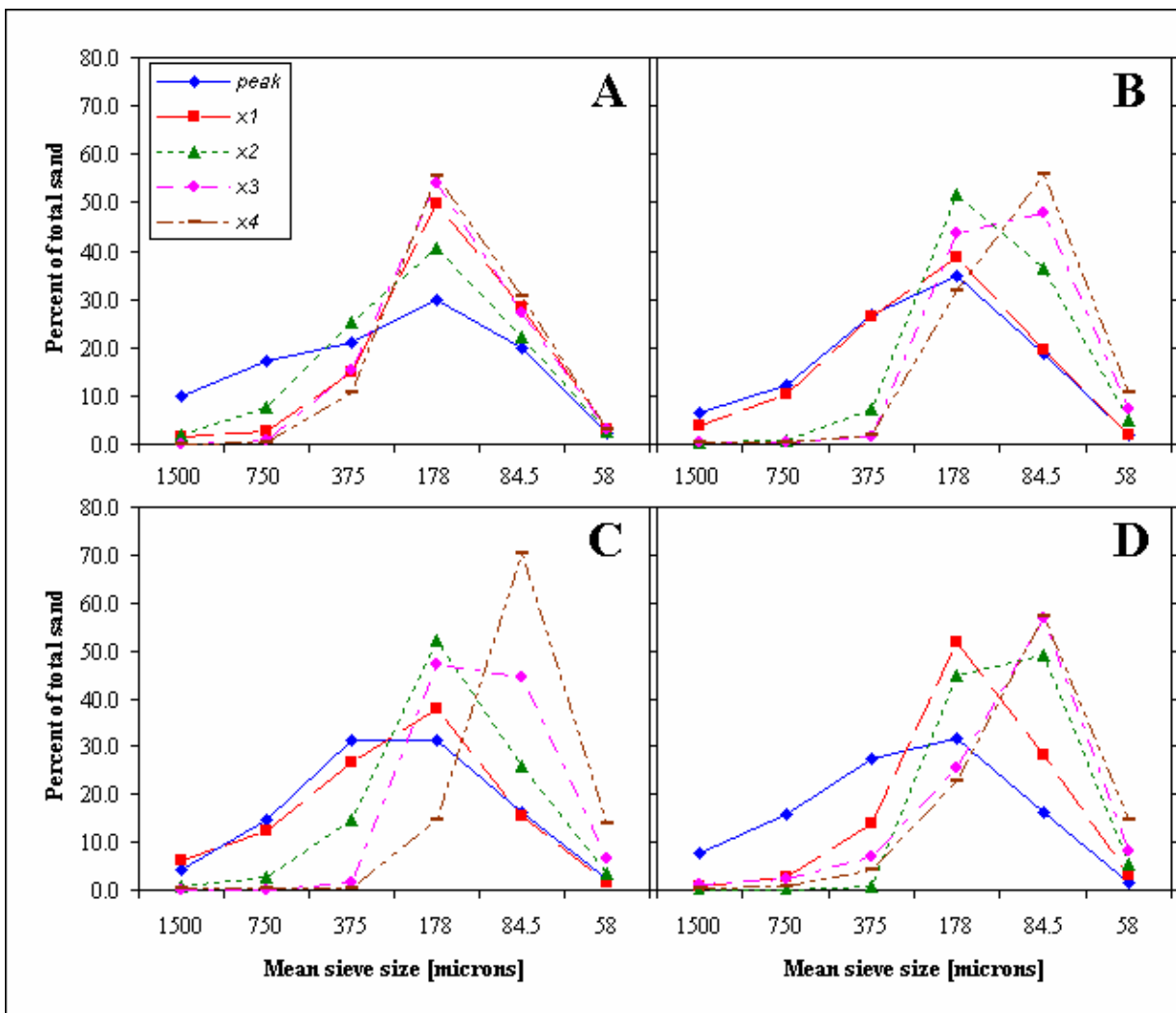


Figure 3.26: The sand sieve analysis results for each configuration. The transverse-averaged median sand grain size for each x-grid position is plotted separately for the (A) free flow, (B) silt fence, (C) tree protection fence, and (D) jute/coir.

3.4 Results analysis

A method similar to but simpler than the quickest path method described in section 3.3.1.5 is proposed to project a median grain size of capture for each configuration based solely on the hydrodynamics. In this analysis, we assumed that the e1- (longitudinal) component of the flow velocity, averaged over all 25 grid locations and both depths, represents the actual downstream flow field for each baffle configuration:

$$V_1 = V_{j=e1} = \frac{1}{n} \sum_{i=1}^n V_{i,j=e1} \quad ; n=50 \text{ grid locations} \quad (3.13)$$

By equating the conventional Stoke's setting velocity for spherical grains at small Reynolds numbers with the ratio of pond depth, h , to minimum residence time, $T_r=L/V_1$ (L =distance from intake to near-exit sample locations=580cm), the captured grain diameter can be projected for each baffle configuration as:

$$D(V_1) = \sqrt{\frac{18\nu}{g(SG - 1)} \frac{h}{T_r}} \quad (3.14)$$

where $SG=2.65$ is the specific gravity of quartz grains, d is the grain diameter in cm, $g=980$ cm/s is the acceleration of gravity and $\nu=0.008513$ cm²/s is the kinematic viscosity of water at 27 degrees Celsius. Equation 3.14 differs from equation 3.10 in that the average of all depth-averaged x-component velocities within the pond are used to determine the residence time, as opposed to the quickest path velocity (eq. 3.7). By averaging $D(V_1)$ over all flow rates, it is assumed that $D(V_1)$ represents a median capture size that is comparable to a representative grain size (D_{50}) from the hydrometer and sand sieving analysis of samples taken at distance L (see fig. 3.25).

The transverse-averaged D_{50} at the x- grid position nearest the exit compares well to the projected median captured grain size $D(V_1)$ for the jute/coir baffle (fig. 3.27a). The longitudinal (or x-) component of the flow velocity, averaged over all grid locations, is progressively less representative of the actual flow for the tree fence baffle, silt fence baffle, and free flow cases respectively (moving left-to-right in fig. 3.27a). This result corresponds to that suggested by the transverse variances in mean flow velocity and vertical velocity analysis: the flow with jute/coir baffles is much closer to calculated flow assuming full involvement of the basin cross section, suggesting optimal distribution of flow compared to the other configurations tested.

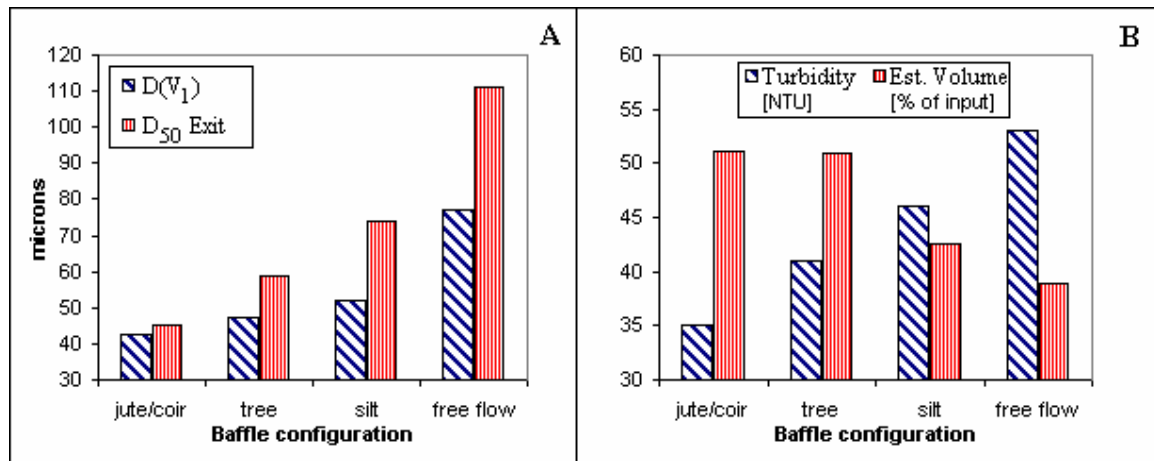


Figure 3.27: (A) The projected median grain capture diameter ($D(V_1)$) (based on Stoke's settling and the measured flow velocities) compared to the D_{50} computed from the soil samples at the x-grid location nearest the exit. (B) The measured turbidity and estimated volume within the measurement grid expressed as a percent of the volume of sediment injected per baffle configuration.

The permeability of each baffle was assessed using an optometric methodology. Open space percentage (OSP) for each baffle was determined optically and compared to the measured mean captured sediment grain size (D_{50}). Also included was the input D_{50} which, theoretically, represents a baffle of zero permeability and infinite sediment storage space. This comparison allows the OSP spectrum to be divided into three functional

regimes: (1) Hydraulically unstable regime, indicative of low permeability that leads to overtopping, fabric failure, and turbulent resuspension, (2) optimum diffusion regime, which diffuses incoming energy across the full width and depth of the pond without introducing turbulence, and (3) partial diffusion regime, which is less effective than optimum (fig. 3.28). These results also suggest that an optimal baffle permeability may exist. Further study would be required to determine if the optimum baffle permeability may be a function of flow rate, pond size and geometry, or baffle separation distance. This possibility is suggested by the flow rate dependence on the flow direction orthogonal, independent zones of rotation within the silt fence experiments (see Section 3.3.1.3). These findings may be important in specifying an economically and functionally optimal baffle material for field applications with known geometrical and maximum flow rate limitations.

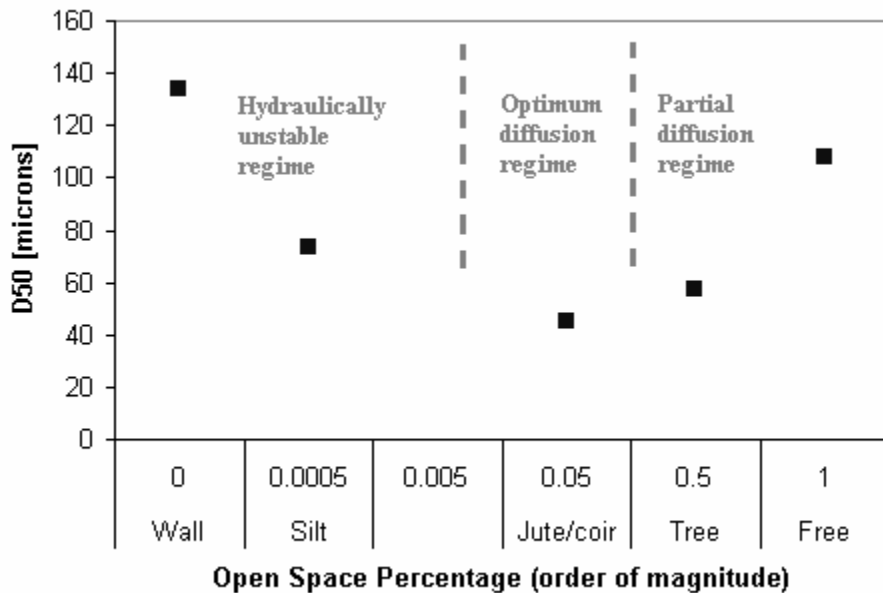


Figure 3.28: The measured median grain size of captured sediment versus measured baffle open pore space (OSP) - an indicator of baffle hydraulic permeability. Findings suggest that an optimal permeability exists.

3.5 Conclusions

The baffles we investigated substantially reduced mean flow velocities and velocity fluctuations (turbulence) compared to the standard, open sediment basin. Measured values of flow velocities and signal-to-noise ratios indicated that the jute/coir baffles out performed the tree protection baffles and especially the silt fence baffles in two primary respects: (1) the greatly reduced mean flow velocity magnitude, the small transverse variance in mean flow velocity magnitude, and the weak vertical velocity gradients suggested that the jute/coir baffles more effectively diffused the incoming energy such that more of the pond volume participated in the sediment settling process, and (2) a reduced signal-to-noise ratio for the jute/coir baffles beyond the intake cell suggested that turbulent energy density was best dispersed by the jute/coir baffles.

We found that the first baffle provided most of the benefit, with marginal reductions in velocities and turbulence with each additional baffle. Estimation of residence times from the “quickest path” of flow indicated that the jute/coir baffle would capture finer materials ($30\text{-}45\mu\text{m}$) compared to open basins ($65\text{-}90\mu\text{m}$) under the flow conditions in this study. This was confirmed for the jute/coir baffles in experiments with sediment-laden water, but the actual capture size for the silt baffles and an open basin were actually much higher than estimated due to high velocity variation and turbulence.

The high transverse variance in mean flow velocity magnitude measured for the silt fence baffle supports the observations that the weirs cut in the baffle produced localized jets of turbulent flow, which may contribute to sediment resuspension. Also, the very low permittivity of the silt fence baffle established a high pressure gradient which

caused moderately intense flows to occur at unpredictable locations as overtopping or through weak points in the baffle structure.

Qualitative observations of flow behavior indicated that a minimum inflow momentum was required to establish repeatable free flow patterns with predictable dead zone locations, although overall dead storage may remain unaffected. This suggested that designers of retention ponds, which rely on pond geometry and the location and orientation of the inlet and outlet for trapping efficiency optimization in the field, should consider flow rate dependence when assessing the effectiveness of their design. In addition, an observed reduction in large-scale vorticity meant that all baffles tested eliminated dead storage at the axes of large-scale rotations occurring in free flow and reduced the likelihood of pond wall scour. Finally, pond hydrodynamic measurements and observations presented in this paper suggest that porous baffles perform better than the silt fence baffle in overall sediment trapping efficiency.

Appendix 3.A - Hydrodynamic Data

In the tables below are the depth-averaged velocity and signal-to-noise ratio data for all runs performed on the sediment retention pond. The layout of the tables corresponds to the data acquisition grid shown in figure 3.A.1. Given are the flow velocity magnitudes, the x-component of the velocities and the signal to noise ratio magnitude at each of the 25 grid locations. All values are depth averaged. For a complete set of raw data, please contact the author.

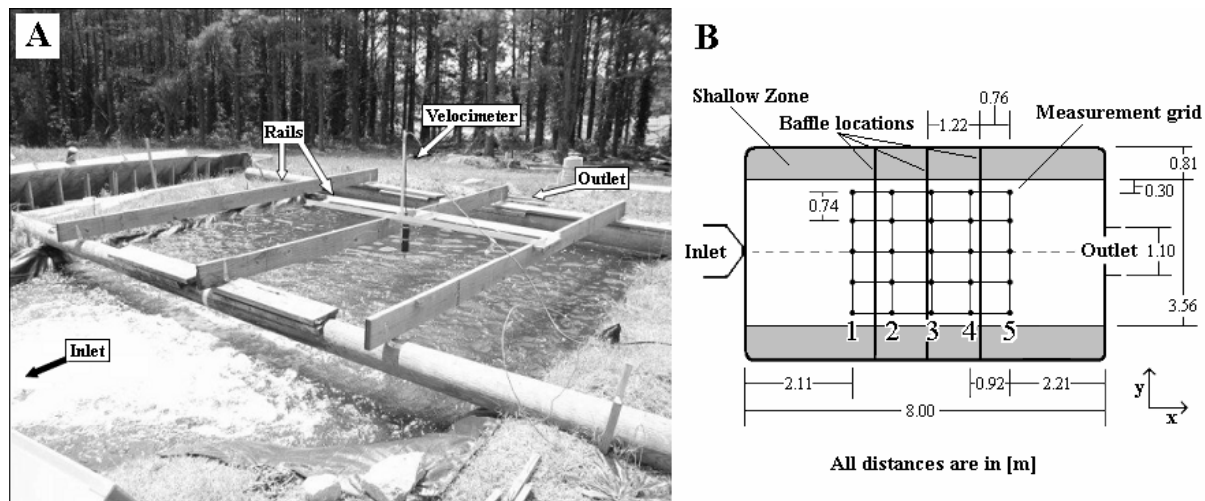


Figure 3.A.1: Sediment retention pond layout and dimensions.

Table 3.A.1: Free flow - clear water runs - 14 L/s

14 L/s	x=1	x=2	x=3	x=4	x=5
V [cm/s]					
y=5	4.310333	4.489897	6.262917	7.824773	6.545044
y=4	9.262088	9.094745	4.843909	6.034889	5.747647
y=3	9.090741	3.922961	3.796045	2.08905	3.765838
y=2	4.053931	4.052875	5.141118	5.564667	3.901274
y=1	4.962337	6.155093	6.672924	5.088034	3.723005
Vx [cm/s]					
y=5	-3.65914	3.938152	6.083306	7.651954	5.943145
y=4	5.770343	6.053236	4.500814	5.108387	3.047971
y=3	6.984273	0.635406	1.32753	0.014322	-0.14299
y=2	-1.75328	-3.20572	-4.91686	-5.23289	-2.94075
y=1	-4.71028	-6.04953	-6.64234	-4.97181	-3.47234
SNR [dB]					
y=5	50.078	51.12527	49.22701	49.29065	47.63748
y=4	51.83009	50.11466	46.23614	46.47478	45.77757
y=3	51.72281	36.47402	41.30648	41.25165	45.84273
y=2	42.65218	40.80413	41.4171	42.03276	44.15033
y=1	38.18134	38.81056	38.75694	39.44617	37.96708

Table 3.A.2: Free flow - clear water runs - 28 L/s

28 L/s	x=1	x=2	x=3	x=4	x=5
V [cm/s]					
y=5	5.965648	8.39304	8.010299	9.34388	9.740577
y=4	10.23624	12.87477	6.172754	6.371511	4.303352
y=3	7.094447	3.259783	6.892945	4.218718	3.043249
y=2	10.7858	2.963167	3.59935	4.425863	3.581653
y=1	7.902868	5.339242	4.329432	6.765294	8.311169
Vx [cm/s]					
y=5	0.370029	1.924074	-0.67295	0.591709	1.194428
y=4	-1.42122	-0.17002	0.757052	2.156318	-0.69248
y=3	-0.88563	0.251963	0.042615	0.54455	1.04503
y=2	3.09471	-0.90451	0.410137	2.777395	1.432772
y=1	-1.98286	-0.14348	-0.30214	-1.24621	-0.45745
SNR [dB]					
y=5	44.60282	44.83814	41.68448	41.67936	42.11336
y=4	43.91782	44.11678	43.96752	43.73322	41.44095
y=3	48.68901	46.05723	44.28022	43.05857	40.9599
y=2	49.01351	43.29327	42.52549	43.45306	40.86539
y=1	43.71987	46.73706	45.88974	43.61599	45.25738

Table 3.A.3: Free flow - clear water runs - 42 L/s

42 L/s	x=1	x=2	x=3	x=4	x=5
V [cm/s]					
y=5	8.455772	11.1288	10.15377	8.477564	5.566245
y=4	9.838722	8.099549	2.86813	4.874663	7.548934
y=3	8.220808	6.114327	3.050465	5.066933	8.215871
y=2	19.90876	10.84767	6.941759	9.453106	9.521267
y=1	6.17262	2.53792	7.076206	7.583953	5.230804
Vx [cm/s]					
y=5	-7.74252	10.88046	-10.067	-8.09927	-4.21108
y=4	-7.34472	-7.14955	-2.80571	-2.97637	-0.9449
y=3	-4.86821	-0.4124	1.861452	2.081597	3.632648
y=2	16.77487	9.723802	6.756391	7.608035	7.193604
y=1	-2.01231	1.800528	6.551185	7.142246	4.004336
SNR [dB]					
y=5	39.26928	40.91603	42.4749	45.86068	44.00714
y=4	42.89079	42.73092	41.6383	46.02948	48.53644
y=3	42.20706	44.67431	44.98849	49.40917	50.23197
y=2	63.29516	57.22583	53.77363	54.32756	52.66659
y=1	54.19468	59.67356	56.00933	54.154	51.73149

Table 3.A.4: flow - sediment laden runs - 14 L/s

14 L/s	x=1	x=2	x=3	x=4	x=5
V [cm/s]					
y=5	1.818256	1.672311	2.388417	2.502862	1.586317
y=4	5.092504	6.106903	2.081744	2.201352	1.993703
y=3	7.69326	5.629272	3.508383	2.512111	1.66625
y=2	4.235884	4.502937	4.441837	4.026703	2.172439
y=1	2.638369	3.206325	3.8479	4.081841	3.279027
Vx [cm/s]					
y=5	-0.5758	-0.99681	-1.71447	-0.84059	-1.3496
y=4	-4.92599	-5.5885	-1.41445	-0.27297	-0.1517
y=3	-7.07188	-5.04665	-3.3506	-0.57223	0.393312
y=2	-3.11758	-3.51412	-2.87601	-1.88191	0.823316
y=1	0.299688	-1.95387	-0.39429	1.683164	3.080389
SNR [dB]					
y=5	78.11004	77.45102	74.97573	73.55937	73.3468
y=4	78.17921	75.80616	75.73333	74.66915	74.03977
y=3	77.3114	77.78604	76.2849	75.09007	74.40682
y=2	80.8839	79.13884	76.98805	75.0231	73.88837
y=1	77.69065	77.98546	77.36848	75.18293	74.82257

Table 3.A.5: flow - sediment laden runs - 28 L/s

28 L/s	x=1	x=2	x=3	x=4	x=5
V [cm/s]					
y=5	4.891903	4.677769	2.929606	5.973227	2.260994
y=4	6.299453	7.357346	10.10216	6.012173	5.672037
y=3	9.268988	6.693029	5.542413	3.341874	4.845753
y=2	6.601762	6.891852	4.515392	4.309622	3.079075
y=1	2.945635	4.82555	2.695667	5.372186	4.796246
Vx [cm/s]					
y=5	-0.93308	-0.33002	-0.5725	3.870507	0.152032
y=4	-3.89025	-6.7021	0.276302	3.405223	1.774379
y=3	-0.86852	-5.56094	-4.24408	-0.5142	-3.31982
y=2	-6.20459	-6.35781	-3.81629	-2.75201	-0.22937
y=1	-1.83634	-3.28762	-0.55891	3.417885	1.219168
SNR [dB]					
y=5	75.15765	75.77803	75.41385	75.53125	74.83394
y=4	76.02555	73.86908	73.96423	73.89394	71.4798
y=3	76.44246	75.12105	74.8339	74.35802	72.54359
y=2	76.41808	74.33718	73.74612	72.5827	71.77291
y=1	71.48588	71.18469	73.2058	73.56512	70.26804

Table 3.A.6: Free flow - sediment laden runs - 42 L/s

42 L/s	x=1	x=2	x=3	x=4	x=5
V [cm/s]					
y=5	12.85661	13.81695	10.18788	10.59255	9.69211
y=4	9.677356	12.3918	8.878189	4.637347	4.359222
y=3	13.05009	6.456721	5.070197	5.487955	4.277578
y=2	8.223735	4.354929	7.493222	4.184999	3.314609
y=1	5.90451	5.551744	7.255154	10.50314	11.77321
Vx [cm/s]					
y=5	-11.4428	-11.9651	-8.9659	-10.3961	-8.00186
y=4	-6.79853	-9.82726	-7.47528	-3.32407	-1.94484
y=3	-11.3083	-5.84819	-0.65909	-4.64837	-3.71874
y=2	-6.89781	-2.95572	-5.54577	-0.48032	0.921148
y=1	4.73816	1.376461	4.736737	8.753071	10.7148
SNR [dB]					
y=5	70.47769	70.42201	70.34224	70.38589	71.74217
y=4	72.18695	71.71997	71.41016	71.2795	71.99792
y=3	74.14095	75.39321	74.86734	71.57774	71.82806
y=2	75.76774	77.62166	74.79916	73.17762	72.12509
y=1	75.18116	75.81566	75.99754	74.83068	74.36084

Table 3.A.7: Silt fence - clear water runs - 14 L/s

14 L/s	x=1	x=2	x=3	x=4	x=5
V [cm/s]					
y=5	2.353687	1.54201	2.643926	1.084924	2.766455
y=4	1.992901	0.978091	1.175409	1.080349	0.854626
y=3	9.47863	1.059502	1.432226	0.917307	0.758365
y=2	3.911423	0.936608	1.673983	0.965563	0.817197
y=1	2.567726	0.789161	2.079928	0.938411	0.98648
Vx [cm/s]					
y=5	-2.07656	-1.07929	0.781607	0.53377	2.645552
y=4	-0.26642	-0.23211	-0.87858	0.464625	0.747095
y=3	8.64068	-0.28875	0.025178	0.676319	-0.33205
y=2	1.957806	0.200108	0.781621	-0.18256	0.272002
y=1	-2.2568	-0.21673	1.063296	0.722735	0.142905
SNR [dB]					
y=5	43.56831	39.51694	40.31676	38.28978	37.98228
y=4	47.90292	39.531	53.29549	39.77257	38.35428
y=3	57.06696	39.67739	43.24765	38.76208	38.2591
y=2	50.96362	37.32603	36.28744	38.68452	37.86187
y=1	46.29164	38.4294	40.71255	39.77163	37.58323

Table 3.A.8: Silt fence - clear water runs - 28 L/s

28 L/s	x=1	x=2	x=3	x=4	x=5
V [cm/s]					
y=5	5.566042	2.624256	4.452004	2.379675	4.347806
y=4	4.682648	1.812098	2.267435	1.931368	1.316229
y=3	16.1503	2.336306	0.392234	1.245	0.801173
y=2	1.650122	1.975138	2.898356	1.167063	1.479017
y=1	4.7528	3.38617	3.700253	2.729448	1.601232
Vx [cm/s]					
y=5	-4.9631	0.249453	0.786606	1.414351	4.2344
y=4	0.384565	0.065889	-0.23719	1.526304	1.264293
y=3	14.87527	0.711562	-0.01712	0.727471	-0.48648
y=2	-0.09554	-0.42966	0.628379	0.220557	1.277793
y=1	-4.42133	1.363462	1.590742	1.54892	0.639576
SNR [dB]					
y=5	55.83419	45.82165	47.67264	40.06298	37.93396
y=4	60.23013	42.14441	46.93041	39.89475	37.4364
y=3	65.4205	41.44578	64.93038	41.09487	37.32625
y=2	59.72865	43.39952	43.75594	41.62316	37.8979
y=1	58.40439	47.06819	48.63396	46.73337	44.6186

Table 3.A.9: Silt fence - clear water runs - 42 L/s

42 L/s	x=1	x=2	x=3	x=4	x=5
V [cm/s]					
y=5	9.597421	3.811048	2.944734	2.519533	3.548391
y=4	10.75029	3.2755	3.694197	3.154506	2.368558
y=3	20.88611	2.278322	1.325037	1.568271	2.07097
y=2	4.27991	2.585544	5.471441	1.512715	2.738998
y=1	5.576454	2.638639	3.364044	3.2135	2.113268
Vx [cm/s]					
y=5	-7.79793	-0.65258	-0.20805	-0.01657	3.327433
y=4	-6.48993	-1.51185	-0.776	2.726289	2.253668
y=3	20.37342	-0.85019	-0.2536	1.260904	-0.6096
y=2	-3.0895	-0.78614	-1.15236	1.231846	0.711133
y=1	-5.48758	-0.02446	-0.03503	1.578677	1.188341
SNR [dB]					
y=5	59.45547	46.86041	50.69758	43.74797	42.84863
y=4	62.93843	46.95663	49.21787	46.76466	42.51957
y=3	65.68198	47.08525	72.39208	46.76292	43.56307
y=2	62.24736	49.59022	54.32273	49.93049	45.65074
y=1	63.97385	55.99306	56.83732	55.71511	50.72423

Table 3.A.10: Silt fence - sediment laden runs - 14 L/s

14 L/s	x=1	x=2	x=3	x=4	x=5
V [cm/s]					
y=5	9.670749	6.476922	9.141173	2.11292	6.439343
y=4	9.148727	4.136018	4.24945	1.809018	1.842029
y=3	14.83539	2.667225	1.493909	1.823539	0.920427
y=2	4.772619	2.691315	3.145145	2.754508	0.576883
y=1	5.189505	4.503922	4.549866	1.814001	0.200785
Vx [cm/s]					
y=5	-3.93271	4.216249	8.706156	-0.12387	5.59377
y=4	5.188195	0.801997	-1.47956	0.786245	-1.47552
y=3	14.24631	-1.32468	-0.75784	1.100972	-0.04819
y=2	-4.34056	-0.36521	-0.14536	1.681893	0.013189
y=1	-4.63684	0.465894	0.204986	-0.50533	-0.03214
SNR [dB]					
y=5	82.81835	80.12831	80.73913	76.08195	75.88277
y=4	82.74756	77.88862	79.15258	74.16691	74.25322
y=3	85.57995	77.71117	78.3745	75.26685	73.87378
y=2	83.58433	78.70323	77.51324	72.71262	69.6629
y=1	48.14763	76.43665	73.66404	68.31025	68.02887

Table 3.A.11: Silt fence - sediment laden runs - 28 L/s

28 L/s	x=1	x=2	x=3	x=4	x=5
V [cm/s]					
y=5	8.870455	3.793365	2.690297	3.396541	5.342923
y=4	15.22461	3.703949	6.361953	2.463671	1.463839
y=3	18.1275	3.504067	8.660437	2.62936	1.744717
y=2	9.43097	4.069812	5.87211	1.321281	1.259007
y=1	9.402019	3.418713	2.967378	2.740883	0.80783
Vx [cm/s]					
y=5	-5.20269	0.619601	-0.17381	0.255806	3.9462
y=4	7.872069	-0.39291	-1.57224	0.6452	-0.70019
y=3	16.90293	-1.24439	-5.85463	1.83128	-0.21285
y=2	-7.3173	0.750005	-2.11353	-0.06144	-1.08558
y=1	-7.46741	0.901324	0.279966	-1.20505	0.633818
SNR [dB]					
y=5	81.50218	79.18842	65.58551	80.08443	77.5602
y=4	82.93813	79.53782	81.25812	77.63002	75.22463
y=3	82.38455	78.31229	67.78376	76.3644	73.68482
y=2	83.04919	76.4377	83.44692	74.42935	70.37245
y=1	53.72402	76.02938	78.16224	74.23609	70.17917

Table 3.A.12: Silt fence - sediment laden runs - 42 L/s

42 L/s	x=1	x=2	x=3	x=4	x=5
V [cm/s]					
y=5	15.34363	4.365325	7.993627	3.171624	8.250948
y=4	13.24734	4.227308	5.686642	1.997346	2.099787
y=3	7.743386	4.803701	6.73277	3.391964	2.064139
y=2	13.28207	3.010486	14.33344	2.991741	1.927229
y=1	8.57169	3.977703	8.515373	6.520156	1.380232
Vx [cm/s]					
y=5	-13.4639	-1.30311	-3.07366	1.565103	6.359327
y=4	5.014763	0.015337	-1.37247	1.28815	0.639268
y=3	5.793978	-1.48187	-1.92425	2.910651	-1.53132
y=2	-12.8805	0.140762	-7.44562	0.524449	-1.56095
y=1	-4.18428	-0.30732	-0.35357	1.186806	1.261993
SNR [dB]					
y=5	82.23899	74.55374	63.27808	72.30812	69.8632
y=4	82.0936	75.02539	74.36209	74.41472	69.51549
y=3	82.54334	76.65951	83.50233	75.09767	70.13297
y=2	79.87623	76.8037	80.03469	75.67005	70.21847
y=1	59.58749	73.69527	76.08118	76.54626	69.13821

Table 3.A.13: Tree fence - clear water runs - 14 L/s

14 L/s	x=1	x=2	x=3	x=4	x=5
V [cm/s]					
y=5	3.926836	0.28414	0.71024	0.751324	0.38151
y=4	3.850655	1.097529	0.80671	0.793155	1.029707
y=3	3.072044	0.428114	0.57126	0.857772	1.15246
y=2	4.335507	2.066754	1.203224	0.607321	0.984849
y=1	1.730414	0.629621	1.198553	0.789808	0.714995
Vx [cm/s]					
y=5	-3.83376	0.185029	-0.00131	0.32941	0.312368
y=4	2.495113	-0.88301	0.122456	0.264907	0.987803
y=3	0.845836	-0.26595	-0.00539	-0.06776	1.018784
y=2	0.31458	1.482165	0.42896	0.087539	0.914951
y=1	-1.19602	-0.07292	0.784898	0.663232	0.632784
SNR [dB]					
y=5	38.96957	30.96174	31.71175	32.19413	31.31178
y=4	48.25706	34.11359	24.48785	31.59704	31.98784
y=3	51.05925	32.12601	33.66613	31.81883	31.53695
y=2	50.71906	42.10802	34.36472	32.12985	31.67722
y=1	43.51629	36.21026	29.33406	32.08773	32.0261

Table 3.A.14: Tree fence - clear water runs - 28 L/s

28 L/s	x=1	x=2	x=3	x=4	x=5
V [cm/s]					
y=5	2.660488	1.363763	3.736855	1.395864	0.474886
y=4	8.136013	1.164415	1.580435	1.456206	0.798852
y=3	13.69461	1.736932	0.812774	1.71433	1.208602
y=2	2.410374	3.162678	2.937693	2.624244	0.951366
y=1	6.541904	2.751467	3.083114	1.95681	1.301558
Vx [cm/s]					
y=5	-1.80827	-1.00276	-1.11216	0.616724	0.30521
y=4	-7.23879	-0.71621	-1.47696	0.530718	0.647442
y=3	13.57218	-1.5484	-0.7085	0.38293	1.062476
y=2	-0.15375	0.2494	-0.02449	1.834821	0.862949
y=1	-6.2394	1.374297	1.991096	0.728242	1.269
SNR [dB]					
y=5	34.94406	34.66901	39.36437	34.2704	32.03785
y=4	56.60413	34.17555	36.83909	36.87303	34.77955
y=3	60.02623	38.74939	34.9568	38.2617	35.75713
y=2	55.27418	50.56454	46.5067	42.01154	36.46289
y=1	53.23735	51.98292	47.47868	46.29284	42.31542

Table 3.A.15: Tree fence - clear water runs - 42 L/s

42 L/s	x=1	x=2	x=3	x=4	x=5
V [cm/s]					
y=5	3.747805	2.238675	5.546347	2.360051	1.451152
y=4	8.759734	2.748103	4.395778	3.524025	2.584044
y=3	7.28507	2.386392	2.8115	2.533463	1.988126
y=2	4.797731	1.960442	4.746832	2.733579	1.59071
y=1	7.520901	2.51761	2.854017	3.01515	2.145248
Vx					
y=5	-3.02755	-2.09876	-1.61106	0.056944	0.531988
y=4	-7.88423	-2.25623	-0.71624	1.86255	2.066105
y=3	6.959862	-1.75653	-1.73641	2.065894	0.65439
y=2	0.346219	-0.67009	-1.00282	0.395264	0.232461
y=1	-7.10086	0.796993	0.526162	-0.59755	1.951148
SNR [dB]					
y=5	33.31048	39.92469	40.67032	41.18375	30.88277
y=4	42.68004	28.47361	45.78058	40.39155	41.55263
y=3	54.21189	36.52565	44.56831	38.67322	40.99296
y=2	54.22489	42.16888	44.96107	43.69016	38.10571
y=1	54.24135	47.99223	47.8063	50.25466	47.03548

Table 3.A.16: Tree fence - sediment laden runs - 14 L/s

14 L/s	x=1	x=2	x=3	x=4	x=5
V [cm/s]					
y=5	4.897675	3.778041	3.189289	0.830925	0.480051
y=4	3.881146	4.016388	4.514781	0.736632	0.263443
y=3	4.189835	1.80974	2.643864	0.392444	0.536067
y=2	4.980259	1.063753	0.828017	0.48172	0.637554
y=1	8.722788	1.595732	1.281937	0.653593	0.672324
Vx [cm/s]					
y=5	-4.63175	1.707598	0.021724	0.40314	0.313511
y=4	-1.587	-0.55792	-1.63192	-0.45231	0.238926
y=3	2.518296	-1.69828	-1.45172	-0.08931	0.439742
y=2	-0.36572	-0.91751	-0.62811	-0.07854	0.61792
y=1	-5.69375	-0.82636	0.302168	0.485308	0.583282
SNR [dB]					
y=5	82.59035	80.08494	79.47048	73.32863	72.95907
y=4	83.57558	78.83978	80.12533	75.447	71.78203
y=3	84.72995	77.27005	77.31486	73.56814	71.64549
y=2	81.00786	75.97288	74.50068	70.9453	69.57556
y=1	78.16157	72.0761	73.61399	68.19914	65.99018

Table 3.A.17: Tree fence - sediment laden runs - 28 L/s

28 L/s	x=1	x=2	x=3	x=4	x=5
V [cm/s]					
y=5	14.62118	4.595162	4.700048	0.930452	0.691331
y=4	10.74736	2.871474	4.411436	1.679633	0.956817
y=3	11.4313	3.073347	3.127829	1.836841	1.004991
y=2	15.3835	2.296547	1.552094	1.094513	1.201589
y=1	6.135391	1.754722	2.395935	0.986568	1.111481
Vx [cm/s]					
y=5	-13.6163	4.407335	4.024495	0.223174	0.485073
y=4	-5.47294	-1.28848	-0.18844	-0.03283	0.921241
y=3	0.799694	-2.72373	-1.16527	0.199522	0.783272
y=2	3.859484	-1.72003	-0.83914	0.283511	1.124775
y=1	-4.14478	-1.24891	0.637583	0.77397	0.763829
SNR [dB]					
y=5	86.05062	82.37523	84.18898	76.28894	71.72363
y=4	85.08862	81.52541	81.81278	72.75692	65.52534
y=3	81.64569	76.57492	76.87488	74.23806	73.40437
y=2	79.49134	76.94472	75.0186	73.56009	73.69423
y=1	76.91835	77.43751	73.64219	72.73674	72.64739

Table 3.A.18: Tree fence - sediment laden runs - 42 L/s

42 L/s	x=1	x=2	x=3	x=4	x=5
V [cm/s]					
y=5	22.0009	6.983399	4.041926	0.888707	1.226642
y=4	8.627071	4.359257	4.960231	0.920255	1.210531
y=3	11.76731	1.933134	3.056603	0.636884	1.213346
y=2	9.306911	2.393364	1.063763	2.227461	1.30543
y=1	2.915432	2.381679	3.174922	1.300122	1.621687
Vx [cm/s]					
y=5	-16.2816	3.214692	0.60025	-0.16511	1.103462
y=4	-3.31818	-0.20818	-2.02736	-0.07147	1.115728
y=3	-1.55508	-0.57639	-1.89187	0.210733	1.205655
y=2	0.876107	-1.77788	-0.10163	1.762007	1.279903
y=1	-2.8017	-1.41388	-0.71678	0.83794	1.434112
SNR [dB]					
y=5	86.00616	85.18379	80.58787	75.76466	74.82152
y=4	84.23626	85.52042	82.70159	75.65017	74.98786
y=3	83.03859	83.11104	80.44942	76.10204	74.72602
y=2	80.72834	79.53576	80.02274	74.80813	71.90521
y=1	80.28751	76.07525	71.93339	74.79044	74.5834

Table 3.A.19: Jute fence - clear water runs - 14 L/s

14 L/s	x=1	x=2	x=3	x=4	x=5
V [cm/s]					
y=5	3.703065	0.337982	0.319428	0.364906	0.860175
y=4	3.449774	0.369616	2.084551	0.219636	0.758929
y=3	5.111117	0.769481	0.315469	0.277142	0.433191
y=2	3.585606	0.832693	0.537212	0.74349	0.144958
y=1	2.683263	0.424186	0.264764	0.431845	0.448101
Vx [cm/s]					
y=5	-3.33279	0.261494	0.136319	0.150059	-0.34806
y=4	1.872184	0.266436	-0.82146	0.045088	0.550761
y=3	4.422821	0.45729	0.257681	0.055786	0.286807
y=2	0.124687	0.712925	0.515644	0.5404	-0.04483
y=1	-1.53128	0.216148	4.420904	0.222202	-0.24001
SNR [dB]					
y=5	46.25473	31.31605	36.8787	33.51263	33.50587
y=4	48.67258	30.0474	32.01268	31.15113	29.93811
y=3	54.21736	36.23222	31.91696	32.31434	30.12292
y=2	50.66799	41.68518	40.78394	34.1521	30.58257
y=1	45.3534	30.43158	54.69306	31.86967	29.82572

Table 3.A.20: Jute fence - clear water runs - 28 L/s

28 L/s	x=1	x=2	x=3	x=4	x=5
V [cm/s]					
y=5	5.70982	0.696625	1.690939	0.666074	1.015097
y=4	7.187811	0.60865	2.026318	0.385463	1.017541
y=3	14.27935	2.349136	0.803156	0.535492	0.334462
y=2	5.231869	0.751165	0.659743	0.864693	0.44719
y=1	7.49467	3.944246	2.63279	1.132157	1.251362
Vx [cm/s]					
y=5	-4.63073	0.498145	0.315464	0.376519	0.926895
y=4	-3.76278	-0.19709	0.85957	0.338448	0.783067
y=3	14.09386	2.145156	0.488491	0.43543	0.125381
y=2	-2.02391	0.115147	0.470635	0.724048	0.234219
y=1	-6.36414	3.025702	-0.09165	0.922388	0.868462
SNR [dB]					
y=5	52.94246	30.75673	34.82731	37.14841	30.13752
y=4	60.09521	34.39001	39.30669	36.49725	31.69237
y=3	62.91513	58.34411	36.73765	32.07656	33.39066
y=2	58.45997	42.32902	41.71075	34.08558	30.11414
y=1	57.10605	45.52268	43.8685	34.02596	31.43096

Table 3.A.21: Jute fence - clear water runs - 42 L/s

42 L/s	x=1	x=2	x=3	x=4	x=5
V [cm/s]					
y=5	5.349218	1.503152	0.411352	1.453145	0.815121
y=4	5.402154	1.128303	2.943742	1.446494	0.678495
y=3	6.704389	1.479499	2.623941	1.790779	0.967077
y=2	4.059743	3.001996	2.645781	2.171558	1.764108
y=1	6.039595	3.402591	0.433132	1.951606	1.495813
Vx [cm/s]					
y=5	-5.271	-1.37014	-0.04658	-0.48939	0.638047
y=4	1.21678	-0.07875	0.277202	0.090655	-0.13705
y=3	5.060524	1.309819	0.659258	-0.15122	0.691851
y=2	3.225044	0.415	0.183262	1.703897	-1.08531
y=1	-5.12823	1.161318	0.161231	-0.16906	0.442461
SNR [dB]					
y=5	45.61782	35.93253	39.63321	34.54953	32.77423
y=4	57.60488	35.29535	47.53814	36.64246	33.47947
y=3	62.24272	55.19474	37.35929	43.34619	34.34926
y=2	62.56514	44.68012	38.78305	43.75639	36.10255
y=1	60.28511	48.52797	59.13972	49.6084	40.70895

Table 3.A.22: Jute fence - sediment laden runs - 14 L/s

14 L/s	x=1	x=2	x=3	x=4	x=5
V [cm/s]					
y=5	4.38009	0.505998	0.794757	0.871646	0.745426
y=4	4.935905	0.597868	0.894356	0.495678	0.826843
y=3	5.702335	0.501851	0.735675	0.413641	0.685448
y=2	6.588713	0.850363	1.145689	0.713244	0.860642
y=1	7.198263	1.560257	0.333217	0.821543	0.420854
Vx [cm/s]					
y=5	-3.12685	0.153697	0.516285	0.697613	0.717896
y=4	2.815022	0.255748	-0.04958	0.418818	0.800996
y=3	-5.29671	0.261177	0.478213	-0.18319	0.429404
y=2	4.610601	0.263609	0.420645	0.620122	0.731772
y=1	0.067388	1.048087	0.259224	0.754165	0.341753
SNR [dB]					
y=5	75.79462	71.33126	70.10965	67.57174	65.97965
y=4	80.18127	74.11961	74.14494	69.46362	67.16068
y=3	83.19834	74.82131	74.29236	70.23966	67.95225
y=2	81.9228	72.26504	42.98081	71.54154	69.08357
y=1	75.29205	73.82262	57.97944	67.61723	71.16724

Table 3.A.23: Jute fence - sediment laden runs - 28 L/s

28 L/s	x=1	x=2	x=3	x=4	x=5
V [cm/s]					
y=5	9.398196	0.42269	1.30831	1.326786	1.044843
y=4	10.46299	1.644737	1.293375	0.848409	1.397519
y=3	23.82571	1.437678	1.441749	1.416203	1.430964
y=2	3.28993	0.442727	2.080752	0.828991	1.693726
y=1	5.967513	1.075862	0.597018	1.220764	0.5923
Vx [cm/s]					
y=5	-7.21778	-0.23703	0.898868	1.325094	1.034897
y=4	-5.78807	1.110308	0.672925	0.796308	1.387243
y=3	22.55721	1.179834	0.652032	1.247701	1.418975
y=2	-2.13504	-0.0038	1.763213	0.761743	1.66626
y=1	-4.90459	0.588824	0.509673	1.136553	0.533409
SNR [dB]					
y=5	78.44699	70.8782	69.11379	67.24737	67.22475
y=4	80.33009	74.43966	69.39596	60.48052	66.37753
y=3	81.1729	76.38773	73.62587	69.59231	67.99583
y=2	80.71119	73.73464	57.53189	71.42148	69.08691
y=1	77.55928	75.39926	58.71823	69.4213	68.06852

Table 3.A.24: Jute fence - sediment laden runs - 42 L/s

42 L/s	x=1	x=2	x=3	x=4	x=5
V [cm/s]					
y=5	11.68255	0.389017	1.765326	1.263421	1.702408
y=4	14.67067	0.539673	1.250213	0.917886	1.767159
y=3	30.89523	0.878668	1.886685	1.281393	1.564875
y=2	6.377489	0.457721	0.647925	1.304443	2.22727
y=1	12.72468	1.990711	0.810776	1.713257	1.300421
Vx [cm/s]					
y=5	-9.91603	-0.00671	1.195263	1.248203	1.697099
y=4	-8.1973	0.525957	0.898847	0.898671	1.766163
y=3	28.57467	0.789171	0.875147	1.229288	1.559629
y=2	3.477483	0.134033	0.20875	1.200058	2.22374
y=1	-1.19391	1.868194	0.501865	1.633387	1.260772
SNR [dB]					
y=5	81.06556	73.81495	71.73571	67.35275	66.00294
y=4	82.14725	72.40985	71.17958	65.98471	64.36943
y=3	81.38479	72.95272	70.4397	68.1717	65.45089
y=2	79.59903	74.57381	23.17393	67.64532	66.62123
y=1	76.46644	76.10852	41.71759	69.52592	66.22871

Appendix 3.B - Vertical velocity maps

Below are the depth-averaged vertical velocities for each experiment performed within the sediment retention pond. The pond dimensions were 8 m long, 5.2 m wide, and 0.92 m deep. Vertical (z-component) velocities were taken at 25 grid points and at two depths below the still ponded surface: 0.13 m and 0.26 m. Baffles were installed at 1.22 m distance from each other. The vertical velocity maps were obtained via GRASS GIS module *r.surf.rst* which interpolated between the velocity grid sample points with a tension strength of 50 and a smoothness value of 0.1.

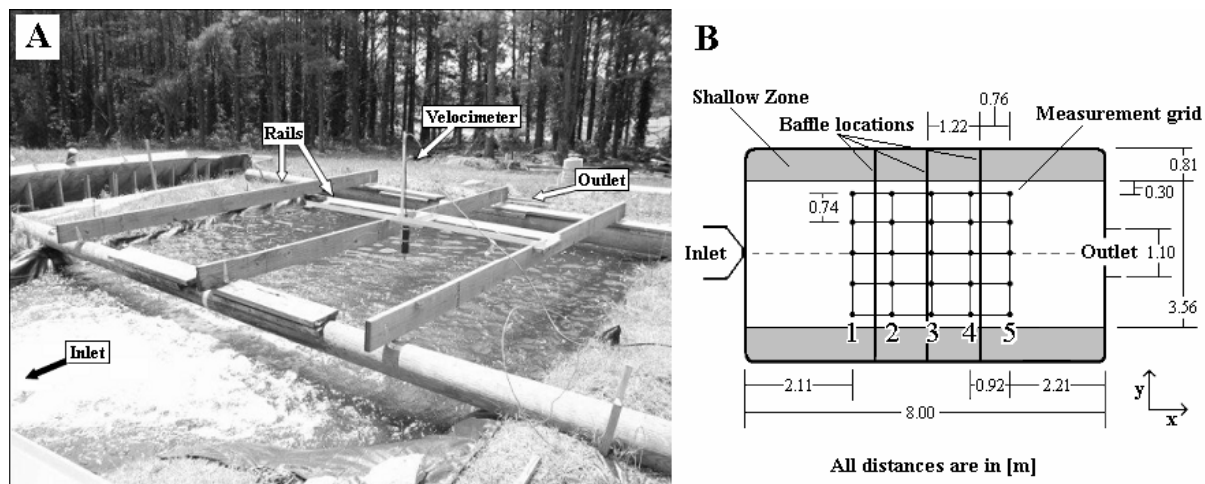
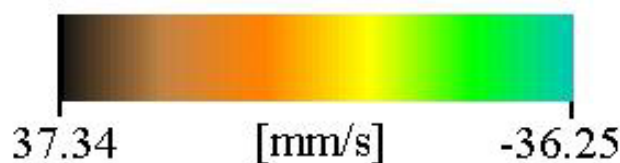


Figure 3.B.0: Sediment retention pond layout and dimensions.

The key for the vertical velocity maps is given below:



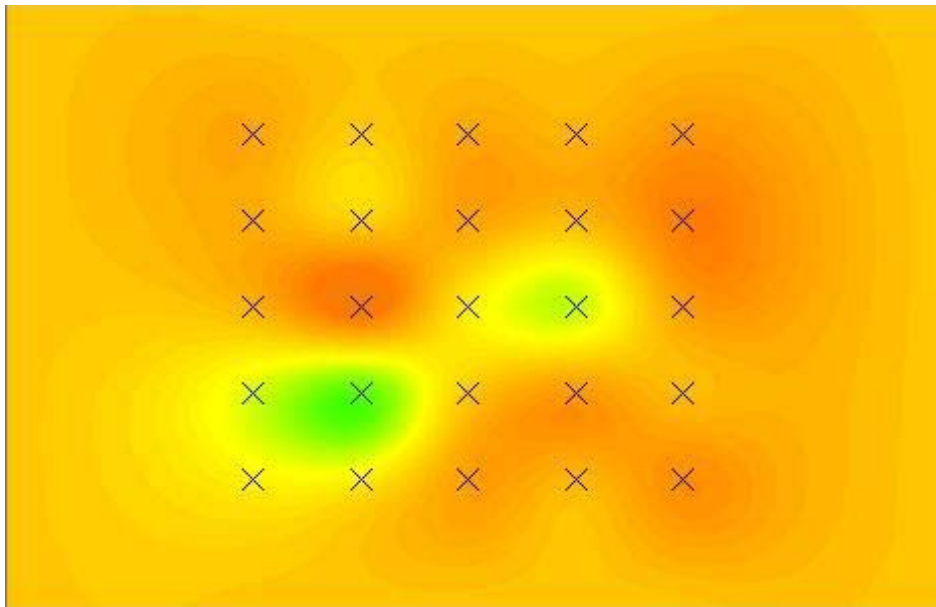


Figure 3.B.1: Free flow at 14 L/s for the clear water run. Flow is left to right.

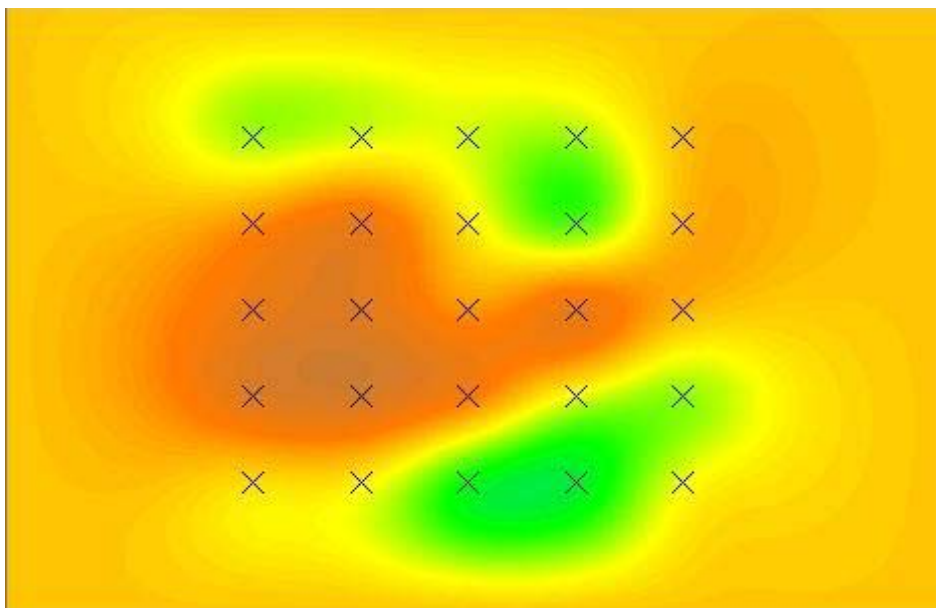


Figure 3.B.2: Free flow at 14 L/s for the sediment laden run. Flow is left to right.

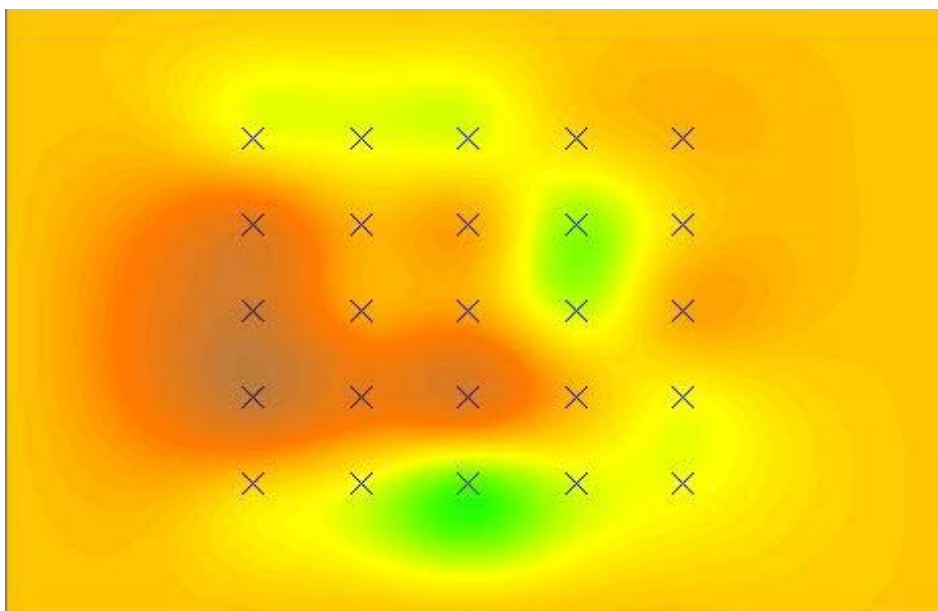


Figure 3.B.3: Free flow at 28 L/s for the clear water run. Flow is left to right.

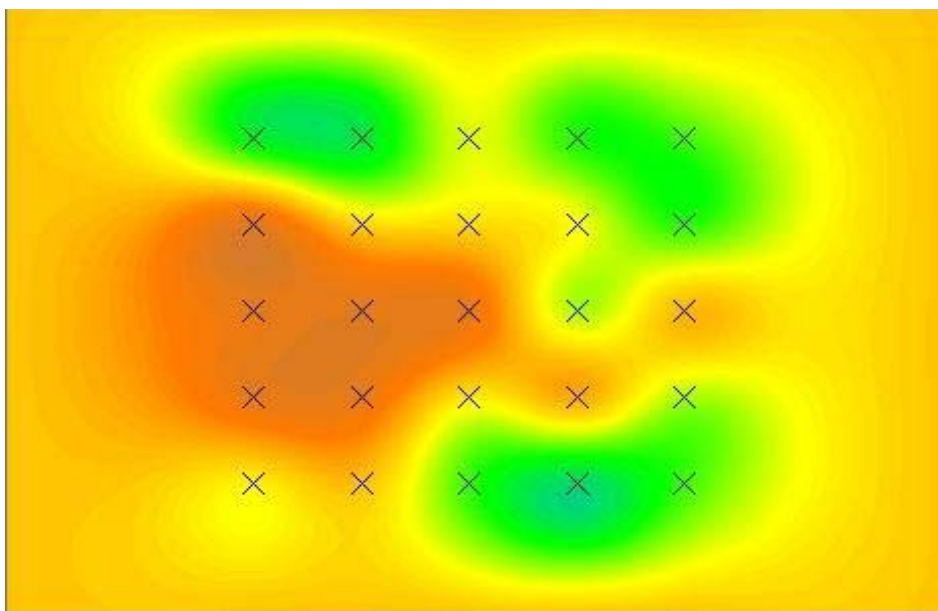


Figure 3.B.4: Free flow at 28 L/s for the sediment laden run. Flow is left to right.

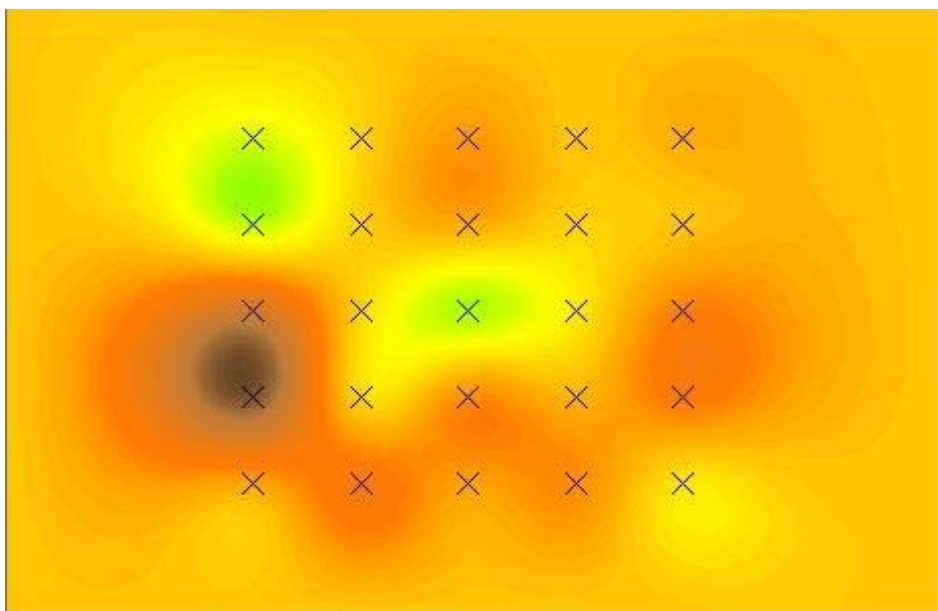


Figure 3.B.5: Free flow at 42 L/s for the clear water run. Flow is left to right.

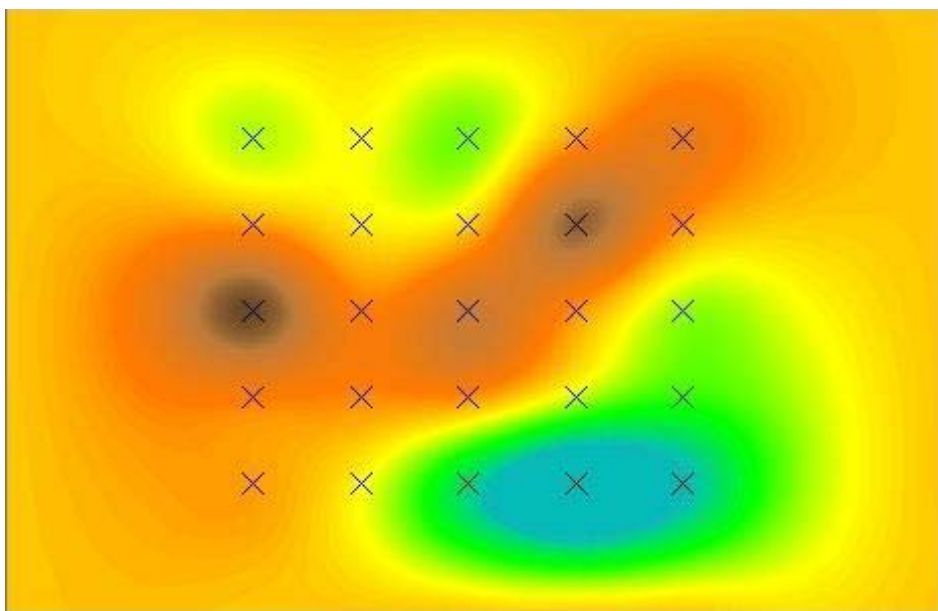


Figure 3.B.6: Free flow at 42 L/s for the sediment laden run. Flow is left to right.

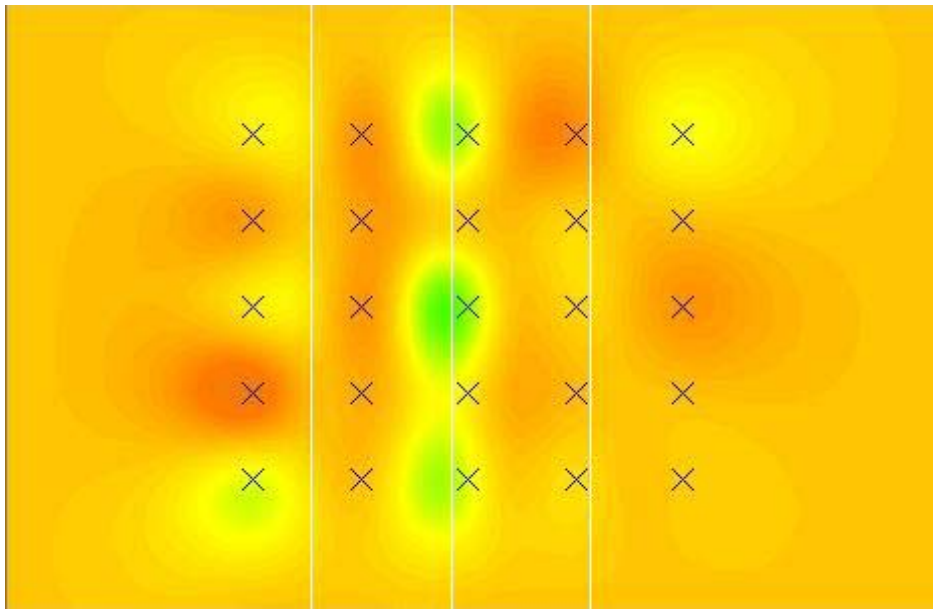


Figure 3.B.7: Silt fence at 14 L/s for the clear water run. Approximate baffle locations indicated by white lines. Flow is left to right.

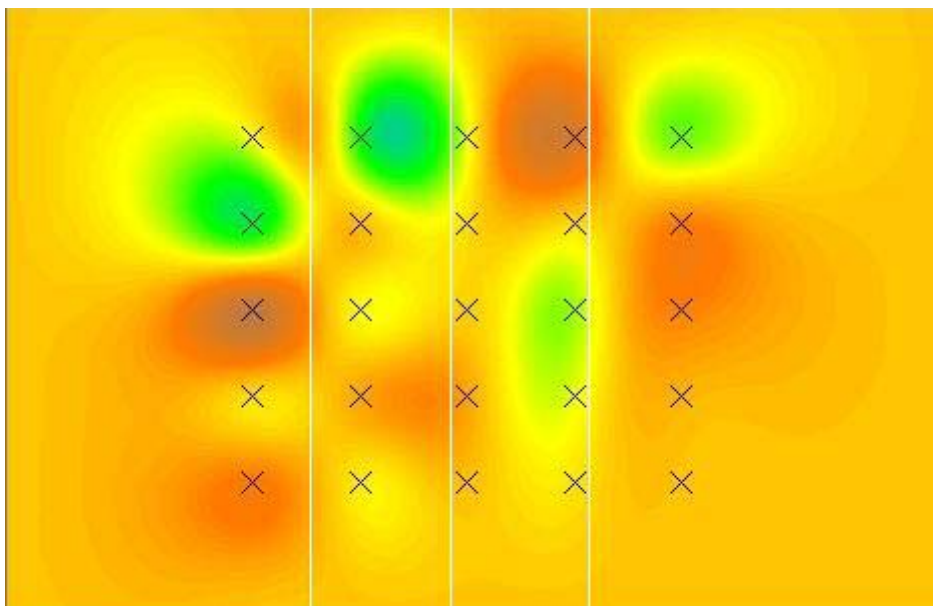


Figure 3.B.8: Silt fence at 14 L/s for the sediment laden run. Approximate baffle locations indicated by white lines. Flow is left to right.

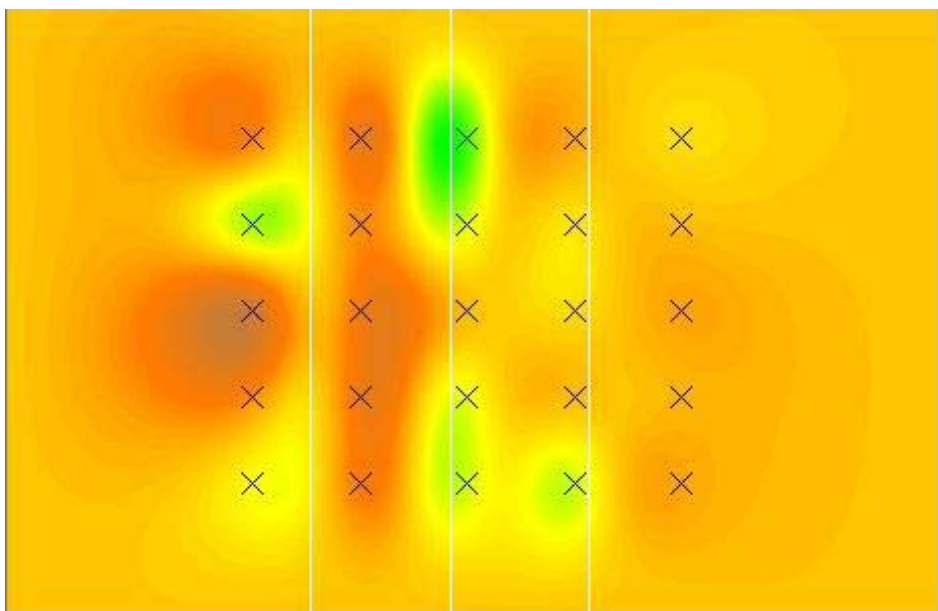


Figure 3.B.9: Silt fence at 28 L/s for the clear water run. Approximate baffle locations indicated by white lines. Flow is left to right.

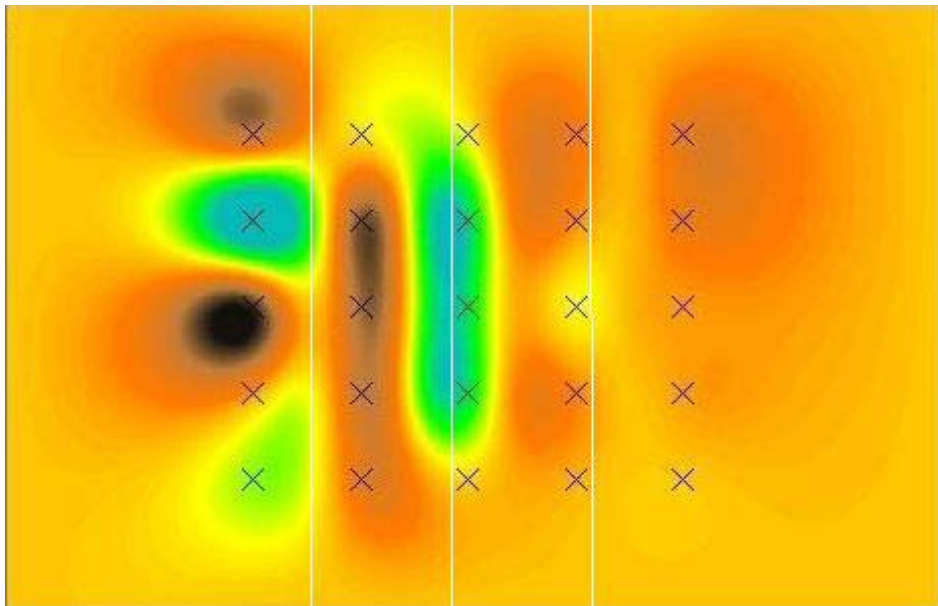


Figure 3.B.10: Silt fence at 28 L/s for the sediment laden run. Approximate baffle locations indicated by white lines. Flow is left to right.

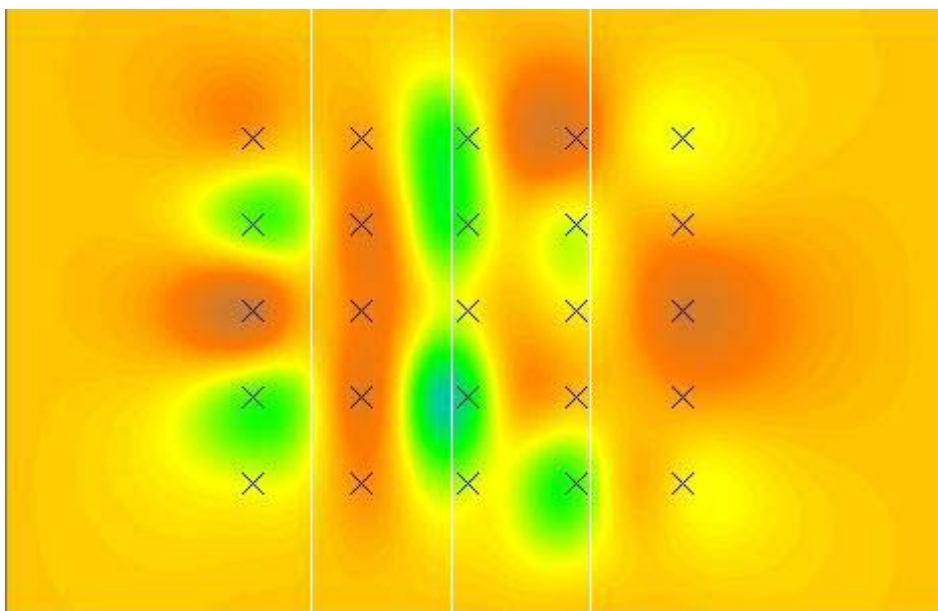


Figure 3.B.11: Silt fence at 42 L/s for the clear water run. Approximate baffle locations indicated by white lines. Flow is left to right.

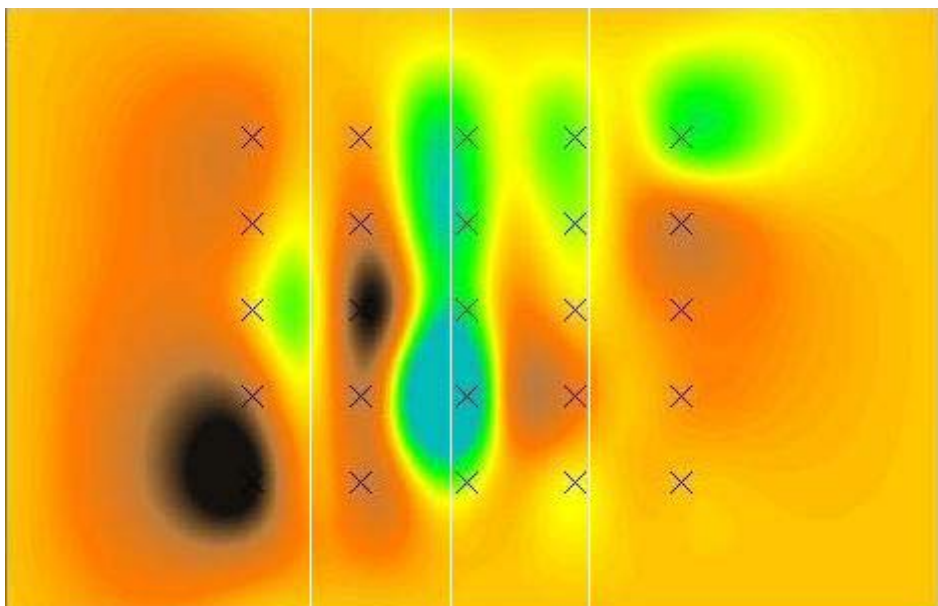


Figure 3.B.12: Silt fence at 42 L/s for the sediment laden run. Approximate baffle locations indicated by white lines. Flow is left to right.

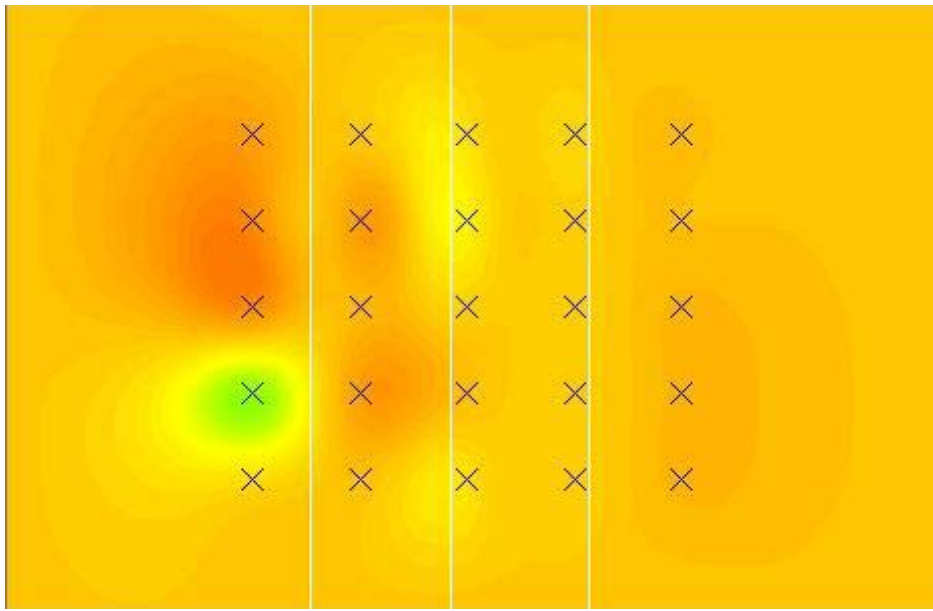


Figure 3.B.13: Tree protection fence at 14 L/s for the clear water run. Approximate baffle locations indicated by white lines. Flow is left to right.

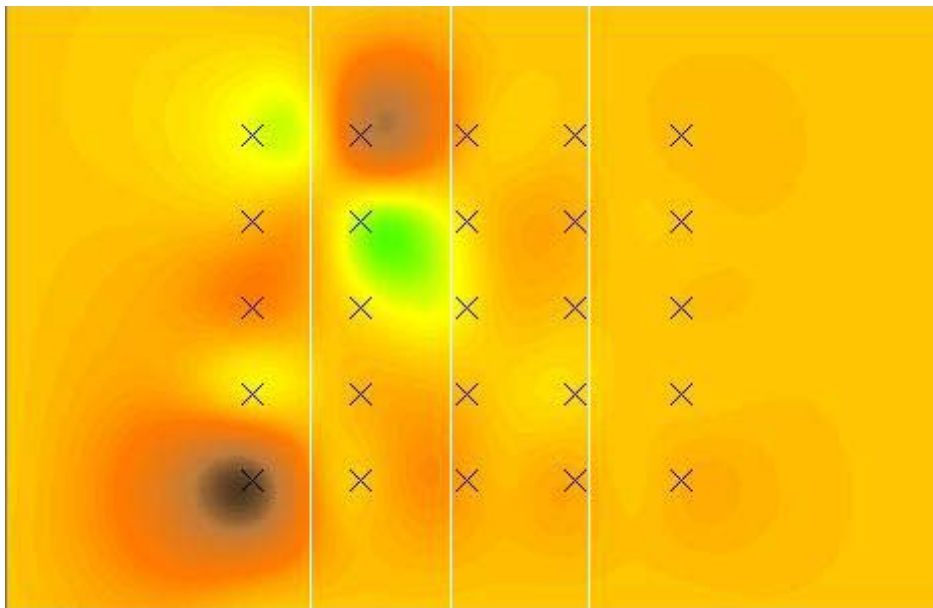


Figure 3.B.14: Tree protection fence at 14 L/s for the sediment laden run. Approximate baffle locations indicated by white lines. Flow is left to right.

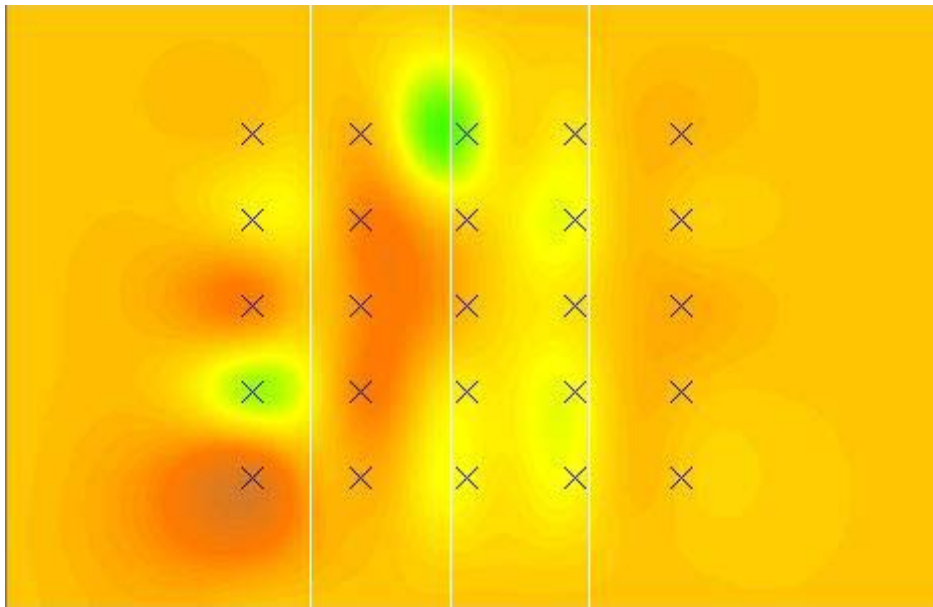


Figure 3.B.15: Tree protection fence at 28 L/s for the clear water run. Approximate baffle locations indicated by white lines. Flow is left to right.

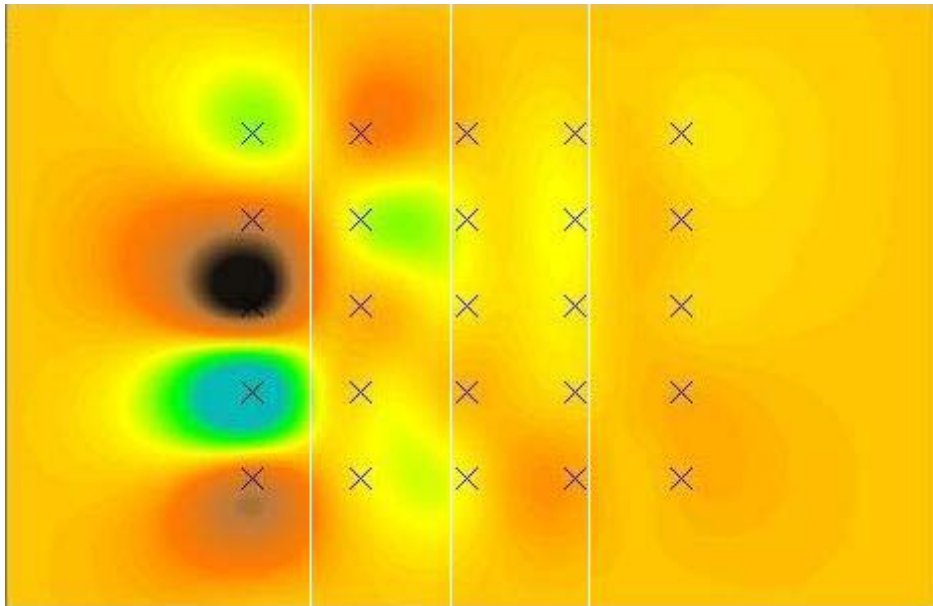


Figure 3.B.16: Tree protection fence at 28 L/s for the sediment laden run. Approximate baffle locations indicated by white lines. Flow is left to right.

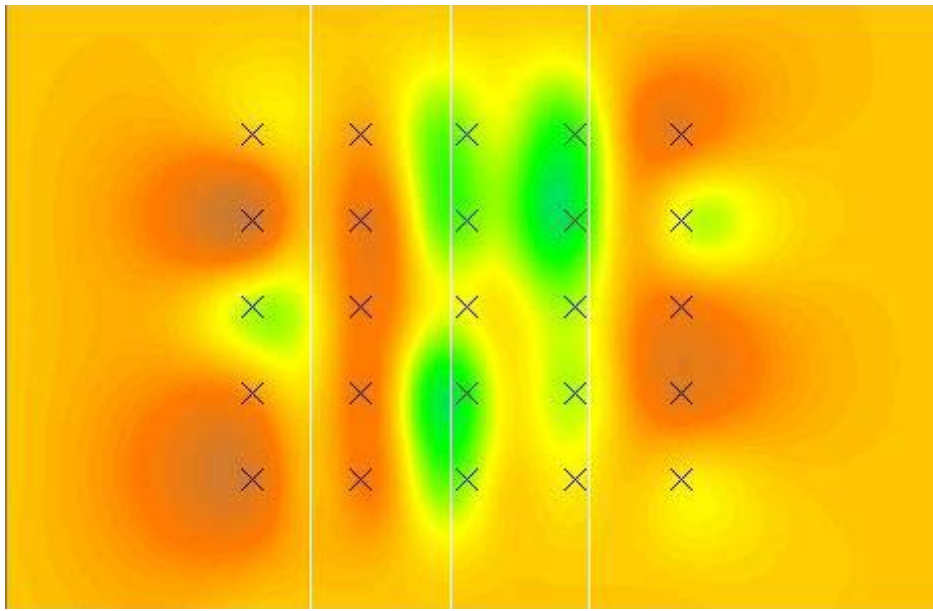


Figure 3.B.17: Tree protection fence at 42 L/s for the clear water run. Approximate baffle locations indicated by white lines. Flow is left to right.

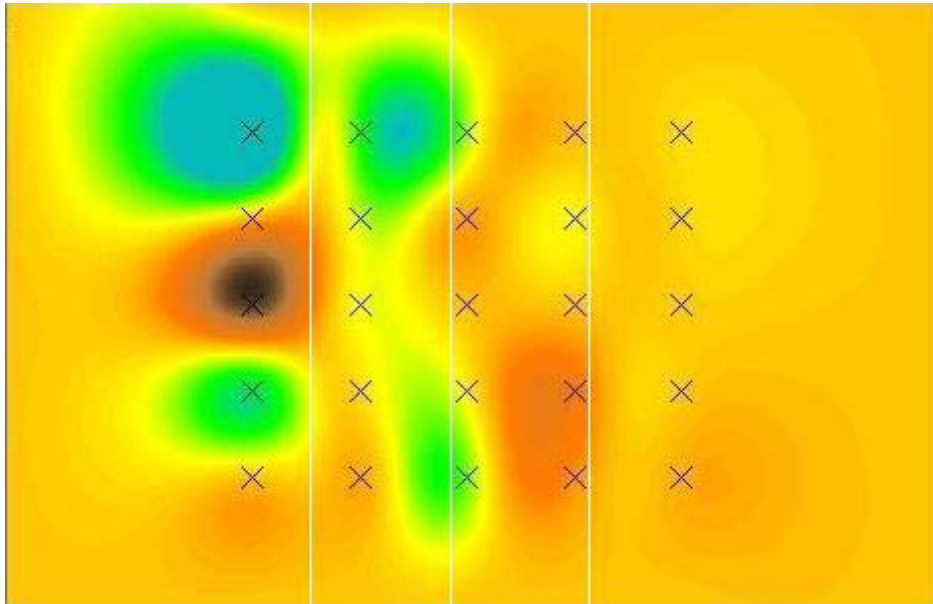


Figure 3.B.18: Tree protection fence at 42 L/s for the sediment laden run. Approximate baffle locations indicated by white lines. Flow is left to right.

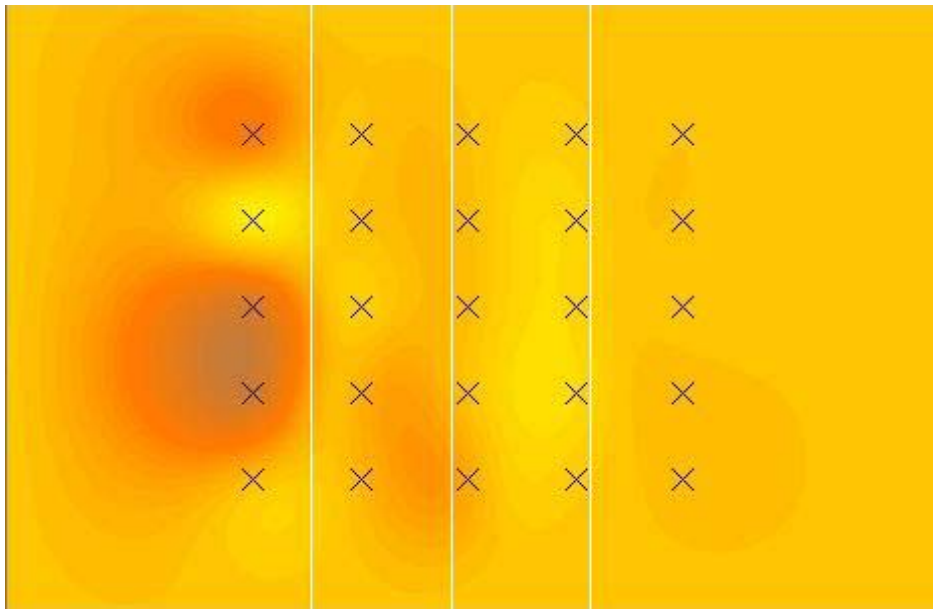


Figure 3.B.19: Jute/coir at 14 L/s for the clear water run. Approximate baffle locations indicated by white lines. Flow is left to right.

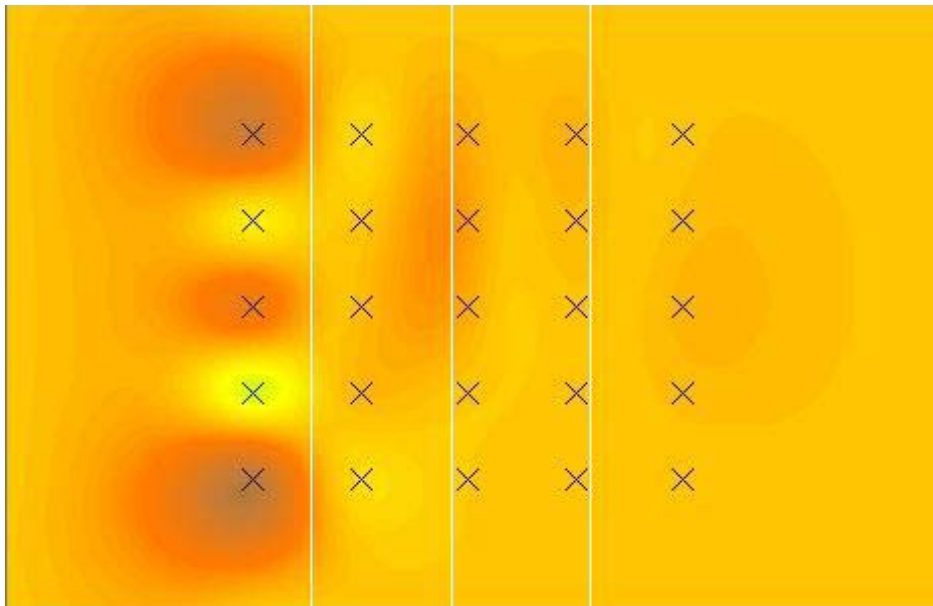


Figure 3.B.20: Jute/coir at 14 L/s for the sediment laden run. Approximate baffle locations indicated by white lines. Flow is left to right.

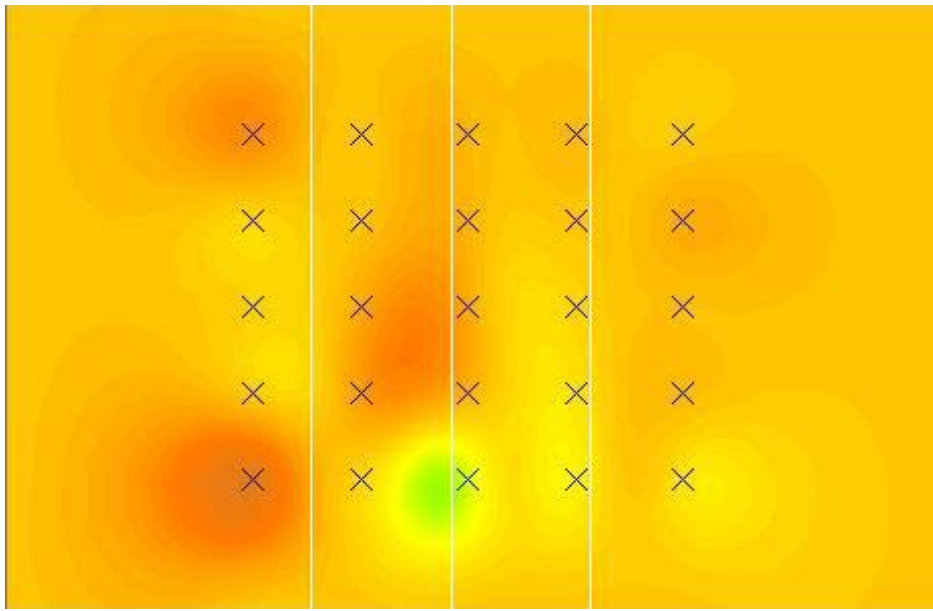


Figure 3.B.21: Jute/coir at 28 L/s for the clear water run. Approximate baffle locations indicated by white lines. Flow is left to right.

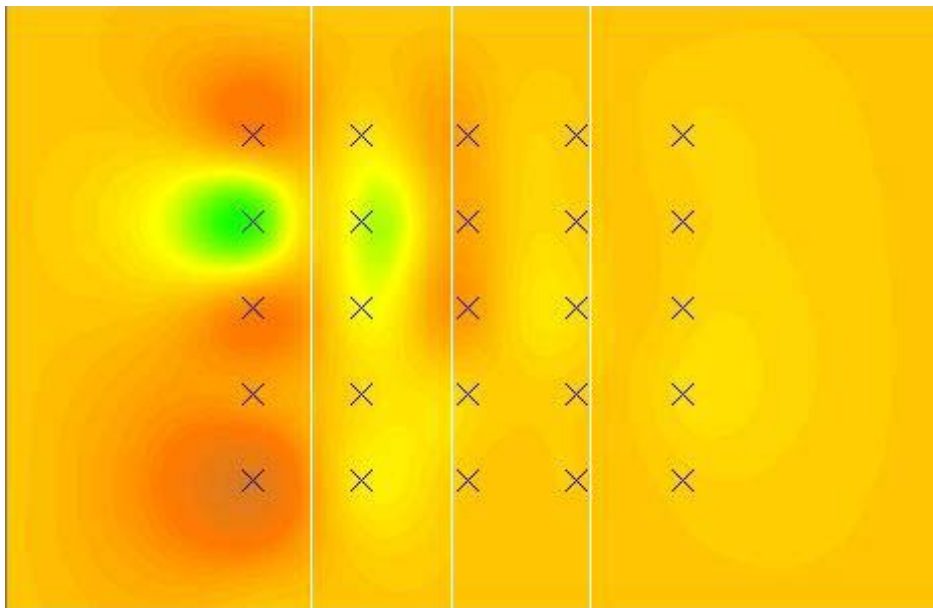


Figure 3.B.22: Jute/coir at 28 L/s for the sediment laden run. Approximate baffle locations indicated by white lines. Flow is left to right.

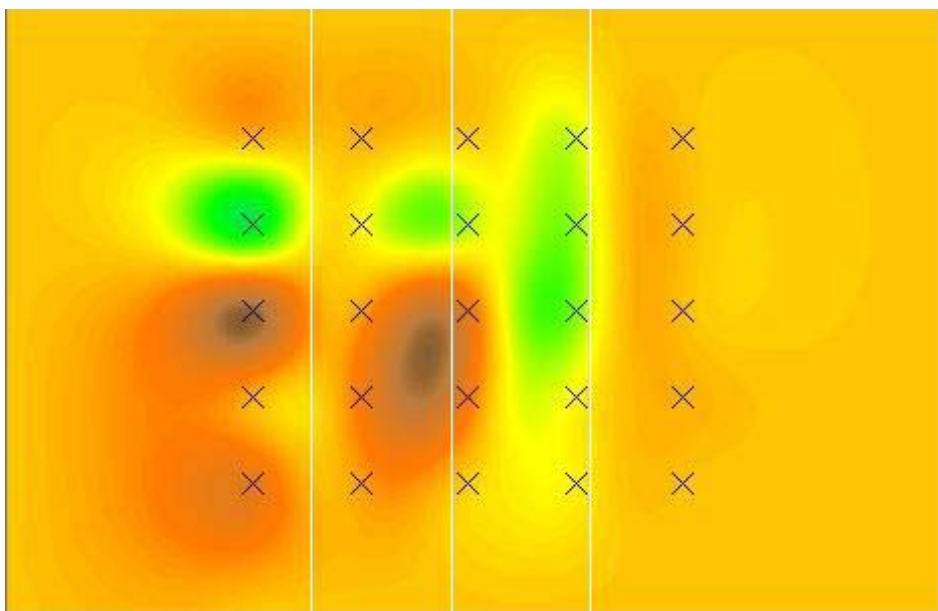


Figure 3.B.23: Jute/coir at 42 L/s for the clear water run. Approximate baffle locations indicated by white lines. Flow is left to right.

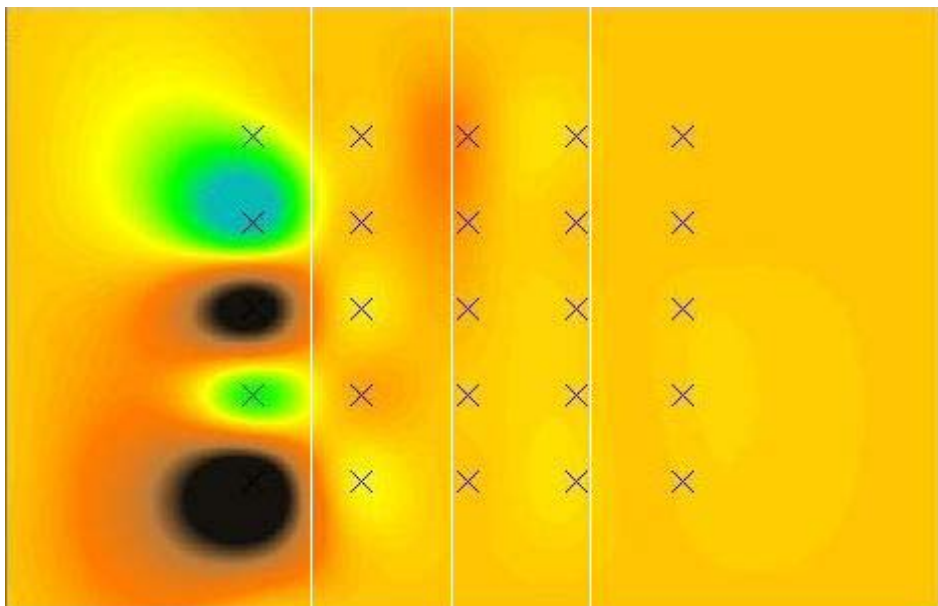


Figure 3.B.24: Jute/coir at 42 L/s for the sediment laden run. Approximate baffle locations indicated by white lines. Flow is left to right.

Appendix 3.C - Vertical velocity statistics

In the below table are the statistics for the vertical velocity maps in appendix 3.B. (The vertical velocity maps were obtained via GRASS GIS module *r.surf.rst* which interpolated the depth averaged values at 25 grid points with a tension strength of 50 and a smoothness value of 0.1). The statistics were derived using GRASS GIS module *r.univar*.

KEY: Run ID is XYZZ, where: X=C for clear water runs, X=S for sediment laden runs, X=A for average between clear water runs and sediment laden runs; Y=F for free flow, Y=S for silt fence, Y=T for tree fence, Y=J for jute/coir; ZZ is the flow rate in L/s.

Table 3.C.1: V_z statistics for each run.

Free flow V _z [cm/s]					Silt fence V _z [cm/s]				
Run ID	MEAN	VAR	MIN	MAX	Run ID	MEAN	VAR	MIN	MAX
CF14	0.069	0.125	-1.762	1.093	CS14	-0.056	0.097	-1.714	1.152
CF28	0.014	0.426	-1.928	2.314	CS28	-0.066	0.241	-2.199	2.184
CF42	0.163	0.304	-1.322	3.034	CS42	-0.098	0.433	-3.452	2.041
SF14	-0.120	0.602	-2.661	1.975	SS14	-0.944	0.394	-3.237	2.282
SF28	-0.408	0.821	-3.141	1.825	SS28	0.165	1.028	-5.184	4.174
SF42	-0.205	1.503	-5.004	2.981	SS42	0.176	1.679	-8.107	4.584
AF14	-0.025	0.130	-1.238	1.319	AS14	-0.075	0.134	-1.844	1.358
AF28	-0.197	0.533	-2.108	1.889	AS28	0.115	0.457	-3.220	3.179
AF42	-0.021	0.474	-2.248	2.634	AS42	0.039	0.714	-5.770	2.449
Tree fence V _z [cm/s]					Jute fence V _z [cm/s]				
Run ID	MEAN	VAR	MIN	MAX	Run ID	MEAN	VAR	MIN	MAX
CT14	0.014	0.055	-1.364	0.937	CJ14	0.147	0.115	-0.460	2.211
CT28	-0.003	0.134	-1.747	1.762	CJ28	0.049	0.075	-1.243	1.422
CT42	-0.007	0.492	-2.888	2.030	CJ42	0.050	0.394	-2.699	2.764
ST14	0.151	0.248	-1.684	3.190	SJ14	0.178	0.131	-0.912	2.386
ST28	-0.025	0.622	-5.589	4.511	SJ28	0.005	0.128	-2.033	1.604
ST42	-0.343	1.125	-6.973	3.431	SJ42	0.107	0.925	-4.587	5.979
AT14	0.083	0.062	-0.874	1.516	AJ14	0.163	0.076	-0.446	1.503
AT28	-0.014	0.239	-3.377	2.665	AJ28	0.027	0.744	-1.109	1.512
AT42	-0.175	0.385	-3.529	1.647	AJ42	0.078	0.502	-3.625	3.734

Chapter 4

Integration of Grain-Size Dependent Terrain Evolution into Distributed Soil Erosion Simulations

4.1 Introduction

We present a new GRASS GIS (Geographical Information System) module *r.terrodyn* that evolves a given terrain using sediment flux information provided by the SIMWE (SImultaed Water Erosion) GRASS GIS modules *r.sim.water* and *r.sim.sediment* originally developed by Mitas and Mitasova (1998). SIMWE is a distributed, bivariate, steady-state watershed scale sediment erosion, transport, and deposition model that employs a path sampling Monte Carlo method. Module *r.terrodyn* modifies the original digital elevation model (DEM) over time steps, each corresponding to a single rainfall event, which is then used as the input DEM for subsequent SIMWE and *r.terrodyn* iterations. New techniques were derived that include the application of a gravitational diffusion term within GRASS GIS, an approximate Neumann boundary condition routine for use with GRASS GIS module *r.slope.aspect*, a comparative band-pass filter for numerical stability of the iterative feedback system, and a rainfall excess calculation methodology derived from accumulated runoff curve number tables that enables spatially distributed infiltration. Application of *r.terrodyn* to a sample watershed demonstrates results from the newly developed code and compares different grain size specific parameterizations within the model.

4.2 Theoretical Review

4.2.1 Water

Overland water flow is shallow and laminar due to the dominance of viscous forces over inertial forces (Julien & Simons, 1985). Flow is considered turbulent if rainfall impact and surface roughness is sufficiently high or once flow becomes channelized into gulleys, creeks and rivers near the outlets of catchments. These flows are characterized by deeper flow but are usually less steep than overland flow (Govers, 1992). Empirical formulae for open channels such as Manning's equation (turbulent flow over rough surfaces), the Chezy equation (turbulent flow over relatively smooth surfaces), and the Darcy-Weisbach equation (laminar flow, i.e. flows in pipes) are used to describe flow velocities (or "flux-concentration equations" (Ven te Chow et. al., 1988) for overland flow.

The Saint-Venant equations can be used to govern water flow in erosion models (e.g. Mitas & Mitasova, 1998). Application of these equations assumes one dimensional, gradually varied flow through an approximately straight channel with a small slope and a fixed bed. In addition, Manning's equation is assumed to apply. The Saint-Venant equations are comprised of continuity and momentum conservation:

$$\frac{\partial h}{\partial x} + \frac{\partial (vh)}{\partial x} = i = R - f \quad (4.1)$$

$$g(S_f - S_0) + g \frac{\partial h}{\partial x} + v \frac{\partial v}{\partial x} + \frac{\partial v}{\partial t} = 0 \quad (4.2)$$

(1) (2) (3) (4) (5)

in the range of $t > 0$ and $0 < x < L$, where L is the length of slope. Here, $h(x,t)$ [m] is the mean overland flow depth, $v(x,t)$ [m/s] is the depth-averaged flow velocity, S_o is the slope of the hillslope, S_f is the friction slope (or slope of the total energy line), $R(x,t)$ [m/s] is the rainfall rate, $f(x,t)$ [m/s] is the infiltration rate, $i(x,t)$ [m/s] is the excess runoff rate, and g [m/s²] is the acceleration of gravity. Note that equation (4.2) neglects lateral inflow, wind shear effects, eddy losses, and assumes flow that is uniform across the channel width (Boussinesq coefficient is unity). Equation (4.2) shows that the difference between the gravity force (term (1)) and the friction force (term (2)) results from the pressure forces stemming from changes in downstream water depth (term (3)), convective acceleration (term (4)), and local acceleration (term (5)). The convective and local acceleration terms represent the effect of inertial forces on the flow.

The complete dynamic wave equation (4.2) for unsteady, non-uniform flow can be simplified to reduce computational costs in flow routing. The simplest form of equation (4.2) is achieved by neglecting the force terms (3), (4), and (5) in equation (4.2) which leads to the *kinematic wave* approximation (steady-uniform flow) in which $S_f = S_o$, which, according to Singh (2002) is more realistic for steeper slopes. Backwater effects from downstream pools or tributary junctions are ignored and the flow does not dissipate as it moves downstream. To overcome these problems, term (3) in equation (4.2) can be included which leads to the *diffusion wave* approximation (steady, quasi-uniform flow). Dingman (1984) combines equations (4.1) and (4.2) to arrive at an alternative governing equation for the diffusion wave, the *convective-diffusive equation*, which is:

$$\frac{\partial h}{\partial t} + v_k \frac{\partial h}{\partial x} - D \frac{\partial^2 h}{\partial x^2} = \frac{q}{w} \quad (4.3)$$

where w [m] is the width of the water surface and q [m^2/s] is the total discharge per unit width. The kinematic wave velocity, v_k [m/s] is defined as:

$$v_k \equiv \frac{5}{3} \left(\frac{u_M S_0^{1/2} h^{2/3}}{n} \right) \quad (4.4)$$

where n is the Manning's roughness and u_M is a unit conversion factor. The diffusion coefficient [m^2/s] is:

$$D = \frac{u_M h^{5/3}}{2nS_0^{1/2}} \quad (4.5)$$

This unique formulation explicitly demonstrates that diffusion increases with increased mean water depth and decreases for steeper slopes.

It should be noted that the application of the Saint-Venant equations in two dimensions introduces dispersive flow effects which are lost in one-dimensional implementations. For example, models based on 2-D Saint-Venant equations (Mitas and Mitasova, 1998) show that flow over a convex surface may lead to a reduction in water depth (and possibly sediment deposition), whereas models based on the 1-D form would predict an increase in flow depth.

The friction slope can be related to the velocity via Manning's equation:

$$v = \frac{C}{n} h^{2/3} S_f^{1/2} \quad (4.6)$$

where n is known as *Manning's n* and C (=1) is a unit conversion factor.

Flowing water applies a shear stress (a function of bed roughness) to the bed which is partially responsible for sediment entrainment. (Shear stress is commonly treated as a time-averaged value - the relative contribution of instantaneous turbulence

and vertical velocity gradients to entrainment is dependent on the type of flow and bed roughness.) A common form for stress in erosion modeling is:

$$\tau_f = \gamma RS \quad [\text{kg/m/s}^2] \text{ (e.g. Haan, et. al., 1994)} \quad (4.7)$$

Here, γ is the specific gravity of water [kg/m^3], R is the wetted perimeter [m] (commonly, $R=h$ for shallow flow (Julien & Simons, 1985)), and S is the bed slope [m/m] equal to the sine of the slope angle for gentle slopes. This gives rise to the shear velocity, a term commonly used to describe the thickness of the boundary sublayer:

$$U^* = \sqrt{\frac{\tau_f}{\rho_w}} \quad (4.8)$$

The shear velocity, namely the critical shear velocity which occurs at the initiation of motion under bedload conditions, was used by Shields (1936) (see Simons & Senturk (1992)) to characterize flow as hydraulically smooth, transitional, or fully rough, the first of which yields conditions for the application of Stokes' settling relation (used by WEPP).

Stream power is another parameterization of flow commonly used in sediment transport applications:

$$\Omega = \tau u \quad (4.9)$$

where

$$\begin{aligned} \Omega &= \text{stream power per unit wetted area } [\text{kg/s}^3] \\ u &= \text{flow velocity } [\text{m/s}] \end{aligned}$$

Energy theories such as Bagnold's stream power method (Bagnold, 1966) and Velikanov's gravitational theory (1954) are based on the stream power method, originally introduced by Rubey (see Watson, 1969). More recently applied concepts such the

balance between transport capacity and detachment capacity (discussed below) are somewhat analogous to the energy expenditure theories of Rubey.

4.2.2 Sediment

Studies of sediment transport have yielded a wide range of sediment transport equations for total load, suspended load, bedload, and wash load in forms ranging from time-averaged, total discharge to instantaneous, distributed erosion/deposition models. Commonly used sediment transport equations include but are not limited to: Bagnold (1980), Yalin (1963), Govers (1990), Low (1989) and Yang (1973), Einstein (1950), as well as modifications to these equations based on local conditions or research interests (e.g. WEPP [Foster et al., 1989] – Yalin; EUROSEM [Morgan et. al., 1998] - Govers). Julien and Simons (1985) as well as Simons and Sentuk (1994, Chapter 9) discuss the limits of application and parameterizations for a number of sediment transport equations.

Many current sediment transport models are based on the continuity equation of sediment flux (e.g. Foster, 1982; Bennett, 1974). The continuity equation for overland flux is:

$$\frac{\partial q_s}{\partial x} + \rho \frac{\partial (cy)}{\partial x} = D_R + D_I = D_F \quad (4.10)$$

D_R = rill detachment rate [$kg / m^2 / s$]

D_I = interrill detachment rate [$kg / m^2 / s$]

D_F = flow (rill and interrill) detachment rate [$kg / m^2 / s$]

q_s = sediment load [$kg / m / s$]

ρ = sediment density [kg / m^3]

c = sediment concentration [m^3 / m^3]

y = water depth [m]

The first term in equation (4.10) is the spatial variation of the sediment flow rate. The second term is the sediment storage within the water column which is commonly neglected for bedload analysis (Chang & Hill, 1976) and quasi-steady sediment flow (shallow flows with gradual variations) (Haan et. al., 1994). For now, we combine rill and interrill detachment into D_F . Here, rainfall detachment is included in D_F as well by assuming that sediment detached and transport by rainfall impact will be absorbed in the interrill component of detachment, D_F .

Foster and Meyer (1972) propose that the rill detachment/deposition rate, D_F [kg/m/s], is proportional to the difference between the transport capacity of the flow and the actual sediment load:

$$D_F = C(T_C - q_s) \quad (4.11)$$

C is the dimensionless first-order reaction coefficient and T_C [kg/m/s] is the *transport capacity* of the flow. If $D_F > 0$, detachment occurs at a rate governed by the excess in transport capacity – if $D_F < 0$, sediment load exceeds capacity and deposition occurs. It should be noted that D_F from equation (4.11) is a *net* rate and can not be equated with either detachment or deposition directly since in reality both occur simultaneously, especially for a spectrum of grain size populations. However, equation (4.11) is well validated for deposition of sediment (Einstein, 1968; Foster & Huggins, 1977a; Davis, 1978) but less so for detachment-limited transport. Huang et. al. (1999) caution the use of equation (4.11) under erosion conditions.

By defining a *detachment capacity*, D_C [kg/m/s] (or *maximum potential detachment*):

$$D_C = CT_C \quad (4.12)$$

the following equation is obtained:

$$\frac{D_F}{D_C} + \frac{q_S}{T_C} = 1 \quad (4.13)$$

Transport capacity in shallow flow is well represented by the Yalin equation (Foster & Meyer, 1972), and can be simplified for high tractive forces to:

$$T_C = C_t \tau_f^{3/2}. \quad (4.14)$$

Transport capacity, introduced in the energetics model of Bagnold (1968), takes many forms (Mitasova et al. 1996; Lei et al., 1997; Govers, 1990; Low, 1989; Yalin, 1963; Yang, 1973). Julien and Simons (1985) present a derivation of transport capacity from dimensional analysis in which T_c is comprised of several empirical coefficients and exponents - equation (4.14) is a popular simplified formulation. Essentially, transport capacity is analogous to the energy available to transport sediment, which can be in the form of suspended load or bedload transport. A low sediment-to-water volumetric ratio need not exist for flows (and therefore transport capacity) to exist (e.g. mud flows); although the treatments reviewed and extended here assume that water flow is the primary medium for energy delivery.

Several researchers have challenged the concept of transport capacity. The complexity of fluid-grain interactions across the full spectrums of flow, grain size, suspended sediment concentration, and bed roughness limits the usefulness of a transport capacity defined solely on applied shear stress. Turbulence is critical for soil entrainment into the water column (Nearing and Parker, 1994; Nelson et al., 1995); however, turbulent intensity is reduced for flows with higher sediment concentrations (Einstein and Chien, 1954; Wijetunge and Sleath, 1998). Some researchers (McEwan et al., 1999; Ellison and Ellison, 1947) argued that the collisions of saltating grains in bed load motion

may be a primary agent in the entrainment of bed grains into the flow; however, Jiang and Haff (1993) suggest that these collisions are damped by the fluid that is squeezed out from between grains just prior to contact. In fact, the existence of bedload may shield the bed from further detachment (Polyakov and Nearing, 2003). In addition, hydraulic friction may change as a result of deposition (e.g. if a rough surface is smoothed by the deposition of fine grains).

Other researchers show evidence that the transport capacity is not a unique value for a given set of flow and cover conditions. In developing a formalism for computing equilibrium near-bed suspended sediment concentrations in alluvial channels based on a balance between an entrainment flux, governed by turbulent bursting, and a deposition flux, governed by the product of near-bed concentration and the hindered settling velocity of sediment, Cao (1999) discovered that two transport capacities are possible depending on upstream flow or initial conditions – one at low concentrations and one at hyperconcentrated flow. Flume experiments by Polyakov and Nearing (2003) indicate that a hysteresis effect occurs in which the equilibrium maximum sediment concentration differs depending on whether it was approached from the sediment excess or sediment deficit state. Nelson et al. (1995), using laser-Doppler velocimetry and cinematography in flume experiments, provided conclusive evidence that bed shear stress is not sufficient in unsteady or non-uniform flows, such as those over bedforms, in addressing the grain-fluid interactions governing bed morphology; this implies that transport capacity as defined in equation 4.14 is limited to steady, uniform flows over smooth beds.

In addition, Huang et. al. (1999) found that surface hydrologic parameters such as drainage and seepage influence the transport capacity. Others (e.g. Hsieh Wen Shen and

Julien, 1993; Reid et al., 1997) suggested that the concept of transport capacity may be ineffective in describing wash load since the concentration of wash load depends mainly on the availability of small grains and not on the applied flow. Wash load may contribute significant amounts of sediment to the total load, especially in areas with high clay content or in disturbed watersheds where small grains (<0.053mm) are abundant on the surface (Thaxton et al., 2003).

Regardless of these concerns, it is the current practice of watershed erosion / deposition researchers to neglect the effects of suspended sediment concentrations and deposition on flow dynamics (e.g. Govindaraju and Kavvas, 1991; Mitas and Mitasova, 1998) and to parameterize turbulent influences (e.g. mixing length model, e.g. Tennekes and Lumley, 1972) such that a unique transport capacity that fully governs sediment transport for a given set of flow and cover conditions is assumed.

Similar to equation 4.14, the detachment capacity can be written:

$$D_C = C_d (\tau_f - \tau_c)^{3/2}. \quad (4.15)$$

where τ_c the critical shear stress [kg/m/s^2] and C_d is the detachment capacity coefficient (erodibility parameter). Foster and Meyer argue that, since erosion begins near the top of slopes, the critical shear stress in equation (4.15) can be neglected. With this assumption, from equations (4.12), (4.14) and (4.15),

$$C = \frac{C_d}{C_t}. \quad (4.16)$$

and the detachment rate (equation 4.11) can be re-written as:

$$D_F = D_C \left(1 - \frac{q_s}{T_C}\right) = C_d \tau_f^{3/2} \left(1 - \frac{q_s}{T_C}\right) \quad (4.17)$$

4.3 Landscape-scale sediment transport

Below is a review of three sediment erosion, transport, and deposition models: the Universal Soil Loss Equation ([M/R]USLE), the Water Erosion Prediction Project (WEPP), and the GRASS GIS implementation of the SIMulated Water Erosion (SIMWE) model. These are presented to outline the primary theoretical and practical issues presently facing the landscape modeling community and to establish a foundation for the introduction of a terrain evolution routine based on SIMWE to be described in section 4.5. Borah and Bera (2003) provide an overview of an extended subset of watershed-scale and nonpoint-source pollution models currently in use or development.

4.3.1 The Universal Soil Loss Equation ((R/M)USLE)

The Universal Soil Loss Equation (USLE), originally developed by Wischmeier and Smith (1965, 1978) for use in farm management applications, was the first widely successful empirically based field scale model to predict soil erosion. The USLE equation multiplicatively combines factors important to erosion processes to arrive at an average soil loss per unit acre (in Normal English units):

$$A = RKLSCP \quad (4.18)$$

where (in English units):

A = average soil loss per unit acre [tons / acre / yr]

R = rainfall / runoff factor [ft · tonf · in./acre · hr · yr]

K = soil erodibility factor [tons · acre · hr / acre · ft · tonf · in.]

L = slope length factor

S = slope steepness factor

C = cover management factor

P = supporting conservation practice factor

NOTE: tonf = "tons of force"

Each of the factors in the USLE equation is derived from empirical data, many of which have been tuned, for example, to specific geographic locations, different soil types and land covers, seasonal and climatic variations, and local slope tillage and concavity (see Haan, et al. 1994). Applications are limited by the fact that USLE is not intended for estimating the soil loss from a single rainfall event. In addition, USLE is an erosion equation incapable of estimating channel or gully erosion, nor is it capable of predicting deposition. It is intended primarily for predicting soil loss over extended periods. Foster et al. (1977b), however, presented improved R and L values to reduce error when applying USLE to single storm events. More widely applied are the modifications proposed by Williams (1975, 1976, 1977, 1978) who replaced the R factor in USLE with a new R factor that was a function of runoff volume, V , and peak discharge rate, Q_p :

$R \rightarrow R_w = 95(VQ_p)^{0.56}$. The single storm sediment yield [tons] becomes:

$$Y = 95(VQ_p)^{0.56} [K]_a [LS]_a [CP]_a \quad (4.19)$$

Where $[K]_a$, $[LS]_a$, $[CP]_a$ are area weighted average USLE parameters for a given watershed. This form of the USLE equation is referred to as MUSLE (Modified USLE). MUSLE allows the application of USLE to single storm events. In addition, Williams (1975, 1978) introduced MUSLE routing procedures that allow the application of MUSLE to heterogeneous watersheds.

The Revised USLE (or RUSLE) model (Renard et al., 1993; Foster et al., 2001) provides additional improvements which include revised slope and slope length factors, rilling susceptibility factors, time-varying freeze-thaw effects on erodibility, and subfactors for cover and management based on new data. The Unit Stream Power Erosion-Deposition (USPED) model uses drainage area and the slope angle in place of

the slope length factor in computing the *LS* topographic factor in RUSLE (Mitasova et al., 1996).

4.3.2 Water Erosion Prediction Project (WEPP)

In WEPP (Foster et al., 1989), deposition and detachment occur given the conditions on D_F as defined for equation (4.13) above. Hydrologic inputs include peak runoff [m/s], effective runoff duration [s] (computed as the total runoff volume divided by the peak runoff), and effective rainfall intensity [m/s], which are provided by the hydrologic component of the WEPP model. Transport capacity is defined as:

$$T_C = k_t \tau_f^{3/2} . \quad (4.20)$$

where k_t [$\text{m}^{1/2}\text{s}^2/\text{kg}^{1/2}$] is the *transport coefficient* (i.e. C_t from equation (4.14)). In actuality, T_{ce} , the transport capacity at the end of the slope which is computed from the Yalin equation, is used to calibrate k_t via equation (4.20). The shear stress as a function of downslope distance is computed from the Darcy-Weisbach uniform flow equation:

$$\tau_f(x) = \gamma \left[\left(\frac{P_r}{C'} \right) xs \right]^{0.6} \quad (4.21)$$

where P_r is the peak runoff rate [m/s], s is the localized slope, γ is the specific gravity of water, and C' is the Chezy discharge coefficient given in terms of the total rill friction factor, f_t :

$$C' = \sqrt{\frac{8g}{f_t}} . \quad (4.22)$$

The case in which $T_C \approx q_s$ (transport-capacity limited), deposition occurs and is governed by equation (4.11), with the first-order reaction coefficient defined:

$$C = \frac{\beta V_f}{q}. \quad (4.23)$$

Here, $\beta=0.5$ [m] is the rainfall turbulence coefficient, V_f [m/s] is the effective fall velocity, and q [m^2/s] is the flow discharge per unit width (Foster, 1982). For channelized flow, Foster (1982) proposes that the flow rate would be greater than that of overland flow and recommends that $\beta=1.0$ be used. Sensitivity analysis (Nearing et al., 1989) has shown acceptable values of β between 0.2 and 3.2 within WEPP, depending on slope length (5-300m) and angle (5^0 - 20^0). Note that the rate of deposition may be several orders of magnitude slower for clays as compared to larger particles such as sand grains.

For the case in which $T_C > q_s$ (detachment-limited), detachment occurs only if the applied stress exceeds the critical stress:

$$D_F = K_r (\tau_f - \tau_c)^b \left(1 - \frac{q_s}{T_C} \right) \quad (4.24)$$

Note from equations (4.11), (4.12), and (4.24) the implied relationship:

$$D_C = CT_C = K_r (\tau_f - \tau_c)^b ; \quad b = 1 . \quad (4.25)$$

K_r [s/m] is the *rill erodibility* parameter (i.e. C_d from equation (4.15)) which, in WEPP, represents the resistance of the soil bed to erosion by the flow (e.g. cohesiveness), not necessarily the grain size explicitly. Nearing et al. (1989) state that detachment limited erosion occurs primarily in interrill areas, where applied shear remains low relative to channels. $K_r=0.0001-0.01$ and $\tau_c=0.0-10.0$ are the baseline values used in WEPP.

Parameters used for normalization are defined for both rill and interrill detachment, which include effects of soil consolidation time after tillage, freeze-thaw, ground cover, canopy, rill spacing, and below-ground residue on sediment generation. Finally,

normalized erosion and deposition equations are achieved which take the form of continuity (equation (4.10)), with D_F defined for deposition via equation (4.11) (with (4.23)) and for erosion via equation (4.24).

4.3.3 SIMulated Water Erosion (SIMWE) Model

In GRASS GIS, the modules *r.sim.water* and *r.sim.sediment* are the implementation of the sediment erosion/deposition model referred to as SIMWE (SIMulated Water Erosion) developed by Mitas & Mitasova (1998). The governing continuity equation is solved via a path sampling Monte Carlo method in which erosion, transport, and deposition conditions are treated as a continuous field, resulting in fully distributed erosion/deposition patterns. In *r.sim.water*, shallow water is modeled via the two-dimensional form of the Saint Venant equations (4.1-4.2) with the kinematic wave approximation $\mathbf{s}_f \approx \mathbf{s}_o$. Unit discharge is defined as:

$$\bar{q}(\vec{r}, t) = \bar{v}(\vec{r}, t)h(\vec{r}, t) \quad (4.26)$$

where $v(\mathbf{r}, t)$ is the flow velocity and $h(\mathbf{r}, t)$ is the water depth. Note that spatial variability is explicit through the governing equations for SIMWE. Manning's relation:

$$\bar{v}(\vec{r}, t) = \frac{C}{n(\vec{r})} h^{2/3}(\vec{r}, t) |\vec{s}_f(\vec{r})|^{1/2} \hat{s}_{f0}(\vec{r}) \quad (4.27)$$

closes the system of equations. Here, $n(\mathbf{r})$ is the Manning's roughness coefficient, $C=1$ [$\text{m}^{1/3}/\text{s}$] is the dimensional constant, and $\mathbf{s}_{f0}(\mathbf{r})$ is the unit vector in the friction slope ($\mathbf{s}_f(\mathbf{r})$) direction. To approximate the diffusive wave effects, a diffusion term is incorporated into the continuity equation, such that the final form of continuity for *r.sim.water* is:

$$-\frac{\epsilon}{2} \nabla^2 [h^{5/3}(\vec{r})] + \vec{\nabla} \cdot [h(\vec{r}) \bar{v}(\vec{r})] = i_e(\vec{r}) \quad (4.28)$$

In *r.sim.sediment*, the continuity of sediment mass equation

$$\frac{\partial [\rho_s c(\vec{r}, t) h(\vec{r}, t)]}{\partial t} + \vec{\nabla} \cdot \vec{q}_s(\vec{r}, t) = D(\vec{r}, t) \quad (4.29)$$

is simplified by assuming steady state

$$\vec{\nabla} \cdot \vec{q}_s(\vec{r}) = D(\vec{r}). \quad (4.30)$$

Here, the sediment flow rate (sediment load) is proportional to and in phase with the water flow rate (steady state):

$$\vec{q}_s(\vec{r}, t) = \rho_s c(\vec{r}, t) \vec{q}(\vec{r}, t) \quad (4.31)$$

where ρ_s is the density of the sediment [kg/particle], $c(\vec{r}, t)$ is the sediment concentration [particles/m³], and $\vec{q}(\vec{r}, t)$ is the water unit flow discharge. The final form of the sediment continuity equation is:

$$-\frac{\omega}{2} \nabla^2 \varphi(\vec{r}) + \vec{\nabla} \cdot [\varphi(\vec{r}) \vec{v}(\vec{r})] + \varphi(\vec{r}) \sigma(\vec{r}) |\vec{v}(\vec{r})| = \sigma(\vec{r}) T(\vec{r}) \quad (4.32)$$

where

$$\varphi(\vec{r}) = \rho_s c(\vec{r}) h(\vec{r}) \quad [\text{kg/m}^3] \quad (4.33)$$

Similar to WEPP, SIMWE defines transport capacity as:

$$T_c(\vec{r}) = K_t(\vec{r}) \tau_f(\vec{r})^p \quad (4.34)$$

(analogous to T_c from equations 4.14 and 4.20-WEPP) and the detachment capacity as:

$$D_c(\vec{r}) = K_d(\vec{r}) (\tau_f(\vec{r}) - \tau_e(\vec{r}))^q ; \quad q = 1 \quad (4.35)$$

(analogous to D_c from equations 4.15 and 4.25-WEPP). Here, $K_t(\vec{r})$ is the same as C_t in equation (4.14) and k_t in equation (4.20); $K_d(\vec{r})$ is the same as C_d in equation (4.15) and K_r in equation (4.25). The exponent in equation 4.34, p , is assumed to be unity (non-Yalin) - calibration to field data has suggested values less than that proposed by Foster &

Meyer (WEPP, 1989). The first order reaction term is defined as $\sigma(\mathbf{r})=D_c(\mathbf{r})/T(\mathbf{r})$. If $p=q=1$, and critical shear is neglected, $\sigma(\mathbf{r})$ equates to C from equation (4.16). The flow shear stress is defined at every location in the watershed as simply (see equation (4.7)):

$$\tau_f = \rho_w g h(\vec{r}) \sin \beta(\vec{r}) \quad (4.36)$$

Here, $\rho_w g = \gamma$ is the specific gravity of water, $h(\mathbf{r})=R$ is the hydraulic radius and $\sin(\beta)$ is the bed slope (gentle slopes assumed).

The bivariate formalism of SIMWE is a powerful alternative to the steepest slope methods used by WEPP and others. In the transport-limited case for which $T_C \leq q_s$ (transport-limited):

$$\frac{D_F}{D_C} + \frac{q_s}{T_C} (\approx 1) = 1 \quad (4.37)$$

Mitas and Mitasova (1998) apply the continuity condition and solve for D_F in terms of profile curvature, κ_p , and tangential curvature, κ_t . In their resulting bivariate solution,

$$D_F = \vec{\nabla} \cdot q_s \hat{s}_o = \vec{\nabla} \cdot T_C \hat{s}_o = K_t \rho_w g \left\{ \vec{\nabla} h \cdot \hat{s}_o \sin \beta - h [\kappa_p + \kappa_t] \right\} \quad (4.38)$$

the local flow acceleration in both the gradient and tangential directions play equally important roles in the spatial distribution of erosion and deposition (see Mitas and Mitasova, 1998, Appendix). Here, β is the slope angle, s_o is the unit vector in the steepest slope direction, and h is the depth of overland flow. This process includes soil properties via K_t and is superior when compared to conventional univariate formalisms which underpredict deposition in areas of tangential concavity. Unlike WEPP, however, which employs grain size dependence via settling velocity in their deposition condition (equation (4.23)), grain size dependence is limited to the first order reaction term, σ . In the case of $T_C \gg q_s$ (detachment-limited),

$$\frac{D_F}{D_C} + \frac{q_S}{T_C} (\approx 0) = 1 \rightarrow D_F = D_C \quad (4.39)$$

and detachment is dictated by equation (4.35).

It should be noted that much of the analysis performed on SIMWE uses the first order reaction coefficient defined as $\sigma = D_C/T_C = K_d/K_t$. This condition is true only if $\tau_C=0$ and $p(\text{equation (4.34)})=q(\text{equation (4.35)})$. Assuming a critical shear of zero is supported by Foster (1982) who states that the presence of a critical shear will underestimate sediment load. With these limitations understood, the transport limited case is described by Mitas and Mitasova as $\sigma \rightarrow \infty$ ($K_t \leq K_d$); however, although this condition is satisfied with a dominant K_d , detachment limited erosion will occur as long as the sediment load is less than the transport capacity. The detachment limited case is described by Mitas and Mitasova as $\sigma \rightarrow 0$ ($K_d \ll K_t$). Although this condition is satisfied with a dominant K_t , transport limited erosion will occur as long as the sediment load is close to the transport capacity. Care should be taken when using relative values of K_d and K_t as inputs to SIMWE in forcing detachment or transport limited conditions within the model.

4.4 Grain-size dependent sediment transport

Equation (4.13) can be interpreted as an analogy to the energy in the flow available for sediment transport or detachment/deposition resulting from the hill slope and flow depth. It assumes that the oscillatory energy associated with molecular and turbulent fluctuation of the flow and intergranular collisions common to bedload transport are either appropriately represented or do not significantly effect net detachment and deposition rates in watershed-scale overland flow systems. The grain-size dependent effects of vertical bedload sorting (see Chapter 2.0), flow-bed interaction, and preferential detachment and deposition may lead to small-to-intermediate scale patterns and bedforms that may, if unaccounted for in predictive models, lead to significant errors in erosion/deposition patterns and total sediment discharge estimates. However, gross behaviors in soil detachment and deposition based on grain size are represented in models such as WEPP and SIMWE via the transport and detachment coefficients, the critical shear stress, and fall velocity. These treatments allow for prediction of observed longitudinal sorting behavior: large grains, transported primarily as bedload, migrate slowly relative to the fine grains which, transported primarily as suspended load, are deposited much further downstream or are discharged from the region of interest with the flow.

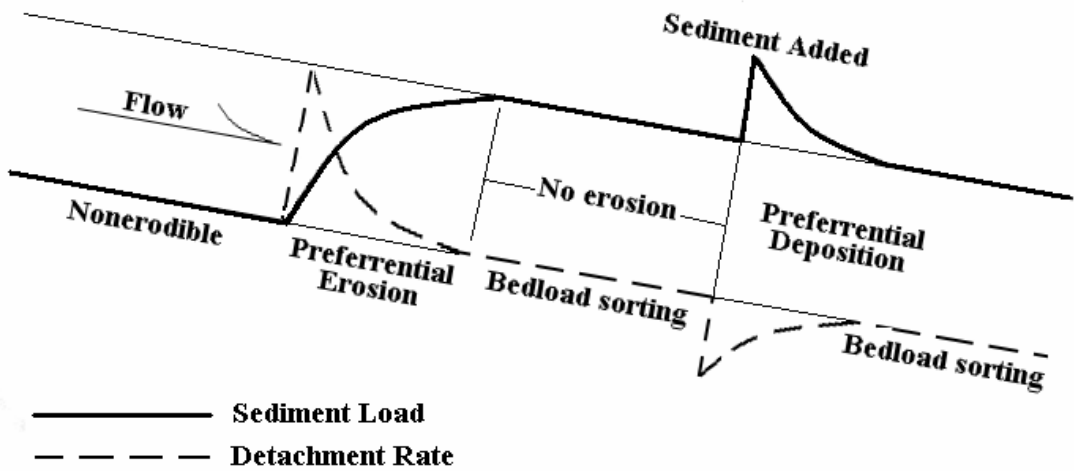


Figure 4.1: A modification of Foster & Meyer (1972) in which grain-size dependent processes have been included. Grain size sorting occurs in the bed (bedload) when stress is applied to an erodible (movable) bed. Grains are detached and deposited preferentially – for detachment, the size of entrained grains is proportional to the applied stress and for deposition, large grains settle first.

Grain size dependent erosion, transport, and deposition over bare soils is governed explicitly by the terrain geometry and the flow and soil properties; however, in most cases, land cover such as vegetation exists which has a profound impact on grain size dependent detachment and deposition. For example, sediment-laden flow over poorly covered soil that encounters a downstream vegetated region near a stream will lose significant transport capacity and deposit sediment. In this case, most likely only the smallest grains in suspension will be transmitted through the vegetation into the drainage network. The absence of vegetal filter zones near streams in disturbed areas would allow more sediment and larger grains to enter the higher shear stress conditions within the channel networks and would encourage significant channel bank erosion. In general, although vegetated land cover may increase localized flow turbulence, it decreases soil detachment rates and mean flow velocities, and suppresses the formation of rills.

Vegetated land cover is arguably the most effective and desirable sediment erosion control measure. Boundaries in variable land cover usually correspond to changes in flow properties and to gradients in transport and detachment capacities.

4.4.1 Vertical bedload sorting

Julien & Simons (1985) and Singh (1997) state that bedload transport is most likely the dominant sediment transport process in overland flow since saltation and even suspension may be limited in the shallow waters. Sediment flow in mountainous channel beds, dominated by gravel and large sand grains, is primarily bedload. Preferential detachment and deposition, as parameterized by the critical shear stress and the transport and detachment coefficients (see below), is the primary agent in current landscape scale models (WEPP and SIMWE) for longitudinal sorting.

Vertical bedload sorting (see Chapter 2.0), however, may be assumed to be of little consequence for overland, interrill, and rill sediment transport since soil surfaces are usually more cohesive than in alluvial channels (Singh, 1997). In addition, the depth of motion of the bed is negligible. The absence of these physical processes limits granular sorting to situations of preferential detachment, deposition and impact fractionation (to a degree) which are processes accounted for in the detachment and deposition processes explicitly. As a result, vertical bedload sorting in overland areas may be neglected. Vertical bedload sorting will be most evident in channels with higher stresses due to flow depth, bed mobility and depth of motion, as well as the availability of coarser grains due to channel wall degradation. Future inclusion of channel bedload sorting in this treatment would initially be based upon parameterization from simulations under steady flow in

which transport is dominated by intergranular collisions (Drake and Calantoni, 2001); however, our initial watershed-scale models neglect bedload.

4.4.2 Soil, Land cover, and Flow Property Coefficients

Presently, WEPP and SIMWE contain grain size dependence in the following parameters:

- (1) First order reaction coefficient, C (σ in SIMWE)
- (2) Detachment capacity coefficient (erodibility), C_d (K_d in SIMWE)
- (3) Transport capacity coefficient, C_t (K_t in SIMWE)
- (4) Critical shear stress, τ_c

Note that WEPP uses empirical equations for C_d and τ_c . The variable definitions used in SIMWE will be used hereafter. If critical shear is neglected due to high applied shear stress and if p and q in equations (4.32) and (4.33), respectively, are equal, the first order reaction coefficient is simply $\sigma = D_C/T_C = K_d/K_t$. The detachment and transport capacity coefficients, K_d and K_t , are generally considered independent functions. Foster and Meyer (1972) describe K_d as a function of the resistance of the soil to erosion by flow and K_t as being explicitly a function of particle size and density. Table 4.1 outlines the typical sediment characteristics for Midwestern soil (Young and Onstad, 1978; Foster, 1982). Note that due to the difficulty in defining values for K_t and K_d , may times a value of σ is used instead.

Table 4.1: Typical sediment characteristics for Midwestern soil from Young, et. al. (1978) and Foster (1982). Also used by AnnAGNPS

Soil type	Specific gravity	Size [microns]	V_f [mm/s]	$\sigma = D_c/T_c$ [1/m]
Clay	2.65	2	0.00311	0.0089
Silt	2.60	10	0.0799	0.074
Small aggregate	1.80	200	23.1	22.0
Sand	2.65	20	0.381	0.31
Large aggregate	1.60	500	34.7	32.0

4.4.2.1 Detachment and transport capacity coefficients

The transport capacity coefficient, K_t , scales the applied shear stress to yield a value for transport capacity (eq. 4.14). Applied shear alone will entrain sediment, if for no other reason than the increased granular temperature of the bed due to resulting intergranular collisions under bedload transport (McEwan et al., 1999). The vertical gradients in flow velocity and the turbulent energy density (or eddy viscosity) are considered by many to be the dominant mechanisms for sediment lift and entrainment (Nearing and Parker, 1994; Nelson et al., 1995) - these effects could be considered contained within K_t (e.g. the transport capacity for a highly turbulent flow would be greater than for a laminar flow with the same applied shear, which is a "mean" value). The excess T_c after comparison to the sediment load is then used to govern the rate of detachment, D_f , along with the maximum detachment coefficient, D_c (eq. 4.17). As stated by Foster and Meyer (1972), D_c is primarily a function of macroscopic soil properties including cohesion, compactification, and grain availability as well as granular properties such as particle size, shape, and density, all of which scale the rate of detachment. D_c also includes the effects of land cover. In addition, it is argued that D_c would contain information about flow-grain interactions that dictate entrainment rate, such as bedload shielding (Polyakov and Nearing, 2003) and shear reduction to threshold (Bagnold, 1956) or equilibrium (Seminara et al., 2002) due to momentum absorption by the movable bed. Obviously, D_c is a complicated function of several variables that the community needs to expand and define as research continues.

4.4.2.2 Critical Shear Stress

The critical shear stress depends directly upon the balance between the frictional force on the bed and the gravitational force (Bagnold, 1966; Hunt, 1999). For example, for non-cohesive grains:

$$\tau_c = \frac{1}{6}(\rho - \rho_w)gd \quad (4.40)$$

Critical shear is a primary controlling factor in grain size dependent detachment. Detachment will not occur unless the applied shear is high enough. Presently, SIMWE provides the option to define a distributed critical shear stress via a raster file. The value for τ_c at each location could be defined as a spatially uniform parameter initially and would change based on the redistribution of grain sizes (represented by a D_{50}) with progressive iterations of SIMWE.

4.4.3 Wash load

Wash load is comprised of small particles, finer than channel bed material originating from the channel bank or from upslope sources (Haan et al., 1994; Simons and Senturk, 1992). Due to the small grain diameters, wash load typically has very low settling velocities and, once entrained, remains in the water column for extended periods of time unless forced to settle via the addition of chemical flocculants (Chen, 1975; Camp, 1973). For the purposes herein, wash load will not be treated explicitly: wash load will be characterized with the same physical properties (and numerical parametrizations) as fine clay.

4.4.4 SEDATE (Sediment Erosion Deposition And Terrain Evolution) Model: an example application

To model the relationships described in equations 4.11-4.17, a one-dimensional erosion/deposition model was developed in MATLAB™ - the Sediment Erosion, Deposition, and Terrain Evolution (SEDATE) model. SEDATE includes a transport capacity coefficient, C_t , maximum detachment coefficient, C_d , and critical shear stress, τ_c , all of which are spatially distributed, allowing grain size dependent behavior to be modeled. SEDATE evolves the terrain at each time step based on the non-diffusive continuity equation.

First, SEDATE computes the applied stress using equation (4.36) with a fixed water depth. It then determines the transport capacity based on equation (4.20) and the detachment/deposition rates for transport and detachment limited conditions. A fall shear stress, τ_f , is employed which determines the minimum applied shear below which deposition occurs spontaneously under detachment limited conditions. A large τ_f represents large grains while a near-zero value represents fine particles. Using the trapezoidal method, the model then integrates the continuity equation to solve for q_s , which is accumulated (erosion) or diminished (deposition) along the direction of steepest slope. The gradient in q_s equates to the change in terrain elevation for each time step. An optional smoothing algorithm may be employed to mimic diffusive processes. The smoothing algorithm attenuates localized terrain variations based on a user-definable hillslope threshold that is compared to a running average of terrain elevation.

To model simple grain size dependent effects, three SEDATE simulations were performed on a simple downward slope of angle 5.7^0 with a fixed water height of 0.10 m. Grain size parameters used are derived from table 4.1 with $C_t=0.01$ (within the WEPP

baseline values). Figure (4.2) illustrates the results in which $\sigma=0.009$ ($C_d=9E^{-5}$, $C_t=0.01$), $\tau_c=0.01$, $\tau_f=0$, $V_f=0.003$, and no smoothing - these parameters would be indicative of clay-sized particles. Figure (4.3) shows the results for silt-sized grains: $\sigma=0.074$ ($C_d=7.4E^{-4}$, $C_t=0.01$), $\tau_c=0.01$, $\tau_f=0$, $V_f=0.080$. Figure (4.4) shows the results for sand-sized grains: $\sigma=22$ ($C_d=0.22$, $C_t=0.01$), $\tau_c=0.01$, $\tau_f=0$, $V_f=0.380$. In all three runs, the elapsed time was 1 hour real time. Note that for the clay- and silt-sized grains, the sediment load, q_s , increases exponentially until it reaches the transport capacity at which point transport-limited deposition dominates ($Dc<0$) such that deposition occurs instantaneously.

For the clay sized grains, the sediment traveled the full length of the slope (up to 30m) before depositing at the bottom of the slope. For the sand sized grains, the sediment moved in short, localized bursts as indicated by the sharp peaks in detachment rate (see figure 4.4, bottom). When summed over 3600 time steps ($\Delta t=1$ s), the surface appeared to have moved as one sheet a total of approximately 3m. This behavior is commonly observed on hillslopes - large grains tend to roll and saltate short distances, while the silt and clay sized particles become entrained and travel in the flow long distances before settling out.

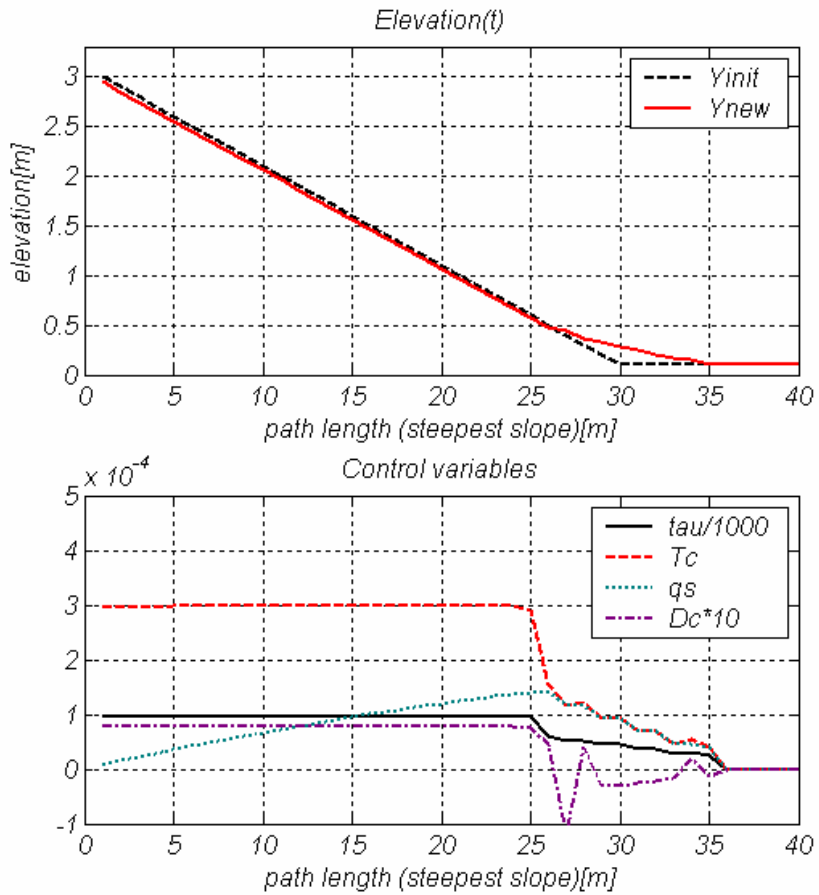


Figure 4.2: A simple downward slope of angle 5.7° with $h=0.01$ m, using the input parameters for clay: $\sigma=0.009$ ($C_d=9\text{E}^{-5}$, $C_r=0.01$), $\tau_c=0.01$, $\tau_f=0$, $V_f=0.003$. Terrain change is exaggerated by 2x. Models rainfall for 1 hour of real time.

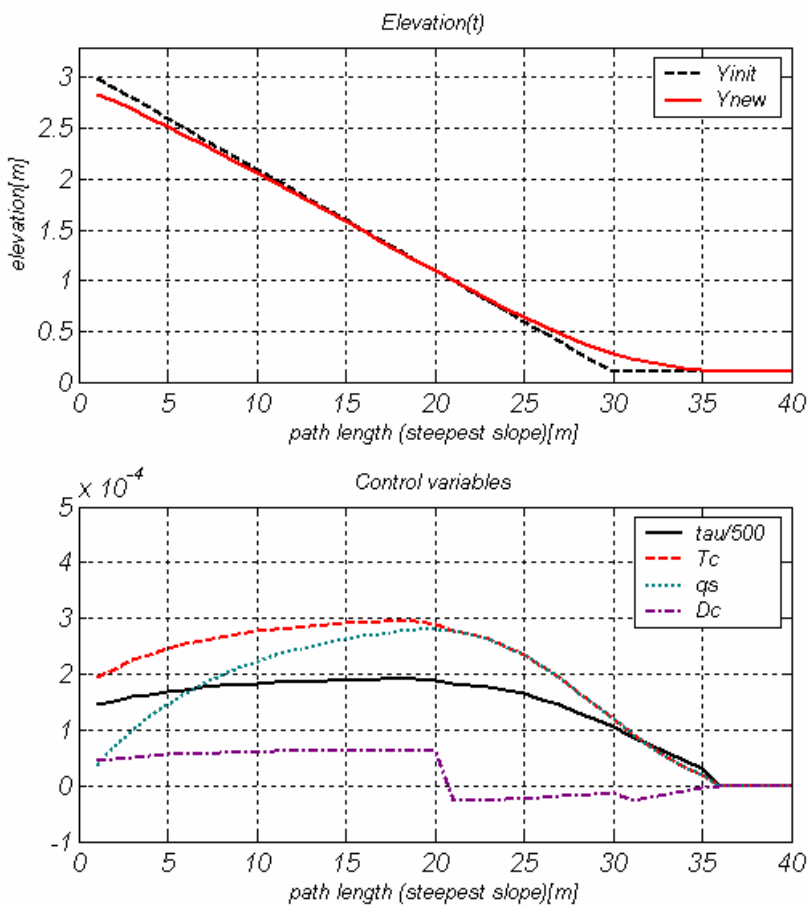


Figure 4.3: A simple downward slope of angle 5.7° with $h=0.01$ m, using the input parameters for silt: $\sigma=0.074$ ($C_d=7.4E^{-4}$, $C_r=0.01$), $\tau_c=0.01$, $\tau_f=0$, $V_f=0.074$. Models rainfall for 1 hour of real time.

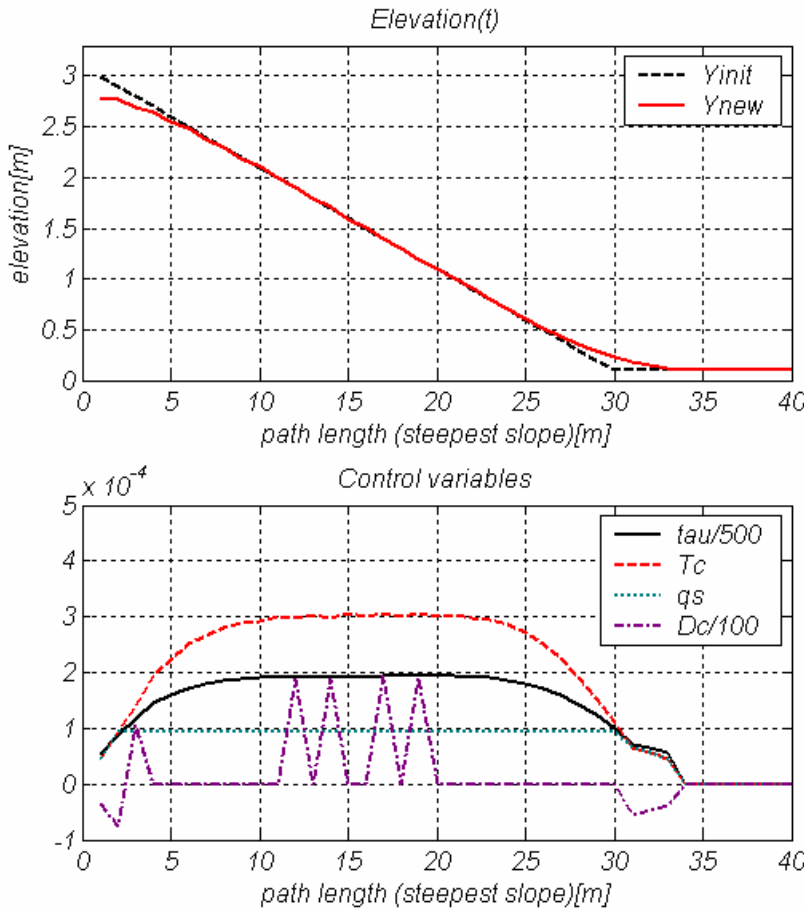


Figure 4.4: A simple downward slope of angle 5.7° with $h=0.01$ m, using the input parameters for sand: $\sigma=22$ ($C_d=0.22$, $C_t=0.01$), $\tau_c=0.01$, $\tau_f=0$, $V_f=0.381$. Models rainfall for 1 hour of real time.

In figures 4.5-4.7, a hillslope was modified such that two flat shelves 5 m in length interrupted the slope at evenly spaced intervals. In figures 4.5 and 4.6, the grain sizes were clay-silt and small gravel, respectively. In figure 4.7, clay-silt sized grains are originally on the hillslopes with gravel on the shelves. Note that in figure 4.7 the smoothing algorithm (diffusion) was employed to deter unrecoverable instabilities on the downslope side of the gravel terraces - this resulted in predicted clay deposition on the upslope side of the terraces that was not observed in the clay-size runs (see fig. 4.5). The shelves erode very little with pseudo-avalanche conditions just downhill from each shelf.

This behavior is observed frequently on hillslopes in which a gravel bed road is incised into the hill and loses integrity as erosion ensues.

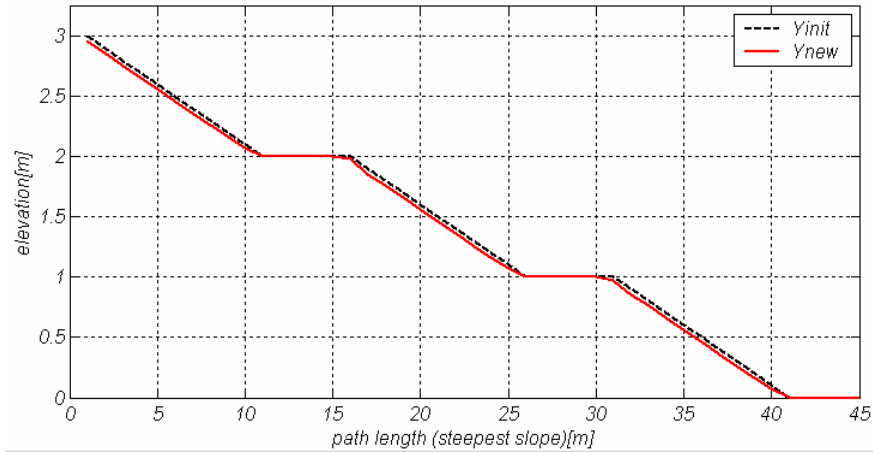


Figure 4.5: A terraced hillslope with $\sigma=0.01$ (clay-silt sized particles).

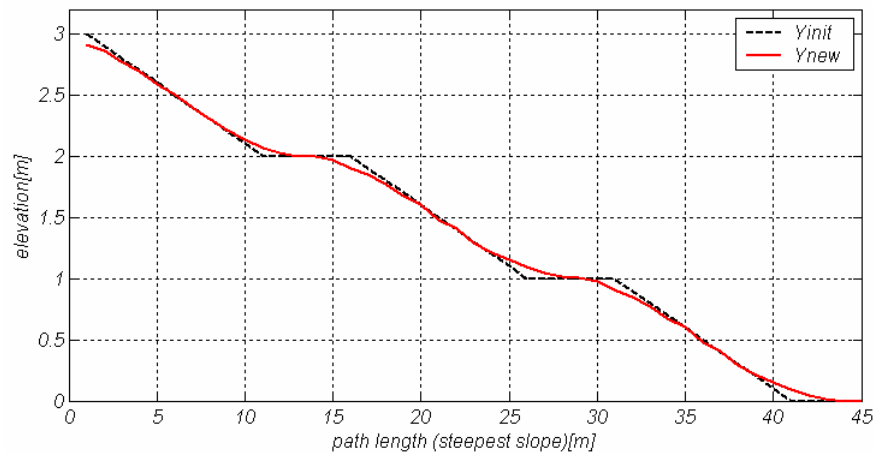


Figure 4.6: A terraced hillslope with $\sigma=1.0$ (small gravel sized particles).

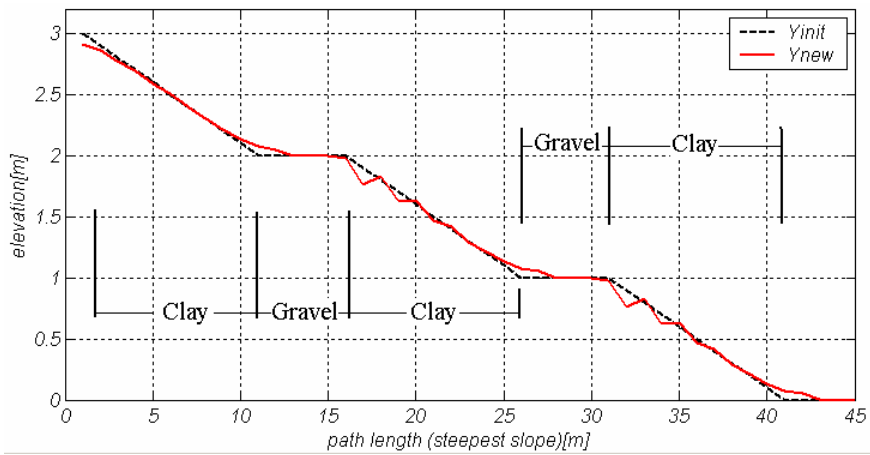


Figure 4.7: Terraced hillslope - on the hillslopes, $\sigma=0.01$ (clay) and on the terraces, $\sigma=1.0$ (gravel).
The smoothing algorithm (diffusion) was employed to deter unrecoverable instabilities on the downslope side of the gravel terraces.

4.5 Grain size dependent terrain evolution in SIMWE

Terrain evolution is implemented via the GRASS GIS module *r.terrodyn* introduced below. Module *r.terrodyn* computes elevation change as the divergence of the sediment flux computed from the GRASS GIS module *r.sim.sediment*. Direct computation of terrain change based on sediment flux yields instabilities in localized areas: as a result, a comparative band pass filter is implemented, as well as a smoothing routine, to maintain realistic terrain evolution over many iterations.

4.5.1 Governing equations

The terrain evolution equation used in this treatment is (e.g. Willgoose et al., 1991; Lei et al., 1997):

$$\frac{\partial z(\vec{r}, t)}{\partial t} = -\frac{1}{\rho_b(\vec{r})} \vec{\nabla} \cdot (q_s(\vec{r}, t) \hat{s}_0(\vec{r}, t) - \varepsilon_g(\vec{r}) \nabla z(\vec{r}, t)) \quad (4.41)$$

where $D_b(\mathbf{r})$ [kg/m³] is the bulk density of the sediment

$$\rho_b(\vec{r}) = \rho_s(1 - \lambda(\vec{r})) \quad (4.42)$$

Here, ρ_s [kg/m³] is the density of the sediment and $\lambda(\mathbf{r})$ [dimensionless] is the bed porosity. The diffusion coefficient, $\varepsilon_g(\mathbf{r})$ [m²/s], and the bulk density can vary spatially depending on the soil type. Equation (4.41) without the diffusion term is the basic sediment conservation equation (a.k.a. the Exner equation) commonly used in terrain change models (Tucker et al., 2001; Parker et al., 2000; Dietrich et al., 1993; Hoefel and Elgar, 2003; Karrambas and Koutitas, 2002). The second term in equation (4.41) is a gravitational diffusion term which takes into account the effects of local curvature. Physically, the diffusion term represents the localized migration and settling of soil that

occurs during and between rainfall events. It is similar in nature to the diffusive hillslope erosion term used by Tucker and Bras (1998), except that in this case, diffusion is not forced based on a landslide stability threshold but rather is a correction that is proportional to the continuous slope.

Limits on $\varepsilon_g(\mathbf{r})$ should be such that the diffusive term does not dominate equation (4.41) in all space:

$$\varepsilon_g(\vec{r}) \ll \left| \frac{\vec{\nabla} \cdot q_s(\vec{r}, t) \hat{s}_0(\vec{r}, t)}{\nabla^2 z(\vec{r}, t)} \right| \quad (4.43)$$

In our simulations, this condition is consistently violated in localized areas that together compose no more than 1% of the entire region. None of these local areas exceeded 2 grid cells in size. Physically, these areas represent the localized terrain discontinuities indicative of avalanche conditions with high values of curvature which forces the right side of equation (4.43) to near zero. Numerical simulations by Calantoni (2002) have shown that cohesionless spheres have an angle of repose of $\sim 28^\circ$, while Bagnold (1956) shows an angle of repose for natural sand of $\sim 32^\circ$. Cohesive soils would have the potential for higher angles of repose. It is therefore desirable for the diffusion term, in high curvature areas, to dominate and smooth out these discontinuities within the current *r.terrady* time step. Numerically, the diffusion term prevents the terrain from growing indefinitely and therefore allows conditions for dynamic equilibrium. In all other areas, the diffusion term is selected to meet the criterion of equation (4.43).

In our current implementation of equation (4.41) we assume that $\varepsilon_g(\mathbf{r}) = \varepsilon_g$ and $D_b(\mathbf{r}) = D_b$ are constants,

$$\frac{\partial z(\vec{r}, t)}{\partial t} = -\frac{1}{\rho_b} \vec{\nabla} \cdot (q_s(\vec{r}, t) \hat{s}_0(\vec{r}, t)) + \frac{\varepsilon_g}{\rho_b} \nabla^2 z(\vec{r}, t). \quad (4.44)$$

4.5.2 Implementation via GRASS GIS module *r.terrodyn*

To implement the terrain evolution equation within *r.terrodyn*, equation (4.44) is solved via a two-stage time stepping routine. First, the elevation change due to the erosion/deposition rates is computed via the boundary value equation at time step $t+\frac{1}{2}$:

$$z(\vec{r}, t + \frac{1}{2}) = z(\vec{r}, t) - \frac{\Delta t}{2} \frac{1}{\rho_b} \vec{\nabla} \cdot [q_s(\vec{r}, t) \hat{s}_0(\vec{r}, t)] \quad (4.45a)$$

A band-pass filter is applied to the elevation change (the second term in equation (above)) prior to solving for $z(\vec{r}, t)^{t+\frac{1}{2}}$. The final elevation change is then computed at time t based on the elevation at time $t+\frac{1}{2}$:

$$z(\vec{r}, t + 1) = z(\vec{r}, t + \frac{1}{2}) + \frac{\Delta t}{2} \frac{\varepsilon_g}{\rho_b} \nabla^2 z(\vec{r}, t + \frac{1}{2}) \quad (4.45b)$$

This is a diffusive (parabolic) PDE which is subject to numerical stability constraints (see below). Finally, the user has the option of smoothing the resulting terrain change locally to remove small scale fluctuations on the order of λ_x . The flowchart for *r.terrodyn* is illustrated in figure 4.8. This is a feedback network, susceptible to rapidly divergent behavior due to signal amplification. The band-pass filter and the smoothing algorithm are intended to attenuate numerical instability of the feedback system that emerges in the form of localized regions of exponential terrain change. The gravitational diffusion term assists in this process inherently, although it is intended to model the actual physical behavior of the soil that migrates and settles during and between rainfall events.

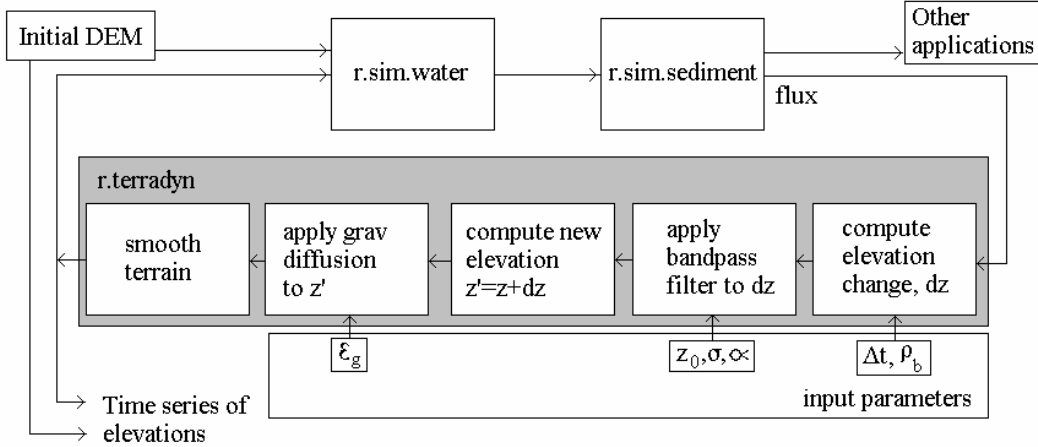


Figure 4.8: Flowchart of *r.terrodyn* module.

Numerical implementation of *r.terrodyn* is done within GRASS GIS as a UNIX shell script. To compute the terrain at time $t+1$, *r.terrodyn* requires the DEM (digital elevation model) at time t , the slope and aspect angles of the DEM, the sediment load as output from *r.sim.sediment* (SIMWE sediment module), as well as control parameters which include the bulk density, the time step size, the gravitational diffusion coefficient, and control values for the smoothing and band-pass filter algorithms (discussed below). The initial DEM is obtained from existing data (available, for example, via USGS National Elevation Data (NED) data set), ground field surveys, or LIDAR (Light Detection And Ranging) airborne surveys (see Neteler and Mitasova, 2002). Once the DEM is in raster form, the slope and aspect are determined using GRASS GIS module *r.slope.aspect* which employs the definitions of slope and aspect described in Neteler and Mitasova (2002). The divergence of the sediment flux (as well as the Laplacian of the elevation) is computed by *r.slope.aspect* via Horn's method (Horn, 1981) as:

$$\vec{\nabla} \cdot q_s \hat{s}_o = \frac{\partial}{\partial x}(q_s \cos(\alpha)) + \frac{\partial}{\partial y}(q_s \sin(\alpha)) \quad (4.46)$$

where α is the aspect angle (see Neteler and Mitasova, 2002). The smoothing routine uses GRASS GIS module *r.neighbors method=average size=X* (where X is user defined. X is odd and can range from 1 to 25).

4.5.3 Numerical stability

The form of equation (4.41) is

$$\frac{\partial z}{\partial t} = G + \varepsilon_g \nabla^2 z \quad (4.47)$$

in which G is not an explicit function of z :

$$G = -\frac{1}{\rho_b} \vec{\nabla} \cdot q_s \hat{s}_0 \quad (4.48)$$

where

$$q_s = \rho_b q = \rho_b v h \quad (4.49)$$

Without the diffusion term, equation (4.47) is not a conventional initial value advective PDE but rather a boundary value problem: we need not be concerned with meeting time stepping stability criterion (e.g. Courant condition) for G within *r.terrodyn*. However, the diffusive term, implemented in a conventional FTCS (forward time-centered space) scheme (Press et al., 1990) via equation (4.45b), must cohere to the stability criterion:

$$\frac{\varepsilon_g}{(\Delta x)^2} \left(\frac{\Delta t}{\rho_b} \right) \leq 1 \quad (4.50)$$

where ε_g is in [m²/s]. Analytical stability requires that $\varepsilon_g \geq 0$. In our application below, $\Delta t=60$ minutes (~ 3600 s) was chosen to represent one rainfall event (one *r.terrodyn* cycle) and the porosity set to $\lambda=0.5$, such that $\Delta t/\rho_b=2.7$ [m³s/kg]. The grid spacing was $(\Delta x)^2=36$ leading to the stability restriction $0 < \varepsilon_g < 13$. In the applications presented

below, $\varepsilon_g \approx 0.2$ was chosen somewhat arbitrarily, although this value was tuned based on the calibration of model results to observed and/or expected morphology. Generally, the diffusive time scale, τ , is of the order ζ/ε_g^2 , where ζ is the spatial scale of interest (usually, $\zeta \gg \lambda x$) and diffusive evolution becomes noticeable after $\zeta^2/(\lambda x)^2$ time steps (Press et al., 1990). In our case, due to the relatively large $\lambda x (\approx 2m)$, ζ is on the scale of λx , such that as few as 2-10 *r.terrodyn* iterations are required to detect non-negligible diffusive effects. However, small scale features (e.g. numerical ripples) remain intact, though stable, throughout the full span of *r.terrodyn* evolution simulations.

There is no numerical link between the time step size within SIMWE and *r.terrodyn*. However, the parameter space of the band-pass filter (discussed below) and the time step size are inexorably linked - if the time step for *r.terrodyn* is too large resulting in large changes of elevation, the filter will dominate the terrain evolution. Changes in *r.terrodyn* time step size require a re-tuning of the filter parameters to avoid instability or loss of valuable signal.

4.5.4 Boundary conditions

Ideally, the SIMWE and *r.terrodyn* modules are run within a watershed with Dirichlet boundary conditions assumed:

$$f(\vec{r} = \text{boundaries}) = 0 \quad (4.51)$$

for all time steps. Here, f is the variable of interest such as water depth, water discharge, sediment flux, and terrain elevation change. In practice, the boundaries should be defined such that the majority of water and sediment discharged at the outlet of interest originates within the defined region. For example, if SIMWE and *r.terrodyn* are run in the boxed region in figure 4.9, significant runoff and sediment load originating upstream

from the region would not be included. In this case, the total amounts and rates of water and sediment flux into the region would need to be defined at the upstream boundaries. This is a difficult task, requiring manual input of data derived from field measurements or accompanying simulations performed on the excluded regions. As a result, definition of a region (watershed) boundary that eliminates the need for these adjustments is highly recommended. Simulations run within regions adjacent to the region of interest may also shed light on the behavior of the model at the boundaries in which the time-dependent behavior is difficult to predict.

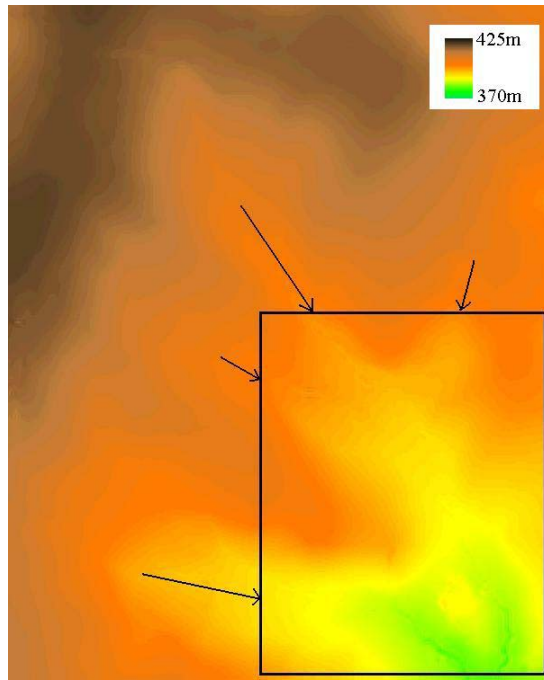


Figure 4.9: Example of a poorly defined region (box) for SIMWE and *r.terradyne* simulations. The arrows indicate zones of high water and sediment flux that would be excluded, unless they are defined at the boundaries manually.

Implementation of module *r.terradyne* required a modification to the boundary handling algorithm provided by GRASS GIS module *r.slope.aspect*. This treatment is outlined in Appendix 4.A.

4.5.5 Use of a comparative band-pass filter for terrain change stability

Because shear stress is proportional to water depth (equation 4.36), in locations in which depth exceeds the effective boundary layer responsible for bed shear stress, erosion continues unimpeded, in some cases to the point in which singularities form. Increased diffusion does not rectify this effect in all cases. This is not a numerical instability but one that is strictly dependent upon the application of shallow water assumptions to deeper water flows. A possible solution would be to limit the depth of water in the stress equations to a maximum threshold. Another would be to redefine the shear stress based on flow velocity as is common in bedload transport formalisms. In the absence of these or other analytical approaches, a band-pass filter was developed to reduce or prohibit the rate of growth of such singularities within the channels. As will be shown, mass conservation was approximately satisfied due to the symmetry of elevation change histograms.

Figure 4.8 illustrates the flowchart for *r.terrodyn* - a feedback network in which the elevation has the potential to grow unchecked. The band-pass filter was introduced to eliminate this potential problem, although localized rippling still occurs. For each iteration, *r.terrodyn* computes a "requested" elevation change based on equation 4.45a. At each location, the filter first computes a "rolling average" (via GRASS GIS module *r.neighbors*) of the pre-existing elevation. It then finds the difference between the requested elevation change with the rolling average and compares it to a threshold, σ [m]. For locations in which the threshold is exceeded, an attenuation scalar, α , is applied to the requested elevation change; for all other locations, no attenuation is performed. The span

of the rolling average, the threshold value, and the attenuation scalar are user-definable within *r.terrodyn*.

The basic concept of this filter is well known in electronics applications; however, here it is not applied in Fourier space, rather to the histogram of discrete requested elevation change "bins". Figure 4.10 illustrates the application of the filter to a symmetric example histogram and the relationship between the control parameters. In this ideal case, mass is conserved due to the symmetry about the mean requested elevation change - the same amount of mass restricted from erosion is also restricted from deposition. The net effect is to "squeeze", or contract, the histogram, increasing the number of raster cells (frequency) requesting small to mid-range elevation change. A quasi-symmetric histogram, as found in *r.terrodyn* applications, would violate mass conservation (given that the threshold is smaller than the range of bins); however, it will be assumed for now that mass is conserved, as illustrated below.

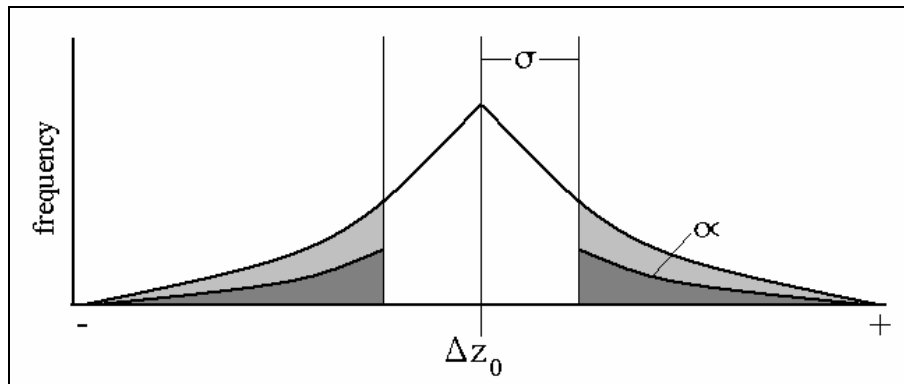


Figure 4.10: The histogram of requested elevation changes for any given raster cell. The x-axis represents the discrete series of bins of requested height change, the y-axis is the frequency (or number of cells) per bin.

To investigate the effects of varying the filter parameters, *r.sim.water* and *r.sim.sediment* were called within *r.terrodyn* with parameters *niter* (*number of iterations*) = 1000 and *nwalker* (*number of walkers*) = 250,000, with spatially uniform transport capacity and detachment coefficients, Manning's n, infiltration, and critical shear. These

were applied to a small sub-region of the Lake Wheeler Road farm watershed at North Carolina State University - 22 rows x 18 columns of raster cells and for a single *r.terrodyn* time cycle. With no bandpass filtering (figs 4.11a, 4.12a, 4.13a), deep incisions were formed within the channel. With σ and α set to zero, the *r.neighbors size* parameter, used to define the span of the average terrain elevation for comparison to local terrain values, was varied from 3 (fig 4.11b) to 5 (fig 4.12b) to 25 (fig 4.13b). As the *r.neighbors size* parameter was increased, the smoothing effect that the filter had on the terrain change (Δz) increased to the point where, with *r.neighbors size*=25, the terrain change features were eliminated. In its simplest form (with $\sigma=\alpha=0$), the filter's effect on Δz is equivalent to the application of the *r.neighbors* smoothing operation only (equivalent to the smoothing operation performed at the end of each *r.terrodyn* cycle).

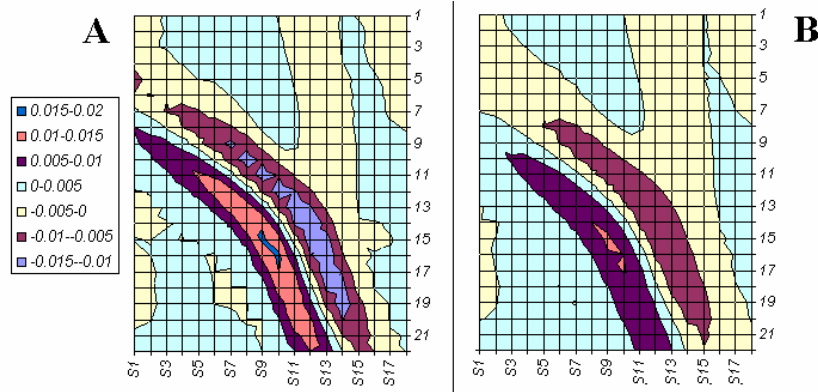


Figure 4.11: Sample of Lake Wheeler Road watershed (A) change in terrain via continuity without filtering or diffusion over one time step; (B) same as (A) but with band-pass filter applied with $\sigma=0m$, $\alpha=0$, and r.neighbors averaging size=3. Elevation legend is in meters.

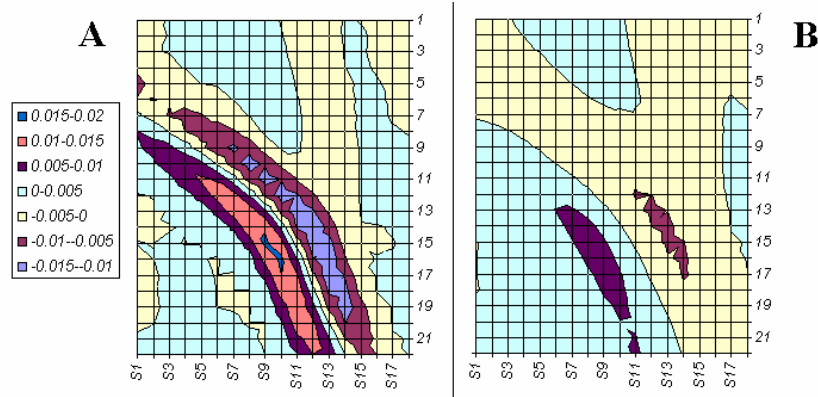


Figure 4.12: Sample of Lake Wheeler Road watershed (A) change in terrain via continuity without filtering or diffusion over one time step; (B) same as (A) but with band-pass filter applied with $\sigma=0m$, $\alpha=0$, and r.neighbors averaging size=5. Elevation legend is in meters.

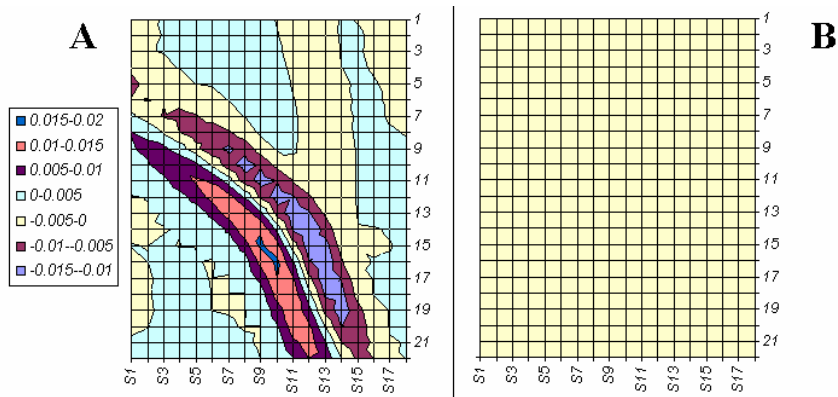


Figure 4.13: Sample of Lake Wheeler Road watershed (A) change in terrain via continuity without filtering or diffusion over one time step; (B) same as (A) but with band-pass filter applied with $\sigma=0m$, $\alpha=0$, and r.neighbors averaging size=25. Elevation legend is in meters.

Identical runs were performed on the Lake Wheeler Road farm watershed at North Carolina State University to test the filter in which the scaling multiplier, α , was set to 0.1 and to 0.5. For each, the threshold value σ was set to 0.01 m, 0.005 m, and 0.001 m. The *r.neighbors size* parameter was set to 25. As seen in figure 4.15 for $\alpha=0.5$, the histogram contracted to a greater extent as σ was decreased. Accordingly, the amplitude of requested elevation change, Δz , also decreased (figure 4.16a-d). The same effect was observed for the runs in which $\alpha=0.1$ (figures 4.17, 4.18). The degree of histogram contraction was greater for the $\alpha=0.1$ runs, especially for smaller cutoff thresholds. In general, the central bins of the histogram grew in response to the filtering, although, for the $\alpha=0.1$ runs, the "reassignment" of the outlying bins was weighted to the outer edges of the contracted histogram. This effect, however, did not appear to affect the performance of the model over future runs.

Ideally, the use of the filter should be minimized; however, if it is necessary, the cutoff threshold value (σ) should be as large as possible to minimize the loss of valuable channel formation information for later cycles. However, the slight loss of resolution may be deemed acceptable if at higher iterations singularities emerge. In general, large-scale features that develop from small perturbations remain free to develop, as long as they do not change too quickly within the time frame of an *r.terrodyn* cycle. The parameter space of the band-pass filter and the time step size are inexorably linked - if the time step for *r.terrodyn* is too large resulting in large changes of elevation, the filter will dominate the terrain evolution. Changes in *r.terrodyn* time step size require a re-tuning of the filter parameters to avoid instability or loss of valuable signal.

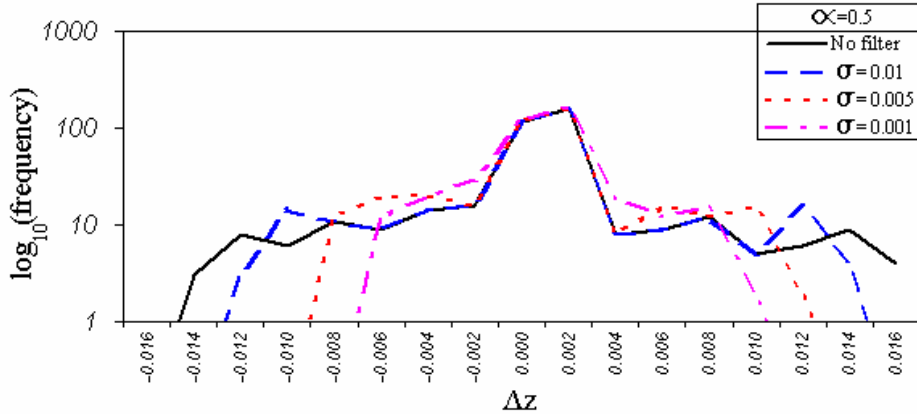


Figure 4.14: A comparison of histograms for the same Lake Wheeler watershed section as in figure 4.11. The band-pass filter is applied with *r.neighbors* averaging size=25 and $\alpha=0.5$. σ values of 0.01m, 0.005m, and 0.001m are shown with the unfiltered histogram.

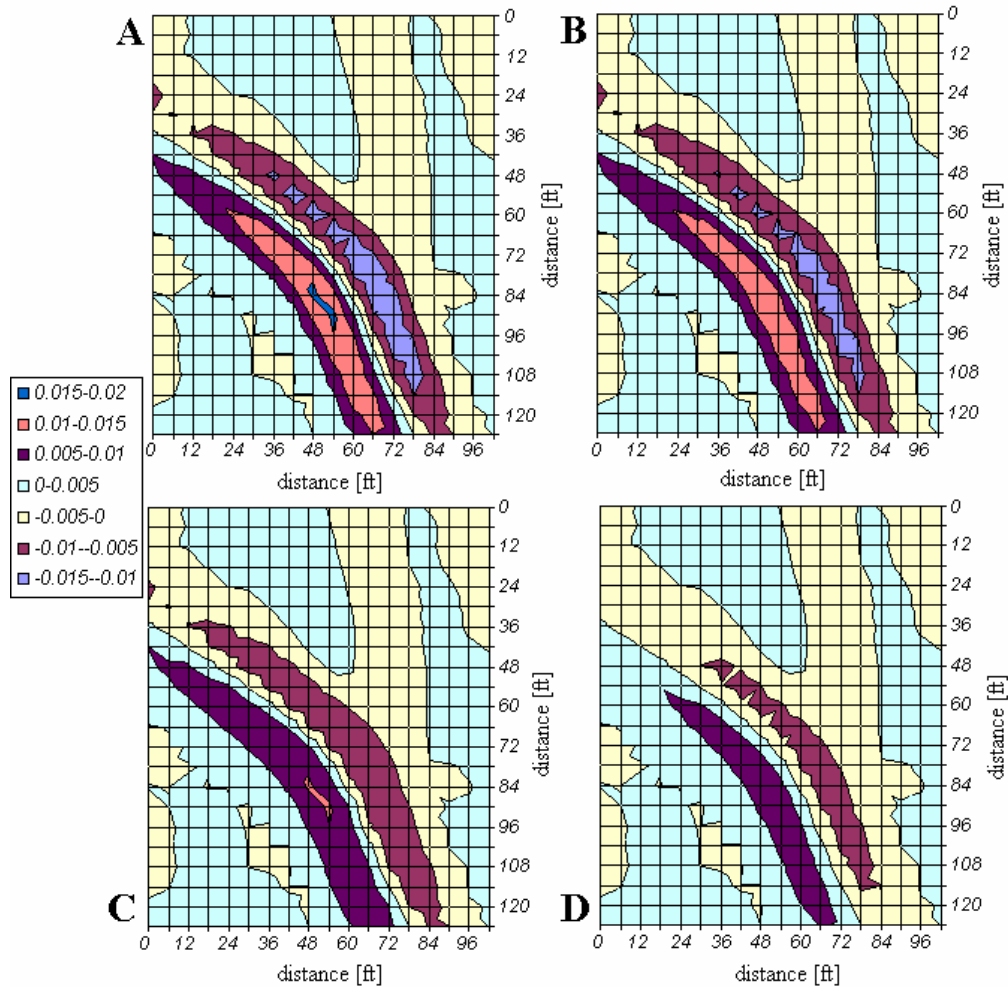


Figure 4.15: Application of the band-pass filter corresponding to figure 4.14 with *r.neighbors* averaging size=25 and $\alpha=0.5$. (A) original unfiltered terrain change with no diffusion for one time iteration (B) with $\sigma=0.01\text{m}$, (C) $\sigma=0.005\text{m}$, (D) $\sigma=0.001\text{m}$. Elevation legend is in meters.

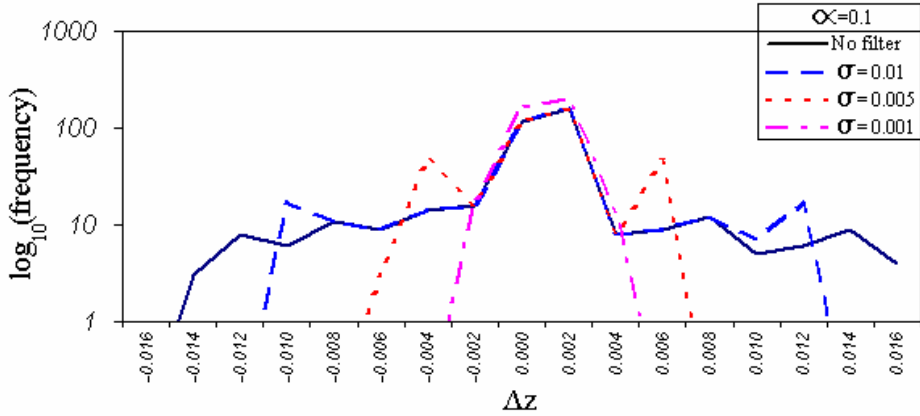


Figure 4.16: A comparison of histograms for the same Lake Wheeler watershed section as in figure 4.11. The band-pass filter is applied with *r.neighbors* averaging size=25 and $\alpha=0.1$. σ values of 0.01m, 0.005m, and 0.001m are shown with the unfiltered histogram.

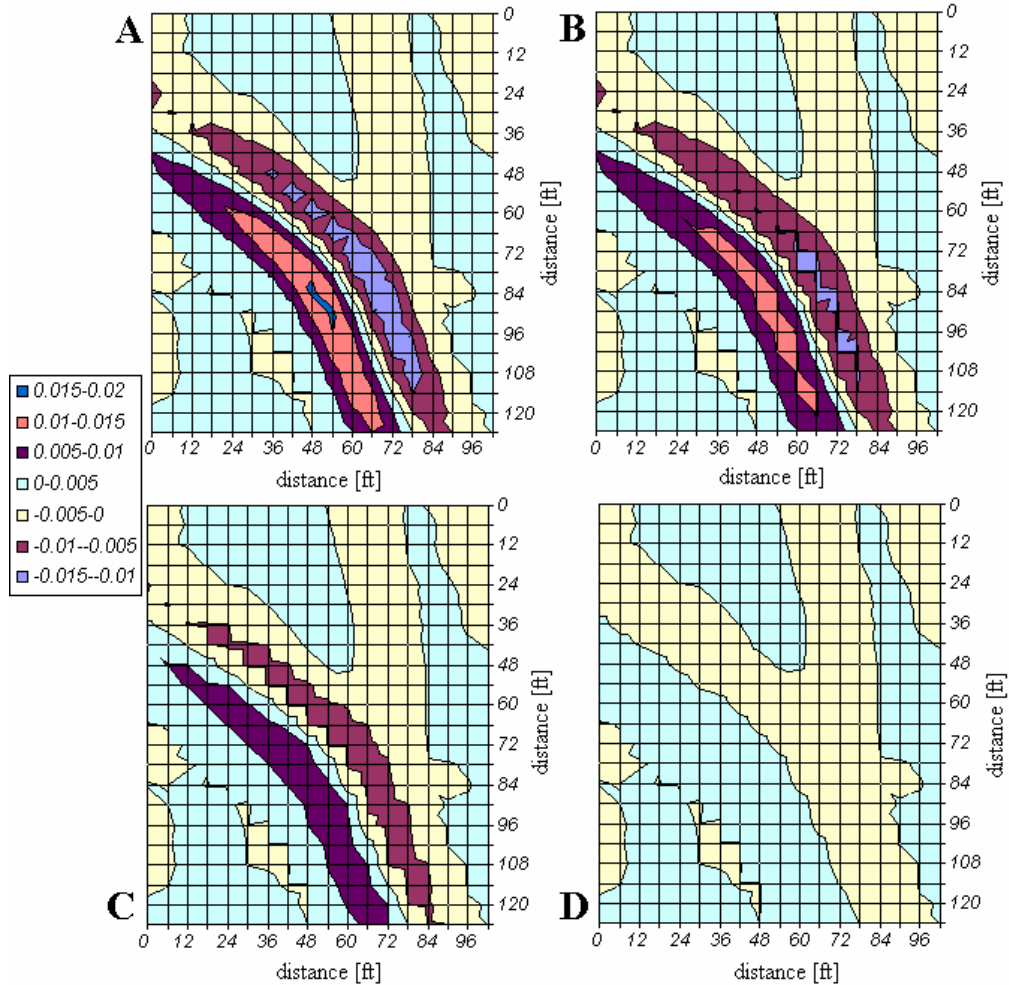


Figure 4.17: Application of the band-pass filter corresponding to figure 4.16 with *r.neighbors* averaging size=25 and $\alpha=0.1$. (A) original unfiltered terrain change with no diffusion for one time iteration (B) with $\sigma=0.01$ m, (c) $\sigma=0.005$ m, (D) $\sigma=0.001$ m. Elevation legend is in meters.

4.5.6 *r.terrodyn* Input parameters

Input parameters for SIMWE and *r.terrodyn* include spatially uniform and distributed values. The distributed values include infiltration (rainfall excess), manning's roughness, critical shear stress, the transport capacity coefficient, and the detachment capacity coefficient, although these can be specified as spatially uniform. These are based on land cover and associated properties. Spatially uniform parameters include the band-pass filter control inputs, gravitational diffusivity, rainfall rate, and the *r,sim.water* hydrodynamic diffusion and diffusion correction coefficients. Rainfall amounts can be specified from field measured data, given as a constant value for each *r.terrodyn* iteration, or randomized for each iteration.

4.5.5.1 Random Rainfall

Actual rainfall amounts and durations within a watershed over time spans on the order of one year can vary dramatically. To model this effect in the absence of actual rainfall data, rainfall as input to *r.sim.water* is varied about a mean value via a random number generator such that, for each *r.terrodyn* iteration, the rainfall rate can range from 0 - to - 2 times the mean value. The rainfall rate, R_i [m/s], for iteration i is thus:

$$R_i = \Re(7.0556 \times 10^{-6} r); \quad 0 \leq R_i \leq 2 \cdot (7.0556 \times 10^{-6} r) \quad (4.52)$$

where r is the median rainfall rate [inches/hour] and \Re is the randomization operator. The random number generator runs as a shell script by calling the Linux 9.0 special character file */dev/urandom*. For future reference, a rainfall log is created for each *r.terrodyn* run, **.rain.log*, which is stored into the current active directory. Numerically,

a variable rainfall amount dampens systemic instabilities that may develop independent of the numerical methods used to model the governing differential equations.

4.5.5.2 Rainfall excess

Rainfall excess, the source input to the hydrological continuity equation (4.28), is defined as the difference between rainfall and infiltration rates [m/s]:

$$i_e(\vec{r}, t) = R - I(\vec{r}, t) \quad (4.53)$$

Instead of computing i_e based on actual infiltration values, the rainfall excess is computed from the excess rainfall runoff using the curve number method. The accumulated precipitation per square millimeter, P_i [mm], for iteration i is:

$$P_i = 1000R_i D_i \quad (4.54)$$

where D_i [s] is the duration of the rainfall event. The commonly used accumulated runoff volume (e.g. Haan, et al., 1994) per square millimeter, Q_i [mm], is:

$$Q_i = \frac{(P_i - 0.2S_i)^2}{(P_i + 0.8S_i)}; \quad P_i > 0.2S_i \quad (4.55)$$

where S_i is sometimes called the *maximum soil water retention parameter*, given as:

$$S_i = \frac{25400}{CN} - 254 \quad Q_i, S_i, P_i \text{ in mm.} \quad (4.56)$$

where CN is the *curve number* (Soil Conservation Service, 1986). Note that a minimum rainfall rate is required to produce runoff, as specified via $P_i > 0.2S_i$: for very absorbent and highly resistive land cover, the rainfall rates required to produce runoff may exceed 1 inch per hour. The rainfall excess, i_e [m/s] is recovered as:

$$i_e = \frac{Q_i}{1000D_i} \quad (4.57)$$

which is used directly as input to *r.sim.water* as the *rainin* parameter (*infil* is set to 0.0).

Curve numbers for antecedent conditions (from Chow et al., 1988) are *CN(I)*, which refers to little rainfall preceding, and *CN(III)*, corresponding to considerable rainfall prior to the current rainfall event. *CN(II)*, the nominal values of taken from rainfall and runoff data, are used to derive *CN(I)* and *CN(III)*:

$$CN(I) = \frac{4.2CN(II)}{10 - 0.058CN(II)} \quad (4.58)$$

$$CN(III) = \frac{23CN(II)}{10 + 0.13CN(II)} \quad (4.59)$$

Equation (4.56) and therefore equation (4.55) take on a range of values depending upon the antecedent conditions for *CN*. The module *r.terrodyn* is designed such that rainfall duration and antecedent conditions can vary with iteration.

4.6 Application of *r.terrodyn* - Lake Wheeler Road Watershed

The Lake Wheeler Road farm complex at North Carolina State University was used as an experimental watershed for development and verification of *r.terrodyn*. The facility is comprised mostly of open fields and row crops, with thin woods scattered throughout, as well as roads and buildings at various locations (figure 4.18). The DEM was obtained from field surveys at 2m x 2m (x-y grid) resolution. Simulations were performed on a sub-watershed (boxed region in figure 4.18) of roughly 200 x 200 grid cells in size (~33 acres). The southeast corner of the study region is bounded by roads which are elevated ~1.5m relative to the watershed DEM in that area. GRASS GIS 5.03 and 5.3 versions were run on Linux workstations running Redhat™ 9.0. The 3-D images were generated via GRASS GIS module *nviz* with an elevation exaggeration of 3.0 to 4.0.

The *r.terrodyn* module called *r.sim.water* and *r.sim.sediment* with *niter=1000* (the number of SIMWE iteration) and *nwalkers=1000000* (the number of SIMWE walkers), *diffc=0.3* (the SIMWE water diffusion coefficient) and *halpha=10* (the SIMWE diffusion correction term). The number of walkers used in these simulations produced the accuracy necessary for terrain evolution at the chosen grid resolution and the number of iterations allowed for water flow and sediment flux equilibrium. The band pass filter parameters were set to $\sigma=0.01$, $\alpha=0.1$, and *r.neighbors size* (averaging span)=25. With $\sigma=0.01$, it was assumed that the corresponding maximum allowable elevation change (10 mm) per iteration would not noticeably effect the long term net terrain evolution results within the parameter spaces simulated. The gravitational diffusion term, ε_g , was set to 0.2 - this value was chosen based on stability criterion and was observed to produce results that most accurately modeled expected terrain change.

The duration of each rainfall event was set to $\Delta t=60$ minutes, the sediment density 2650 kg/m³, and the porosity was $\lambda=0.5$ such that $\Delta t/\rho_b=2.7$ [m³s/kg]. Artificial smoothing was applied only for display of the net erosion / deposition (*erdep*) raster files produced by *r.sim.sediment* (*r.neighbors method=average size=3*). Simulations were run out to 30 iterations (~2 years). Randomized rainfall about a mean of 1.0E-5 was employed for all simulations unless otherwise noted - rainfall logs are shown as a time series imbedded in the elevation DEM results from each run (e.g. fig. 4.21). Unless otherwise indicated, all results presented conform to the master color keys in figure 4.19 (A) elevation change [m], (B) water depth [m], (C) sediment flux [kg/m/s], (D) water discharge [m³/s], and (E) erosion / deposition rate [kg/m²/s] from SIMWE.

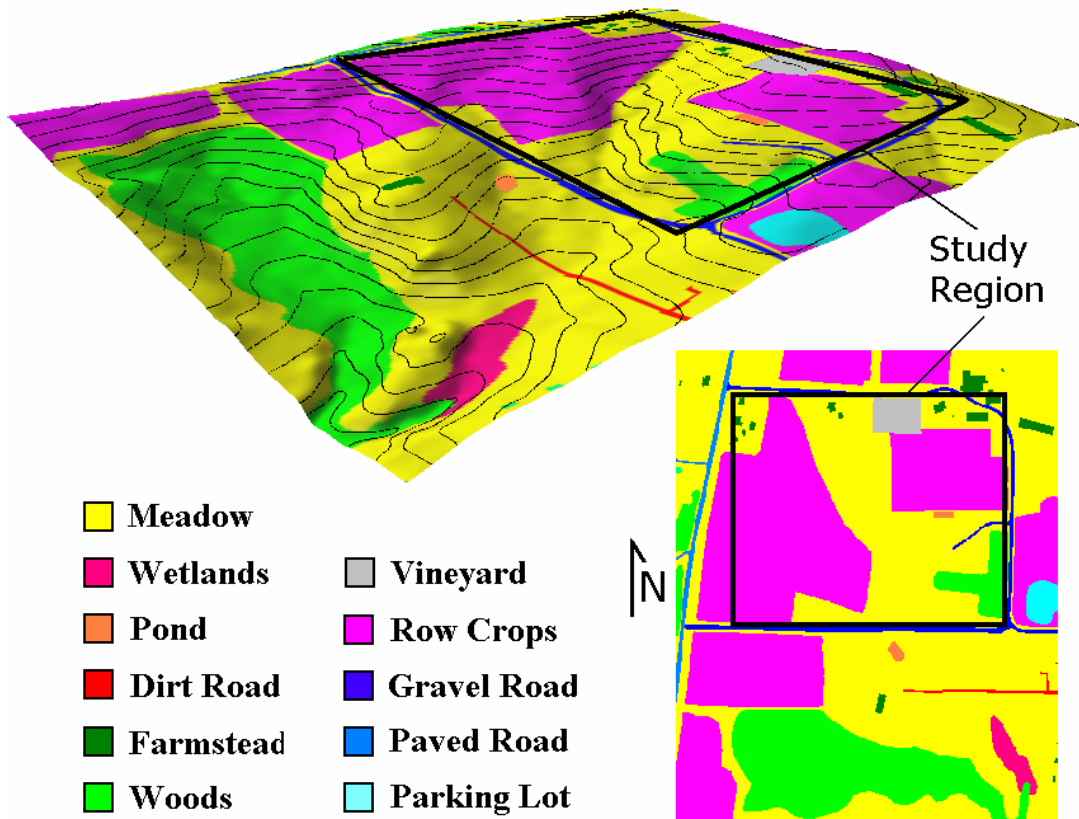


Figure 4.18: The Lake Wheeler Road farm watershed at NC State University. Land cover is indicated by the color key. Simulations were performed on the sub-region indicated by the box.

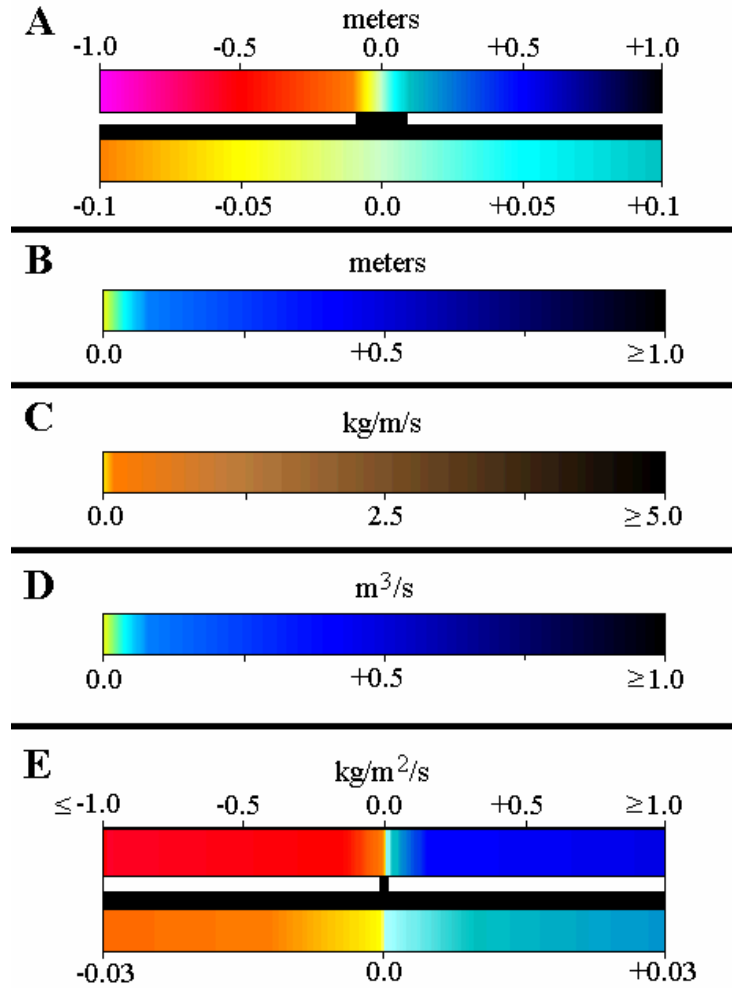


Figure 4.19: The master color keys for all results presented (unless otherwise indicated): (A) elevation change [m], (B) water depth [m], (C) sediment flux [kg/m/s], (D) water discharge [m^3/s], and (E) erosion/deposition rate [$\text{kg}/\text{m}^2/\text{s}$] from SIMWE (erdep).

4.6.1 Baseline

The original DEM corresponding to the study region (see figure 4.18) is shown in figure 4.20, with contour lines at 5 m intervals. Geographic North is aimed toward the top-right of the image and the image is lit from a source located on the left (Southwest) such that shadows fall Northeast. Figure 4.21 shows the modified DEM overlaid by the colors representing net elevation change after 30 iterations of *r.terrodyn* with the spatially uniform parameters defined as: Manning's $n=0.5$, $K_t=0.001$, $K_d=0.001$, $\sigma=1.0$, $\tau_c=0.01$,

rainfall infiltration=0.0. Rainfall was randomized and is displayed as a time-series log over 30 rainfall events in figure 4.21.

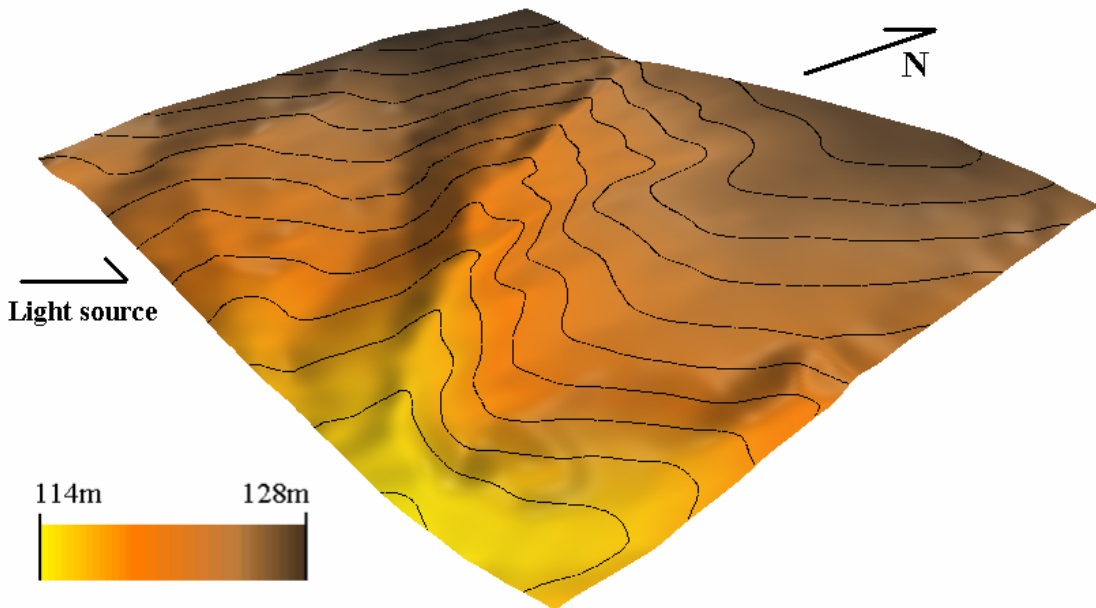


Figure 4.20: The DEM of the sub-watershed outlined in figure 4.19. The contour lines are at 5ft increments.

For this simulation, primary terrain changes included the erosion of the steepest hill slopes and of the channel banks, as well as deposition in areas of upward concavity and within the main channels along the bottom of the hillslopes where transport capacity was reduced. Competition between channel incision and deposition produced small scale braiding and meandering of flow paths within the channels (Fig. 4.21-A). The net elevation changes generally matched the patterns of erosion and deposition predicted by the SIMWE output raster file *erdep*, although the divergence of the sediment flux, not the *erdep* file, was used to govern terrain modification. These results are used for comparison to the distributed land cover, distributed infiltration, and the grain size dependent results presented below.

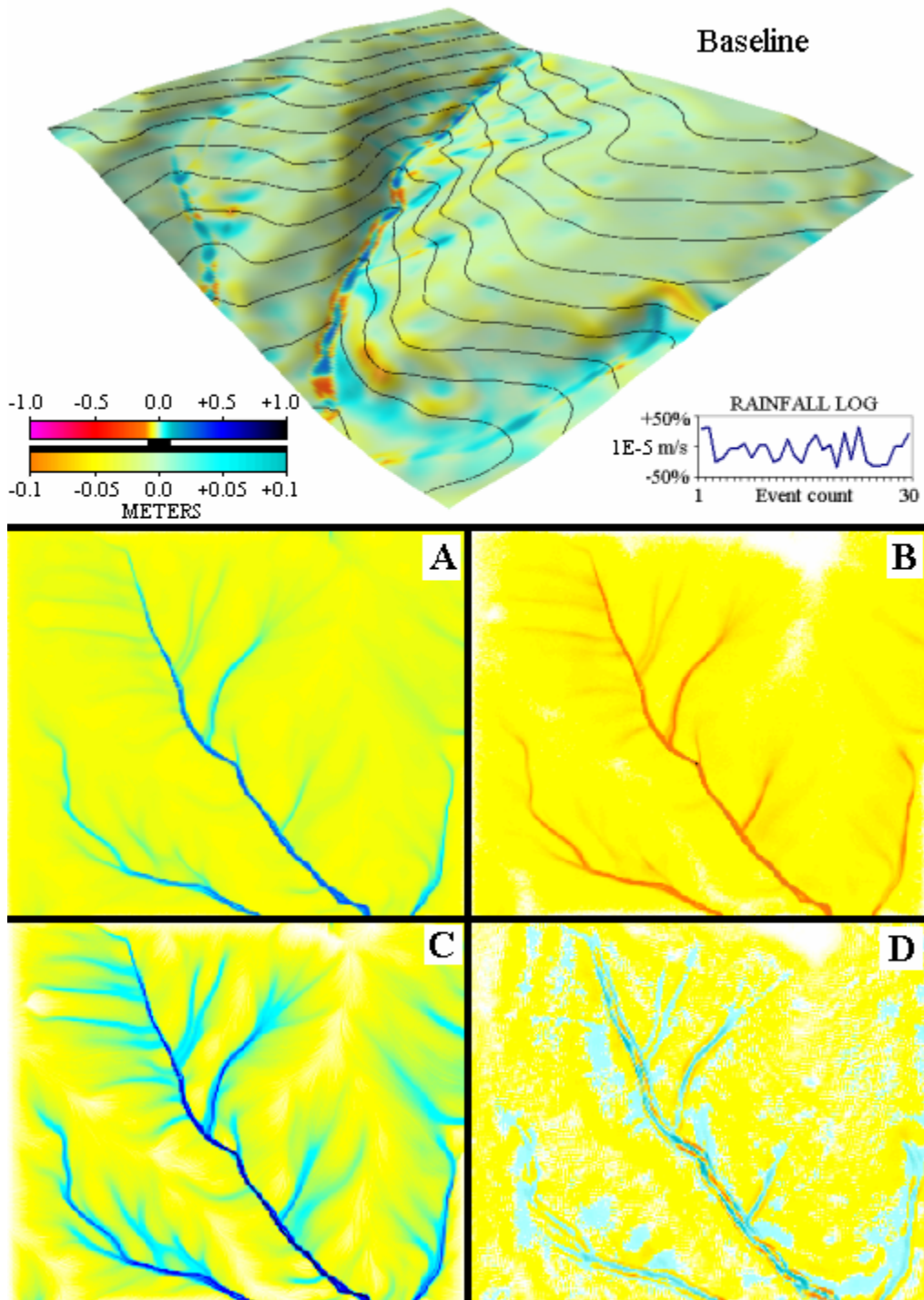


Figure 4.21: The modified DEM of the Lake Wheeler sub-watershed after 30 r.terrodyn iterations with uniform land cover and infiltration. Also included are the (A) water depth [m], (B) sediment flux [$\text{kg}/\text{m}^2/\text{s}$], (C) flow discharge [m^3/s], and (D) erosion / deposition pattern (smoothed) [$\text{kg}/\text{m}^2/\text{s}$] from r.sim.sediment (not used by r.terrodyn) at iteration #30 in which the rainfall was $1.2\text{E}-5 \text{ m/s}$.

Photographs were taken of the Lake Wheeler Road farm just following a rainfall event of 1.07 inches/hour on July 29, 2003 as recorded by the State Climate Office of North Carolina (<http://www.nc-climate.ncsu.edu>), at the location indicated (figure 4.22). The water that was confined to channel flow was approximately 0.3m deep in agreement with predicted steady state water depths from *r.terrodyn*.

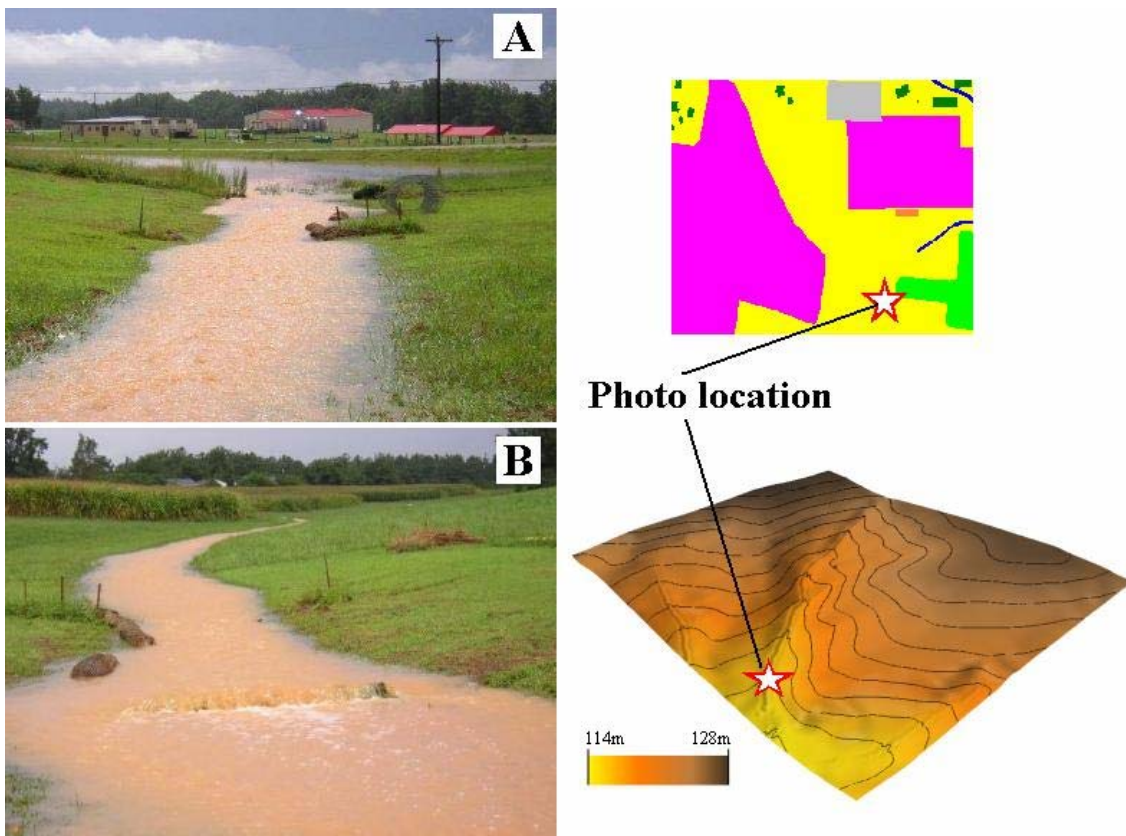


Figure 4.22: Photographs of the study region during a rain event. Photos were taken at the location in the study region indicated by the star in the topographical reference maps. Perspectives are (A) downhill toward the region of net sediment deposition and (B) uphill toward the channel incision.

4.6.2 Results from distributed infiltration

For runoff calculation, curve numbers (CNII, from Haan, et al., 1994, Appendix 3C) were used for the land cover present on the Lake Wheeler road farm as defined in table 4.2 and figure 4.23. To achieve maximum difference in runoff conditions, only soil

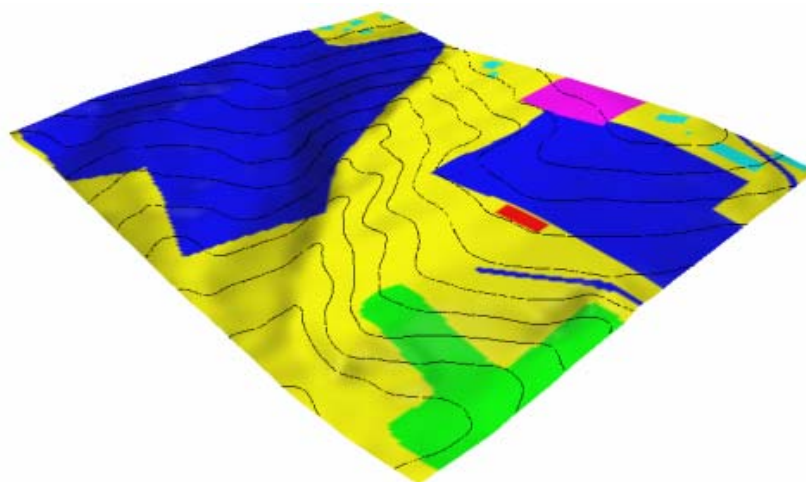
types A and D were used (see table 4.3). The curve numbers for antecedent conditions (CNI and CNIII) in table 4.2 were obtained via equations (4.59) and (4.60) from section 4.5.5.2.

Table 4.2: Land cover and curve numbers for the Lake Wheeler Road farm.

ID	Cover	Soil type A			Soil type D		
		CNI	CNII	CNIII	CNI	CNII	CNIII
0	Meadow	15	30	50	60	78	89
1	Pond	95	98	99	95	98	99
2	Woods	15 [†]	30 [†]	50 [†]	67 ^{††}	83 ^{††}	92 ^{††}
3	Farm buildings	37	59	77	72	86	93
4	Parking Lot	95	98	99	95	98	99
5	Paved road	67	83	92	85	93	97
6	Gravel road	57	76	88	81	91	96
7	Vineyard	58	77	89	87	94	97
8	Row crop	46 [†]	67 [†]	82 [†]	81 ^{††}	91 ^{††}	96 ^{††}
9	Wetlands	95	98	99	95	98	99
10	Dirt road	52	72	85	77	89	95

[†] Good cover conditions: Woods- litter, small brush and trees intact; Row crops- with conservation treatments.

^{††} Poor cover conditions: Woods- litter, small brush and trees destroyed by heavy grazing or regular burning; Row crops- without conservation treatments.



	CNI-A	CNII-D	CNIII-D
■	95	98	99
■	58	94	97
■	46*	91	96
■	37	86	93
■	15	83	92
■	15	78	89

* Gravel road has a CNI-A value of 57

Figure 4.23: The infiltration conditions simulated for the Lake Wheeler sub-watershed.

Table 4.3: Soil textures (from Haan, et al., 1994)

HSG	Soil Texture
A	Sand, loamy sand, or sandy loam
B	Silt loam or loam
C	Sandy clay loam
D	Clay loam, silty clay loam, sandy clay, silty clay, or clay

Figures 4.24, 4.25, and 4.26 illustrate the modified DEM overlaid by the colors representing net elevation change, with (A) water depth, (B) sediment flux, (C) discharge, and (D) SIMWE erosion / deposition patterns corresponding to the soil infiltration antecedent conditions of CNI soil type A (CNII-A), CNII soil type D (CNII-D), and CNIII soil type D (CNIII-D), respectively. For the curve numbers CNI-A (fig. 4.24), very little terrain modification was detected due to the high infiltration rates associated with the sandy soil type and with the dry antecedent conditions. The highly absorbent, dry soil did not yield significant runoff - the only runoff for the CNI-A runs came as overflow from a small pond (fig. 4.24-A) and the vineyard which produced minimal sediment flux (fig. 4.24-B). More substantial erosion of steep slopes and channel banks as well as deposition in areas of reduced transport capacity occurred for the CNII-D (fig. 4.25) and the CNIII-D runs (figs. 4.26). As expected, the flow depths increased for increased curve numbers and reduced soil permeability. Flux patterns generally follow the water depth patterns. The sediment flux for the CNIII-D antecedent condition is the largest of all conditions tested due to the larger water depths

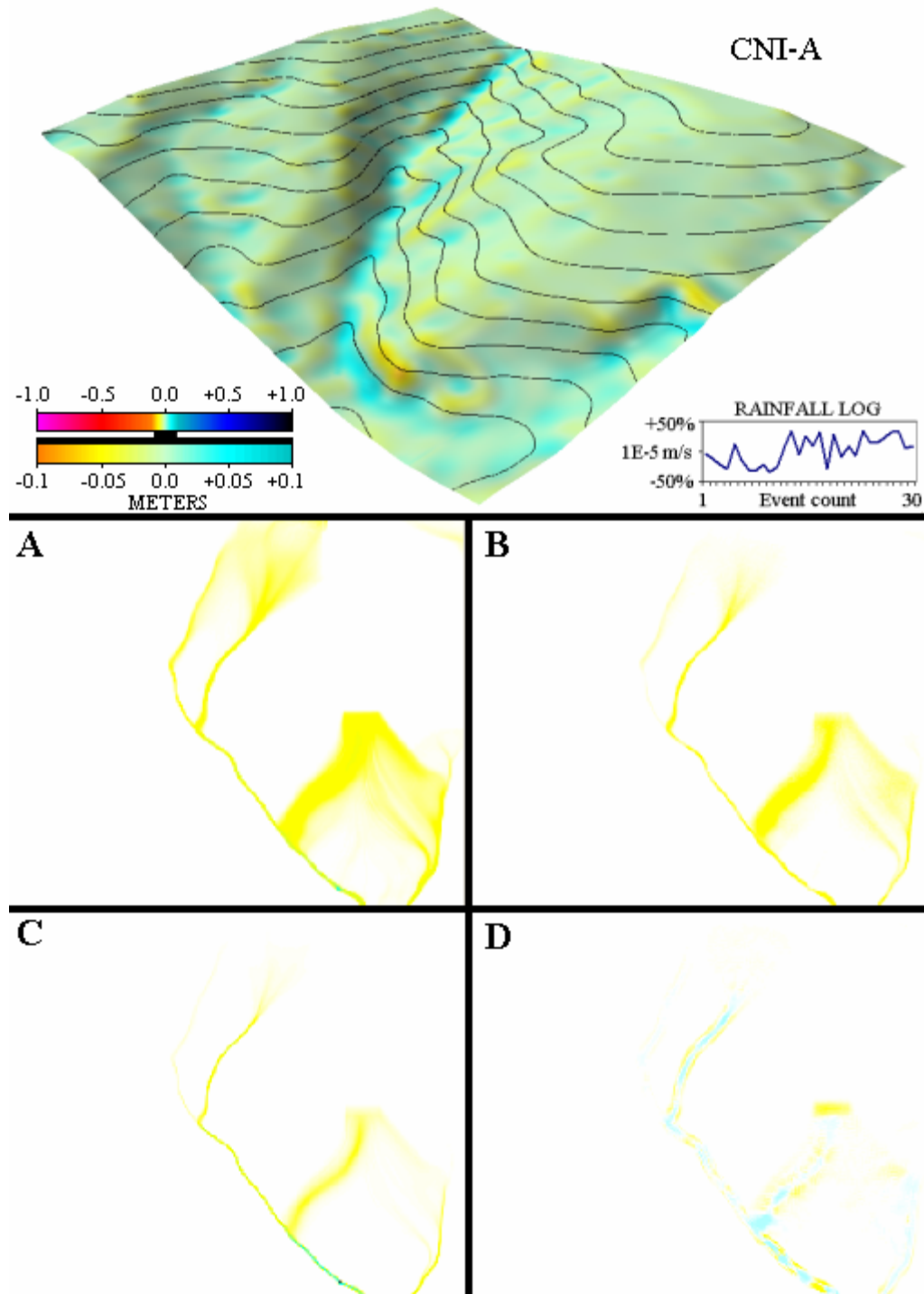


Figure 4.24: The modified DEM of the Lake Wheeler sub-watershed after 30 r.terrodyn iterations with CNI-A infiltration conditions. Also included are the (A) water depth [m], (B) sediment flux [$\text{kg}/\text{m}^2/\text{s}$], (C) flow discharge [m^3/s], and (D) erosion / deposition pattern (smoothed) [$\text{kg}/\text{m}^2/\text{s}$] from r.sim.sediment (not used by r.terrodyn) at iteration #27 in which the rainfall was $1.4\text{E}-5 \text{ m/s}$.

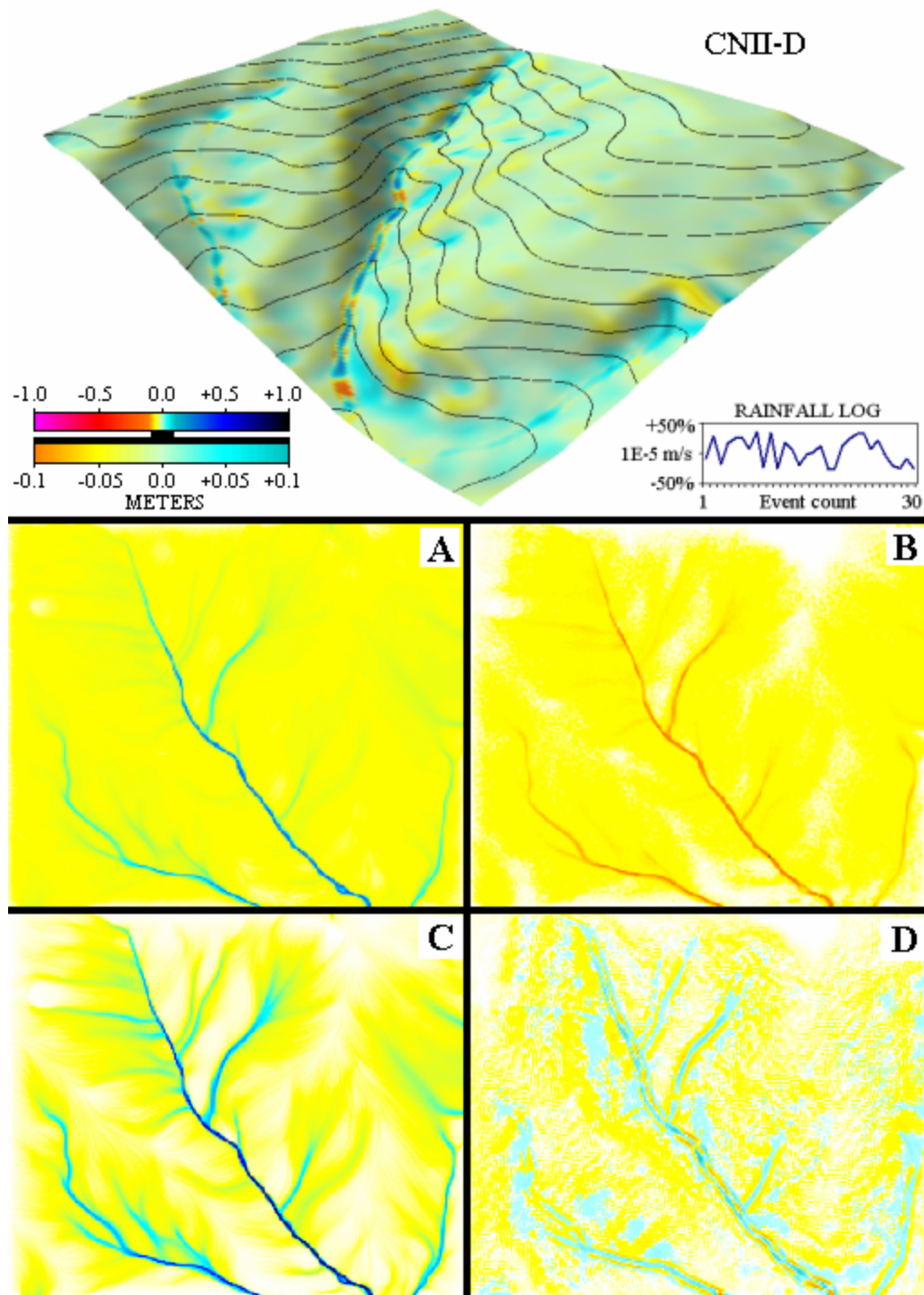


Figure 4.25: The modified DEM of the Lake Wheeler sub-watershed after 30 r.terrodyn iterations with CNII-D infiltration conditions. Also included are the (A) water depth [m], (B) sediment flux [kg/m/s], (C) flow discharge [m^3/s], and (D) erosion / deposition pattern (smoothed) [kg/ m^2/s] from r.sim.sediment (not used by r.terrodyn) at iteration #25, in which the rainfall was 1.2E-5 m/s.

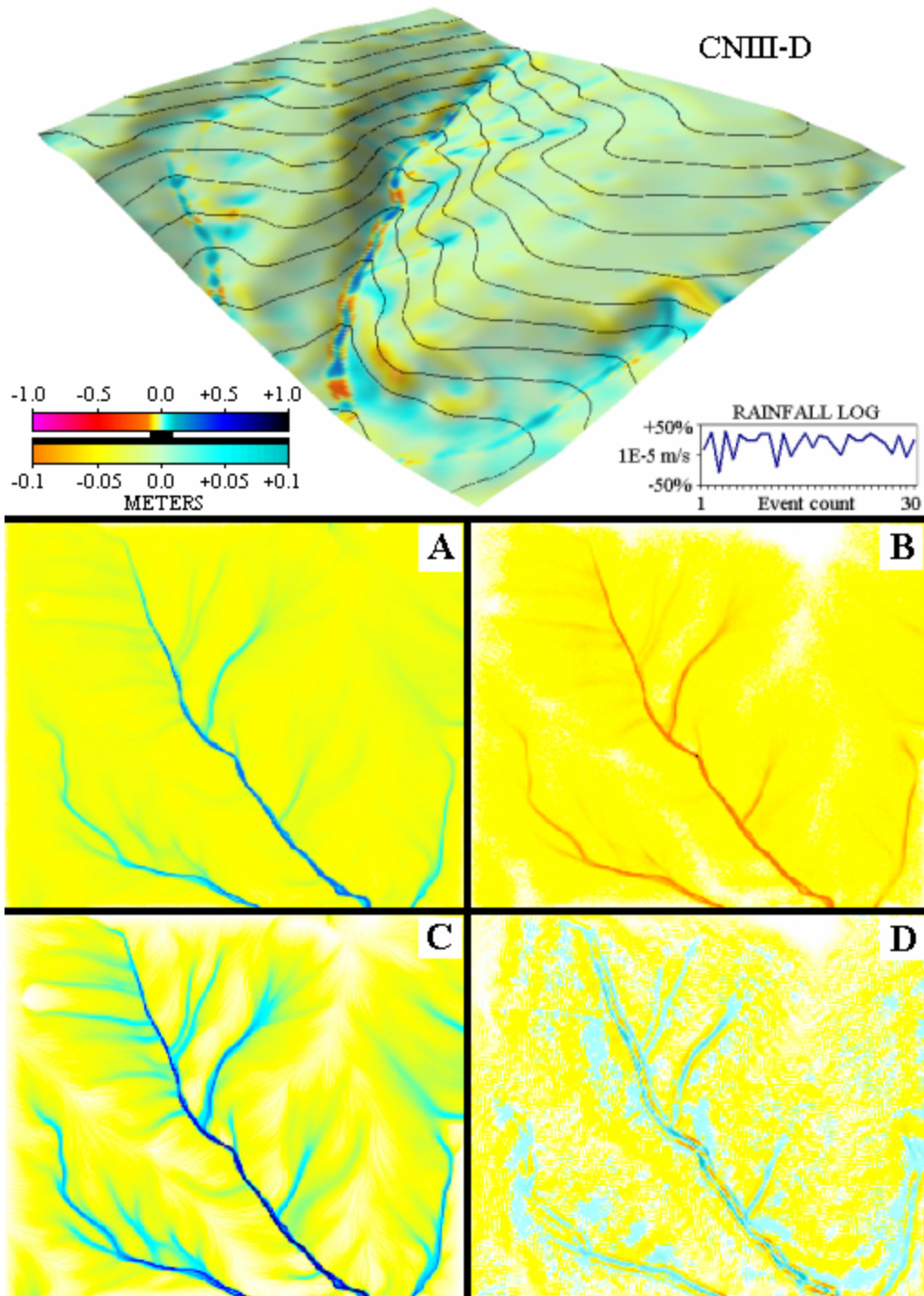


Figure 4.26: The modified DEM of the Lake Wheeler sub-watershed after 30 r.terrodyn iterations with CNIII-D infiltration conditions. Also included are the (A) water depth [m], (B) sediment flux [kg/m/s], (C) flow discharge [m^3/s], and (D) erosion / deposition pattern (smoothed) [$\text{kg}/\text{m}^2/\text{s}$] from r.sim.sediment (not used by r.terrodyn) at iteration #30, in which the rainfall was $1.3\text{E}-5 \text{ m/s}$.

4.6.3 Results from distributed land cover

A set of simulations was performed with the same setup as the baseline runs and with the CNII-D infiltration conditions; however, here the input parameters Manning's n , K_d , K_t , and τ_c were distributed values (see figure 4.27). These values (table 4.4) were obtained from previous runs on similar watersheds on the North Carolina State University campus (see: <http://skagit.meas.ncsu.edu/~helena>).

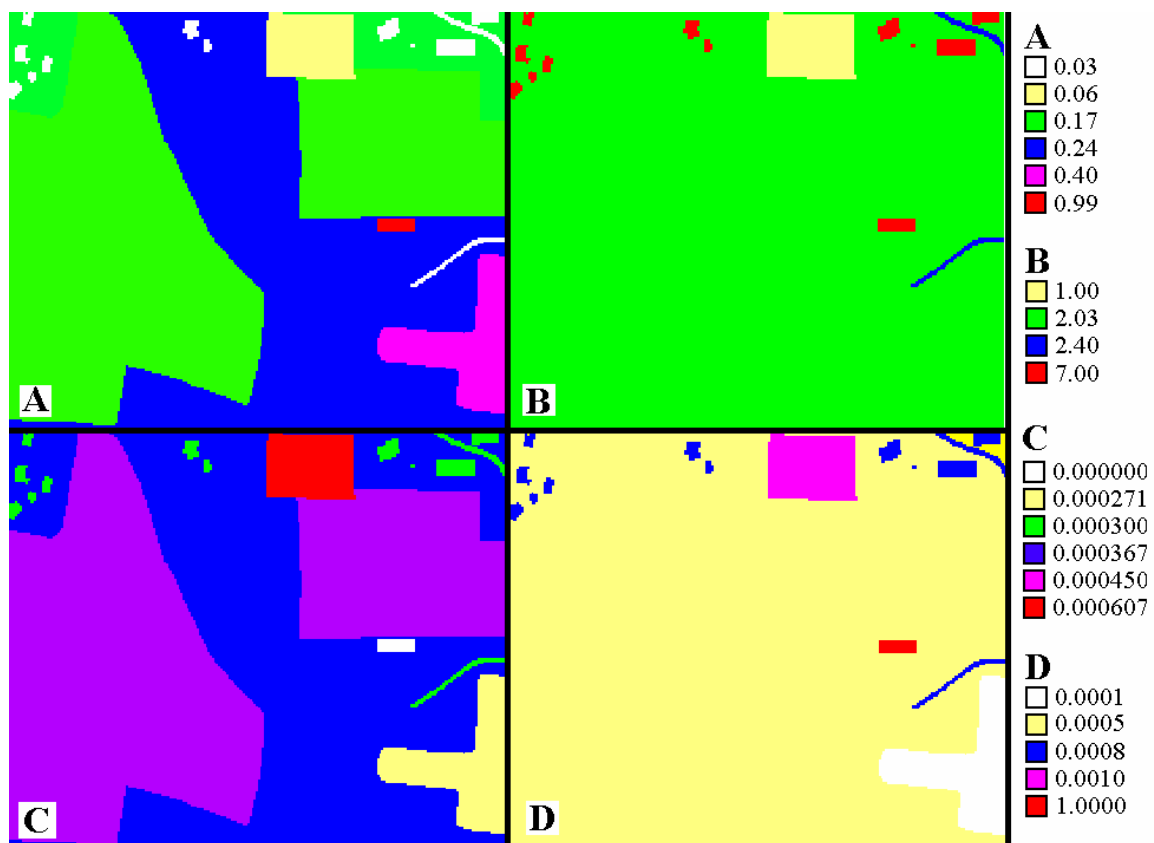


Figure 4.27: The distributed land cover parameters (A) Manning's n , (B) critical shear, (C) K_d , (D) K_t .

Table 4.4: Cover and soil parameters used in the distributed simulations.

ID	Cover	n	K _t	K _d	τ _c
0	Meadow	0.24	0.0005	0.000367	2.03
1	Pond	0.99	1.0000	0.000000	7.00
2	Woods	0.40	0.0001	0.000271	2.03
3	Homestead	0.03	0.0008	0.000300	7.00
4	Parking lot (gravel)	0.03	0.0008	0.000300	2.40
5	Paved road	0.01	1.0000	0.000000	7.00
6	Gravel road	0.03	0.0008	0.000300	2.40
7	Vineyard (bare soil)	0.06	0.0010	0.000607	1.00
8	Row crops	0.17	0.0005	0.000450	2.03
9	Wetlands	0.99	1.0000	0.000000	7.00
10	Dirt road	0.03	0.0008	0.000300	2.40

Figure 4.28 shows the modified DEM after 30 *r.terrodyn* iterations overlaid by the colors representing net elevation change as well as the water depth, sediment flux, discharge, and SIMWE erosion / deposition patterns. Comparison to the CDII-D runs (fig. 4.25) shows that, in general, water depth, discharge, and sediment flux were reduced with the land cover. These results suggest that the existence of extensive land cover diminishes the sediment transport and discharge from the watershed, as well as the net terrain change.

To further investigate the terrain changes with land cover, the simulations were repeated but with a median rainfall rate that was 2x that of the original distributed land cover simulations. The results for the terrain change are summarized in figure 4.29. Notably, the woods in the south-east corner of the sub-region (bottom-right of image) accrued significant sediment due to the imposed reduction in transport capacity of the land cover. This effect has been observed in the field and illustrates the potential for damaging sediment accumulation (and elevation increase) in vegetal zones designed for sedimentation control.

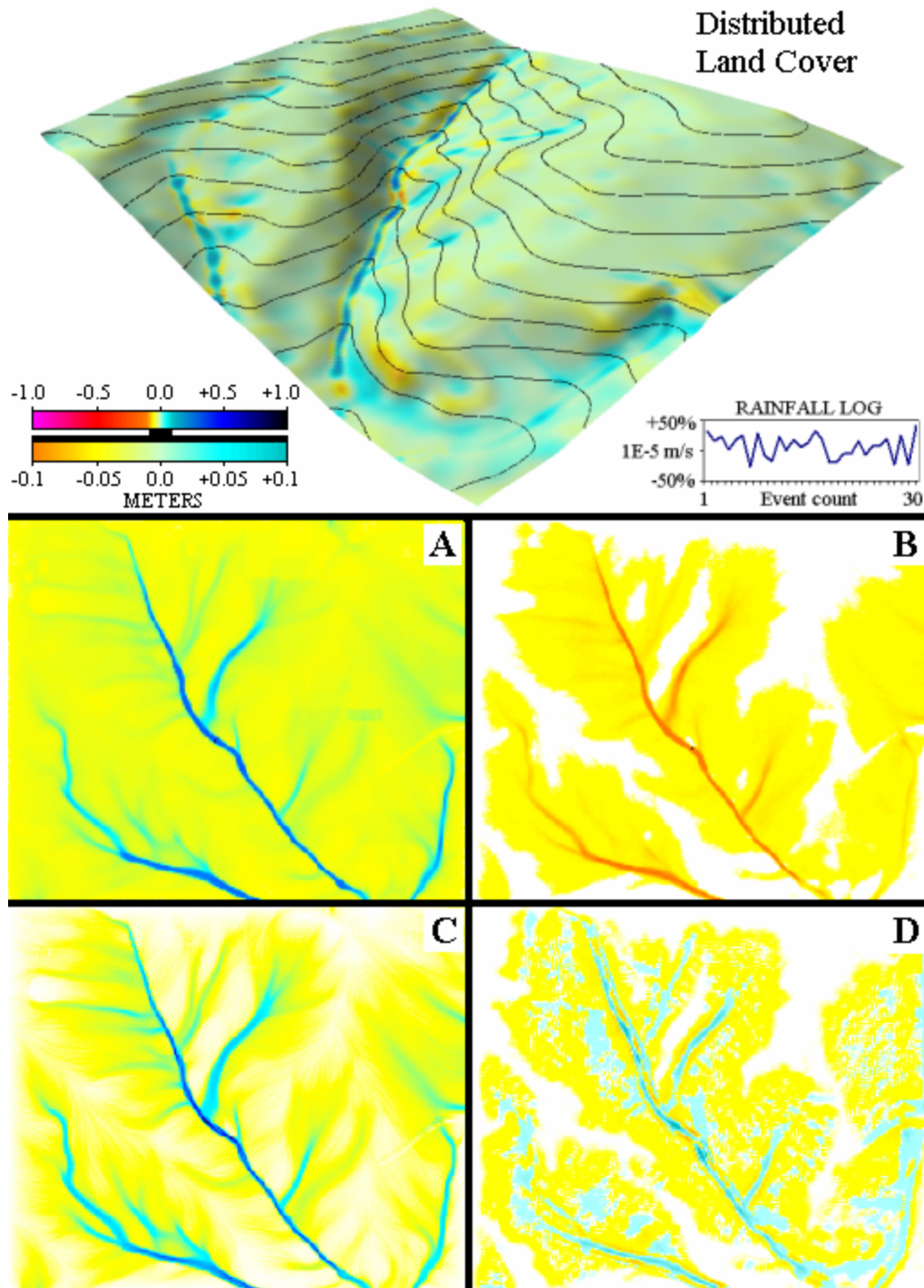


Figure 4.28: The modified DEM of the Lake Wheeler sub-watershed after 30 r.terrodyn iterations with distributed land cover per table 4.4 with CNII-D distributed infiltration. Also included are the (A) water depth [m], (B) sediment flux [kg/m/s], (C) flow discharge [m^3/s], and (D) erosion / deposition pattern (smoothed) [$kg/m^2/s$] from r.sim.sediment (not used by r.terrodyn) at iteration #29, in which the rainfall was $1.3E-5$ m/s.

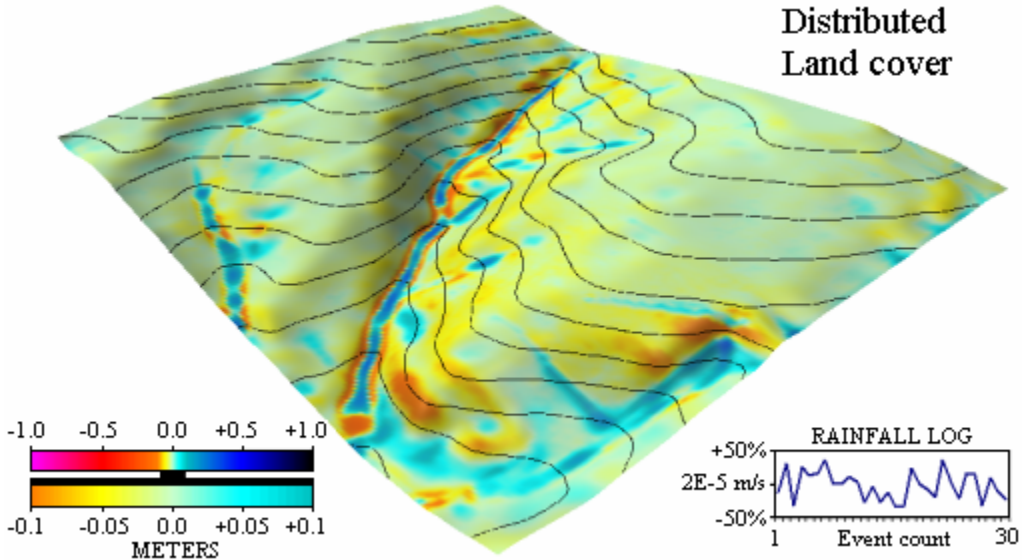


Figure 4.29: The modified DEM of the Lake Wheeler sub-watershed after 30 r.terrodyn iterations with distributed land cover per table 4.4 and distributed infiltration values for CNII-D. The rainfall rate was twice the rainfall rate of figure 4.28 which produced a substantial elevation increase in the wooded area (bottom right).

4.6.4 Grain size dependent simulations

In the following suite of simulations, it is assumed that the land cover consists of bare soil. A spatially uniform Manning's n was set to 0.05 and the runoff rate was equated with the rainfall rate (infiltration rate = 0.0).

4.6.4.1 Investigations of soil erodibility

A set of simulations was performed to investigate the relative effect of varying the detachment capacity (erodibility) coefficient, K_d . While K_t remained constant at 0.1 and the critical shear at 0.01, K_d was adjusted such that σ was defined for each soil type according to the values in table 4.5 for clay, silt, sand, small aggregates, and large aggregates (SEDATE model, described above, employed these methods). Because K_t may widely vary over soil grain diameter, these parameter definitions were not intended

to model the behavior of actual soil. The assignment of the soil type names to the different values of K_d are simply for bookkeeping purposes for this set of simulations.

Table 4.5: Typical sediment characteristics for Midwestern soil from Young, et. al. (1978) and Foster (1982). Also used by AnnAGNPS.

Soil type	Specific gravity	Size [microns]	V_f [mm/s]	$\sigma = D_c / T_c$ [1/m]
Clay	2.65	2	0.00311	0.0089
Silt	2.60	10	0.0799	0.074
Sand	2.65	20	0.381	0.31
Small aggregate	1.80	200	23.1	22.0
Large aggregate	1.60	500	34.7	32.0

Figures 4.30 shows the DEMs, overlaid by the colors representing net elevation change after 30 iterations of *r.terrodyn*, for the baseline and for each of the soil types in table 4.5. The net elevation change for the sand, small aggregate and large aggregate soil types was very similar. The maximum net elevation change occurred for the silt soil type. This suggests that, for a fixed $K_t=0.1$, $K_d=0.0074$ resulted in a near-optimal overland erosion parameter space close to but not quite transport limited, allowing for a more spatially uniform increase in sediment load with down slope distance less sensitive than transport limited erosion to flow variations. In general, erosion was detachment-limited for the clay and silt soil types and transport-limited for the larger soil types.

Figures 4.31-4.34 show the water depth, sediment flux, discharge, and SIMWE erosion / deposition patterns for the clay, silt, sand, and small aggregate soil types, respectively. The large aggregate results were very similar to the small aggregate results and are therefore excluded.

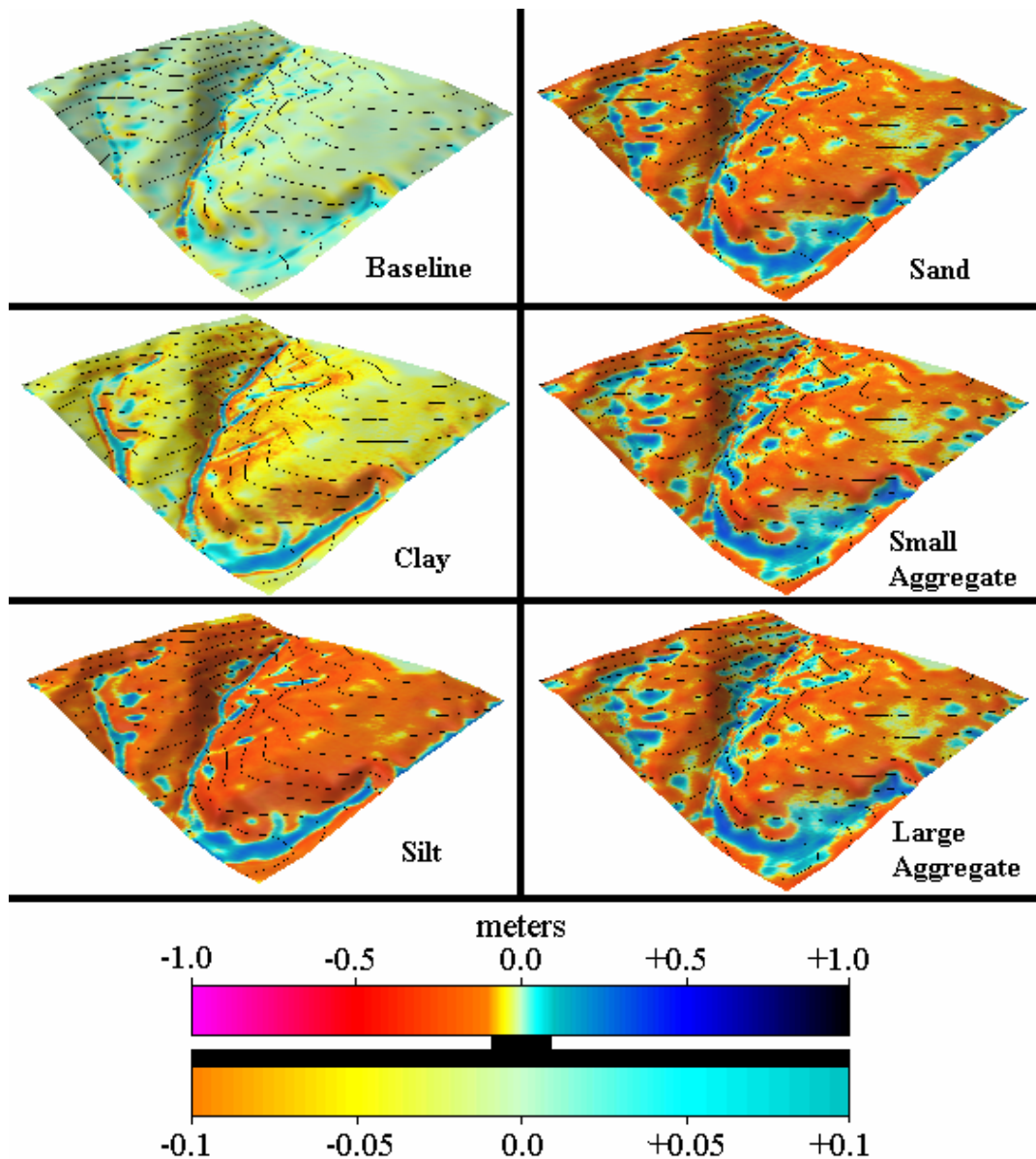


Figure 4.30: The modified DEM of the Lake Wheeler sub-watershed after 30 r.terrodyn iterations for the baseline and for the 5 soil types in which $K_t=0.1$ was constant and $K_d = 0.00089$ (clay), $=0.0074$ (silt), $=0.031$ (sand), $=2.2$ (small aggregates), $=3.2$ (large aggregates).

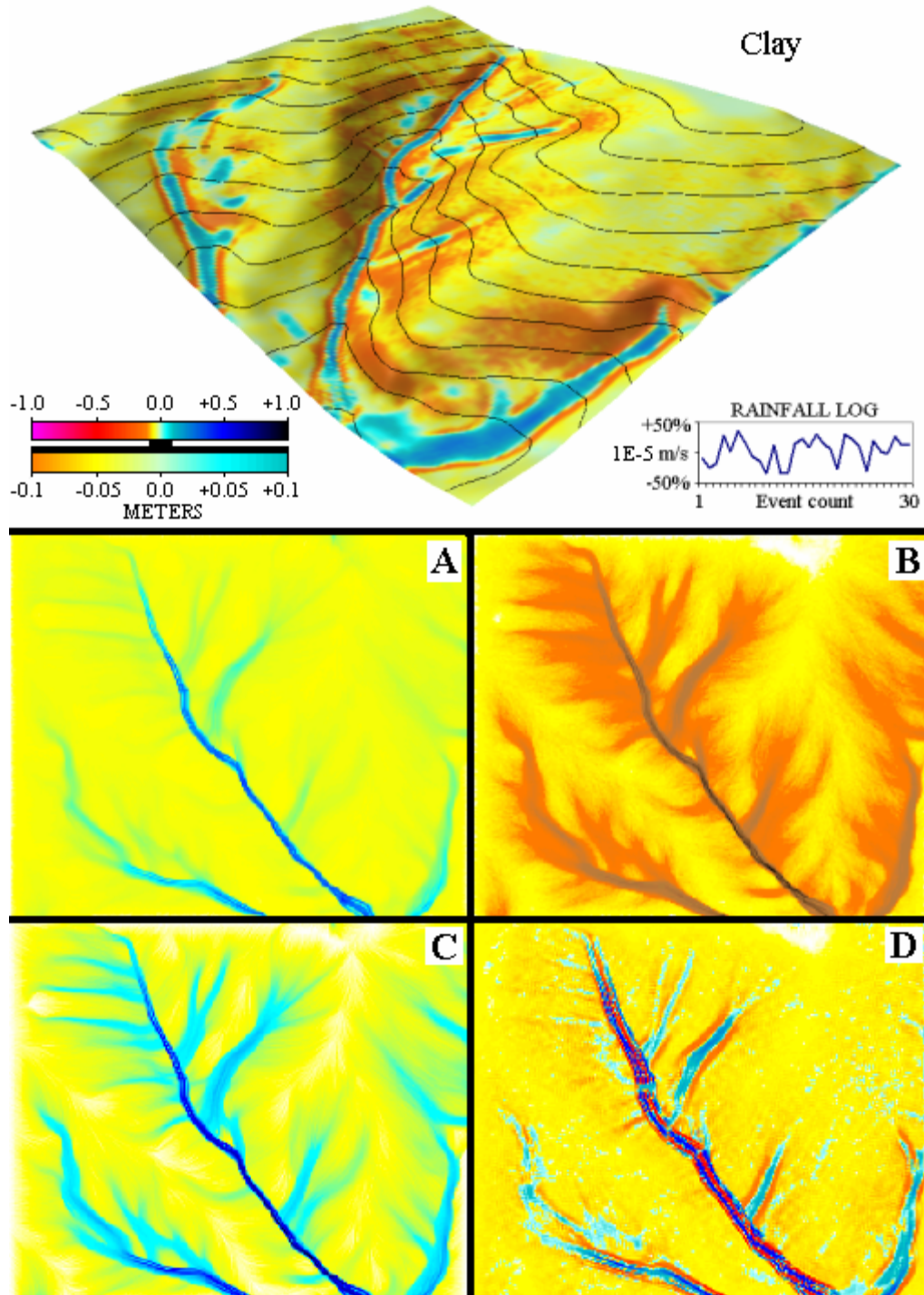


Figure 4.31: The modified DEM of the Lake Wheeler sub-watershed after 30 r.terrodyn iterations with $K_t=0.1$ and $K_d=0.00089$ (clay). Also included are the (A) water depth [m], (B) sediment flux [$\text{kg}/\text{m}/\text{s}$], (C) flow discharge [m^3/s], and (D) erosion / deposition pattern (smoothed) [$\text{kg}/\text{m}^2/\text{s}$] from r.sim.sediment (not used by r.terrodyn) at iteration #28, in which the rainfall was $1.4\text{E}-5 \text{ m/s}$.

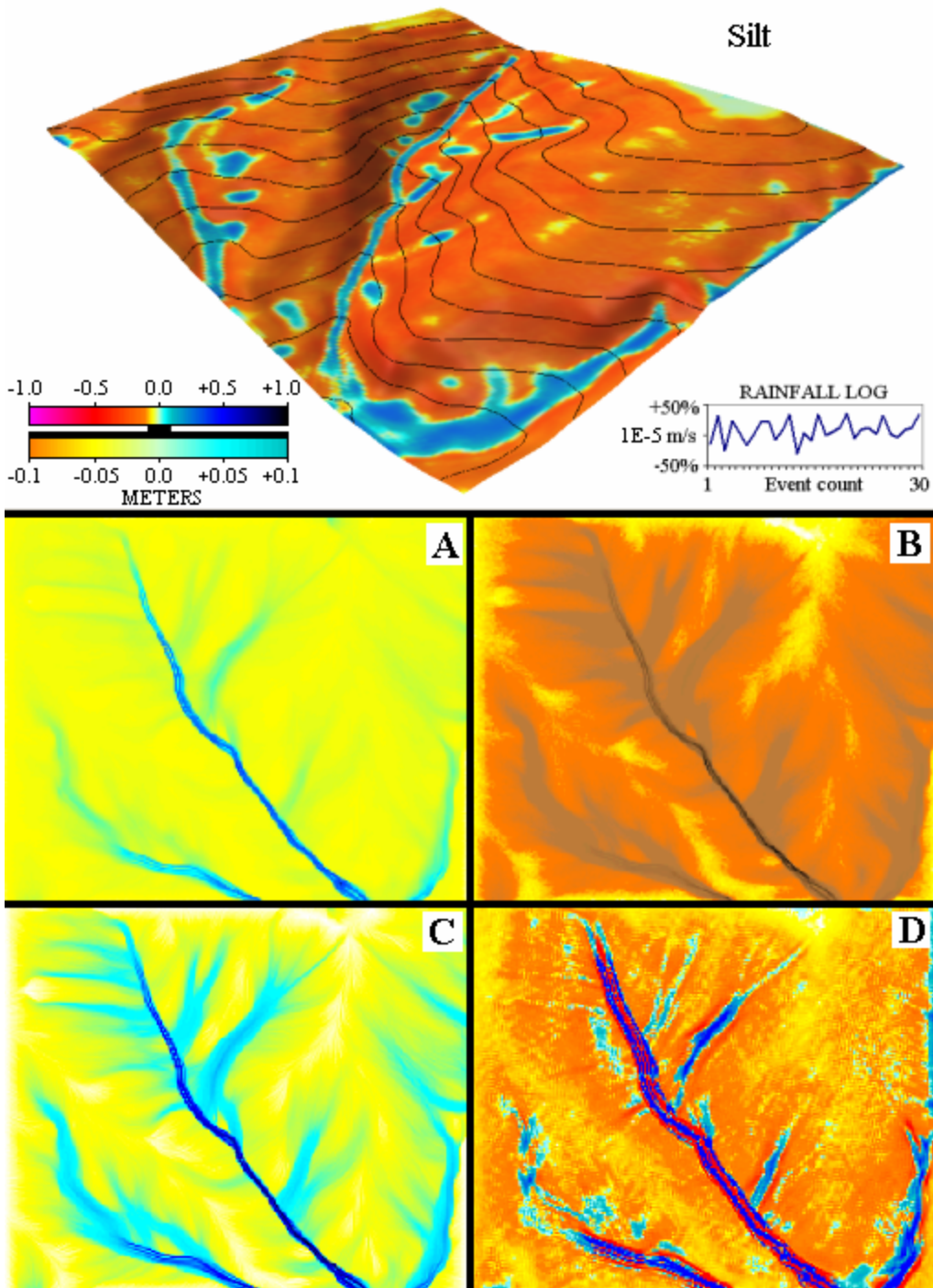


Figure 4.32: The modified DEM of the Lake Wheeler sub-watershed after 30 r.terrodyn iterations with $K_t=0.1$ and $K_d=0.0074$ (silt). Also included are the (A) water depth [m], (B) sediment flux [kg/m/s], (C) flow discharge [m^3/s], and (D) erosion / deposition pattern (smoothed) [$kg/m^2/s$] from r.sim.sediment (not used by r.terrodyn) at iteration #30, in which the rainfall was $1.5E-5$ m/s.

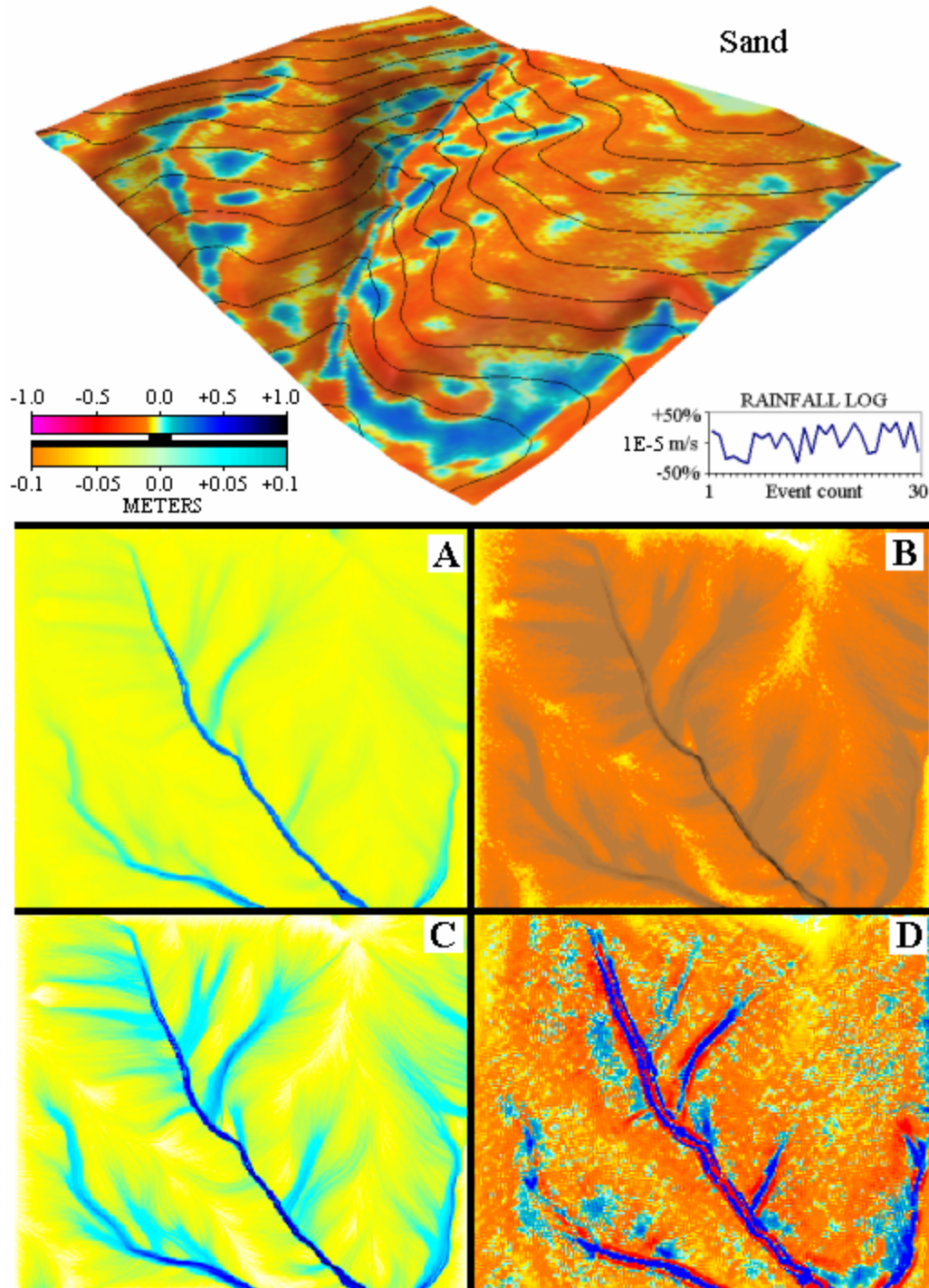


Figure 4.33: The modified DEM of the Lake Wheeler sub-watershed after 30 r.terrodyn iterations with $K_t=0.1$ and $K_d=0.031$ (sand). Also included are the (A) water depth [m], (B) sediment flux [$\text{kg}/\text{m}^2/\text{s}$], (C) flow discharge [m^3/s], and (D) erosion / deposition pattern (smoothed) [$\text{kg}/\text{m}^2/\text{s}$] from r.sim.sediment (not used by r.terrodyn) at iteration #27, in which the rainfall was $1.5\text{E}-5 \text{ m/s}$.

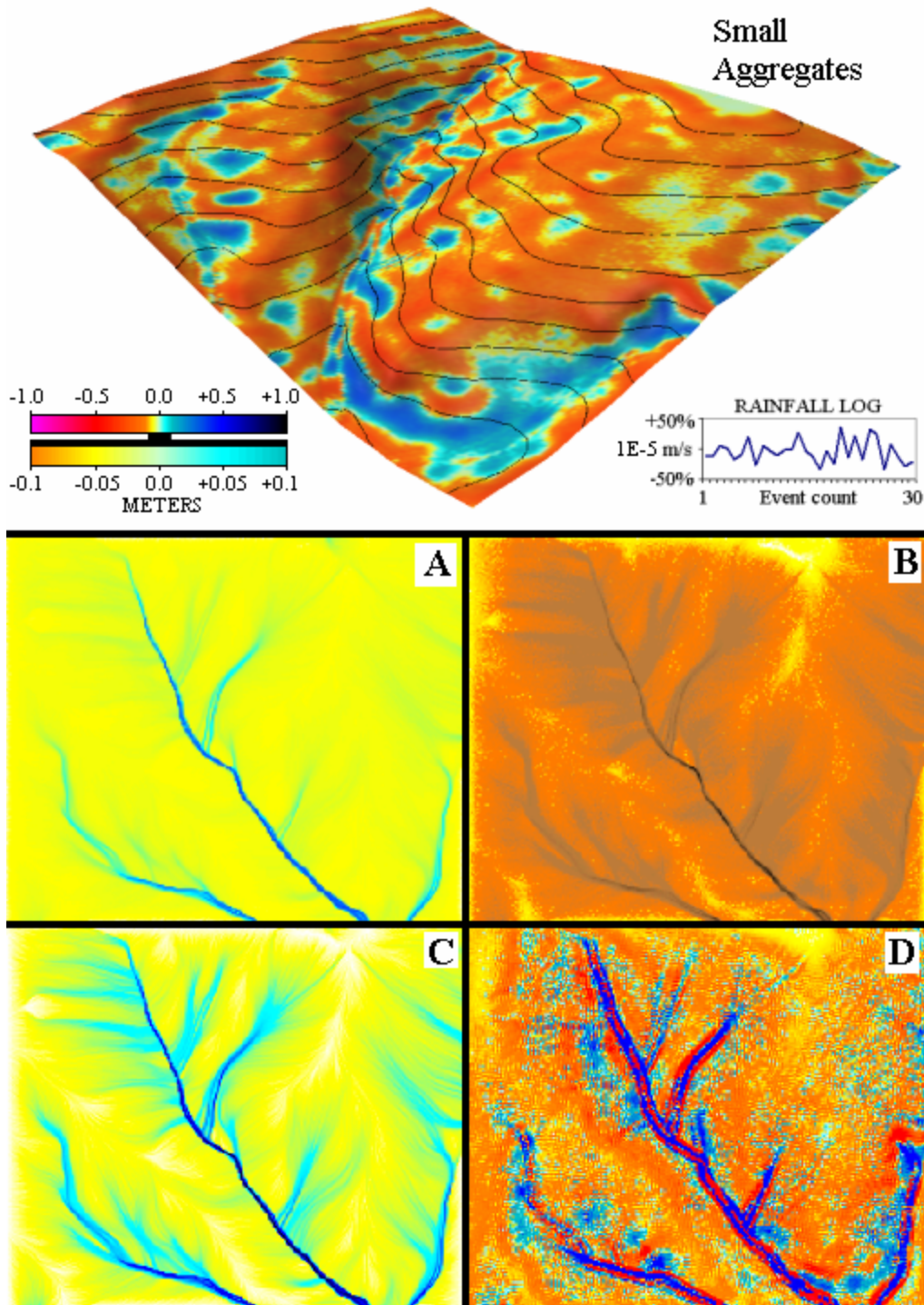


Figure 4.34: The modified DEM of the Lake Wheeler sub-watershed after 30 r.terrodyn iterations with $K_t=0.1$ and $K_d=2.2$ (small aggregates). Also included are the (A) water depth [m], (B) sediment flux [$\text{kg}/\text{m}^2/\text{s}$], (C) flow discharge [m^3/s], and (D) erosion / deposition pattern (smoothed) [$\text{kg}/\text{m}^2/\text{s}$] from r.sim.sediment (not used by r.terrodyn) at iteration #25, in which the rainfall was $1.3\text{E}-5 \text{ m/s}$.

4.6.4.2 Terrain evolution for different soil types

To more closely simulate the actual behavior of different soil types within *r.terrodyn*, a second set of simulations were performed in which K_t , K_d , and τ_c were varied per table 4.6. The values for σ from table 4.5 were maintained while K_t decreased and K_d increased with increasing grain size. Critical shear varied from 0.01 for clay to 1.0 for the large aggregates.

Table 4.6: Grain size specific parameters chosen for the soil types simulated.

Soil type	K_t	K_d	σ	τ_c
Clay	0.1000	0.00089	0.0089	0.01
Silt	0.0200	0.00148	0.0740	0.05
Sand	0.0050	0.00155	0.3100	0.10
Small Aggregates	0.0005	0.01100	22.000	0.80
Large Aggregates	0.0004	0.01280	32.000	1.00

Figures 4.35 shows the DEMs, overlaid by the colors representing net elevation change after 30 iterations of *r.terrodyn*, for the baseline and for each of the soil types in table 4.6. As seen in figure 4.36 for sand, all soil types showed negligible sensitivity to the change in critical shear stress - variations in the DEM due to changes in shear stress between 0.01 and 1.00 were on the same scale as those induced by the random fluctuations in rainfall rates applied in these simulations. For silt and larger grain sizes, a marked reduction in erosion and deposition was obtained as compared to the fixed K_t runs. As in the fixed K_t runs, the maximum net elevation changed occurred for the silt sized grains, although with the reduced K_t and K_d , terrain modification was much more similar in magnitude of the clay sized grains.

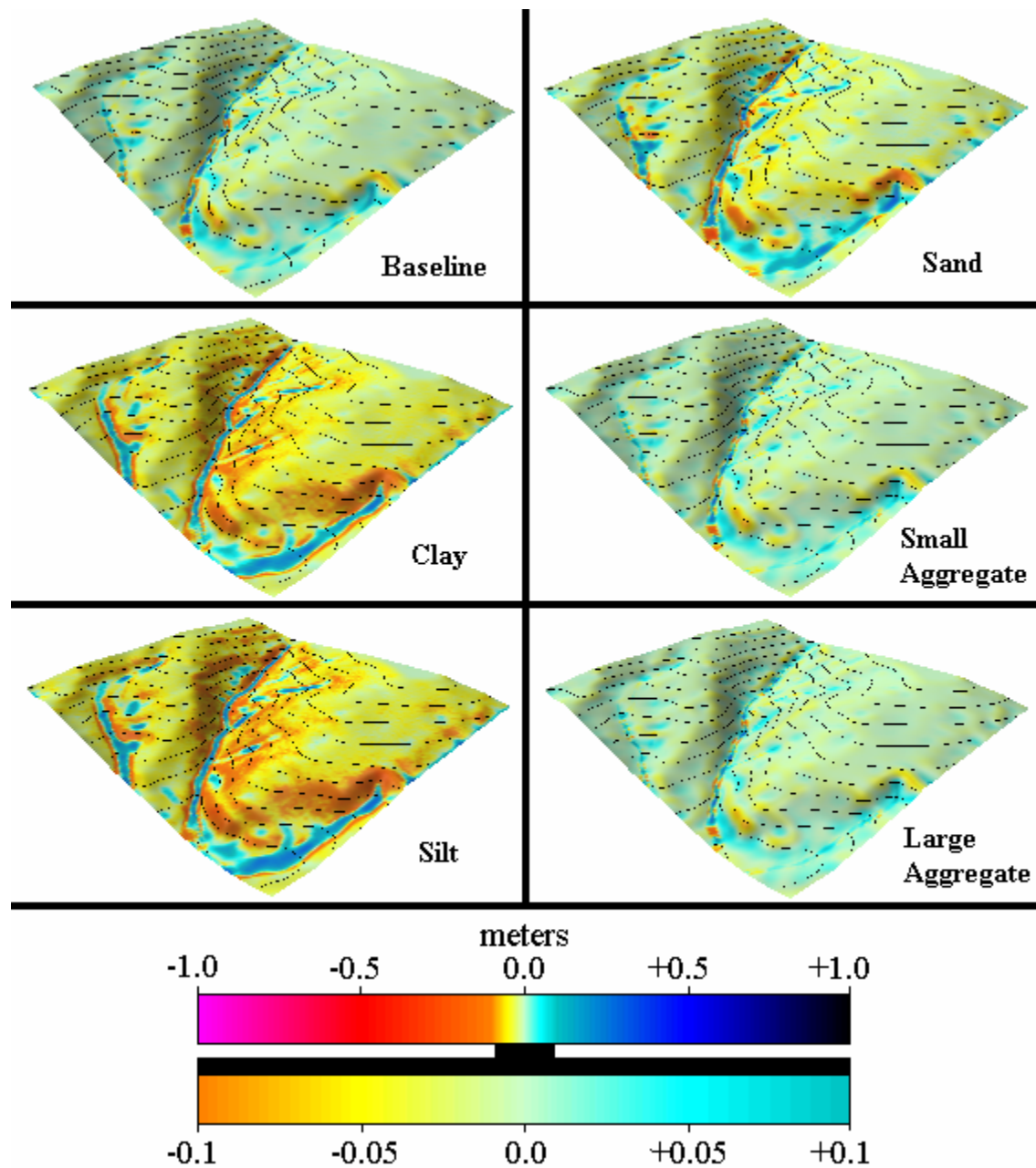


Figure 4.35: The modified DEM of the Lake Wheeler sub-watershed after 30 r.terrodyn iterations for the baseline and for the 5 soil types in which $K_t=0.1$ and $K_d=0.00089$ (clay), $K_t=0.02$ and $K_d=0.00148$ (silt), $K_t=0.005$ and $K_d=0.00155$ (sand), $K_t=0.0005$ and $K_d=0.0110$ (small aggregates), and $K_t=0.0004$ and $K_d=0.0128$ (large aggregates).

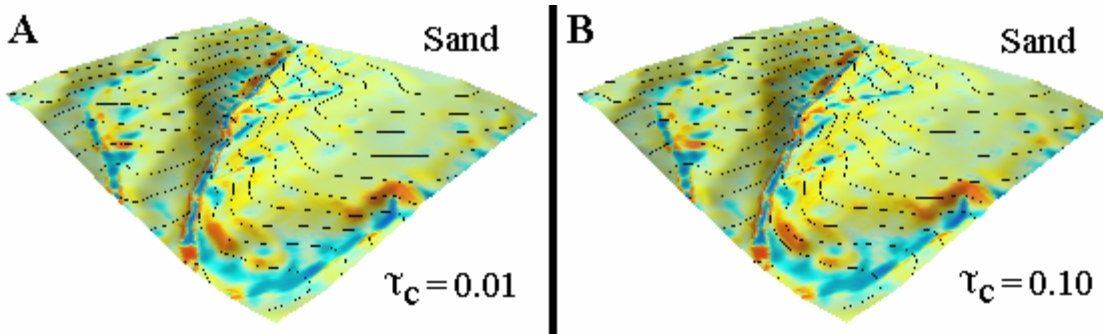


Figure 4.36: The modified DEM of the Lake Wheeler sub-watershed after 30 r.terrodyn iterations for sand with critical shear stress f (A) 0.10 and (B) 0.01 (all other parameters were equivalent).

Figures 4.37-4.40 show the water depth, sediment flux, discharge, and SIMWE erosion / deposition patterns for the clay, silt, sand, and small aggregate soil types, respectively. The large aggregate results were very similar to the small aggregate results and are therefore excluded. Although clay had a much higher transport capacity once entrained in the flow, the detachment of clay was limited by a low erodibility factor, producing erosion and deposition that was significantly greater than the baseline run but much less than the larger grain sizes with the same K_t (figs. 4.30-4.34). The higher erodibility of the larger grains was offset by the low transportability once entrained - this resulted in a much less active net erosion / deposition behavior within the watershed. However, the susceptibility of the larger grains to localized variations in shear stress, transported under transport-limited conditions, yielded more spatial variation in the net erosion / deposition patterns, which was best observed at high values K_t (figs. 4.32-4.34). Larger grain sizes are observed in the field to be detached with greater ease but are transported over shorter distances, a behavior which may explain the simulation results presented.

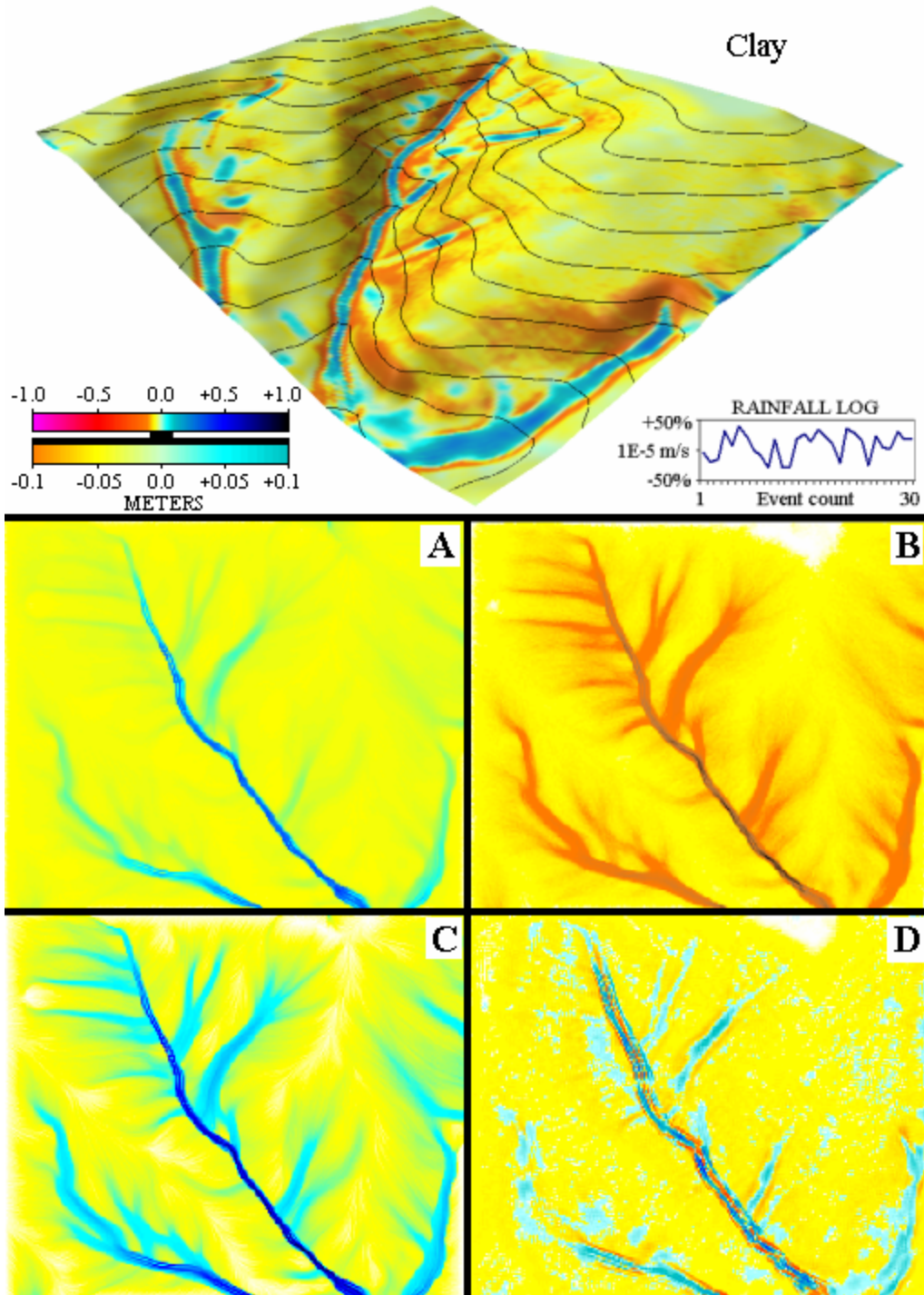


Figure 4.37: The modified DEM of the Lake Wheeler sub-watershed after 30 r.terrodyn iterations with $K_t=0.1$ and $K_d=2.2$ (small aggregates). Also included are the (A) water depth [m], (B) sediment flux [$\text{kg}/\text{m}^2/\text{s}$], (C) flow discharge [m^3/s], and (D) erosion / deposition pattern (smoothed) [$\text{kg}/\text{m}^2/\text{s}$] from r.sim.sediment (not used by r.terrodyn) at iteration #30, in which the rainfall was $1.2 \times 10^{-5} \text{ m/s}$.

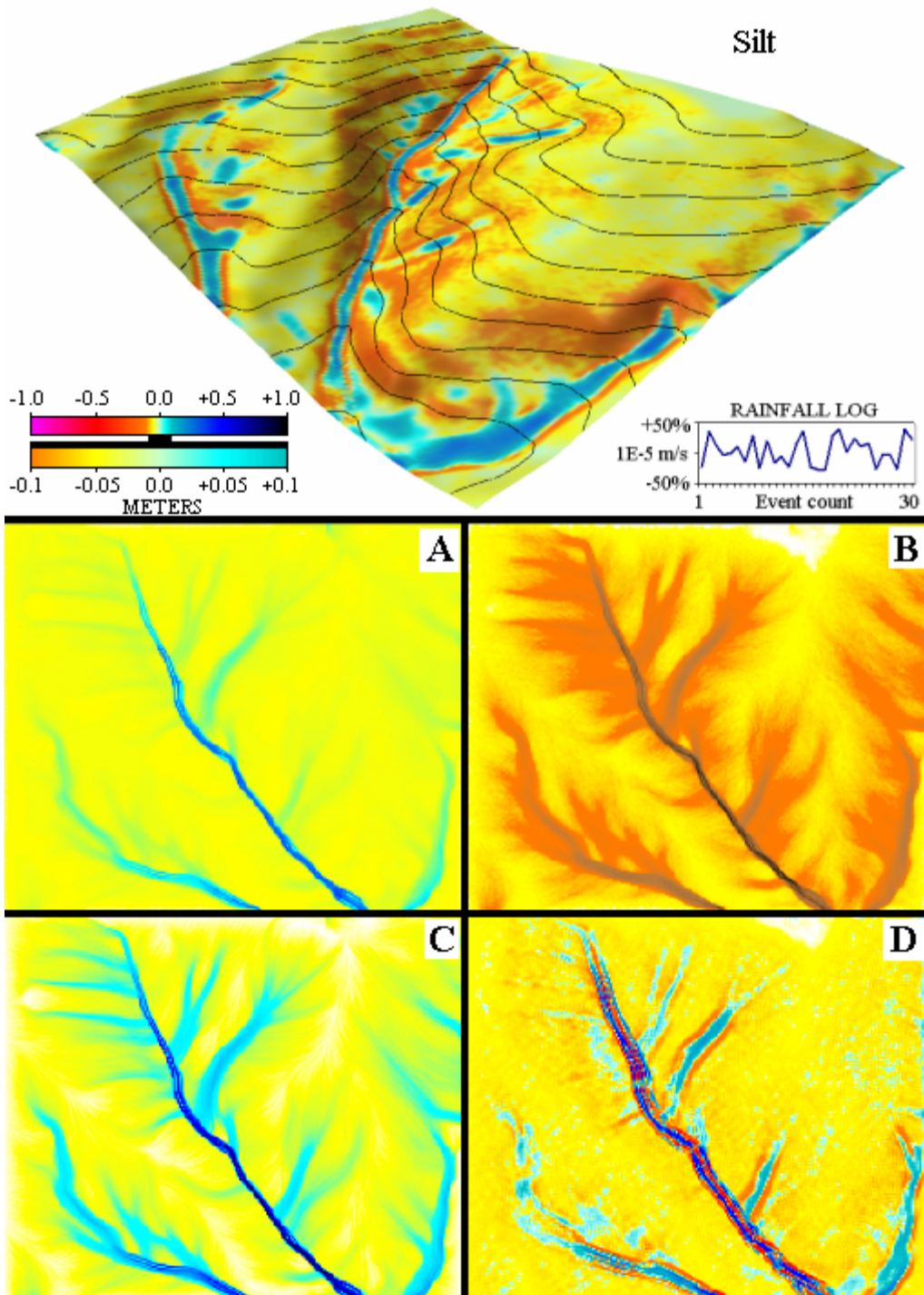


Figure 4.38: The modified DEM of the Lake Wheeler sub-watershed after 30 r.terrodyn iterations with $K_t=0.1$ and $K_d=2.2$ (small aggregates). Also included are the (A) water depth [m], (B) sediment flux [kg/m/s], (C) flow discharge [m^3/s], and (D) erosion / deposition pattern (smoothed) [kg/m²/s] from r.sim.sediment (not used by r.terrodyn) at iteration #30, in which the rainfall was 1.2E-5 m/s.

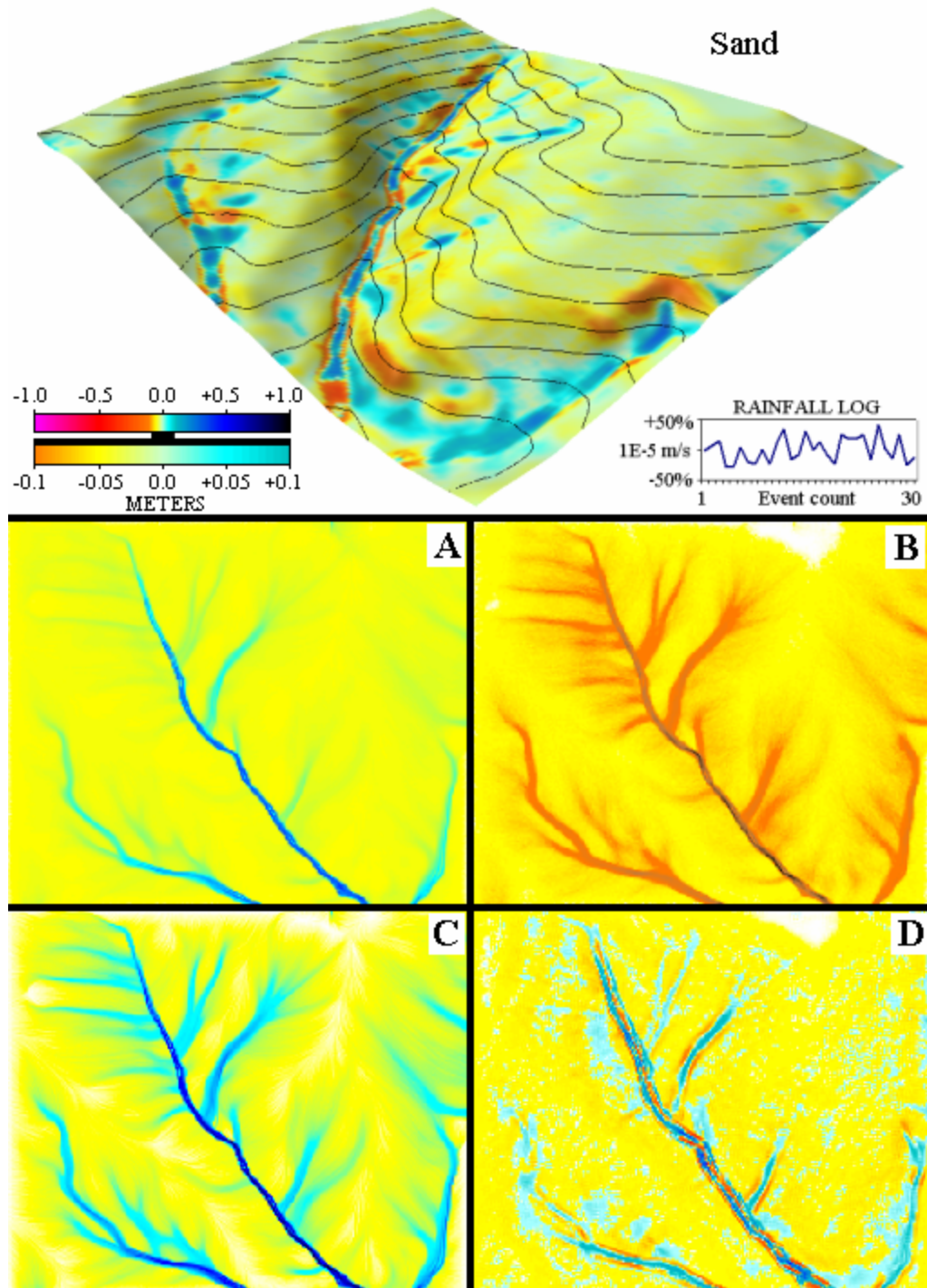


Figure 4.39: The modified DEM of the Lake Wheeler sub-watershed after 30 r.terrodyn iterations with $K_t=0.1$ and $K_d=2.2$ (small aggregates). Also included are the (A) water depth [m], (B) sediment flux [$\text{kg}/\text{m}/\text{s}$], (C) flow discharge [m^3/s], and (D) erosion / deposition pattern (smoothed) [$\text{kg}/\text{m}^2/\text{s}$] from r.sim.sediment (not used by r.terrodyn) at iteration #28, in which the rainfall was $1.3\text{E}-5 \text{ m}/\text{s}$.

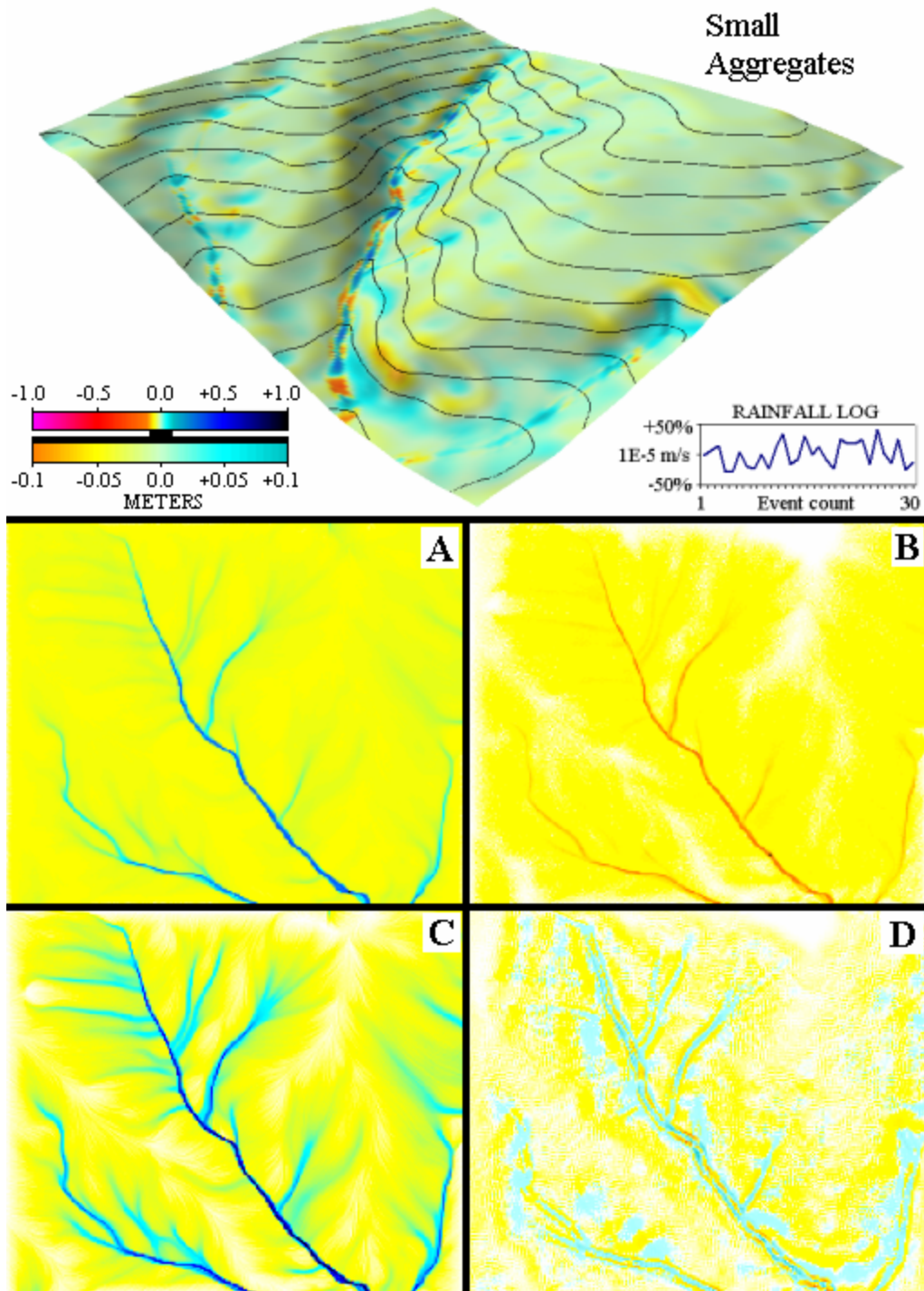


Figure 4.40: The modified DEM of the Lake Wheeler sub-watershed after 30 r.terrodyn iterations with $K_t=0.1$ and $K_d=2.2$ (small aggregates). Also included are the (A) water depth [m], (B) sediment flux [$\text{kg}/\text{m}^2/\text{s}$], (C) flow discharge [m^3/s], and (D) erosion / deposition pattern (smoothed) [$\text{kg}/\text{m}^2/\text{s}$] from r.sim.sediment (not used by r.terrodyn) at iteration #30, in which the rainfall was $1.0\text{E}-5 \text{ m/s}$.

4.6.4.3 Results from a disturbed watershed

A final set of simulations was performed to model the effects of disturbance by removing the land cover at selected locations within the study region (fig. 4.41). The region was assumed to have the same distributed land cover as in figure 4.27 but with the previously identified areas of row crops (see fig. 4.18) replaced by the cover properties of bare clay with a Manning's n of 0.10, K_t of 0.10, K_d of 0.00089, and a τ_c of 0.01. Distributed rainfall infiltration as in figure 4.23 for the CNII-D antecedent and soil conditions was applied but with an infiltration of 94 for the bare clay. Module *r.terrodyn* was run for 15 iterations (~1 year) to model the duration of an extended construction project in the disturbed areas. The results of this simulation are presented in figure 4.42. Erosion was predicted for the disturbed areas with significant deposition along the boundaries. Deposition within the channels was confined upstream from the watershed outlet due to the buffer land cover (grass-meadow). Vegetation within these areas of deposition would be threatened by the accumulation of sediment.

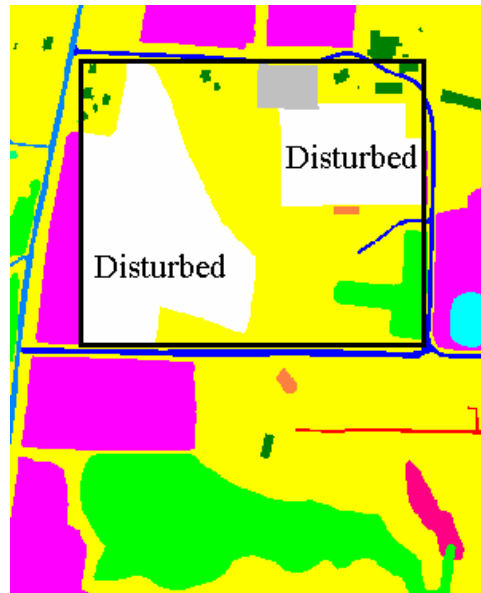


Figure 4.41: The disturbed land cover map of the Lake Wheeler sub-watershed in which the cover properties of bare clay were applied in the areas previously identified as row crops.

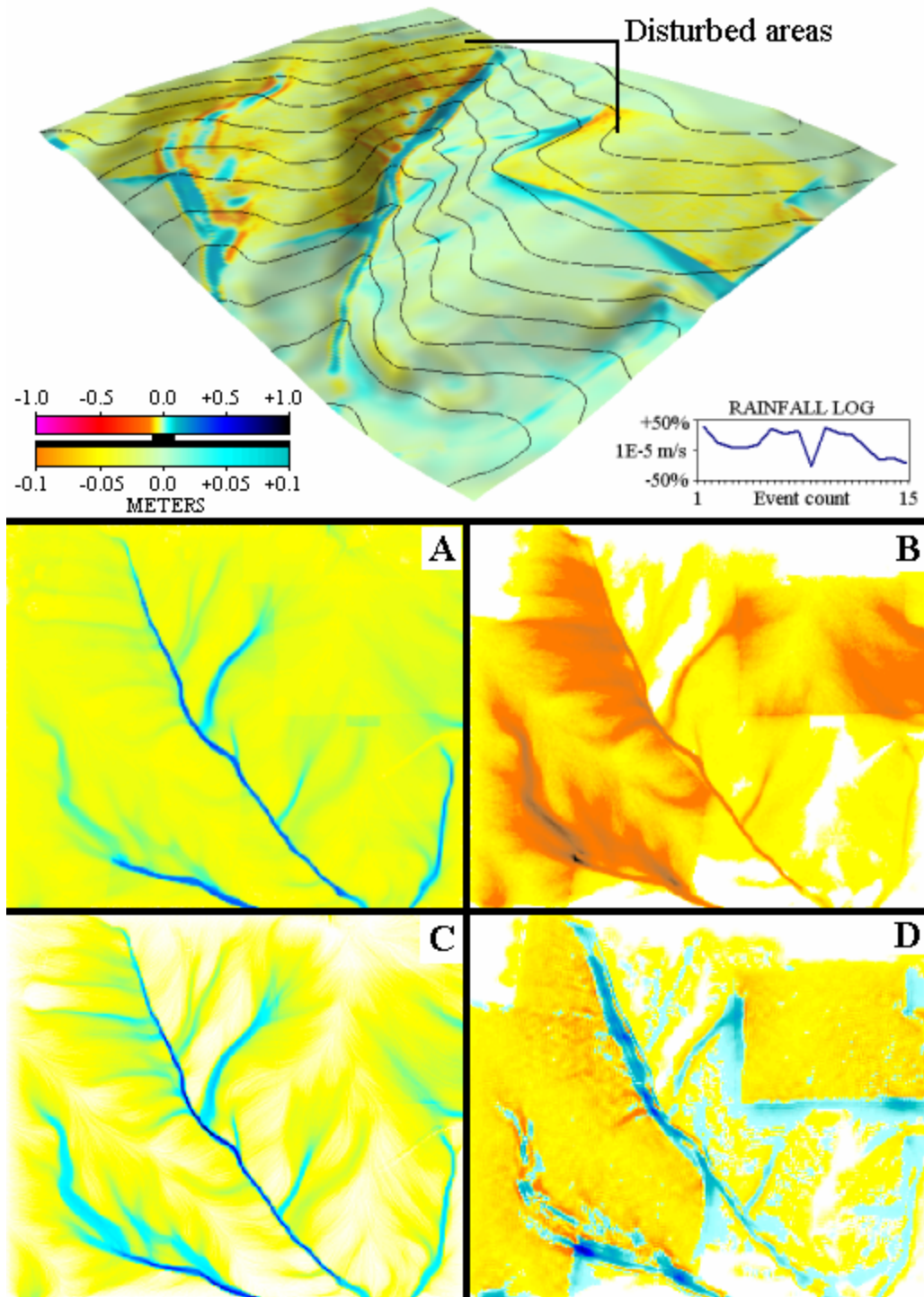


Figure 4.42: The modified DEM of the Lake Wheeler sub-watershed after 30 r.terrodyn iterations with $K_t=0.1$ and $K_d=2.2$ (small aggregates). Also included are the (A) water depth [m], (B) sediment flux [$\text{kg}/\text{m}^2/\text{s}$], (C) flow discharge [m^3/s], and (D) erosion / deposition pattern (smoothed) [$\text{kg}/\text{m}^2/\text{s}$] from r.sim.sediment (not used by r.terrodyn) at iteration #12, in which the rainfall was $1.3E-5$ m/s.

4.6.5 Discussion and Conclusions

Due to the lack of field measurements corresponding to these simulations, model verification is limited to observations at the Lake Wheeler Road watershed. However, due to the shallow hill slopes and the existence of substantial, static land cover throughout the watershed, elevation changes in general have been minimal over the span of the last 2 years. This is consistent with the small terrain changes modeled as seen for the baseline runs and for the distributed land cover and rainfall infiltration runs. In general, primary terrain change took the form of erosion of steeper slopes and channel banks, as well as deposition in areas of reduced transport capacity. During the evolution of the terrain, channels braided and meandered and rills are either incised or filled in, depending on the intensity of the individual rainfall events. Less terrain change was modeled for drier antecedent conditions (CNI) and for the type A soils, as well as for simulations employing distributed land cover. Higher rainfall rates were employed in the distributed land cover simulations to illustrate the potentially damaging sediment deposition in areas of lower transport capacity such as wooded areas. This effect was also obtained from simulations in which disturbed areas of bare clay were included in the study region.

Bare soil simulations used for grain size comparison demonstrated with reasonable skill the relative behaviors of grain size dependent erosion and deposition normally observed in the field. These results are also consistent with the presented SEDATE model runs. Small grains, transported under detachment-limited conditions, were detached but did not redeposit without significant reductions in transport capacity as seen in the channels and other areas of upward topographical convexity. Larger grains,

transported under transport-limited conditions, detached and were transported small distances such that the terrain evolved with higher spatial variation in the erosion / deposition patterns relative to the small grain size runs. In addition, the grain size dependent simulation results showed that sediment erosion and deposition and terrain evolution was weakly sensitive to changes in the critical shear stress ranging from 0.01 to 1.00 - the magnitude of sensitivity toward this range in critical shear was on the same scale as variations in soil erosion and deposition and terrain evolution that arose due to the randomization of the input rainfall rates.

In this version of *r.terrodyn*, terrain change stability is highly sensitive to the channel morphology. Without the band-pass filter, channel incision artificially dominated under all land cover conditions presented here - important small scale effects on the hillslopes become difficult to discern due to the processing necessary to visualize the results. Ideally, the band-pass filter would not be necessary. This would only be possible if the applied shear stress was not dependent on flow depth above a depth threshold. In the channels, where the water is the deepest, shear could be expressed as a function of flow velocity, as is common in bedload transport formalisms. Alternatively, SIMWE as currently defined could be modified such that the shear stress is based on the depth of the boundary layer - not the total flow depth. A maximum allowable flow depth, possibly scaled by flow velocity, could be imposed upon the algorithm for calculating shear stress. These or similar corrections would desensitize SIMWE to channel (deeper water) flows and permit *r.terrodyn* to function without concern for exponential channel incision or the need for the band-pass filter designed to attenuate this effect.

Appendix 4.A - Neumann boundary algorithm for use with *r.slope.aspect*

In *r.terrodyn*, an approximation to Neumann boundary conditions is applied. The values of the normal gradients of all functions are forced to near zero, for example:

$$(\vec{\nabla} \cdot \vec{z})_{\perp} \approx 0. \quad (4.52)$$

In all differentiation computations, *r.slope.aspect* replaces the boundary cells with null values. Module *r.terrodyn* replaces these nulls with an approximate value based on the average of the nearest non-null cells. The module *r.neighbors* is applied to the boundary cells with *method=sum* and *size=3*. The sum is then divided by 3 and placed into the previously null cell. The result is a boundary zone ($x=1, x=nx, y=1, y=ny; nx=number\ of\ x\ cells, ny=number\ of\ y\ cells$) that contains values that are approximately equivalent to the next innermost layer ($x=2, x=nx-1, y=2, y=ny-1$). This method approximates Neumann conditions well for smoothly varying boundaries (Figure 4.A.1). For boundaries with steep gradients in elevation, Neumann is violated but the boundaries remain stable (no divergent terrain change due to this treatment) and the model is allowed to run for many iterations (~100) before boundary effects infringe into the watershed by more than 2% of the domain (Figure 4.A.2). Other methods available through GRASS commands either produce unrecoverable errors (e.g. *r.fillnulls*) or prohibitively violate Neumann conditions (e.g *r.neighbors method=average, minimum, maximum, mode*), leading to errors that either rapidly migrate into the watershed or diverge into approximate singularities, primarily near the watershed outlet. In current applications, analysis is performed on a redefined region after the completion of all *r.terrodyn* time steps such that the new boundaries fall well within the original boundaries.

0.10	0.11	0.12	0.13	0.14
	0.11	0.12	0.13	
Boundary				Previously NULL (from r.slope.aspect)

NULL NULL NULL NULL NULL

Figure 4.A.1 For smoothly varying boundaries, Neumann conditions are satisfied very well. The normal gradient in this example is exactly zero.

0.11	0.10	0.12	0.17	0.13
	0.11	0.12	0.13	0.14
Boundary				Previously NULL (from r.slope.aspect)

NULL NULL NULL NULL NULL

Figure 4.A.2: For steeply varying boundaries, Neumann conditions are not well satisfied. However, since the normal gradients are less than that of the lateral variations, boundary evolution remains localized and stable over many iterations.

Appendix 4.B - Random number generator (*rng.sh*) for randomizing rainfall rates

The random number generator script used by *r.terrodyn* for random rainfall generation is as follows:

```
RandomDevice=/dev/urandom
MaxRand=18446744073709551616      # 2^64
[ $# -lt 1 ] && set -- $MaxRand
hex=`dd if=/dev/urandom bs=1 count=8 2>/dev/null |
od -tx1 | head -1 | cut -d' ' -f2- |
tr -d ' ' | tr '[a-f]' '[A-F]'` 
dec=`echo "ibase=16; $hex" | bc` 
echo >&2 "DEBUG: hex=<$hex>; dec=<$dec>" 
echo "$dec % $1 + 1" | bc
```

Bibliography

- Andersen, K.H. 2001. A particle model of rolling grain ripples under waves, *Physics of Fluids* 13(1): 58-64
- Bagnold, R.A. 1956. The flow of cohesionless grains in fluids, *Philosophical Transactions of the Royal Society of London Series A-Mathematical and Physical Sciences*, 249 (964), 235-&.
- Bagnold, R.A., 1966. An approach to the sediment transport problem from general physics, U.S. Geol. Survey Prof. Papers, 429-I, 33pp.
- Bagnold, R.A. 1980. An empirical correlation of bedload transport rates in flumes and natural rivers, *Proceedings of the Royal Society of London A* 372, pp. 453-473
- Barfield, B.J., R.C. Warner, and C.T. Haan. 1983. *Applied hydrology and sedimentology for disturbed areas*, Stillwater Oklahoma: Oklahoma Technical Press
- Barrett, M.E., J.F. Malina Jr., and R.J. Charbeneau. 1998. An evaluation of geotextiles for temporary sediment control. *Water Environment Research* 70(3): 283-290
- Batchelor, G.K. 1967. *An introduction to fluid dynamics*, 615 pp., Cambridge University Press, Cambridge
- Bennett, J.P. 1974. Concepts of mathematical modeling of sediment yield, *Water Resources Research* 10(3): 485-492
- Borah, D.K. and M. Bera. 2003. Watershed-scale hydrologic and nonpoint-source pollution models: review of mathematical bases, *Transactions of the ASAE* 46(6): 1553-1566
- Brown, C.B. 1950. Sedimentation transportation. In *Engineering Hydraulics*, Edited by H. Rouse, Chapter 12. Hoboken, NJ: John Wiley & Sons.
- Breu, A.P.J., H.M. Ensner, C.A. Kruele, and I. Rehberg. 2003. Reversing the brazil-nut effect: competition between percolation and condensation, *Physical Review Letters* 90(1):014302-1 - 014302-3
- Brune, G.M. 1953. Trap efficiency of reservoirs, *Trans. American Geophysical Union* 34(3): 407-418

Cairns, J. and K.L. Dickson. 1971. A simple method for the biological assessment of the effects of waste discharges on aquatic bottom-dwelling organism. *Journal Water Pollutant Control Federation* 43(5): 755-772

Calantoni, J. 2002. *Discrete particle model for bedload sediment transport in the surf zone*, Ph.D. Thesis, North Carolina State University, Raleigh.

Camp,T.R., 1973. Discussion of “Sedimentation in Quiescent and Turbulent Basins” by J.J. Slade, Jr., ASCE Transactions, Vol.102, pp306-314, 1937. In *Civil Engineering Classics – Outstanding Papers of Thomas R. Camp*. New York, NY: ASCE.

Camp,T.R. 1946. Sedimentation and the design of settling tanks, *Trans. Am. Soc. Civil Eng.* 111:895-958

Cao, Z. 1999. Equilibrium near-bed concentration of suspended sediment, *Journal of Hydraulic Engineering*, 125(12), pp. 1270-1278

Chang, H.W. and J.C. Hill. 1976. Computer modeling of erodible flood channels and deltas, *Journ. of the Hydraulics Div., Proc. of the ASAE* 14(4):625-628

Chen, C. 1975. Design of sediment retention basins. In *Proceedings National Symposium of Urban Hydraulic Sediment Control*. Lexington, KY: Univ. of Kentucky

Chow, V.T., D.R. Maidment, and L.W. Mays. 1988. *Applied hydrology*, McGraw-Hill, NY, NY

Clesceri, L.S., A.E. Greenberg, and A.D. Eaton, eds. 1998. *Standard methods for the examination of water and wastewater, 20th edition*, American Public Health Association, American Water Works Association, and water Environmental Federation, pp.2-57,2-58

Cline, L.D., R.A. Short, and J.V. Ward. 1982. The influence of highway construction on the macroinvertebrates and epilithic algae of a high mountain stream. *Hydrobiologia* 96: 149-159

Daily, J.W., and D.R.F. Harleman. 1966. *Fluid Dynamics*. Reading, Massachusetts: Addison-Wesley

Davis, S.S. 1978. *Deposition of nonuniform sediment by overland flow on concave slopes*, M.S. Thesis, Purdue University, West Lafayette, IN, pp. 137

Deigaard, R. and J. Fredsoe, 1978, Longitudinal grain sorting by current in alluvial streams, *Nordic Hydrology* Vol. 9:7-16

- Dietrich, W.E., C. J. Wilson, D. R. Montgomery, and J. McKean. 1993. Analysis of erosion thresholds, channel networks, and landscape morphology using a digital terrain model, *Journal of Geology*, 101(1), 259-278
- Dingman, S.L. 1984. *Fluvial hydrology*, W.H. freeman & Co., New York
- Dobbins, W.E. 1944. Effect of turbulence on sedimentation. *Trans. ASCE* 109: 629-678
- Drake, T.G. and J. Calantoni. 2001. Discrete particle model for sheet flow sediment transport in the nearshore, *Journal of Geophysical Research - Oceans*, 106(C9), 19859-19868
- Drake, T.G., R.L. Shreve, W.E. Dietrich, P.J. Whiting, and L.B. Leopold. 1988. Bedload transport of fine gravel observed by motion-picture photography, *Journal of Fluid Mechanics*, 192:193-217
- Dolgunin, V.N., A.N. Kudy, and A.A. Ukolov. 1998. Development of the model of segregation of particles undergoing granular flow down and inclined chute, *Powder Technology* 96: 211-218
- Einstein, H.A. 1950. The bedload function for sediment transportation in open channel flows. *U.S. Department of Agriculture Technical Bulletin No. 1026*. Washington, D.C.: USDA
- Einstein, H.A. 1968. Deposition of suspended particles in a gravel bed, *Journal of Hydraulics Div., Proc. of the ASCE* 94(HY5), 1197-1205
- Einstein, H.A. and N. Chein. 1954. *Second approximation to the solution of the suspended load theory*, Fluid mechanics laboratory, University of California, Berkeley
- Elgar, S. 1987. Relationships involving 3rd moments and bispectra of a harmonic process, *IEEE Transactions on Acoustics, Speech, and Signal Processing*, 35(12): 1725-1726
- Environmental Protection Agency. 1986. *Methodology for analysis of detention basin design for control of urban runoff*. Office of Water Nonpoint Division, EPA 440/5-87-001, pub. no. 841B86108. Washington, D.C.: U.S. Environmental Protection Agency

- Ehrhart, B.J., R.D. Shannon, and A.R. Jarrett. 2002. Effects of construction site sedimentation basins on receiving stream ecosystems. *Trans. ASAE* 45(3): 675-680
- Ellison, W.D. and O.T. Ellison. 1947. Soil erosion studies part VI, soil detachment by surface flow, *Agricultural engineering* 28(9): 402-405
- Fennessey, L.A.J. and A.R. Jarrett. 1997. Influence of principle spillway geometry and permanent pool depth on sediment retention of sedimentation basins. *Transactions of the ASAE* 40(1): 53-59
- Fisher, L.S. and A.R. Jarrett. 1984. Sediment retention efficiency of synthetic filter fabric. *Transactions of the ASAE* 27(2): 429-436
- Foster, G.R. 1982. Modeling the Erosion Process, from *Hydrologic Modeling of Small Watershed*, ed. By C.T. Haan, H.P. Johnson, D.L. Brakensiek, ASAE
- Foster, G.R., L.J. Lane, M.A. Nearing, S.C. Finkner, and D.C. Flanagan. 1989. *USDA-Water Erosion Prediction Project (WEPP), Hillslope Profile Model Documentation*, Chapter 10, Erosion Component, NSERL Report No. 2, USDA-ARS National Soil Erosion Research Laboratory, West Lafayette, IN
- Foster, G.L. and L.D. Meyer. 1972. A closed-form soil erosion equation for upland areas, in *Sedimentation: Symposium to honor Professor H.A. Einstein*, ed. By H.W. Shen, pp. 12.1-12.19
- Foster, G.L. and L.F. Huggins. 1977a. Deposition of sediment by overland flow on concave slopes, in: *Soil Erosion Prediction and Control*, Special Publication No. 21, Soil Conservation Society of America, Ankeny, IA, pp. 167-182
- Foster, G.R., L.D. Meyer, and C.A. Onstad. 1977b. A runoff erosivity factor and variable slope length exponents for soil loss estimates, *Transactions of the ASAE*, 20(4): 683-687
- Foster, G.R., D.C. Yoder, G.A. Weesies, and T.J. Toy. 2001. The design philosophy behind RUSLE2: evolution of an empirical model, pp. 95-98 in *Soil Erosion Research for the 21st Century, Proc. Int. Symp.* (3-5 January 2001, Honolulu, HI, USA). Eds. J.C. Ascough II and D.C. Flanagan. St. Joseph, MI: ASAE. 701P0007.
- Ferguson, R., T. Hoey, S. Wathen, and A. Werritty. 1996. Field evidence for rapid downstream fining of river gravels through selective transport, *Geology* 24: 179-182

- Gallagher, E.L., S. Elgar, and R.T. Guza. 1998. Observations of sand bar evolution on a natural beach, *Journal of Geophysical Research*, 103(C2): 3203-3215
- Gasparini, N.M., G.E. Tucker, R.L. Bras, 1999, Downstream fining through selective particle sorting in an equilibrium drainage network, *Geology* 27(12): 1079-1082
- Goldman, S.J., K. Jackson, and T.A. Bursztynsky. 1986. *Erosion and sediment control handbook*. New York, NY: McGraw-Hill
- Govers, G. 1990. *Empirical relationships for the transport capacity of overland flow*, IAHS publication 189: 44-63
- Govers, G. 1992. Evaluation of transporting capacity formulae for overland flow, Chapter 11 in: *Overland Flow: hydraulics and erosion mechanics*, Ed. By A.J. Parsons and A.D. Abrahams, London, UCL Press
- Govindaraju, R.S. and M.L. Kavvas. 1991. Modeling the erosion process over steep slopes: approximate analytical solutions, *Journal of Hydrology*, 127: 279-305
- Graf, W.H.. 1971. *Hydraulics of Sediment Transport*. New York, NY: McGraw-Hill
- Gray, L.J. and J.V. Ward. 1982. Effects of sediment releases from a reservoir on stream macroinvertebrates. *Hydrobiologia* 96: 177-184
- Greb, S.R. and R.T. Bannerman. 1997. Influence of particle size on wet pond effectiveness. *Water Environment Research* 69(6): 1134-1138
- Greenwood, B. and Z. Xu. 2001. Size fractionation by suspension transport: a large scale flume experiment with shoaling waves, *Marine Geology* Vol. 176: 157-174
- Griffin, M.L., B.J. Barfield, and R.C. Warner. 1985. Laboratory studies of dead storage in sediment ponds. *Transactions of the ASAE* 28(3): 799-804
- Guza, R.T. and E.B. Thornton. 1980. Local and shoaled comparisons of sea surface elevations, pressures, and velocities, *Journal of Geophysical Research*, 85C, 1524-1530.
- Haan, C.T., B.J. Barfield, and J.C. Hayes. 1994. *Design Hydrology and Sedimentology for Small Catchments*. San Diego, California: Academic Press

- Hayes, S. 2003. *Polyacrylamide use for erosion and turbidity control on construction sites*, Master's thesis, Department of Soil Science, North Carolina State University, Raleigh, NC
- Hazen, A. 1904. On sedimentation. *Trans. ASCE*. 53: 45-71
- Hoefel, F. and S. Elgar. 2003. Wave induced sediment transport and sandbar migration, *Science* 299: 1885-1887
- Horikawa, K. 1988. *Nearshore dynamics and coastal processes*, University Tokyo Press, Tokyo.
- Horn, B.K.P. 1981. Hill shading and the reflectance map, *Proceedings of the IEEE*, 69(1), 14-47.
- Hsieh Wen Shen and P.Y. Julien. 1993. Erosion and sediment transport, Chapter 5 in: *Handbook of Hydrology*, ed. By D.R. Maidment, McGraw Hill, New York
- Huang, C., L.K. Wells, and L.D. Norton. 1999. Sediment transport capacity and erosion processes: model concepts and reality, *Earth Surface Processes and Landforms* 24, pp. 503-516
- Hunt, A.G. 1999. A probabilistic treatment of fluvial entrainment of cohesionless particles, *Journal of Geophysical Research*, 104(B7), pp.15,409-15,413
- Jarrett, A.R. 1996. Sedimentation basin evaluation and design improvements, final completion report for Orange County Board of Commissioners. Hillsborough, NC.
- Jiang, Z. and P.K. Haff. 1993. Multiparticle simulation methods applied to the micromechanics of bed load transport, *Water Resources Research* 29: 388-412
- Julien. P.Y. and D.B. Simons, 1985, Sediment transport capacity of overland flow, *Transactions of the ASAE* 28(3), 755-762
- Karrambas, T.V. and C. Koutitas. 2002. Surf and swash zone morphology evolution induced by nonlinear waves, *Journal of Waterway, Port, Coastal and Ocean Engineering*, 128(3), 102-113.
- King, D.B. 1991. *Studies in oscillatory flow bedload sediment transport*, 184p., Ph.D. dissertation thesis, University of California San Diego.
- Kleinhaus, M.G. 2001. The key role of fluvial dunes in transport and deposition of sand-gravel mixtures, a preliminary note, *Sedimentary Geology* 143: 7-13

- Knighton, A.D. 1999. The gravel-sand transition in a distributed catchment, *Geomorphology* 27: 325-341
- Kraus, N.C., A. Lohrmann, and R. Cabrera. 1994. New acoustic meter for measuring 3D laboratory flows, *Journal of Hydraulic Engineering* 120(3): 406-411
- Kuenen, P.H. 1956. Experimental abrasion of pebbles: 2. Rolling by current, *Journal of Geology* 64: 336-368
- Lei, T., M.A. Nearing, K. Haghghi, and D.A. Bulgakov. 1997. A model of soil erosion in a rill: Temporal evolution and spatial variability, ASAE Paper No. 973068, *ASAE Annual International Summer Meeting*, ASAE, St. Joseph, MI: ASAE
- Lemmin, U. and R. Lhermitte. 1999. ADV measurements of turbulence: can we improve their interpretation? *Journal of Hydraulic Eng.*, Sept. 1999: 987-988
- Line, D.E. and N.M. White. 2001. Efficiencies of temporary sediment traps on two North Carolina construction sites. *Transactions of the ASAE* 44(5): 1207-1215
- Loch, R.J. 2001. Settling velocity - a new approach to assessing soil and sediment properties, *Computers and Electronics in Agriculture*, 31, 305-316
- Low, H.S. 1989. Effect of sediment density on bedload transport, *Journal of Hydraulic Engineering* 115, pp. 124-138
- Madsen, O.S. 1991. Mechanics of cohesionless sediment transport in coastal waters, *Coastal Sediments*, 15-27.
- Maske, H.A., S. Havlin, P.R. King, and H.E. Stanley. 1997. Spontaneous stratification in granular mixtures, *Nature* Vol. 386: 379-324
- Mayack, D.T. and J.S. Waterhouse. 1983. The effects of low concentrations of particulates from paper mill effluent on the macroinvertebrate community of a fast flowing stream. *Hydrobiologia* 107: 271-282
- McEwan, I.K., B.J. Jeffcoate, and B.B. Willetts. 1999. The grain-fluid interaction as a self-stabilizing mechanism in fluvial bed load transport, *Sedimentology* 46: 407-416
- McLaughlin, R. A., W. F. Hunt, N. Rajbhandari, D. S. Ferrante, and R.E. Sheffield. 2001. The sediment and erosion control research and education facility at North Carolina State University, in *Soil Erosion Research for the 21st Century*. J. C. Ascough II and D. C. Flanagan, eds. Am. Soc. Ag. Eng., St. Joseph, MI, USA.

- Millen, J.A., A.R. Jarrett and J.W. Faircloth. 1997. Experimental evaluation of sedimentation basin performance for alternative dewatering systems. *Transactions of the ASAE* 40(4): 1087-1095.
- Mills, T.R. and M.L. Clar. 1976. Erosion and sediment control – Surface mining in the Eastern U.S. EPA 615 /2-76-006. Washington, D.C.: U.S. Environmental Protection Agency.
- Mitas, L. and H. Mitasova. 1998. Distributed soil erosion simulation for effective erosion prevention, *Water Resources Research*, 34(3), pp. 505-516, March
- Mitasova, H., J. Hofierka, M., Zlocha, and L.R. Iverson. 1996. Modeling topographic potential for erosion and deposition using GIS, *International Journal of Geographical Information Systems* 10(5): 629-641
- Montgomery, D.R. and W.E. Dietrich. 2003. Channel initiation and the problem of landscape scale, *Science* Vol. 255: 33-43
- Morgan, R.P.C, Quinton, J.N., Smith, R.E., Govers, G., Poesen, J.W.A., Auerswald, K., Chisci, G., Torri, D., & Styczen, M.E. 1998. The European soil erosion model (EUROSEM) : a process-based approach for predicting sediment transport from fields and small catchments. *Earth Surface Processes and Landforms* 23, 527-544.
- Nearing, M.A., L.D. Ascough, and H.M.L. Chaves. 1989. *USDA-Water Erosion Prediction Project (WEPP), Hillslope Profile Model Documentation*, Chapter 14, WEPP model sensitivity analysis, NSERL Report No. 2, USDA-ARS National Soil Erosion Research Laboratory, West Lafayette, IN
- Nearing, M.A. and S.C. Parker, 1994, Detachment of soil by flowing water under turbulent and laminar conditions, *Soil Science Society of America Journal*, 58(6): 1612-1614
- Nelson, J.M., R.L. Shreve, S.R. McLean, and T.G. Drake. 1995. Role of near-bed turbulence structures in bed load transport and bed form mechanics, *Water Resources Research*, 31(8): 2071-2086
- Neteler, M. and H. Mitasova. 2002. *Open source GIS: A GRASS GIS approach*, Kluwer Academic Publishers, Boston, MA
- North Carolina Department of Environment and Natural Resources (NCDENR), Division of Water Quality. 1995. Stormwater Management Policy T15A:02H.1000. Raleigh, NC: NCDENR

- Paola, C., G. Parker, R. Seal, S.K. Sinha, J.B. Southard, and P.R. Wilcock. 1992. Downstream fining by selective deposition in a laboratory flume, *Science* 258: 1757-1760
- Paola, C. and R. Seal. 1995. Grain size patchiness as a cause of selective deposition and downstream fining, *Water Resources Research*, 31(5), 1395-1407.
- Parker, G. and P.C. Klingeman. 1982. On why gravel bed streams are paved, *Water Resources Research* 18(5): 1409-1433
- Parker, G., P.C. Klingeman, and D.G. McLean. 1982. Bedload and size distribution in paved gravel-bed streams, *Journal of Hydraulic Engineering*, 108(4): 544-571
- Parker, G., C. Paola, and S. Leclair. 2000. Probabilistic Exner sediment continuity equation for mixtures with no active layer, *Journal of Hydraulic Engineering*, 126(11), 818-826
- Polyakov, V.O. and M.A. Nearing. 2003. Sediment transport in rill flow under deposition and detachment conditions, *Catena* v.51, 33-43
- Press, W.H., B.P. Flannery, S.A. Teukolsky, and W.T. Vetterling. 1990. *Numerical recipes, the art of scientific computing (FORTRAN version)*, Cambridge University Press, Cambridge, MA
- Rauhofer, J., A.R. Jarrett and R.D. Shannon. 2001. Effectiveness of sedimentation basins that do not totally impound a runoff event. *Trans. ASAE* 44(4): 813-818
- Reid, I, J.C. Bathurst, P.A. Carling, D.E. Walling, and B.W. Webb. 1997. Sediment erosion, transport, and deposition, Chapter 5 in: *Applied fluvial geomorphology for river engineering and management*, ed. By C.R Thorne, R.D Hey, and M.D. Newson, Wiley, pp. 95-135
- Renard, K.G., G.R. Foster, G.A. Weesies, D.K. McCool, and D.C. Yoder. 1997. *Predicting soil erosion by water: a guide to conservation planning with the revised universal soil loss equation RUSLE*, USDA, Agric. Handbook No. 703, pp. 404, U.S. Department of Agriculture, Washington, D.C.
- Richardson, J.F. and W.N. Zaki, 1954, The sedimentation of a suspension of uniform spheres under conditions of viscous flow, *Chemical Engineering Science*, 3(2): 65-73
- Rosato, A, K.J. Strandburg, F. Prinz, and R.H. Swendsen. 1987. Why the Brazil nuts are on top: size segregation of particulate matter by shaking, *Physical Review Letters* 58(10): 1038-1040

- Savage, S.B. and C.K.K. Lun. 1988. Particle size segregation in inclined chute flow of dry cohesionless granular solids, *Journal of Fluid Mechanics* Vol. 189: 311-335
- Seal, R., C. Paola, G. Parker, J.B. Southard, and P.R. Wilcock. 1997. Experiments on downstream fining of gravel: I. Narrow-channel runs, *Journal of Hydraulic Engineering* 123(1): 874-884
- Seminara, G, L. Solari, and G. Parker. 2002. Bedload on arbitrary sloping beds: Failure of the Bagnold hypothesis, *Water Resources Research*, 38(11), Art. No. 1249
- Seimnara, G.L., M. Colombini, and G. Parker, 1996, Nearly pure sorting waves and formation of bedload sheets, *Journal of Fluid Mechanics*, 312: 253-278
- Shields, I.A., 1936, Application of similarity principles and turbulence research to bedload movement, a translation from the German by W.P. Ott and J.C van Vchelin, U.S. Soil Conservation Service Coop. Lab, California Inst. Of Tech., Pasedena, CA.
- Shinbrot, T. and F.J. Muzzio. 2000. Nonequilibrium patterns in granular mixing and segregation, *Physics Today*, Mar 2000: 25-30
- Singh, V.P. 2002. Is hydrology kinematic?, *Hydrological Processes*, 16, pp. 667-716
- Simons, D.B. and F. Senturk. 1992. *Sediment Transport Technology*. Fort Collins, CO: Water Resources Publications.
- Soil Conservation Service. 1986. Urban hydrology for small watersheds, Technical release No. 55, Soil Conservation Service, U.S. Department of Agriculture, Washington, DC
- Song, T., W.H. Graf and U. Lemmin. 1994. Uniform flow in open channels with moveable gravel bed. *Journal of Hydraulic Engineering* 32(6): 861-876
- Tennekes, H. and J.L. Lumley. 1972. *A first course in turbulence*. Cambridge, Massachusetts: The MIT Press
- Thaxton, C.S and R.A. McLaughlin. 2003. Hydrodynamic and sediment capture assessment of various baffles in a sediment basin, in *Total Maximum Daily Load (TMDL) Environmental Regulations-II Proceedings of the 8- 12 November 2003 Conference* (Albuquerque, New Mexico USA), Proceedings of the TMDL environmental regulations conference, ASAE, St. Joseph, MI: 557
- Thaxton, C.S., J.Calantoni, and R.A. McLaughlin. 2004. Hydrodynamic assessment of various baffles in a sediment retention pond, *Transactions of the ASAE*, In print.

- Thaxton, C.S., J. Calantoni, and T.G. Drake. 2001. Can a single grain size represent bedload transport in the surf zone?: EOS Trans. AGU, 82(47), Fall Meeting Supplement, F587 (Special session in honor of Dr. Thomas Kinder), AGU
- Tucker, G., S. Lancaster, N. Gasparini, and R. Bras. 2001. The channel-hillslope integrated landscape development model (CHILD), in *Landscape erosion and evolution modeling*, edited by R. S. Harmon and W. W. Doe III, pp. 349-388, Kluwer Academic/Plenum Publishers, New York.
- Tucker, G.E. and R.L. Bras. 1998. Hillslope processes, drainage density, and landscape morphology, *Water Resources Research* 34(10): 2751-2764
- Velikanov, M.A.. 1954. Principle of gravitational theory of the movement of sediments, *Acad. of Sci. Bul.*, USSR, Geophy. Series No. 4, pp. 349-359
- Ven Te Chow, D.R. Maidment, and L.W. Mays. 1988. *Applied hydrology*, McGraw-Hill, New York
- Wahl, T.L. 2001. *WinADV32.exe*. Ver. 1.849, Water Resources Laboratory, U.S. Bureau of Reclamation, Denver, CO.
- Ward, A.D., C.T. Haan and B.J. Barfield. 1979. Prediction of sediment basin performance. *Trans. ASAE* 22(1): 126-136
- Warner, R.C. and M.C. Hirschi. 1983. Modeling check dam trap efficiency. ASAE Paper No. 83-2082. St. Joseph, MI: ASAE
- Wathen, S.J., R.I. Ferguson, T.B. Hoey, and A. Werritty. 1995. Unequal mobility of gravel and sand in weakly bimodal river sediments, *Water Resources Research* 31(8): 2087-2096
- Watson, R.L. 1969. Modified Rubey's Law accurately predicts sediment settling velocities. *Water Resources Research* 5:1147-1150
- Werner, B.T. 1995. Eolian dunes: Computer simulations and attractor interpretation, *Geology* 23(12): 1107-1110
- Whiting, P.J., W.E. Deitrich, L.B. Leopold, T.G. Drake, and R.L. Shreve. 1988. Bedload sheets in heterogeneous sediment, *Geology* 16: 105-108
- Wijetunge, J.J. and J.F.A. Sleath. 1998. Effects of sediment transport on bed friction and turbulence, *Journal of Waterway, Port, and Coastal Ocean Engineering*, 124: 172-178

- Willgoose, G., R.L. Bras, and I. Rodriguez-Iturbe. 1991. A coupled channel network growth and hillslope evolution model 1. Theory, *Water Resources Research*, 27(7), 1671-1684
- Williams, J.R. 1975. Sediment routing for agricultural watersheds, *Water Resources Bulletin*, 11(5): 965-974
- Williams, J.R. 1976. Sediment yield prediction with Universal Equation using runoff energy factor, in *Proceedings and prospective technology for predicting sediment yields and sources*, Publication ARS-S-40, Agricultural Research Service, U.S. Department of Agriculture, Washington, D.C.
- Williams, J.R. 1977. Sediment delivery ratios determined with sediment and runoff models, in *Proceedings, erosion and solid matter transport in inland water symposium*, IAHS No. 122: 168-179
- Williams, J.R. 1978. A sediment yield routing model, In *Proceedings, American Society of Civil Engineers conference*, Verification of mathematical and physical models in hydraulic engineering: 662-760, ASCE, New York
- Wilson, B.N. and B.J. Barfield. 1986. Hydrology and Sedimentology Watershed Model, Part I: Modeling Techniques, Dept. of Agricultural Engineering, University of Kentucky, Lexington, KY.
- Wischmeier, W.H. and D.D. Smith. 1965. Predicting rainfall-erosion losses from cropland east of the Rocky Mountains-A guide for selection of practices for soil and water conservation, *Agricultural Handbook No. 282*. U.S. Department if Agriculture, Washington, D.C.
- Wischmeier, W.H. and D.D. Smith. 1978. Predicting rainfall erosion losses -A guide to conservation planning, *Agricultural Handbook No. 537*. U.S. Department if Agriculture, Washington, D.C.
- Yalin, M.S. 1963. An expression for bedload transportation, *Journal of the Hydraulics Division, Proc. of the ASCE* 89, pp. 221-250
- Yang, C.T. 1973. Incipient motion and sediment transport, *Journal of the Hydraulics Division, Proc. of the ASCE* 99, pp. 1679-1703
- Young, R.A. and C.A.Onstad. 1978. Characterization of rill and interrill eroded soil, *Transactions of the ASAE* 21(6): 1126-1130